Miniaturization and Distinguishability Limits of Electrical Impedance Tomography for Biomedical Application

By

Pascal Olivier Gaggero

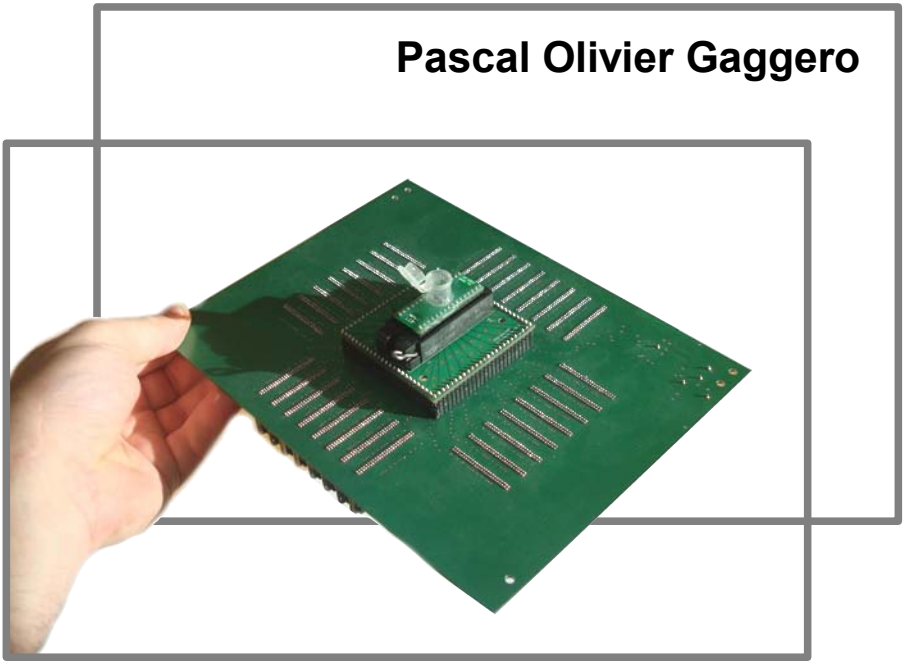

A dissertation submitted to the Faculty of Science
of the University of Neuchâtel for the degree of
Doctor of Science on 23 June 2011

Prof. Pierre Thomann, Université de Neuchâtel, Switzerland
Prof. Peter Seitz, Ecole Polytechnique Fédérale de Lausanne, Switzerland
Prof. Philipp Aebi, Université de Neuchâtel, Switzerland
Prof. Andy Adler, Carleton University, Canada

unine
UNIVERSITÉ DE NEUCHÂTEL

csem centre suisse d'électronique et de microtechnique

Université de Neuchâtel

FACULTE DES SCIENCES
Secrétariat-Décanat de la faculté
Rue Emile-Argand 11
CH-2000 Neuchâtel

IMPRIMATUR POUR LA THESE

Miniaturization and distinguishability Limits of Electrical Impedance Tomography for Biomedical Application

Pascal GAGGERO

UNIVERSITE DE NEUCHATEL

FACULTE DES SCIENCES

La Faculté des sciences de l'Université de Neuchâtel,
sur le rapport des membres du jury

MM. P. Seitz, co-directeur de thèse (IMT-EPF Lausanne),
P. Thomann, co-directeur de thèse (UniNe),
P. Aebi (Université de Fribourg)
et A. Adler (Carleton University, Ottawa, Canada)

autorise l'impression de la présente thèse.

Neuchâtel, le 23 juin 2011

Le doyen :
P. Kropf

Téléphone : +41 32 718 21 00 E-mail : secretariat.sciences@unine.ch www.unine.ch/sciences

Contents

Abstract

mot clés: tomographie, impédance, électrique, TIE, limites physiques, distinguabilité, micro-TIE

key words: tomography , impedance, electrical, EIT, physical limits, distinguishability, micro-EIT

Electrical Impedance Tomography (EIT) calculates an image of the conductivity distribution within a body from electrical stimulation and measurements at the body surface. This work develops advances in signal acquisition hardware, optimization of stimulation patterns, and analysis of detection limits for EIT. The EIT data acquisition and image reconstruction process is systematically analyzed with respect to the influence of noise and other measurement deficiencies on image quality. A complete EIT system with 32 active electrodes has been developed, with which the theoretical predictions could be verified and practical applications could be studied.

The novel concept of distinguishability is developed for a theoretical analysis of EIT system performance. It measures the likelihood that the measured differential EIT signal is generated by actual impedance changes and not by random fluctuations. This distinguishability criterion can be considered as a signal-to-noise ratio, and it serves as a valuable benchmark to assess the performance of EIT systems. Using numerical simulations, we have studied the optimum signal acquisition strategy for differential EIT signals, in order to maximize image quality. The most favorable angles between injecting and sinking electrode are found in the range from 60 to 150 degrees. We have also studied, theoretically as well as experimentally, the miniaturization limits of EIT systems. It is concluded that EIT system miniaturization is essentially determined by the Joule heating effect and the cooling rate of the sample volume. When scaling EIT systems up to very large dimensions, electronic noise on the sample (current injection and voltage measurements) finally limits the distinguishability in reconstructed EIT images.

A prototype of the developed hardware architecture was realized and proof-of-concept studies were carried out using both thoracic-EIT and the micro-EIT setups. As a major application of the work carried out in this thesis, we have demonstrated the capability of the developed EIT system to serve as a cost-effective real-time monitor for the reliable monitoring of the ventilation and cardiac related impedance changes on patients. The advances presented in this work can help build the capability of EIT to monitor and optimize mechanical ventilation of patients in intensive care units, which has the potential of enabling safer, automatic ventilation strategies, possibly preventing the unnecessary death of tens of thousands of patients every year.

Preface

In the first place I would like to thank Prof. Peter Seitz for welcoming me in his research facilities at Nanomedecine division of Centre Suisse d'Electronique et de Microtechnique (CSEM) in Landquart, Switzerland, and giving me the unique opportunity to work on a multidisciplinary and challenging project. When he first presented to me the Electrical Impedance Tomography technology, I was immediately enthusiastic about the multiplicity of applications and the potential to change the way in which the treatment of patients can be made much safer and more reliable. I guess the main reason why I choose this particular project was the potential of EIT to save lives and make a difference on a global scale.

My thanks and gratitude also go to the following people:

- Prof Pierre Thomann who kindly accepted to be my thesis supervisor at the University of Neuchâtel,
- Prof Andy Adler with whom we collaborated very closely,
- Prof Philipp Aebi for being a member of the doctoral thesis jury,
- Dr Josef Brunner, my direct supervisor at CSEM, with whom I had passionate debates about all the technological and marketing aspects of EIT,
- Dr Stephan Böhm, who introduced me to human physiology,
- Dr Killian Imfeld, with whom I had interesting discussions about the system architecture and noise propagation,
- Joachim Nüesch, for our valuable discussions about our mutual thesis projects,
- Thomas Gay, and Jürgen Rothmund, my laboratory colleagues, who helped me with the practical aspects of electronics and taught me how to solder properly and precisely.

- The CSEM Landquart team, whose professionalism and dedication – also during our "social meeting" every Wednesday – make Landquart a unique place to work,
- The collaborators from SUPSI (Scuola Universitaria Professionale della Svizzera Italiana) in Manno, with whom I worked very profitably.

Further my grateful thanks also go to my family, whose unconditional support and dedication, always allow me to pursue my dreams.

Landquart, May 2011 Pascal Olivier Gaggero

Chapter 1

Introduction

1.1 Problem statement

Electrical Impedance Tomography (EIT) is a tomographic imaging technique which calculates images of the conductivity within a body from surface measurements. Alternating electrical current is applied at a set of electrodes on the boundary of a medium, and the resulting potential field is measured. EIT has been investigated in many fields, such as medical imaging, geophysics, industry and life sciences. In general, the key attraction of EIT is that it enables prolonged monitoring of the patient (or medium) without using harmful ionizing radiation. Two EIT applications were of specific interest for this work: 1) monitoring of heart and lung activity in intensive care and anesthetized patients, and 2) label-free monitoring of ionic flow and conductivity targets in small (microlitre) solution volumes. At this time, EIT is still experimental for medical applications, and has not been used for regular patient care.

In the analysis of the author, the major problems restricting EIT from success in these applications, are the lack of a robust and easy to handle hardware system. To address robust measurements, a requirement was identified to carefully analyze electronic and physical noise sources, scalability and system distinguishability. Since most sources of error occur at the electrodes, a novel approach based on an active electrode belt was developed to address robustness and ease of use.

Additionally the success of EIT in non-invasive and real time monitoring of biological functions also depends on its ability to distinguish relevant information from the background noise. The aim of this thesis was therefore to

lay the theoretical grounds for distinguishability, to perform numerical simulations to evaluate the behavior of various EIT parameters and verify the simulation results by practical measurements. For the latter purpose, a complete EIT system was developed and built.

1.2 Goals and objectives

The main goals of the present thesis will be addressed in term of the following 6 objectives:

Objective 1: Development of a suitable architecture for a multipurpose EIT instrument.

EIT instruments can be designed in various ways, each possibility offering its advantages and disadvantages. The objective is to layout the basic design of the architecture in a flexible way facilitating the testing process and the integration of new features. The architecture of the system should allow a convenient handling of the hardware and avoid as far as possible calibration procedures of individual hardware pieces. For instance individual electrode handling should be avoided.

Objective 2 Development of the EIT system hardware.

Since the hardware development is a complex task the help of external partners with specialized skills, like Field-programmable Gate Array (FPGA) programming, is required. The task is to coordinate the outsourced hardware and software development to ensure proper interface compatibility between the modules and to propose enhancements for the next development iterations.

Objective 3: Development of the Graphical User Interface (GUI) and other software for the EIT system.

There is multipurpose GUI software for EIT systems that were available to us. Therefore, it is necessary to develop our own solution. It is also necessary to address the problem of the image reconstruction and to find a suitable way to integrate it in the GUI. Fortunately, there exists an open-source solution called EIDORS[1][4] which can calculates the necessary reconstruction matrices.

Objective 4: Testing of the EIT system.

[1] EIDORS stands for Electrical Impedance Tomography and Diffuse Optical Tomography Reconstruction Software, http://www.eidors.org

The hardware and software need to be carefully tested and understood. The test should be done in three phases: 1) testing of the electronics itself, 2) testing of the EIT system on two saline phantom (diameter 30 cm and 0.9 cm) and 3) testing on healthy volunteers. Volunteers testing is necessary to ensure that the EIT system works as expected and delivers the correct physiologically information about the ventilation and the cardiac activity. A flexible electronic design of the instrument components is necessary to enable quick hardware and software changes, or even to test many possible solutions without the need for a complete costly and time consuming hardware redesign. Nevertheless iterative design steps are necessary to aim toward an improved solution and to conceive new ideas.

Objective 5: Development of micro-EIT system based on the above hardware development.

The literature describes only a few attempts to miniaturize EIT systems. The goal is here to develop our own first micro-EIT prototype.

Objective 6: Study of the scalability and physical limit of an EIT system.

It is not yet clear in the literature what are the ultimate physical distinguishability limits of an object inside a given medium. The goal is to give a first approximate answer to the question and to develop methods to predict achievable imaging capabilities of general EIT systems.

1.3 Contribution per objective

Objective 1

The work done in the present thesis in the frame of the medical imaging problem, in collaboration with the startup company Swisstom AG[2], is our response to the need of the medical care professional for an easy to use and low cost EIT system. Various architectures types were studied and extensively tested during the project. The solution presented in this work is the result of all the research and development work performed. It consists of an active electrode based EIT system with a centralized innovative current source. The digital electronics including DAC, ADC and system controller was also integrated in the same central device as the current source. The electrodes form a belt-like structure which allows an easy handling procedure. Even a single person

[2] http://www.swisstom.com

could use the instrument without the help of someone else to manage the instrument. The developed hardware does not need any calibration nor fine tuning of the components, and therefore qualifies for convenient production and low maintenance costs.

Objective 2

The hardware development contributions are listed hereafter:

- design, PCB layout, mounting and testing of the analog front end,
- design of the node digital communication (embedded table and daisy-chain),
- design of the table selection system,
- design of an innovative and original current source based on the well known Howland principle,
- supervision of the iterative hardware design and manufacturing work executed by third parties.

Objective 3

The Software development contributions are listed hereafter:

- complete development of a GUI software (EITSurfer) to communicate and reconstruct EIT image with the system,
- supervision of the implementation of the FPGA software (including firmware), including the design of the IQ-demodulator,
- development of new features for the node firmwares based on the first software version delivered by third parties.

Objective 4

In a first phase extensive tests on the electronics alone were done. This allows us to better understand how each component worked. Then in a second phase saline tank tests were undertaken. These tests allow to simulate the use of the hardware on patients. The architecture underwent many modification and phase 1 and 2 were many time repeated, with each iteration the know-how increased significantly. In a third phase, once the system was working satisfactory on the saline models, volunteer test were undertaken. This again led to adjustments of the hardware and software.

Objective 5

The micro-EIT development and design were completely carried-out in the framework of the present thesis. We propose a novel approach for fabricating a micro-EIT well based on Printed Circuit Board (PCB) fabrication technology, which is a convenient, reliable and low cost technique. A 32 electrode well of 9 mm in diameter has been fabricated. Electrodes were not printed flat on the bottom, but placed vertically on the edge of the well. They were fabricated with gold coated single vias cut in half. Beside, the electronic developed for the medical-EIT system has been reconfigured and mounted on the manufactured micro-EIT platform. A series of experimental protocols to test the micro-EIT capabilities were proposed and demonstrated.

Objective 6

The theoretical work carried out in this thesis is the result of a collaboration with Prof. Andy Adler of Carlton University in Canada. Preliminary results were presented at the 2010 EIT conference [6]. Extensive practical tests and theoretical work were performed to identify noise sources in the system. A first theoretical analysis for the EIT system scalability is also formulated.

1.4 Miscellaneous contributions

The aim of this section is to record the work done in the thesis but outside the main goals stated above.

- a transparent acrylic saline phantom was designed and manufactured in collaboration with Fuchs Engineering AG[3] in Landquart,
- a software called EITSim has been developed to create and test the state tables implemented in the node firmware,
- a dedicated Matlab[4] toolbox has been created to read the ".eit" data file saved by the EITSurfer and work with the raw data within the Matlab environment[5].
- two patents were submitted based partially on the work done in this thesis:

[3] http://www.fuchs-engineering.ch
[4] http://www.mathworks.com
[5] Many features of this toolbox have been ported to the open source EIDORS project.

  - "Electrode for EIT scanning device and EIT scanning device", Schweizerisches Patentgesuch: 00364/10, 16.03.2010,
  - "Sensor device for electrical impedance tomography imaging, electrical impedance tomography imaging instrument and electrical impedance tomography method", Schweizerisches Patentgesuch: 01638/2010, 7.10.2010.

- four articles have been written:

  - "Adjacent Stimulation and Measurement Patterns Considered Harmful", Andy Adler, Pascal O. Gaggero, Yasheng Maimaitijiang, Physiol. Meas., 32:731−744, July 2011
  - "Active Electrode Based Electrical Impedance Tomography System", Pascal O. Gaggero, Andy Adler, Josef X. Brunner, Stephan Böhm, Peter Seitz, Conf EIT 2011, Bath, UK, 4−6 May 2011
  - "Evaluation of EIT system performance", Yasheng Maimaitijiang, Stephan Böhm, Pascal O. Gaggero, Andy Adler, Physiol. Meas., 32:851−865, April 2011
  - "Distinguishability in EIT using a hypothesis-testing model", Andy Adler, Pascal O. Gaggero and Yasheng Maimaitijiang, Int. Conf. Electrical Bio-Impedance & Electrical Impedance Tomography Gainville, Fl, USA, 4-8 April 2010

Chapter 2

Basics of EIT

2.1 Background

Electrical Impedance Tomography (EIT) is a tomographic imaging technique which makes use of electrical currents to probe the inside of a given medium. A set of electrodes is placed on the medium of interest, and they are used to sequentially inject and to measure current and potential at the medium boundary. A tomographic image is generated by stimulating the medium with the current patterns of different configurations in order to gain as many independent measurements as possible. For each configuration, the non-injecting electrodes are used to measure the potential field. When applied to a circular medium, the electrodes are placed in an equidistant arrangement around the medium, and the system scans the medium in rotating the current source around it, and for each current source position the potential field is measured. All these data are then used by a mathematical image reconstruction algorithm which creates the tomographic image.

EIT finds practical applications in various fields such as medical imaging, geophysics, industry and life sciences. At the time of writing the most explored and promising applications are found in medical imaging. In the literature (see table 2.1 and 2.2), one can find numerous examples of prototypes and few low volume production devices intended to address the medical market. However, for medical applications, EIT is still at the experimental stage; it has not yet been used for regular patient care.

A key benefit is that EIT does not use ionizing radiation, and therefore can be used for continuous or repetitive monitoring of patients. The image resolution of EIT cannot compete with other, well established, tomographic techniques,

such as X-ray Computed Tomography (CT), Positron Emission Tomography (PET) and Magnetic Resonance Tomography (MRI), but all the above suffer from several disadvantages. CT and PET not only use ionizing radiation; both of them are bulky and costly pieces of equipment, which can hardly be dedicated for the monitoring of one single patient. The patient is often enclosed in the machine detectors which limits the medical care during the imaging procedure and therefore their use on severely injured patients. In contrast EIT hardware interface to the patient is limited to a low-cost electrode belt or any kind of electrode arrangement that can easily be placed on the patient body and which covers only a small surface of the latter.

The ability of EIT to detect conductivity changes finds applications in the monitoring of the respiratory and cardiovascular system by means of a chest electrode belt. The conductivity changes are generated by the expansion of the lungs at each inspiration and blood movement of every heart beat. The continuous monitoring of the vital physiological parameters of the ventilated patients in the intensive care units or in the operation theaters will provide medical care professionals with additional feedback about the patient health state or therapy efficacy, which could improve the patient outcomes. According to the business plan of the startup company Swisstom their are 3.8 million people in the developed countries undergoing artificial ventilation each year, about 15 % of them get acute lung injury, and about 5% (190000 patients) of ventilated patients eventually die of acute lung injury. Studies Amato et al. [9], ARDSN [11], Rubenfeld and Herridge [79], Kahn et al. [47] have shown that using protective ventilation strategies could prevent the death of 20 to 40 % of patients; thus more than 30000 patients could be saved each year if EIT were widely used to guide lung protective ventilation.

It has been demonstrated that even a small quantity of ionizing radiation, such as X-rays, is potentially harmful for patients. Especially, if the procedure is regularly repeated as it is the case in cancer screening. Alternative EIT based techniques have been proposed for breast [18, 12, 81] and prostate [15] cancer detection.

Large scale EIT apparatus also find applications in geophysics [23], for instance geological layer analysis [49, 48], soil compositions analysis in agriculture [14], underground structure detection in archeology[68],...

Industrial applications [26] of EIT have been proposed. For instance, pipes and tank monitoring have been reported [91]. EIT is also used where optical or X-rays based methods are not applicable because the medium is opaque or the instrument is too bulky and dangerous, respectively. For instance, a combined sonic tomograph and EIT[1] is used to non-invasively determine the health of trees directly in the field.

[1] http://www.argus-electronic.de/index.php/en/picus-treetronic

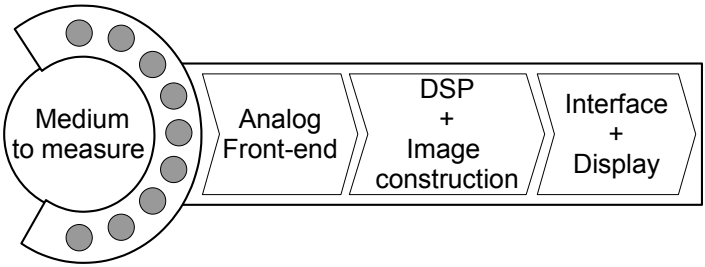

Figure 2.1: General representation of an Electrical Impedance Tomography (EIT) system.

2.2 General concept

This section presents the general concept of EIT. Figure 2.1 schematically depicts the architecture of a modern EIT instrument. The basic idea is to use electrodes to apply an electrical signal at the boundary of a medium, and to measure the resulting signal. Most EIT systems inject a current and measure the resulting potential field, but it is also possible to apply a potential. The reason to inject current is to minimize the sensitivity to the changes of the contact impedance between the electrode and the the medium to measure. The electrodes are driven by the analog front end which connects the digital and analog side of the instrument. After the data coming from the electrodes have been digitized, they are processed by a Digital Signal Processing (DSP) block, and then the image construction block uses these measurements to produce an image. Finally the image is transmitted to a display to be shown to the user. The user interacts with the EIT system using a dedicated interface which could be implemented in a software program communicating with the hardware.

Figure 2.2 depicts the key elements of an EIT instrument which are:

- the signal generator (i.e modulation),
- the current source,
- the analog differential stage and the demodulation,
- the image reconstruction algorithm (i.e. here comprised in the DSP),
- the GUI.

The time reference is often implemented by an oscillator, which provides the clock signals for the whole system and serves as time reference for both signal modulation and demodulation. The digital modulated signal needs to be converted into an analog voltage signal using a DAC. This signal serves as a command signal to drive the current source. The potential field resulting from the application of the current is measured by taking the analog difference between two electrodes. Modern EIT systems directly convert this result into a digital signal using an ADC. The digital signal is then demodulated using a local copy of the digital modulation signal as reference. The calculated amplitude and phase are then stored into memory. The image reconstruction algorithms are based on advanced mathematical knowledge in the field of inverse ill-posed and ill-conditioned problems. These algorithms map the measurements into a tomographic image, which can be displayed to the user. The user interacts with the instrument using a GUI.

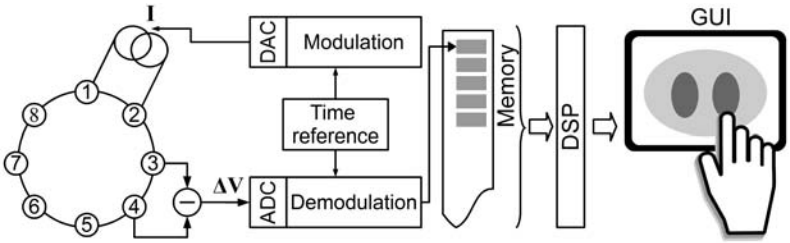

Figure 2.2: Data acquisition basic principle of a modern EIT instrument.

There are various strategies for injecting the current and measuring the potential field; among them a planar electrode arrangement which essentially delivers two-dimensional cross-section images and multi-planar arrangement which enables three-dimensional reconstruction. In the case of the planar electrode arrangement one could argue that the images are not really two-dimensional cross-section but rather 2.5-dimensional images which also take into account off-plane elements. This is due to the fact that the electrical current is not transported along straight lines into matter, like X-rays, but produces a three-dimensional current density field. The maximum of the current density is reached at the level of the electrode plane, between the two injecting electrodes. Objects placed where the current density is high will have a large influence on the measured potential and therefore their chance to appear on the image is increased. Thus the current density at the center of the medium is often lower than at its boundary, object or structure placed there are less likely to be observed on the image.

The measurement strategy is important when considering pair drives (i.e.

only two electrodes are involved in the current injection process). It describes how the current is injected into the medium and how the potential field is measured. For instance an adjacent strategy (see figure 2.4) can be applied, meaning that the current is injected between adjacent electrodes and that the voltages are measured between adjacent electrode pair as well. The words "offset", "interleave" or "spacing" are often used when speaking of the number of electrodes skipped for example between the two injection electrodes (i.e. adjacent = offset 0). In this thesis we will use the term "offset". The notion of offset is of course relative to the total number of electrode of the system and assumes equidistant spacing between all electrodes. To be more general, it is necessary to introduce the notion of injection or measurement angle, respectively. For a circular medium and assuming equidistant electrodes distribution the angle between two electrodes is given by:

$$\alpha_{\text{el}} = \frac{360}{N_{\text{el}}}(O_{\text{ffset}} + 1) \tag{2.1}$$

Where

N_{el} is the number of electrodes,

O_{ffset} is the offset used.

Scanning patterns can also include the injecting electrodes in their measurement sequences. This could be used to assess the contact quality of the electrodes with the medium by directly measuring the voltage drop over the injecting pair of electrode. In general, it is recommended not to use the measurement involving injecting electrodes because it does not respect the four-points measurement scheme. Thus the measured potential is very sensitive to contact impedance changes which could create large artifacts in the reconstructed image. The four-points measurement scheme [16] is an impedance measurement technique which consists of decoupling the current injecting electrodes and the measurement electrodes. If the potential was directly sensed at the injecting electrode (i.e. two-points) the measure of Z_m (see figure 2.3) would be corrupted by the unknown voltage drop of the current I over the contact impedance Z_c of the electrode with the medium. In case one decouples the injecting and measurement function using four different electrodes, it is possible to make the input impedance of the voltmeter high enough so that the current flowing through the contact impedance I_{in} is made very small. In this way the potential measured by the voltmeter is practically only due to the voltage drop of the current I over the impedance of interest Z_m.

The number of electrodes of an EIT instrument will determine the number of theoretically possible independent measurements (see section 3.3.6). The

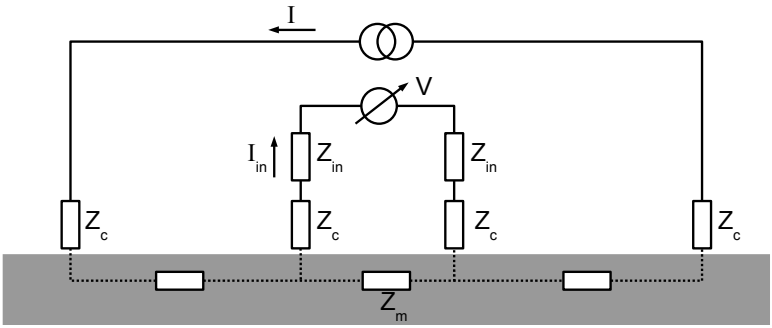

Figure 2.3: The four-points measurement scheme. Z_c are the contact impedance of the electrodes with the medium, z_{in} are the input impedance of the voltmeter, I is the current injected into the medium , I_{in} is the current flowing through the voltmeter and Z_m is the measured impedance.

number of independent measurements is linked with the achievable spatial resolution of an EIT system. Increasing the number of electrodes also automatically increases the hardware costs and the complexity of the architecture of the whole system. Moreover, if the EIT system acquires the measurements in a serial fashion, one pair of electrodes after another pair of electrodes, increasing the number of electrodes increase also the noise on each measurement[2]. Therefore a trade-off between hardware costs, signal quality and architecture complexity needs to be found. In practice, it seems that 16 to 32 electrodes is a good compromise. One additional challenge with managing this high number of electrodes is how to apply them in a convenient manner on a patient. For instance the electrodes can be integrated in a single belt.

Being able to inject currents and to measure potentials with a great accuracy is generally a difficult problem, which needs to be solved if one is interested in absolute impedance images. Fortunately, for most applications time differential (see figure 2.5) or frequency differential EIT images (see section 3.3.1) are sufficient. Time difference imaging is the most often encountered type of reconstruction. It consists of subtracting the measurement with a reference measurement established earlier. For instance one can ask the user to select one measurement to be used as the reference. The choice of the reference is crucial for the image to show the phenomenon of interest. The frequency difference imaging makes use of measurements of the same situation at different excitation frequencies. For instance one tries to use the measurement acquired at frequency A as the reference for measurement acquired at frequency B.

[2]The available measurement (integration) time decreases.

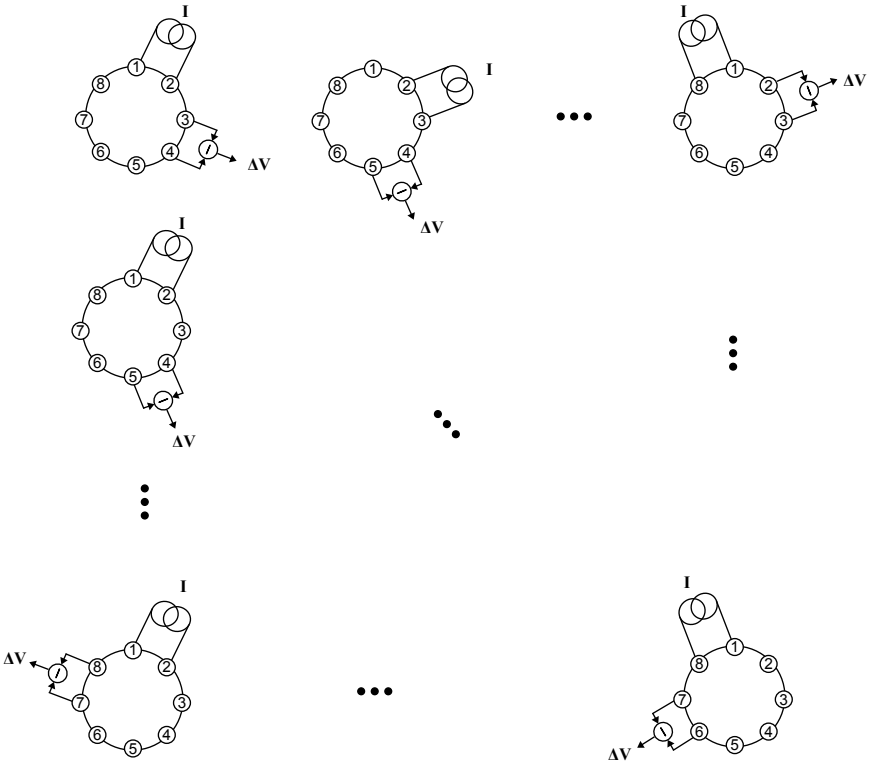

Figure 2.4: The adjacent scanning pattern for a 8 electrodes EIT system.

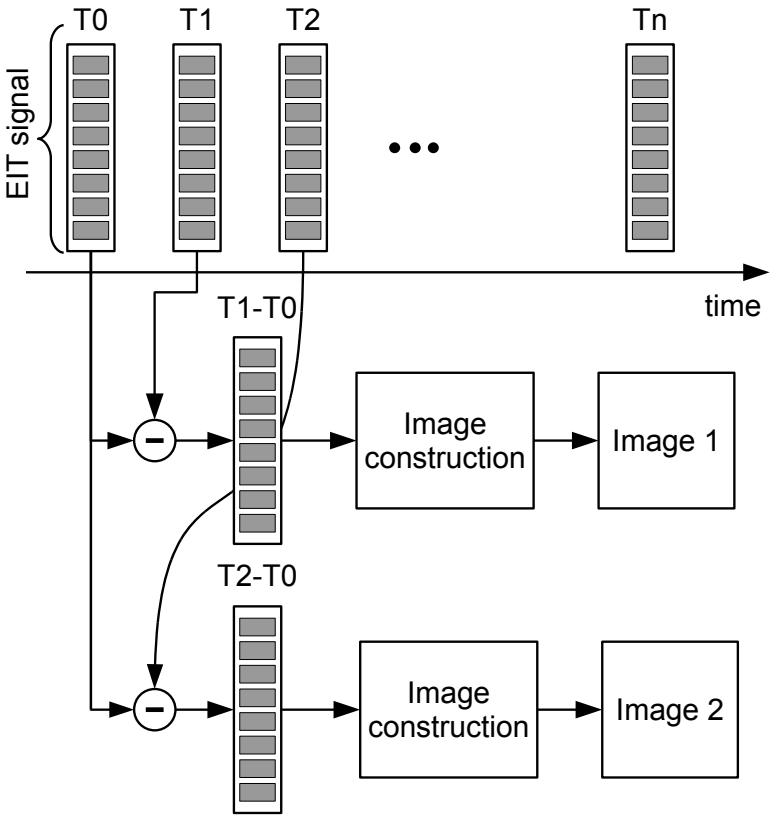

Figure 2.5: EIT time differential imaging. A reference T0 is subtracted with the current measurement Tn. Then the differential signal Tn-T0 is used by the image reconstruction block to create the corresponding "Image n".

2.3 Current state of the art and problems

It is suspected that one of the factors preventing EIT to be used in medical care, is that the hardware is inconvenient. Most of the available EIT devices use bulky centralized electronics to analyze and inject signals from and to the electrodes using loose shielded cables. The individual cables need to be placed individually on the patient, which is a long and fastidious process, which is inconvenient in a medical care environment. Therefore, our approach was to implement a distributed system with active electrodes assembled on a belt. Having a voltage buffer close to the electrode has two beneficial effects: 1) it increases the input impedance of the electrode and 2) it reduces the length of any high impedance path. The input impedance of an active electrode is determined by the stray capacitance of the buffer (2 pF) and other active elements (total about 15 pF). The input impedance of the same electrode, but without active elements with 1 m bus cable, was measured to be at least 200 pF (i.e. stray capacitance of the cable with adjacent ground lines). Being able to transmit signals on low impedance lines also reduce the coupling of external signal on the bus line and the cross-talk between the bus lines.

The active electrode concept has already been described by Rigaud in 1993 [73], who suggested having active electrodes with embedded current source and voltage buffers, whereas the voltage reference (i.e. signal generator) and the signal demodulation happens at a central location. Since he was not using a digital I/Q demodulator but an analog mixer, it was required to correct the phase lag of the signal directly on each electrode, which degrades the input impedance of the electrode by adding switches before the voltage buffer and demands a calibration procedure.

Guardo et al [36] described a multiplexed active electrode system with embedded micro-processor to manage the switches. This solution reduces the number of needed cables, compared with the solution of Li et al presented hereafter. Guardo et al proposed to implement a daisy-chain to assign address number to each electrode. Then once the address number was attributed, the electrodes worked without using the daisy-chain anymore. When one clock was received each node incremented its internal counter. So knowing the number of nodes in the chain, their own address and the value of the state counter it was possible to calculate the state of each node for a particular measurement scheme (in this case adjacent).

Li et al [56, 55] emphasize the advantage using active electrodes instead of doubly shielded passive cables. The latter are liable to cause instabilities and are inconveniently thick. A 32-electrode system using doubly shielded cables will be very inconvenient to handle because of the large bundle of cables between the patient and the EIT instrument. They proposed a similar

architecture as Guardo et al but without the phase lag compensation. The voltage reading was done with only buffers making use of a dedicated cable (i.e. one dedicated bus line per buffer). The measurement was not multiplexed and the measurement scheme was hardcoded. The injection of the current was done using a pair drive of symmetrical current sources. The system could select any pair of electrodes to inject the current. One of the limitation of the proposed architecture was the high number of cables needed to communicate with the electrodes. Li et al also described the use of electrode gel directly on the electrode surface to "reduce the electrode-interface impedance".

One of the key elements of an EIT instrument is its current source. In the literature authors reported the use of the Howland current source and modified Howland current source for biomedical application [78]. A comprehensive study of the Howland topology can be found in this application note [70]. The use of such symmetric current sources (i.e. one current source injects the current and the other sinks the current (injects a 180° dephased current)) is also described by Holder [43]. This configuration allows the common mode to be reduced. Nevertheless, this solution is difficult to implement in practice because both current sources need to be precisely balanced and an extra return path electrode is often needed to drain excessive charges. A reduction of the common-mode can also be achieved using a common mode feedback [77] electrode.

In modern EIT systems such as the one described in [37] the signal generation and the demodulation are done in the digital domain, which removes the need for complex analog circuits. Digital waveform synthesizers have the advantage of being able to generate any signal desired, provided that the DAC can accurately convert the digital signal into an analog signal. For the signal acquisition, digital I/Q demodulator have the advantage that they can easily be implemented in FPGA hardware, and parallelized for as many frequencies as needed, provided of course that the FPGA is large enough. Given all the above advantages there are no more needs for analog implementation of those functions.

Earlier work in micro-EIT has been done by Williams et al in 1995 [99], who tested a 16-electrode micro-EIT instrument with well diameter of various size (13, 50, 100, 150 and 500 mm). Griffiths et al [34] succeeded imaging a human hair in a 0.9 mm diameter electrode well. They used a complex set-up of 16 electrodes made of gold wires arranged around the well and spaced apart with nylon wires. Linderholm et al [58], studied the feasibility of electrical impedance tomography using micro-fabricated electrodes (1-dimensional array); he proposed in his conclusions the construction of a micro-fabricated micro electrode well. The PCB micro-fabrication of 8 flat electrodes has been used by Dharia et al [25], to make images of Xenopus Oocytes (frog eggs) in

a 1.2 mm well. Sun et al [90] used PCB technology as well to fabricate a flat 16-electrode micro-EIT system within a 6 mm well.

For high-resolution EIT images Liu et al [59] proposed the use of scanning micro-EIT. In this case an electrode is placed at the tip of an AFM cantilever and is used to make impedance measurement in a scanning fashion on the sample. Alternatively, Multi-Electrode Array (MEA) of microfabricated electrodes [44] on the bottom of a well can be used for high resolution micro-EIT without having recourse to moving parts.

In order to make a classification of the EIT systems general key features can be defined:

- number of electrodes,
- arrangement of the electrodes: Cables connect individual electrodes as it is the case with ECG electrodes (cable), some belt-like structures support subsets of the electrodes (module) or a unique belt-like structure connects all the electrodes (belt).
- signal injection: voltage drive or current drive; The signal applied, on the medium to measure, can either be a potential or a current, then the resulting current at the boundary or the resulting potential field is measured, respectively.
- signal drive: pair drive or multi drive; The system can either apply the signal using a unique pair of electrodes or multiple electrodes, as it is the case, for example, in trigonometric excitation patterns,
- system frequency band: single frequency, multi discrete frequency, continuous frequency range; Systems with single frequency or multiple discrete frequency often need precise calibration at their operating frequencies,
- system waveform: sinus, multi-sinus, square; The use of multi-sinus (combination of sinus) or square waveform allows the system to do spectroscopy measurements,
- modulation: analog or digital; modern EIT systems use digital waveform synthesis and convert the obtained numerical signal in its analog counterpart using Digital to Analog Converters (DAC),
- demodulation: analog or digital; Modern EIT systems convert the differential voltage signal in the digital domain using an Analog to Digital Converter (ADC) and then demodulate the signal numerically,

- signal acquisition: serial, semi-serial or parallel; Parallel acquisition of the signal means that all the measurements for a given configuration are done in parallel, which increases the integration time of the individual measurement.
- electrodes: passive, active: An electrode is considered active if the first active element, such as a voltage buffer, is placed less than 5 cm away from the electrode itself.
- transmission cables shielding: no shielding (none), passive shielding (single) or active and passive shielding (double),
- measurement strategy: fixed, programmable or flexible; Fixed means that the measurement strategy is defined by hardware connections and requires hardware modification to be changed. Programmable means that software modifications only are necessary to change the measurement strategy, but the system firmware needs to be reprogrammed. Flexible means that the measurement strategy can be changed on the fly by the user without the need for firmware reprogramming.

2.4 Physical principles

2.4.1 EIT electromagnetic formulation

This section gives an overview over the basic laws of physics governing the EIT problem. As always in electromagnetism, one starts with Maxwell's equations:

$$\nabla \cdot \overrightarrow{E} = \frac{\rho}{\epsilon_0} \tag{2.2}$$

$$\nabla \cdot \overrightarrow{B} = 0 \tag{2.3}$$

$$\nabla \times \overrightarrow{E} = -\frac{\partial \overrightarrow{B}}{\partial t} \tag{2.4}$$

$$\nabla \times \overrightarrow{B} = \mu_0 \overrightarrow{J} + \mu_0 \epsilon_0 \frac{\partial \overrightarrow{E}}{\partial t} \tag{2.5}$$

where

Table 2.1: A comparison of the major EIT system described in the literature.

Origin	Nickname	Status, Last version	# El	Electrode arrangement	Signal injection	Signal drive	Electrodes type	Cable shielding
Montréal, Guardo Gagnon[37]	Sigmatome III	RD	24	cable	current	pair	passive	none or single?
Göttingen, carefusion, [38]	Goe MF II	RD	32	cable	current	pair	passive	single
Dartmouth, Halter et al[40]	-	RD, 2004	64	-	-	multi	-	-
London (UCL) McEwan et al, [64]	UCLH Mk 2.5	RD, 2006	32	cable	current	multi	passive	none
Rensselaer Polytechnic Institute, Liu et al[60]	ACT 4	RD, 2007	64	module	voltage / current	multi	passive	-
Sheffield, Wilson et al, [100]	Mk 3.5	RD, 2000	8	-	-	-	passive	double
Korea, Kyung Hee University, [53, 69]	KHU Mark 2	RD,	16	cables	current	multi	passive	double
Timpel (Dixtal), [20]	Enlight	RD?, 2011	32	module	current	pair	passive	double
Dräger Medical AG, [67, 27]	PulmoVista 500	pre-production, 2011	16	belt	current	-	passive	-
CSEM SA	-	RD, 2011	32	belt	current	single	active	none
Swisstom SA	-	pre-production, 2011	32	belt	current	single	active	none

Table 2.2: A comparison of the major EIT system described in the literature (cont'd).

Name	Frequency band	Number of frequencies	Waveform	Modualtion	Demodualtion	Signal acquisiton	Image rate	Measurment strategy
Sigmatome III	1 kHz - 10 MHz	-	-	digital	digital	serial	?	programable?
Goe MF II	5 to 500 kHz	-	-	-	-	-	44	-
Dartmouth	10 kHz - 10 MHz	-	-	digital	digital	-	-	-
UCLH Mk 2.5	20 Hz to 256 kHz	30	multi-sinus	digital	digital	serial	10	programable?
ACT 4	300 Hz to 1 MHz	continuous	sinus	digital	digital	parallel	?	programable?
Mk 3.5	2 kHz to 1.6 MHz	30	multi-sinus	digital	digital	parallel	25	-
KHU Mark2	1 to 500 kHz ?	-	sinus	digital	digital	parallel	50	programable
Timpel	-	-	-	-	-	-	50	-
Dräger Medical AG,	80-130 kHz	-	-	-	-	-	40	-
CSEM SA	80 - 400 kHz	continuous	sinus	digital	digital	serial	40	flexible
Swisstom SA	80 - 400 kHz	continuous	sinus	digital	digital	serial	40	flexible

$\overrightarrow{E}$ is the electrical field $\left[\frac{\mathrm{V}}{\mathrm{m}}\right]$,

$\overrightarrow{B}$ is the magnetic field [T] (see section C.2.1 for details),

$\overrightarrow{J}$ is the total current density $\left[\frac{\mathrm{A}}{\mathrm{m}^2}\right]$,

ρ is the charge density $\left[\frac{\mathrm{C}}{\mathrm{m}^3}\right]$,

μ_0 is the vacuum permeability $= 4\pi \cdot 10^{-7}\ \frac{\mathrm{H}}{\mathrm{m}}$,

ϵ_0 is the vacuum permittivity $= 8.85 \cdot 10^{-12}\ \frac{\mathrm{F}}{\mathrm{m}}$,

$\nabla\cdot$ denotes the divergence operator (see section B.1.3 for details),

$\nabla\times$ denotes the curl operator (see section B.1.3 for details).

Maxwell's equations are completed by Lorentz's law of force stating:

$$\overrightarrow{F} = q(\overrightarrow{E} + \overrightarrow{v} \times \overrightarrow{B}) \tag{2.6}$$

where

$\overrightarrow{F}$ is the resulting force, [N],

q are the free to move electrical charges,

$\overrightarrow{v}$ is the speed of the charges q.

current continuity equation As a first step, one needs to derive the current continuity equation $\nabla \cdot \overrightarrow{J} = -\frac{\partial \rho}{\partial t}$, by taking the divergence on both sides of equation 2.5:

$$\nabla \cdot \nabla \times \overrightarrow{B} = \nabla \cdot \left(\mu_0 \overrightarrow{J} + \mu_0 \epsilon_0 \frac{\partial \overrightarrow{E}}{\partial t} \right) \tag{2.7}$$

$$= \mu_0 \nabla \cdot \overrightarrow{J} + \overrightarrow{J}\, \nabla \cdot \mu_0 + \mu_0 \epsilon_0 \nabla \cdot \frac{\partial \overrightarrow{E}}{\partial t} + \frac{\partial \overrightarrow{E}}{\partial t} \nabla \cdot \mu_0 \epsilon_0 \tag{2.8}$$

The second and last terms are equal to zero because μ_0 and ϵ_0 are assumed to be constants, and $\nabla \cdot \nabla \times \overrightarrow{B} = 0$ is a vector calculus identity valid for every vector field, $\overrightarrow{B}$, thus one gets:

$$\mu_0 \nabla \cdot \overrightarrow{J} + \mu_0 \epsilon_0 \nabla \cdot \frac{\partial \overrightarrow{E}}{\partial t} = 0 \tag{2.9}$$

then multiplying both sides by $\frac{1}{\mu_0}$ and reorganizing the terms, one gets:

$$\nabla \cdot \overrightarrow{J} = -\epsilon_0 \nabla \cdot \frac{\partial \overrightarrow{E}}{\partial t} \tag{2.10}$$

The next move is to permute the divergence operator with the temporal derivative. This operation is only valid, if all the second derivatives of the field $\overrightarrow{E}$ are of the type $\mathbb{C}^2$, meaning that all the second derivatives exist and are continuous. This is obviously the case with a realistic field $\overrightarrow{E}$ assuming a medium with reasonable interfaces. After the permutation one gets:

$$\nabla \cdot \overrightarrow{J} = -\epsilon_0 \frac{\partial}{\partial t} \left(\nabla \cdot \overrightarrow{E} \right) \tag{2.11}$$

then by combining equation 2.2 and 2.11 one gets:

$$\nabla \cdot \overrightarrow{J} = -\epsilon_0 \frac{\partial}{\partial t} \left(\frac{\rho}{\epsilon_0} \right) \tag{2.12}$$

After simplifying ϵ_0 one gets the desired result for the current continuity equation

$$\nabla \cdot \overrightarrow{J} = -\frac{\partial \rho}{\partial t} \tag{2.13}$$

current density The next step is to calculate the current density $\overrightarrow{J}$ given by:

$$\overrightarrow{J} = \overrightarrow{J}_c + \overrightarrow{J}_b + \overrightarrow{J}_p \tag{2.14}$$

where

$\overrightarrow{J}_c$ is the conduction current,

$\overrightarrow{J}_b$ is the bound current associated with the magnetization of the material,

$\overrightarrow{J}_p$ is the polarization current resulting of the linear motion of the charges when the electric polarization varies.

The current density $\overrightarrow{J}_c$ is proportional[3] to $\overrightarrow{f}$ the force per unit of charge ($\left[\frac{\mathrm{N}}{\mathrm{C}}\right]$) given by Lorentz's law of force, see equation 2.6:

$$\overrightarrow{J}_c = \sigma \overrightarrow{f} = \sigma \left(\overrightarrow{E} + \overrightarrow{v} \times \overrightarrow{B} \right) \tag{2.15}$$

with the approximation of $\overrightarrow{v}$ being small enough for the terms $\overrightarrow{v} \times \overrightarrow{B}$ to become negligible one receives Ohm's law:

$$\overrightarrow{J}_c = \sigma \overrightarrow{E} \tag{2.16}$$

This assumption can be verified by estimating the speed of the ions in aqueous solution, this done in section C.2.

$\overrightarrow{J}_b$ and $\overrightarrow{J}_p$ are given respectively by:

$$\overrightarrow{J}_b = \nabla \times \overrightarrow{M} \tag{2.17}$$

$$\overrightarrow{J}_p = \frac{\partial \overrightarrow{P}}{\partial t} = \frac{\partial}{\partial t} \left(\epsilon_0 \chi_e \overrightarrow{E} \right) = \frac{\partial}{\partial t} \left(\epsilon_0 \left(\frac{\epsilon}{\epsilon_0} - 1 \right) \overrightarrow{E} \right) = \frac{\partial \overrightarrow{E}}{\partial t} \left(\epsilon \epsilon_0 - \epsilon_0 \right) \tag{2.18}$$

where

$\overrightarrow{M}$ is the magnetic polarization,

$\overrightarrow{P}$ is the electric polarization,

χ_e is the electric susceptibility of the medium.

Provided $\overrightarrow{P} = \epsilon_0 \chi_e \overrightarrow{E}$, one obtains:

$$\overrightarrow{J}_p = \frac{\partial}{\partial t} \left(\epsilon_0 \chi_e \overrightarrow{E} \right) \tag{2.19}$$

where

χ_e is the electric susceptibility of the medium.

[3] the proportionality factor is the conductivity σ in $\left[\frac{1}{\Omega \mathrm{m}}\right]$

Using the relation $\epsilon = \epsilon_0(1 + \chi_e)$ and equation 2.19, one gets:

$$\overrightarrow{J}_p = \frac{\partial}{\partial t}\left(\epsilon_0\left(\frac{\epsilon}{\epsilon_0} - 1\right)\overrightarrow{E}\right) = \frac{\partial \overrightarrow{E}}{\partial t}\left(\epsilon\epsilon_0 - \epsilon_0\right) \tag{2.20}$$

then by inserting equation 2.14 in 2.5, one gets

$$\nabla \times \overrightarrow{B} = \mu_0\left(\overrightarrow{J}_c + \overrightarrow{J}_b + \overrightarrow{J}_p\right) + \mu_0\epsilon_0\frac{\partial \overrightarrow{E}}{\partial t} \tag{2.21}$$

then using equation 2.20 and 2.17, one gets

$$\nabla \times \overrightarrow{B} = \mu_0\left(\overrightarrow{J}_c + \nabla \times \overrightarrow{M} + \frac{\partial \overrightarrow{E}}{\partial t}\left(\epsilon\epsilon_0 - \epsilon_0\right)\right) + \mu_0\epsilon_0\frac{\partial \overrightarrow{E}}{\partial t} \tag{2.22}$$

after reorganizing the terms, we obtain:

$$\nabla \times \left(\frac{\overrightarrow{B}}{\mu_0} - \overrightarrow{M}\right) = \overrightarrow{J}_c + \frac{\partial \overrightarrow{E}}{\partial t}\epsilon\epsilon_0 - \frac{\partial \overrightarrow{E}}{\partial t}\epsilon_0 + \epsilon_0\frac{\partial \overrightarrow{E}}{\partial t} = \overrightarrow{J}_c + \frac{\partial \overrightarrow{E}}{\partial t}\epsilon\epsilon_0 \tag{2.23}$$

In literature, see for example Griffiths [33], the term $\frac{\partial \overrightarrow{E}}{\partial t}\epsilon\epsilon_0 \overset{def}{=} \overrightarrow{J}_d$ is defined as the displacement current, thus one can finally write:

$$\overrightarrow{J} = \overrightarrow{J}_c + \overrightarrow{J}_d \tag{2.24}$$

Quasi-static approximation The last assumption one needs before putting together the relations which describe the EIT physics, is the quasi-static approximation where $\overrightarrow{B}$, the magnetic field, is considered to be constant over time. Using equation 2.4 one gets:

$$\nabla \times \overrightarrow{E} = 0 \tag{2.25}$$

In the quasi-static approximation case, one uses a simple relation between the vector field $\overrightarrow{E}$ and the potential scalar field U:

$$\overrightarrow{E} = -\nabla U \tag{2.26}$$

where

U is the scalar field of the electrical potential,

∇ is the operator gradient.

The validity of equation 2.26 can be verified by taking the curl on both sides of the equation:

$$\nabla \times \overrightarrow{E} = -\nabla \times \nabla U = 0 \tag{2.27}$$

Thus in order to verify the mathematical vector identity $\nabla \times \nabla U = 0$ for all scalar fields U, it is required that $\nabla \times \overrightarrow{E} = 0$. This demonstrates that equation 2.26 is only true under the quasi-static approximation conditions. Combining equations 2.16, 2.24 and 2.13 gives:

$$\nabla \cdot \left(\sigma \overrightarrow{E} + \frac{\partial \overrightarrow{E}}{\partial t} \epsilon\epsilon_0 \right) = -\frac{\partial \rho}{\partial t} \tag{2.28}$$

At this point two further simplifications based on the following assumptions are introduced:

- $\frac{\partial \overrightarrow{E}}{\partial t}\epsilon\epsilon_0$ is supposed to be small enough compared with $\sigma\overrightarrow{E}$, which is equivalent with supposing the medium is completely resistive,
- $-\frac{\partial \rho}{\partial t} = 0$ because the conductive medium is not able to accumulate free charges.

After the simplification based on these assumptions one gets:

$$\nabla \cdot \sigma \overrightarrow{E} = 0 \tag{2.29}$$

then using equation 2.26, the expression for the quasi-static potential, one finds the equation that rules the EIT problem:

$$\nabla \cdot \sigma \nabla \overrightarrow{U} = 0 \tag{2.30}$$

In fact this formula corresponds to the continuum Kirchhoff's laws. If the space is segmented into finite elements, like it is the case in Finite Element Modeling, the EIT problem is equivalent to apply Kirchhoff's law to the system.

2.4.2 Domain of validity of the quasi-static approximation

The domain of validity of the quasi-static approximation has been studied by Steinmetz et al. [89], and Haus and Melcher [42]. Both approaches based their reflections on the approximation of the spatial derivative and temporal derivative by the division by a characteristic length l and a characteristic time τ, respectively. In addition further assumptions are needed:

- only the scalar magnitude of the field is considered and,
- the medium is assumed to be homogeneous, linear and isotropic.

The error arising from the magnetic field when doing the quasi-static approximation can be estimated using Maxwell equation 2.4:

$$\nabla \times \overrightarrow{E} = -\frac{\partial \overrightarrow{B}}{\partial t} \tag{2.31}$$

$$\frac{E_{\text{error}}}{l} = \frac{B}{\tau} \tag{2.32}$$

then equation 2.5 is also estimated:

$$\nabla \times \overrightarrow{B} = \mu_0 \overrightarrow{J} + \mu_0 \epsilon_0 \frac{\partial \overrightarrow{E}}{\partial t} \tag{2.33}$$

$$\frac{B}{l} \leq \mu_0 J + \mu_0 \epsilon_0 \frac{E}{\tau} \tag{2.34}$$

Using $J = \sigma E$, one gets:

$$\frac{B}{l} \leq \mu_0 \sigma E + \mu_0 \epsilon_0 \frac{E}{\tau} \tag{2.35}$$

combining equations 2.32 and 2.35 one gets:

$$\frac{E_{\text{error}}}{E} \leq \frac{\mu_0 \sigma l^2}{\tau} + \frac{\mu_0 \epsilon_0 l^2}{\tau^2} \tag{2.36}$$

in matter, it translates to:

$$\frac{E_{\text{error}}}{E} \leq \frac{\mu \sigma l^2}{\tau} + \frac{\mu \epsilon l^2}{\tau^2} \tag{2.37}$$

where

τ	is the characteristic time identified with the inverse of the angular frequency $\omega^{-1} = \tau = \frac{1}{2\pi f}$
f	is the frequency of the current [Hz],
l	is the path the current has to travel trough the medium [m],
σ	is the conductivity of the medium [S $\cdot$ m],
ϵ_0	is the vacuum permittivity [F/m],
ϵ	is the permittivity in the matter [F/m],
μ_0	is the vacuum permeability [H/m],
μ	is the permeability [H/m].

The intuitive interpretation for equation 2.37 is that the first term on the right, $\frac{\mu\sigma l^2}{\tau}$, implies that the error is bounded by the ratio, $\left(\frac{l}{\mathrm{SD}}\right)^2$, where SD corresponds to the skin depth, $\sqrt{\frac{2}{\sigma\omega\mu}}$. Additionally, the second term, $\frac{\mu\epsilon l^2}{\tau^2}$, means that the error is bounded by the ratio, $\left(\frac{l}{\lambda}\right)^2$, where $\lambda = \frac{\mu\epsilon}{\tau^2} \cong \frac{c^2}{f^2}$ is the wavelength of signal in the medium.

Figure 2.6 depicts the validity domain for the quasi-static approximation, assuming the relative permittivity of the medium to be $\epsilon_r = 80$, which corresponds to the value for water at 20°C. If a relative error of 10% on the electrical field E is acceptable a signal with a frequency of 1 MHz is the highest value possible for which the quasi-static approximation is validated (assuming a medium conductivity of $\sigma = 1$). It appears that the quasi-static approximation is used at its limits of validity for the resolution of the EIT problem.

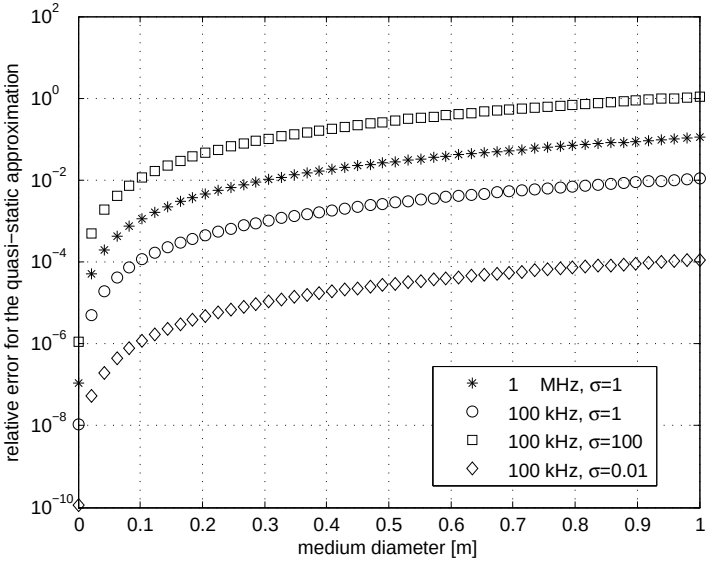

Figure 2.6: Validity domain for the quasi-static approximation calculated for water at 20°C ($\epsilon_r = 80$).

Chapter 3

Theoretical Limits of EIT Systems

3.1 Introduction

This chapter provides the theoretical backbone of the present thesis. The goal is to be able to give a first answer to the question of the theoretical distinguishability and miniaturization limits of EIT. Clearly there is no unique way to address this problem. We chose the term distinguishability to express the likelihood to see a given object in the image. It should be understood in the sense to know whether a structure of interest is distinguishable from the background noise. For this purpose the concept of signal strength (section 3.3.3) and noise (section 3.4) are introduced. We also developed our own Matlab toolbox based on EIDORS to facilitate the simulations and the tests. Theoretical and simulation results are presented in this chapter and in chapter 6. The latter contains also measurements confirming the predictions of the simulation model. Concluding the distinguishability discussion, all these concepts are brought together to build a model of the geometrical scalability of EIT systems, which is used to predict the miniaturization and distinguishability limits.

The concept of intrinsic resolution is also treated at the end of the chapter. It can be formulated as the number of independent measurements that are still relevant at a given noise level. The value of intrinsic resolution of a system is completely independent of the absolute size of a system. One can make a comparison with a digital camera having an intrinsic resolution of 5 MPixels for the image sensor; this value does not depend on the object pictured nor of any input signals. Whereas the concept of distinguishability could be compared, using the same analogy of the digital camera, with the

necessary amount of light to take a picture of a given scenery. With that being said, one should not interpret the concept of intrinsic resolution as the ultimate resolution of a given system under optimal conditions. In a similar sense, the number of pixels of an optic sensor is not its ultimate resolution limit either. For instance, an object having an image size on the sensor less than the pixel size could still be detected (distinguished from the background noise).

Clearly, one sees that there is no simple answer to the question: what is the resolution of an EIT system? In fact the answer depends of the test conditions and of the definition given to the resolution concept. For example, if one would be interested in detecting whether an object was in the test medium or not, the resolution of our system will only be based on this test and will not be taking into account any other parameter, such as for example size and shape of the object.

In summary, this chapter only intends to give an answer to the question: what are the limits of an EIT system given the definition of distinguishability proposed hereafter in section 3.2. The link with other concepts or theoretical limitations is also done, which gives the reader an intuitive feeling about the parameters that play a role when it comes to extracting information from an EIT system[1].

3.2 Distinguishability: a probabilistic approach

The distinguishability is the ability for the end-user to perceive in a tomographic image the structure of interest for his particular application. The idea behind the probabilistic approach is to express distinguishability in terms of probability that the event "the structure is spotted on the image" corresponds to an actual measurement and is not created by the random fluctuations of the signal (i.e. the noise). The distinguishability mathematical expression as given in equation 3.33 can also be interpreted as a Signal-to-Noise Ratio (SNR). A major advantage of this approach is to decouple the reconstruction algorithm from the resolution criterion, unlike other image based criteria such as the Noise Figure (NF), see for example Graham and Adler [32].

This section is adapted from Adler et al. [6] with more detailed derivations and some complementary information. The reader who is not familiar with the Maximum A posteriori Probability (MAP) reconstruction technique can find an introduction in appendix A. The general idea is to start using simple

[1] The word "resolution" is avoided on purpose to give a more general meaning to the previous sentence and to avoid common misunderstanding of this concept.

Bayesian probability concepts and then use the statistical benchmark given by the z-score to characterize the distinguishability. One can start reasoning by writing the potentials $\mathbf{v}$ measured at the boundary of the medium with a given EIT system using the following forward problem[2] operator A:

$$\mathbf{v} = \mathrm{A}(\boldsymbol{\sigma}) + \mathbf{n} \tag{3.1}$$

where

A — is the forward problem operator, which calculates the resulting potential field at the medium boundary given a certain conductivity distribution $\boldsymbol{\sigma}$,

$\mathbf{v}$ — is a $M \times 1$ vector representing the measured potential with the system $\mathrm{A}(\boldsymbol{\sigma})$,

$\boldsymbol{\sigma}$ — is a $N \times 1$ vector containing the impedance distribution inside the measured medium,

$\mathbf{n}$ — is a $M \times 1$ vector containing contribution of the noise that is assumed to be zero-mean, independent and Gaussian.

Since time differential EIT imaging systems take a reference data set $\mathbf{v}_{\mathrm{ref}}$ and then subtract it from the instantaneous data set taken at time $\mathbf{v}_t$, the resulting differential measurement $\boldsymbol{\Delta}\mathbf{v}$ vector equals:

$$\boldsymbol{\Delta}\mathbf{v} = \mathbf{v}_{\mathrm{t}} - \mathbf{v}_{\mathrm{ref}} \tag{3.2}$$

In this case $\mathbf{v}_{\mathrm{ref}}$ is assumed to be the average over a large number of measurements with negligible noise. Thus the noise observed on $\Delta\mathbf{v}$ is only due to $\mathbf{v}_{\mathrm{t}}$.

At this point, one needs to linearize the operator A around $\mathbf{v}_{\mathrm{ref}}$, this is done by calculating the so called sensitivity matrix using the Jacobian of A. Therefore each element $[i, j]$ of the sensitivity matrix $\mathbf{J}$ is given by:

$$[\mathbf{J}]_{i,j} = \left.\frac{\partial \mathrm{A}_i(\boldsymbol{\sigma})}{\partial \boldsymbol{\sigma}_j}\right|_{\boldsymbol{\sigma}=\boldsymbol{\sigma}_{ref}} \tag{3.3}$$

[2]The forward problem consists in calculating a set of parameters out of a physical model. The inverse problem is calculating the physical model using the measured parameters. In the present case, the physical model is essentially given by the conductivity distribution, the system geometrical shape and the current injection strategy. The measured parameters are the voltages at the medium boundary.

where

$\boldsymbol{\sigma}_{\text{ref}}$ is the conductivity distribution at the moment when the reference data set was taken.

The linearized change in conductivity of the medium is denoted $\Delta\boldsymbol{\sigma} = \boldsymbol{\sigma}_{\text{t}} - \boldsymbol{\sigma}_{\text{ref}}$; in this way the linearized expression for the differential measurement can be written using equations 3.1 and 3.3:

$$\Delta\mathbf{v} = \mathbf{J}\Delta\boldsymbol{\sigma} + \mathbf{n} \tag{3.4}$$

In the previous expression, $\Delta\boldsymbol{\sigma}$ is a noiseless variable because we decided to include all the noise components in the $\mathbf{n}$ variable. Of course the linearization operation assumes small changes of conductivity inside the medium to be valid. In other words, it is assumed that a one step calculation (i.e. a non-iterative calculation) is good enough to approximate the solution. Figure 3.6 gives some intuitive insights about using linearization, thus if the conductivity change is small enough one clearly sees that the variations on the potential are linear. The best estimate of the conductivity changes in the sense of the Maximum A posteriori Probability (MAP) is given by equation A.33,

$$\Delta\boldsymbol{\sigma}_{\text{MAP}} = \left(\mathbf{J}^{\text{t}}\boldsymbol{\Sigma}_{\text{n}}^{-1}\mathbf{J} + \mathbf{A}_{\text{prio}}\right)^{-1}\mathbf{J}^{\text{t}}\boldsymbol{\Sigma}_{\text{n}}^{-1}\mathbf{d} \tag{3.5}$$

where

$\boldsymbol{\Sigma}_{\text{n}}$ is the noise co-variance matrix,

$\mathbf{A}_{\text{prio}}$ is the regularization matrix introducing a priori information about the unknown $\Delta\boldsymbol{\sigma}$,

$\mathbf{d}$ are the input data, for instance $\Delta\mathbf{v}$.

In this reasoning, it is desirable to only calculate the $\Delta\boldsymbol{\sigma}_{\text{MAP}}$ for a limited region in the image parameter space. One calls this region the Region Of Interest (ROI). The ROI is defined using an image parameter selection matrix $\mathbf{I}_{\text{ROI}}$ of the size $N \times 1$ where the i^{th} element is given by:

$$\mathbf{I}_{\text{ROI}_i} = \begin{cases} 0 & \text{if } i \subsetneq \text{ROI} \\ 1 & \text{if } i \subset \text{ROI} \end{cases} \tag{3.6}$$

In this way, it is possible to reduce the conductivity changes in the ROI to one single parameter:

$$\Delta\sigma_{\mathrm{ROI}} = \mathbf{I}_{\mathrm{ROI}}\Delta\boldsymbol{\sigma}_{\mathrm{MAP}} = \mathbf{I}_{\mathrm{ROI}}\mathbf{R}\Delta\mathbf{v} = \mathbf{R}_{\mathrm{ROI}}\Delta\mathbf{v} \tag{3.7}$$

where $\mathbf{R}$ and $\mathbf{R}_{\mathrm{ROI}}$ are the image reconstruction matrices for the whole system and for the ROI, respectively.

$\mathbf{R}_{\mathrm{ROI}}$ is calculated using equation A.33 and $\mathbf{J}_{\mathrm{ROI}} = \mathbf{J}\mathbf{I}^{\mathbf{t}}_{\mathrm{ROI}}$:

$$\mathbf{R}_{\mathrm{ROI}} = \left(\mathbf{J}^{\mathrm{t}}_{\mathrm{ROI}}\boldsymbol{\Sigma}_{\mathrm{n}}^{-1}\mathbf{J}_{\mathrm{ROI}} + \mathbf{A}_{\mathrm{prio}}\right)^{-1}\mathbf{J}^{\mathrm{t}}_{\mathrm{ROI}}\boldsymbol{\Sigma}_{\mathrm{n}}^{-1} \tag{3.8}$$

where the a priori or penalty term is $\mathbf{A}_{\mathrm{prio}} = 0$. It is possible to work without regularization because we consider a special case of the problem where $\Delta\sigma_{\mathrm{ROI}}$ is a scalar (only one value), thus regularization is not necessary. The derived formulation for the distinguishability is based on the z-score estimate of the random variable $\Delta\sigma_{\mathrm{ROI}}$, see Urdan [97] for more details about the z-score:

$$z = \frac{\overline{\Delta\sigma_{\mathrm{ROI}}} - \kappa}{\mathrm{std}(\Delta\sigma_{\mathrm{ROI}})} \tag{3.9}$$

where κ is the hypothesis to test against.

Thus one can formulate the distinguishability as the rejection of the null hypothesis (i.e. $\kappa = 0$). Then one needs to calculate the mean of the conductivity change in the ROI and the standard deviation of the conductivity change in the ROI.

Using the mathematical expectation formulation and the MAP solution calculated in equation 3.8, one gets the mean of the conductivity change in the ROI:

$$\overline{\Delta\sigma_{\mathrm{ROI}}} = \mathrm{E}[\Delta\sigma_{\mathrm{ROI}}] = \mathrm{E}\left[\mathbf{R}_{\mathrm{ROI}}\Delta\mathbf{v}\right] \tag{3.10}$$

then using equation 3.4, and the fact that one assumes zero mean noise (i.e. $\mathrm{E}[\mathbf{n}] = 0$):

$$\overline{\Delta\sigma_{\mathrm{ROI}}} = \mathrm{E}\left[\mathbf{R}_{\mathrm{ROI}}\left(\mathbf{J}\Delta\boldsymbol{\sigma} + \mathbf{n}\right)\right] = \mathbf{R}_{\mathrm{ROI}}\left(\mathbf{J}\mathrm{E}[\Delta\boldsymbol{\sigma}] + \underbrace{\mathrm{E}[\mathbf{n}]}_{=0}\right) \tag{3.11}$$

$$= \mathbf{R}_{\mathrm{ROI}}\mathbf{J}\Delta\boldsymbol{\sigma} \tag{3.12}$$

Where $\Delta\boldsymbol{\sigma} = \mathrm{E}[\Delta\boldsymbol{\sigma}]$ is the noiseless impedance change in the medium; $\Delta\boldsymbol{\sigma}$ is the "true" impedance changes inside the medium. If one restricts the conductivity changes to the ROI, the last equation becomes:

$$\overline{\Delta\sigma_{\mathrm{ROI}}} = \mathbf{R}_{\mathrm{ROI}}\mathbf{J}_{\mathrm{ROI}}\Delta\sigma_{\mathrm{ROI}} \tag{3.13}$$

using equation 3.8, one gets:

$$\begin{aligned}
\overline{\Delta\sigma_{\mathrm{ROI}}} &= \left(\mathbf{J}_{\mathrm{ROI}}^{\mathrm{t}}\boldsymbol{\Sigma}_{\mathrm{n}}^{-1}\mathbf{J}_{\mathrm{ROI}} + \underbrace{\mathbf{A}_{\mathrm{prio}}}_{=0}\right)^{-1}\mathbf{J}_{\mathrm{ROI}}^{\mathrm{t}}\boldsymbol{\Sigma}_{\mathrm{n}}^{-1}\mathbf{J}_{\mathrm{ROI}}\Delta\sigma_{\mathrm{ROI}} && (3.14)\\
&= \Delta\sigma_{ROI} && (3.15)
\end{aligned}$$

This demonstrates that $\mathbf{R}_{\mathrm{ROI}}\mathbf{J}\Delta\boldsymbol{\sigma}$ corresponds to the noiseless conductivity changes inside the ROI.

Then one needs to calculate var$[\Delta\sigma_{\mathrm{ROI}}]$ that is equal per definition to:

$$\mathrm{var}\left[\Delta\sigma_{\mathrm{ROI}}\right] = \mathrm{E}\left[\left\|\Delta\sigma_{\mathrm{ROI}} - \overline{\Delta\sigma_{\mathrm{ROI}}}\right\|\right] \tag{3.16}$$

then using equation 3.7, one gets:

$$\mathrm{var}\left[\Delta\sigma_{\mathrm{ROI}}\right] = \mathrm{E}\left[\left\|\mathbf{R}_{\mathrm{ROI}}\Delta\mathbf{v} - \overline{\mathbf{R}_{\mathrm{ROI}}\Delta\mathbf{v}}\right\|\right] \tag{3.17}$$

then using equation 3.4 and the fact that the noise is zero mean, one gets:

$$\begin{aligned}
\mathrm{var}\left[\Delta\sigma_{\mathrm{ROI}}\right] &= \mathrm{E}\left[\left\|\mathbf{R}_{\mathrm{ROI}}(\mathbf{J}\Delta\boldsymbol{\sigma} + \mathbf{n}) - \overline{\mathbf{R}_{\mathrm{ROI}}(\mathbf{J}\Delta\boldsymbol{\sigma} + \mathbf{n})}\right\|\right] && (3.18)\\
&= \mathrm{E}\left[\left\|\mathbf{R}_{\mathrm{ROI}}\mathbf{J}\Delta\boldsymbol{\sigma} + \mathbf{R}_{\mathrm{ROI}}\mathbf{n} - \right.\right.\\
&\qquad \left.\left.\mathbf{R}_{\mathrm{ROI}}\mathbf{J}\Delta\boldsymbol{\sigma} + \underbrace{\overline{\mathbf{R}_{\mathrm{ROI}}\mathbf{n}}}_{=0}\right\|\right] && (3.19)\\
&= \mathrm{E}\left[\|\mathbf{R}_{\mathrm{ROI}}\mathbf{n}\|\right] && (3.20)
\end{aligned}$$

and then per definition of the norm, one gets:

$$\begin{aligned}
\mathrm{var}\left[\Delta\sigma_{\mathrm{ROI}}\right] &= \mathrm{E}\left[\mathbf{R}_{\mathrm{ROI}}\mathbf{n}\mathbf{n}^{\mathrm{t}}\mathrm{R}_{\mathrm{ROI}}^{\mathrm{t}}\right] = \mathbf{R}_{\mathrm{ROI}}\mathrm{E}\left[\mathbf{n}\mathbf{n}^{\mathrm{t}}\right]\mathbf{R}_{\mathrm{ROI}}^{\mathrm{t}} && (3.21)\\
&= \mathbf{R}_{\mathrm{ROI}}\boldsymbol{\Sigma}_{\mathrm{n}}\mathbf{R}_{\mathrm{ROI}}^{\mathrm{t}} && (3.22)
\end{aligned}$$

Where $\mathbf{\Sigma}_\mathrm{n}$ is the covariance matrix, which is per definition equal to :

$$\Sigma_\mathrm{n} = \mathrm{E}\left[\left(\mathbf{n} - \underbrace{E[\mathbf{n}]}_{=0}\right)\left(\mathbf{n} - \underbrace{E[\mathbf{n}]}_{=0}\right)^\mathrm{t}\right] = \mathrm{E}\left[\mathbf{n}\mathbf{n}^\mathrm{t}\right] \tag{3.23}$$

Then using the MAP solution $\mathbf{R}_\mathrm{ROI}$, given in equation 3.8, one gets:

$$\begin{aligned}
\mathrm{var}[\Delta\sigma_\mathrm{ROI}] &= \left(\mathbf{J}_\mathrm{ROI}^\mathrm{t}\mathbf{\Sigma}_\mathrm{n}^{-1}\mathbf{J}_\mathrm{ROI}\right)^{-1}\mathbf{J}_\mathrm{ROI}^\mathrm{t}\underbrace{\mathbf{\Sigma}_n^{-1}\mathbf{\Sigma}_n}_{=1}\mathbf{\Sigma}_\mathrm{n}^{-1}\mathbf{J}_\mathrm{ROI} \\
&\qquad \left(\mathbf{J}_\mathrm{ROI}^\mathrm{t}\mathbf{\Sigma}_\mathrm{n}^{-1}\mathbf{J}_\mathrm{ROI}\right)^{-1} && (3.24)\\
&= \underbrace{\left(\mathbf{J}_\mathrm{ROI}^\mathrm{t}\mathbf{\Sigma}_\mathrm{n}^{-1}\mathbf{J}_\mathrm{ROI}\right)^{-1}\left(\mathbf{J}_\mathrm{ROI}^\mathrm{t}\mathbf{\Sigma}_\mathrm{n}^{-1}\mathbf{J}_\mathrm{ROI}\right)}_{=1} \\
&\qquad \left(\mathbf{J}_\mathrm{ROI}^\mathrm{t}\mathbf{\Sigma}_\mathrm{n}^{-1}\mathbf{J}_\mathrm{ROI}\right)^{-1} && (3.25)\\
&= \left(\mathbf{J}_\mathrm{ROI}^\mathrm{t}\mathbf{\Sigma}_\mathrm{n}^{-1}\mathbf{J}_\mathrm{ROI}\right)^{-1} && (3.26)
\end{aligned}$$

If one assumes that conductivity changes outside the ROI are also considered, then the z-score can be written by combining equations 3.12, 3.26 and 3.9:

$$\begin{aligned}
z &= \frac{\mathbf{R}_\mathrm{ROI}\mathbf{J}\Delta\boldsymbol{\sigma}}{\sqrt{\left(\mathbf{J}_\mathrm{ROI}^\mathrm{t}\mathbf{\Sigma}_\mathrm{n}^{-1}\mathbf{J}_\mathrm{ROI}\right)^{-1}}} && (3.27)\\
z &= \mathbf{R}_\mathrm{ROI}\mathbf{J}\Delta\boldsymbol{\sigma}\sqrt{\mathbf{J}_\mathrm{ROI}^\mathrm{t}\mathbf{\Sigma}_\mathrm{n}^{-1}\mathbf{J}_\mathrm{ROI}} && (3.28)
\end{aligned}$$

If one restricts the conductivity changes to the ROI, then the z-score can be simplified using equation 3.15 instead of equation 3.12 like in the previous calculation step:

$$z = \Delta\sigma_\mathrm{ROI}\sqrt{\mathbf{J}_\mathrm{ROI}^\mathrm{t}\mathbf{\Sigma}_\mathrm{n}^{-1}\mathbf{J}_\mathrm{ROI}} \tag{3.29}$$

The z-score should be interpreted in the sense of the example given in section B.5.2 meaning the higher z is, the better is the distinguishability. Equation 3.29 shows that z increases with increasing conductivity contrast and decreases with the square root of the noise. Apart from that z is also a function of the measurement strategy included in the sensitivity matrix $\mathbf{J}$.

Distributing $\Delta\sigma_\mathrm{ROI}$ under the square root sign gives:

$$z = \sqrt{\Delta\sigma_{\mathrm{ROI}} \mathbf{J}_{\mathrm{ROI}}^{\mathrm{t}} \boldsymbol{\Sigma}_{\mathrm{n}}^{-1} \mathbf{J}_{\mathrm{ROI}} \Delta\sigma_{\mathrm{ROI}}} \tag{3.30}$$

then using equation 3.4 with $\mathbf{n} = 0$ [3]:

$$z = \sqrt{\Delta\mathbf{v}_{\mathrm{ROI}}^{\mathrm{t}} \boldsymbol{\Sigma}_{\mathrm{n}}^{-1} \Delta\mathbf{v}_{\mathrm{ROI}}} \tag{3.31}$$

Letting the noise between measurements be uncorrelated (i.e. noise covariance terms are all equal to zero), the matrix $\boldsymbol{\Sigma}_{\mathrm{n}}$ became diagonal and one gets:

$$z = \sqrt{\sum_{i=1}^{N} \left(\frac{\Delta \mathrm{v}_{\mathrm{ROI},i}}{\sigma_{\mathrm{n},i}} \right)^2} \tag{3.32}$$

If the noise in each channel is assumed to be the same, one gets:

$$z = \frac{1}{\sigma_{\mathrm{n}}} \left\| \Delta\mathbf{v}_{\mathrm{ROI}} \right\|_2 \tag{3.33}$$

Where

$\Delta\mathbf{v}_{\mathrm{ROI}}$ are voltage changes at the medium border generated by the conductivity change $\Delta\sigma_{\mathrm{ROI}}$ inside the ROI,

σ_{n} is the standard deviation of the noise that is assumed to be the same for each channel.

In this case the distinguishability becomes the norm in the L_2 sense of the differential voltage divided by the noise. From this formula, it makes a lot of sense to define the signal strength as $\left\| \Delta\mathbf{v}_{\mathrm{ROI}} \right\|_2$. Equation 3.33 also allowed us to separate the study of the noise from the study of the signal. The following sections are organized based on this consideration.

[3] This notations means that all components of $\mathbf{n}$ are equal to 0.

3.3 Study of the EIT signal

As any other signal, the EIT signal is defined as the useful part of the raw signal coming out of the acquisition system. The non-used or non-useful part of the signal is divided between the noise (random fluctuation) and static errors. Both often perturb the measurements of interest, and will be treated in a separated sections hereafter. Differential imaging is a relatively simple solution to get rid of most of the static errors. This also partially explains why differential imaging is easier than absolute imaging. Concerning the random noise, the only way physics allows us to statistically distinguish the EIT signal from the background noise is to integrate (or take the average of) the raw signal for a sufficiently long time. Doing so a statistical separation occurs because of the different statistical behaviors between noise and signal. For instance on an histogram representation, the noise could appear as white Gaussian and zero-mean, whereas the useful signal[4], provided a sufficient SNR level is reached, usually gets sample counts outside the noise statistics .

3.3.1 General considerations

In the literature many authors proposed various ways for generating an EIT signal that was useful for their specific applications. The EIT signal can be classified into three categories:

- absolute imaging [39],
- time differential imaging [13],
- frequency differential imaging [75, 74].

Despite the fact that in this thesis these three categories are treated separately, it is possible to mix them together [74] and to create mixed-images with temporal and frequency information. The absolute imaging technique, depicted in a) of figure 3.1 is the most demanding one in terms of signal quality, and to our best knowledge concrete and reliable results have only been obtained using fairly low (< 100 Hz) excitation frequencies [22] in geophysical or industrial applications. Essentially the difficulties with absolute imaging are the lack of knowledge about the exact electrode positions, the unknown and possibly varying quality of the contacts, the EIT system stray capacitance and the exact injected current values. The latter could of course be measured and the reconstruction could take that into account, but it increases the difficulty of

[4] One assumes that the signal is a differential signal and therefore static error free.

the overall data acquisition hardware. Absolute imaging in combination with frequency spectral analysis is very difficult to master, but would be of great interest in the medical domain. For example tumor screening as described by Cherepenin et al. [19], Saulnier et al. [82] without exposing the patient to ionizing X-ray based imaging techniques would become possible.

An interesting alternative to overcome the difficulties encountered in the absolute imaging for industrial and biomedical imaging is to work with a very well controlled and known medium, such as a micro well or a saline tank, as depicted in figure 3.1 b). In this situation one takes the homogenous medium of conductivity $\sigma_{1.2}$ as the reference data set. Then one subsequently uses it as the reference like in the normal time difference imaging. In this way, it becomes possible to calculate the absolute changes relative to the homogenous and known medium.

Unfortunately there are situations were none of the above techniques is applicable, and one is forced to apply the so-called time differential imaging. In this case the data set is subtracted from a reference data set taken earlier under similar experimental conditions. As a result, one gets the spatial distribution of the impedance changes between the two situations. The choice of the reference is one of the critical operations in the process of making time difference imaging function properly. To the author's best knowledge, time difference imaging is nowadays the most commonly and successfully applied EIT imaging scheme in the medical domain.

With time difference imaging it is only possible to acquire images of time varying event. These variation times have to stay below a certain limit defined by the drift of the data acquisition system or by the constraints on the measurements. For example, if one is interested to monitor the evolution or the appearance of a breast tumor, it is clearly not an option to let a woman lying for years over a data acquisition system. Absolute imaging could in principle solve the problem of tumor imaging but this technology is at the time of writing still far from being able to produce sufficiently precise results. An alternative could be the frequency differential imaging, see Robitaille [74]. This technique is based on the fact that various media (or tissues) have different characteristic impedance. In the present section the developed reasoning is time difference oriented but the general principle could also be applied to other techniques.

Using the Von Neumann boundary conditions (i.e. apply current and measure voltages), it can be shown that for the non-continuous case the forward problem of calculating the boundary voltage $\mathbf{v}$ can be expressed as:

$$\mathbf{Tc} = \mathbf{v} \tag{3.34}$$

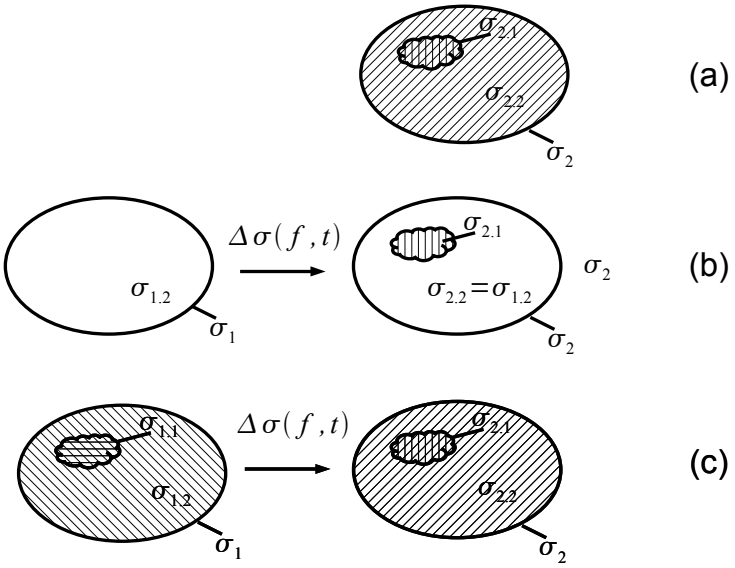

Figure 3.1: Illustration of a) an absolute imaging process, which tries to retrieve the absolute value of the conductivity σ_2 from the voltage measurement at the boundary of the medium, b) and c) time difference imaging processes, which try to retrieve the differential conductivity $\Delta\sigma$ from the voltage measurement at the boundary of the medium. The b) situation is a type of absolute imaging process taking advantage of a suitably controlled background medium, this is the case in a saline tank or in micro-EIT wells for example.

where

T is the transimpedance matrix $M \times M$ defined by the medium and the EIT measurement system,

c is a vector $1 \times M$ representing the applied currents on the electrodes,

v is a vector $1 \times M$ representing the voltages obtained at the electrodes.

For example equation 3.34 could be calculated using FEM, where the space is divided in finite elements, such as triangles for example. Assuming a node based calculation, M, will the number of node of the FEM mesh. For the differential imaging case, it is necessary to consider two transimpedance matrices ($\mathbf{T}_1$ and $\mathbf{T}_2$) representing the two situations:

$$(\mathbf{T}_1 - \mathbf{T}_2)\mathbf{c} = \Delta\mathbf{v} \tag{3.35}$$

From equation 3.35, it is obvious that increasing the current leads to an automatic increase of the EIT signal $\Delta\mathbf{v}$. Therefore addressing the problem of the signal strength for a given situation automatically asks two questions: 1) what are the regulations in force concerning patient electrical safety and 2) what are the technical limitations for the current source. The patient safety issues and an interpretation of the available regulatory documents are presented in section 3.3.2.

At this point, it is not obvious which injection strategy is the best in terms of generated signal. In particular, one can ask what is the best current injection strategy between using a pair of electrodes [5] and using so-called trigonometric current [6] which implies that several electrodes are injecting and sinking current simultaneously. We will investigate this question by considering a time differential imaging strategy as depicted in figure 3.2. The result of applying a current pattern **c** to the medium with a spatial conductivity distribution $\boldsymbol{\sigma}_t$ is given by:

$$\mathbf{v} = \mathbf{T}\boldsymbol{\sigma}_t\mathbf{c} \tag{3.36}$$

where

[5] One electrode for injecting the current and the other one for sinking it.

[6] The current intensity around the medium is spatially modulated with for example a cosine function.

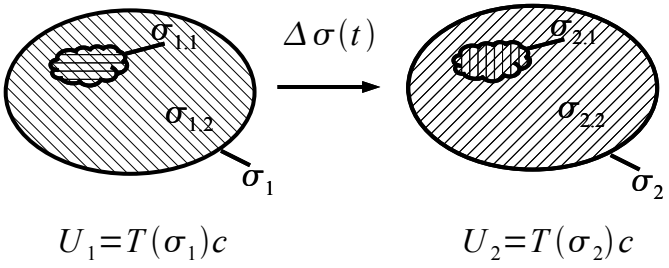

Figure 3.2: Illustration of the temporal change of the internal impedance within the same medium between two situations and their respective transfer impedance matrices.

$\boldsymbol{\sigma}_t$ is the spatial conductivity distribution in the medium at time t.

In the case of differential imaging, one gets the following differential signal of interest:

$$\Delta\mathbf{v} = \mathbf{v}_1 - \mathbf{v}_2 = (\mathbf{T}\boldsymbol{\sigma}_1 - \mathbf{T}\boldsymbol{\sigma}_2)\,\boldsymbol{c} = \mathbf{T}_d\mathbf{c} \tag{3.37}$$

where

$\mathbf{T}_d$ is the time differential transfer impedance matrix, which can be calculated using various techniques, such as analytical analysis or Finite Element Model (FEM),

$\Delta\mathbf{v}$ is the EIT signal between the two situations.

As a benchmark for the resulting EIT signal $\Delta\mathbf{v}$, one calculates the L^2 norm, called signal strength (see equation 3.33). The idea is to give more weight to large values compared with smaller ones. Therefore one seeks to maximize $\|\Delta\mathbf{v}\|^2$ given an optimal choice of the current pattern $\mathbf{c}$. Essentially, there are two interpretations of the applicable current limitation in EIT, the first one limits the sum of absolute amplitude of the injected currents and the second one limits the sum of power of the injected currents. Both limitations make technical sense, but according to our best interpretation of the norm IEC 60601 [1], only the first one is used to define the patient electrical safety limit.

In the case that the absolute amplitude of the current is limited by the regulatory or any other constraints, the L^1 norm of $\mathbf{c}$ is not allowed to be bigger than a given value $c_{\max}$:

$$\|\mathbf{c}\|_1 = \sum_i |c_i| \leq c_{\max} \tag{3.38}$$

In this case, one can demonstrate in two steps that the 2-point injection strategy[7] is the one maximizing the signal strength $\|\Delta\mathbf{v}\|^2$. First, one considers the case where only 1 injecting electrode and 1 sinking electrode are used:

$$\begin{aligned} \|\Delta\mathbf{v}\|^2 &= \mathbf{c}^{\mathrm{t}}\mathbf{T}_{\mathrm{d}}^{\mathrm{t}}\mathbf{T}_{\mathrm{d}}\mathbf{c} && (3.39) \\ &= \begin{pmatrix} \cdots 0 & 1 & 0 & 0 & -1 \cdots \end{pmatrix} \\ &\quad \begin{pmatrix} \cdot & \cdot & \cdot & \max 2 & \cdot \\ \cdot & \cdot & \cdot & \cdot & \cdot \\ \cdot & \max 1 & \cdot & \cdot & \cdot \\ \cdot & \cdot & \cdot & \cdot & \cdot \\ \cdot & \cdot & \cdot & \cdot & \cdot \end{pmatrix} \begin{pmatrix} \vdots \\ 0 \\ 1 \\ 0 \\ 0 \\ -1 \\ \vdots \end{pmatrix} && (3.40) \end{aligned}$$

where

$$\max 1 \geq \max 2 \geq \max 3 \geq \cdots \tag{3.41}$$

The two maximal elements of matrix $\mathbf{T}_d$ can always be identified, therefore a bipolar current pattern $\mathbf{c}$ can always be chosen so that it maximizes the matrix multiplication making use of the two largest terms.

Considering a second case where another strategy as pair drive is used, such as for example a 3-electrode drive strategy, the mathematical expression for the signal strength becomes:

[7] Also called pair drive strategy.

$$\begin{aligned} \|\Delta\mathbf{v}\|^2 &= \mathbf{c}^{\mathrm{t}}\mathbf{T}_{\mathrm{d}}^{\mathrm{t}}\mathbf{T}_{\mathrm{d}}\mathbf{c} = \qquad (3.42)\\ &= \begin{pmatrix} \cdots 0 & 1 & 0 & -\frac{1}{2} & -\frac{1}{2}\cdots \end{pmatrix} \end{aligned}$$

$$\begin{pmatrix} \cdot & \cdot & \cdot & \max 2 & \cdot \\ \cdot & \cdot & \cdot & \cdot & \cdot \\ \cdot & \max 1 & \cdot & \cdot \max 3 & \cdot \\ \cdot & \cdot & \cdot & \cdot & \cdot \\ \cdot & \cdot & \cdot & \cdot & \cdot \end{pmatrix} \begin{pmatrix} \vdots \\ 0 \\ 1 \\ 0 \\ -\frac{1}{2} \\ -\frac{1}{2} \\ \vdots \end{pmatrix} \qquad (3.43)$$

Considering 3.41 it is obvious that involving a potentially smaller term max3 in the matrix multiplication would lead to smaller values of $\|\Delta\mathbf{v}\|^2$. At this point, we demonstrate that under the condition that the sum of the magnitude of the current pattern is the limiting factor, pair drive strategy maximizes the signal strength. As desired the permutation or an alternative distribution of the elements in the matrix $\mathbf{c}$ do not affect the total sum of current magnitude (see equation 3.38). Using simulation tools such as EIDORS, it is possible to calculate a FEM based transimpedance matrix for all possible 32-electrode pair drive strategies and some discrete object positions. For each object position the largest matrix element is identified and displayed on figure 3.3. The results show that pairs of injecting electrodes used in opposite configuration are the best choice as far as the signal strength is concerned. The outlyers observed in the calculation are generated by simulation numerical errors. Changing a little bit the input parameter leads to other outlayers, but the conclusion is that offset 15 is in most cases calculated to be the strategy generating the highest signal strength.

In another case, where the total power of the injected current is considered to be the limiting factor (see equation 3.44), one needs to reconsider the calculation. Therefore another approach is necessary, starting with the transimpedance equation :

$$\|\Delta\mathbf{v}\|^2 = \mathbf{c}^{\mathrm{t}}\mathbf{T}_{\mathrm{d}}^{\mathrm{t}}\mathbf{T}_{\mathrm{d}}\mathbf{c} \qquad (3.44)$$

and taking the Singular Value Decomposition (SVD) of $\mathbf{T}_d = \mathbf{U}\mathbf{D}\mathbf{V}^{\mathrm{t}}$, we obtain:

$$\|\Delta\mathbf{v}\|^2 = \mathbf{c}^{\mathrm{t}}\mathbf{V}\mathbf{D}\underbrace{\mathbf{U}^{\mathrm{t}}\mathbf{U}}_{=1}\mathbf{D}\mathbf{V}^{\mathrm{t}}\mathbf{c} = \mathbf{c}^{\mathrm{t}}\mathbf{V}\mathbf{D}^2\mathbf{V}^{\mathrm{t}}\mathbf{c} \qquad (3.45)$$

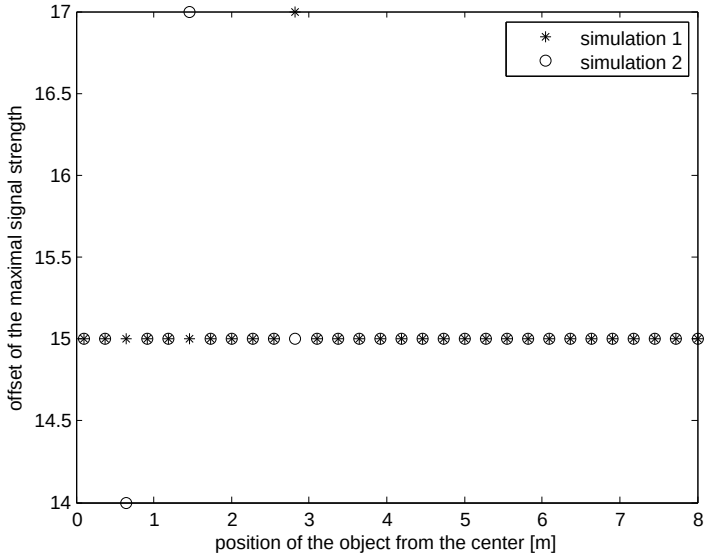

Figure 3.3: Illustration of the ideal current pattern in function of the object distance from the center, the result in the y-axis is given in offset (for equidistant 32-electrode EIT system) to apply to the injecting pair to get the maximal signal strength. A few outlayers are observed due to simulation numerical errors.

The two matrix multiplications $\mathbf{c}^t\mathbf{V}$ and $\mathbf{V}^t\mathbf{c}$ decompose the current vector into the Eigenvector directions given by the column of $\mathbf{V}$:

$$\mathbf{c}^t\mathbf{V} = \left[\mathbf{c}^t\mathbf{v}_1|\mathbf{c}^t\mathbf{v}_2|\cdots|\mathbf{c}^t\mathbf{v}_n\right] \tag{3.46}$$

Where the $\mathbf{v}_i$ are the columns of the matrix $\mathbf{V}$. The product $\mathbf{c}^t\mathbf{V}$ is a vector of which each element is given by the multiplication $\mathbf{c}^t\mathbf{v}_i$. The elements $\mathbf{c}^t\mathbf{v}_i$ should be understood as power terms of the current $\mathbf{c}$ projected in the direction $\mathbf{v}_i$. In other words, the $\mathbf{c}^t\mathbf{v}_i$ elements are the contribution of each eigenvector $\mathbf{v}_i$ to the global $\|\Delta\mathbf{v}\|$. Using equation 3.46 and inserting it in equation 3.45, one gets:

$$\begin{aligned}\|\Delta\mathbf{v}\|^2 &= \left[\mathbf{c}^t\mathbf{v}_1|\mathbf{c}^t\mathbf{v}_2|\cdots|\mathbf{c}^t\mathbf{v}_n\right]\begin{bmatrix} d_1^2 & 0 & \cdots & 0 \\ 0 & d_1^2 & \cdots & 0 \\ \vdots & \vdots & \ddots & \vdots \\ 0 & 0 & \cdots & d_n^2 \end{bmatrix}\begin{bmatrix} \mathbf{c}^t\mathbf{v}_1 \\ \mathbf{c}^t\mathbf{v}_2 \\ \vdots \\ \mathbf{c}^t\mathbf{v}_n \end{bmatrix} \quad (3.47)\\ &= (\mathbf{c}^t\mathbf{v}_1)^2d_1^2 + (\mathbf{c}^t\mathbf{v}_2)^2d_2^2 + \cdots + (\mathbf{c}^t\mathbf{v}_n)^2d_n^2 \quad (3.48)\end{aligned}$$

From the SVD definition one knows that $d_1 \geq d_2 \geq \cdots \geq d_n$, therefore in order to maximize the signal strength it is desirable to maximize the term $(\mathbf{c}^t\mathbf{v}_1)^2$. This is done by "aligning" the vector $\mathbf{c}$ with $\mathbf{v}_1$. In other words, $\mathbf{v}_1$ can be identified as the optimal injection pattern. This can be visualized using EIDORS. In figure 3.4 the optimal current pattern in function of the object position is plotted for a 3D tank where a cylindrical object is moved from the center to the border. In the special case when the object is at the center of the cylindrical tank the best injection pattern is a spatial sinusoidal distribution of the current intensity as predicted also by Isaacson [45].

3.3.2 Constraints on the injected current

Since the more one injects current into a given medium the more signal amplitude we get, it is necessary to study what the limiting factor are for the current. Essentially, there are three types of constraints: 1) the technical constraints given by the practical realization of the current source, 2) the contextual constraints given by the particular experimental conditions and 3) the regulatory rules for safe operation of electrical devices.

The technical constraints on the current source are given by the internal impedance of the current source, the power supply voltage available and the technical limitation of each element of the current source. For example the

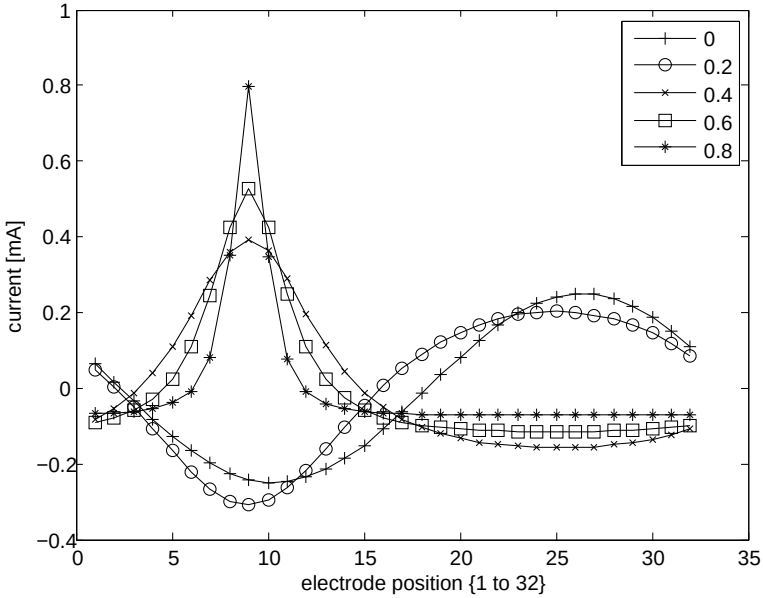

Figure 3.4: Illustration of the optimal current in function of the electrode index for 6 possible positions (from the center 0 m to the near the border 0.8 m) of the object inside a cylindrical tank (1 m radius). One can see that the current pattern corresponding to the case, where the object is put in the middle of the medium can be identified as a sinusoid. The simulated data points were linked with straight lines segments.

Table 3.1: Authorized current limits according to IEC60601-1:2005

Applied Frequency [Hz]	RMS Current Limit Type BF [µA]	RMS Current Limit Type CF [µA]
0	10	10
10 to 10^3	100	10
10^4	1000	100
10^5 to infinity	10000	1000

amount of current that an operational amplifier can deliver is limited. The topic of the current source technical specification is discussed in much greater detail in section 4.2.1.1.

The contextual constraints are given by the experimental conditions. For example in a micro well, it could be desirable not to increase the temperature of the solution up to the boiling point. Thus there will be constraints on the amount of power allowed to avoid the temperature of the solution to rise above a certain threshold. The Joule heating formulas are given in section 3.9.5.

The regulatory rules are of essential importance for applications in the medical imaging domain in which currents are applied to patients. First, it is interesting to note that there are no specific rules concerning medical-EIT safety yet. Nevertheless there are rules concerning devices in contact with the patient with respect to the electrical safety. In particular the IEC60601-1:2005[1] defines so-called "patient auxiliary currents" which are currents applied intentionally to the patient's body. Especially important is the point 8.7.3 e) stating that a current of more than 10 mA_{rms} is not allowed independently of the waveform and the frequency. Our best interpretation of the norm is given in a non-exhaustive way in table 3.1.

The international norm IEC60601-1 recognizes, as far as the electrical safety is concerned, various types of medical devices:

- B type is the category of lowest standard,
- BF type is the same as the B type but with floating "applied parts[8]",
- CF type is the category of highest standard in which the limit current values are lower than for the other categories and it should also be

[8] Applied part refers to all connection to the patient including connections from other devices.

floating. This category is especially suitable " for DIRECT CARDIAC APPLICATION". It is not quite clear what direct means, in another document [17] direct is interpreted as on the heart directly (internally), such as for example for cardiac pacemaker devices. If this interpretation is right EIT would clearly be in the BF category and not in the CF one,

- F type sub-category refers to floating devices. Floating means that the device has to be decoupled from earth potential and main power supply. In the norm IEC60601-1 this is measured using the "Patient leakage current"; the maximally allowed limit currents are the same as for the "patient auxiliary current" see table 3.1,
- "DEFIBRILLATION-PROOF applied part", this category specify essentially 2 safety measures: 1) (IEC section 8.5.5.1) specifies that during defibrillation none of the potentially harmful voltage appears on the device part or enclosure, and 2) (IEC section 8.5.5.2) that the total energy applied on the patient should not be absorbed more than 10% by all "applied parts" (i.e. including other devices attached to the patient).

In the best interpretation of the author, an important consequence of this norm is that it limits the absolute amplitude of the sum of the injected currents, therefore the optimal current injection strategy is pair drive, see section 3.3.1 for details.

3.3.3 Signal strength

In EIT the "useful" signal is the EIT differential signal $\Delta\mathbf{v}$ at the medium boundary measured on the electrodes between a reference state and the present state. The size of the vector $\Delta\mathbf{v}$, assuming that none of the measurements are discarded, is $N_{\text{el}} \cdot N_{\text{el}}$, where N_{el} is the number of electrodes. For example assuming $N_{\text{el}} = 32$ leads to a vector $\Delta\mathbf{v}$ containing 1024 elements. The whole vector can be summarized in one single scalar value, the signal strength, by taking the L^2 norm of the vector $\Delta\mathbf{v}$:

$$\|\Delta\mathbf{v}\|_2 \tag{3.49}$$

This gives us the definition of signal strength used in this thesis. At this point it is also possible to consider normalized signal strength by diving by the number of measurements or the root mean square definition and dividing by the square root of the number of elements. Bill Lionheart in his EIT course[9] also suggested a normalization by the injected current amplitude. In

[9] http://eitrecon.blogspot.com/, 10.12.2010

the present document unless otherwise noted the signal strength is always meant in the sense of equation 3.49.

3.3.4 An analytical approach

This section presents an analytical analysis of the forward problem based on the theoretical results available in the literature. The general idea, in order to make the analysis possible, is that one has to keep the geometry of the problem simple. Therefore in the following, it is assumed that the medium is a disk and that all the inhomogeneities (i.e. the objects to be imaged) are also disks. At first, in section 3.3.4.1 the symmetrical problem is treated based on the result of [45]. Then the solutions given by [84, 85] for the non-symmetrical (i.e. where the inhomogeneities are not at the center anymore) problems are reported in section 3.3.4.2 and the calculations are done using the analytical functions of EIDORS. In both cases, the geometry is kept in two dimensions, the three-dimensional case is broached in section 3.3.5.2 in which a Finite Element Model (FEM) is used for the simulation.

3.3.4.1 The symmetrical problem

Under the assumption that the radius of the medium is normalized to 1 and that one single inhomogeneity is placed at the center of the disk (see figure 3.5), the analytic formulation for the potential is given by Isaacson [45]:

$$v(\theta) = -\sum_{n=1}^{\infty} \frac{1}{n} \frac{1 - \frac{\sigma_1 - \sigma_2}{\sigma_1 + \sigma_2} a^{2n}}{1 + \frac{\sigma_1 - \sigma_2}{\sigma_1 + \sigma_2} a^{2n}} \left(C_n \cos(n\theta) + S_n \sin(n\theta)\right) \tag{3.50}$$

assuming

$$C_n = \frac{1}{\pi} \int_0^{2\pi} j(\theta) \cos(n\theta) d\theta \tag{3.51}$$

and

$$S_n = \frac{1}{\pi} \int_0^{2\pi} j(\theta) \sin(n\theta) d\theta \tag{3.52}$$

where

a is the radius of the disk inhomogeneity,

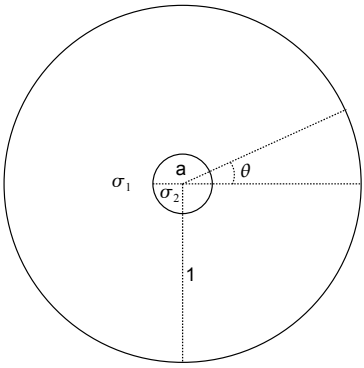

Figure 3.5: Schematic representation of the analytical problem.

σ_1 is the conductivity of the medium,

σ_2 is the conductivity of the inhomogeneity,

$j(\theta)$ is the current density at the medium boundary at angle θ,

$v(\theta)$ is the voltage obtained at the medium boundary at angle θ.

By varying the parameters of equation 3.50, one obtains an intuitive representation of what the influences are on the measured potential at the boundary of the medium of interest. Of course this is a very simplified case of the reality but the basic conclusions are still good approximations of what happens from a physical point of view even considering complete 3D objects. For this purpose we used the function "analytic_2d_circle" given in EIDORS. Then custom programs have been written in order to use EIDORS functions to vary the parameters and create plots.

For the first two calculations presented in figure 3.6 and 3.7 both signal strengths and signal mean are depicted. The signal mean is only depicted in these two figures to obtain a plot without any squaring function. In this way the linear part of the function is better emphasized.

The classic way to begin this analysis is to look at the variation of the EIT signal $v(\theta)$ at the electrodes given the variation of σ_2 while keeping σ_1 constant. The result of the calculation in figure 3.6 shows a symmetrical behavior of the potential curve around the conductivity of the medium σ_1. As it can be observed on the lower plot of figure 3.6, if the conductivity of the inhomogeneity is of the same order of magnitude as the conductivity of the medium, it is reasonable to linearize the EIT problem around the conductivity of the

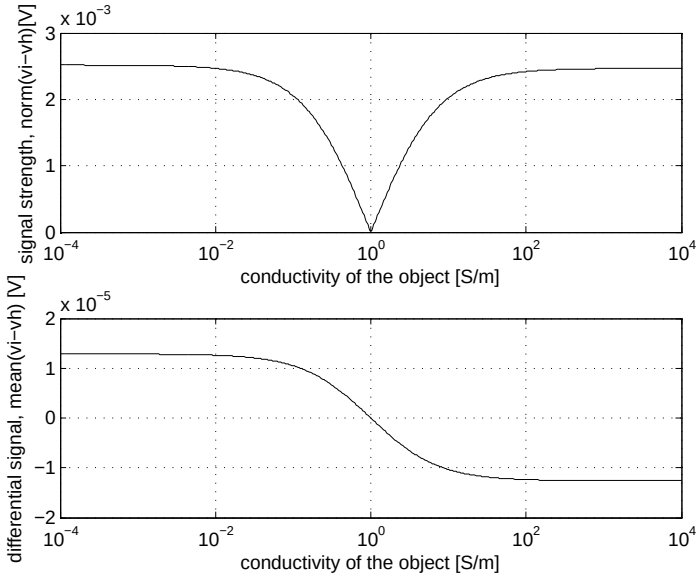

Figure 3.6: Illustration of the effect of the conductivity variation of a centered object of fixed size (10% of the medium radius) calculated for an adjacent type of injection and measurement. The upper plot uses the signal strength as benchmark whereas the lower plot uses the mean of the EIT signal. In both cases the homogeneous situation is set to $\sigma_1 = 1$. If conductivity changes are not too large compare with the homogeneous conductivity, one sees that the voltages at the medium boundary varies almost linearly with the conductivity changes. This analysis is used as a basis to justify the linearization of the EIT problem.

homogeneous medium. Interestingly after a certain conductivity change has been reached, typically 2 orders of magnitude, the generated signal saturates and any further conductivity changes will only have a limited effect on the measured voltages.

The second figure of merit we can look at, is the variation of $v(\theta)$ given the variation of the radius a of an object of fixed conductivity σ_2, see figure 3.7. If the size of the object stays within 50% of the medium size, the linearization of the problem appears to be a fair approximation.

After having set the stage with these two preliminary calculations, we can ask ourselves what are the effects of the measurement strategy on the signal strength. The results of the calculation are presented in figures 3.8 and 3.9.

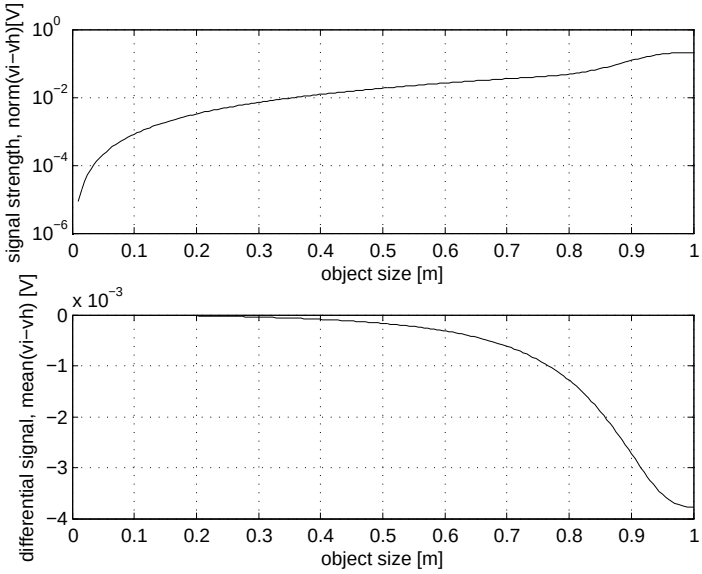

Figure 3.7: Illustration of the effect of the size variation of a centered object of fixed conductivity calculated for an adjacent injection and measurement strategy. Both plots are bounded by the minimal (=0) and maximal size of the tank (=1) which also corresponds to minimal and maximal object size.

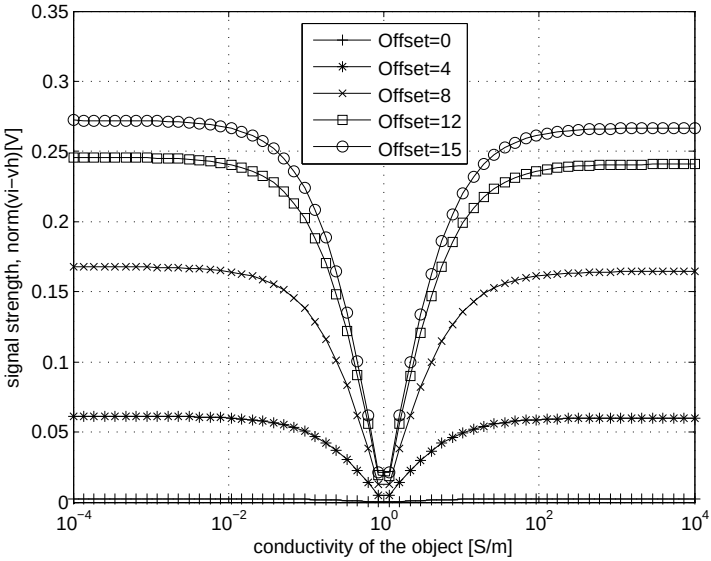

Figure 3.8: Illustration of the effect of the conductivity variation of a centered object of fixed size calculated for various types of injection and measurement offsets. Interestingly the adjacent (offset=0) strategy is the one with the lowest signal strength value. We can also see that the difference between offset 12 and offset 15(opposite) is small if the conductivity change is not larger than 1 order of magnitude compared with the reference.

In both cases the signal strengths were calculated to increase with increasing offset. Therefore, the best distinguishability as defined in equation 3.33 is expected for opposite (offset=15) measurement strategy.

3.3.4.2 The non-symmetrical problem

The development of the non-symmetrical case goes far beyond the scope of the present thesis; nevertheless the interested reader is referred to the following papers [84, 85, 86]. The final results are given here as presented in the original articles with some notation changes. The global idea is to do most part of the calculation in the spatial Fourier domain. Therefore the expression for the transconductance,

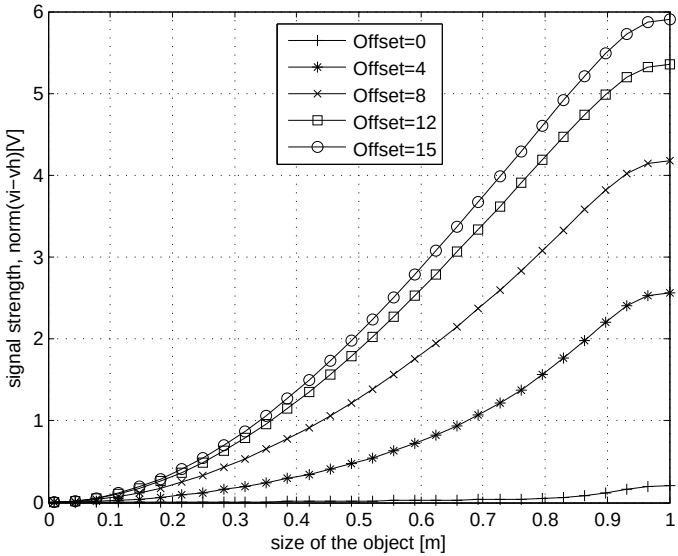

Figure 3.9: Illustration of the effect of the size variation of a centered object of fixed conductivity calculated for various types of injection and measurement strategy. As in figure 3.8 offset 12 and offset 15 are very similar if the size of the object compared to the size of the tank is not larger than 50%.

$$j(\theta) = Tv(\theta) \tag{3.53}$$

becomes in the Fourier domain,

$$J(\Theta) = T^F V(\Theta) \tag{3.54}$$

where $T^F$is given by,

$$T^F = -\left(\frac{R}{\sigma_1}\right)(I - QD)^{-1}(I + QD)\,D^{-1} \tag{3.55}$$

and each element [m, n] of Q is given by,

$$Q_{m,n} = \frac{1}{n}\frac{\sigma_1 - \sigma_2}{\sigma_1 + \sigma_2} e^{i(m-n)\beta} b^{m+n} \sum_{p=1}^{<(m,n)} \begin{pmatrix} m-1 \\ p-1 \end{pmatrix} \begin{pmatrix} n \\ p \end{pmatrix} \left(\frac{a}{b}\right)^{2p} \tag{3.56}$$

and each element [m, n] of D is given by,

$$D_{m,n} = m\delta_{m,n} = \begin{pmatrix} 1 & 0 & \cdots & 0 \\ 0 & 2 & 0 & \vdots \\ 0 & 0 & \ddots & 0 \\ 0 & \cdots & 0 & m \end{pmatrix} \tag{3.57}$$

where

R	is the radius of the medium,
a	is the radius of the disk like inhomogeneity (object),
b	is the distance between the medium center and the inhomogeneity center,
β	is the angle at which the inhomogeneity is placed,
σ_1	is the conductivity of the medium,
σ_2	is the conductivity of the inhomogeneity,
$< (m, n)$	means the lesser of m and n (i.e. for m=2 and n=4 the result is 2),

$\begin{pmatrix} n \\ p \end{pmatrix}$ denotes the binomial coefficient.

Once $V(\Theta)$ is calculated, the inverse Fourier transform is taken to go back in the spatial domain to get $v(\theta)$. The authors observed that this analytic analysis suffers in practice from the lack of sufficiently precise numerical computation, leading to strange effects in the results. This is why we decided not to show these inconclusive results. These problems also illustrate the need for a better way of calculating the forward problem, especially for non-symmetrical geometry. The next section will make use of a FEM based technique to process numerical simulations of the EIT forward problem.

3.3.5 A FEM approach

The Finite Element Method (FEM) is one of the possible ways of calculating the EIT forward problem for situations of complex geometry. If for the FEM calculation only linear interpolation functions are used, one can interpret the FEM as the meshing of the space of interest with discrete resistors. Thus one can apply Kirchhoff's law of current and voltage at each node and each loop, respectively. In this thesis, FEM simulations are done using the open-source program EIDORS [4] which is especially dedicated to EIT calculations within the Matlab environment. More complex calculations using other physical effects such as heat, electromagnetism and chemical reactions are possible using more sophisticated commercial FEM software such as Comsol multiphysics[10], but this goes beyond the scope of the present thesis.

Since we work exclusively with disks and cylinders in this section, it is convenient to define a cylindrical coordinate system, see figure 3.10. The symbol names are given as follow:

r is the radial distance of the object from the z-axis,

h is the height at which an object is placed,

β is the angle between the y-axis and the center of the object,

a is the radius of the object,

R is the radius of the tank (cylinder),

H is the height of the tank,

$\mathbf{M}_R$ represents a radial displacement,

[10] http://www.comsol.com/, 10.12.2010

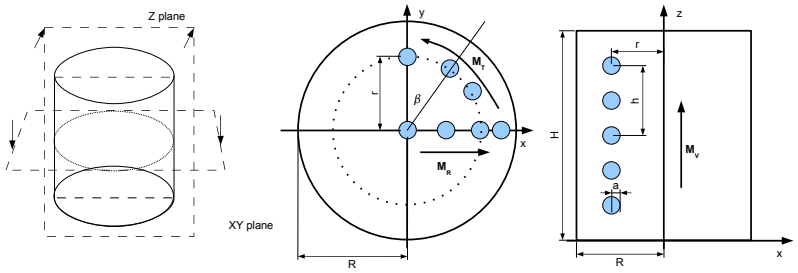

Figure 3.10: The cylindrical coordinate system used for the FEM numerical simulation.

$\mathbf{M}_T$ represents a tangential displacement,

$\mathbf{M}_V$ represents a vertical displacement.

In EIDORS electrode 1, the first electrode, is defined per default to be at position (x=0, y=R) and the electrode numbering proceeds counter-clockwise.

3.3.5.1 Two-dimensional simulations

Although in real life the world is, in most cases, 3D, it is still interesting to look at 2D simulations because they are easier to understood and quicker to simulate. It is also intuitively clear that the 2D case is not too far from the 3D case. For example considering a cylindrical object placed inside a cylindrical tank with electrodes of the same height as the tank, one essentially gets the 2D case[11]. In this section, one only works with simple 2D meshes (see figure 3.11) generated using the netgen[12] interface provided within EIDORS. The size and units used for the simulation are meter/Siemens/mA/mV. Since the results are scalable, the units and sizes used for the simulations are not of great importance. One could also even consider the size of the geometry in percent.

In figure 3.12 the signal strength in function of the object conductivity and measurement strategy is studied. In case the object is placed at the center of the medium, one can observe that the obtained curves are similar to the one calculated using the analytical formula figure 3.8. Nevertheless a slight left-right asymmetry of each curve is observed. It appears that the signal strength

[11]This is only exactly true in the case when the height of the object, the tank and the electrodes tend toward infinity.

[12]http://www.hpfem.jku.at/netgen/ or http://sourceforge.net/projects/netgen-mesher/, 10.12.2010

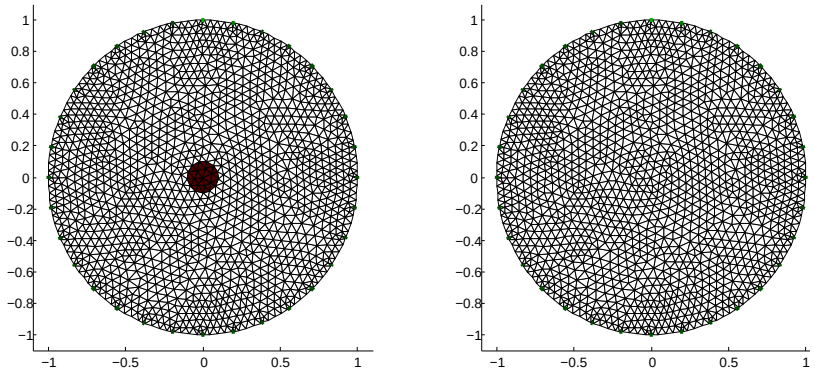

Figure 3.11: An example of a possible FEM mesh generated using netgen; on the left hand side with an object (inhomogeneous) and on the right hand-side without object (homogeneous).

corresponding to objects less conductive than the medium is smaller than the one generated by objects more conductive than the medium. At the time of writing this effect in still an on-going research topic. Possible explanation for it could be numerical error or theoretical mismatch of the FEM model. Yet measurements in section 6.4.2.2 indicate that this effect also appears in reality. This could be an indication that this effect is not due to any FEM theoretical mismatch, but it really exists.

In this second simulation the previous simulation is repeated but with the object placed at a radial distance, r, equal to 80% of the radius, R, of the tank. This leads to an increase of the overall signal strength, see figure 3.13. The increase appears to be larger for small offsets than for large ones.

In another simulation depicted in Figure 3.14, where the object moves from the center to the border of the tank according to the $\mathbf{M}_R$ vector (see figure 3.10), it is observed that the signal strength increases with the object approaching the border of the tank. For large and small offset values the signal strength stays almost constant in function of the object position. This suggests that using large offsets may reduce the image dependencies in function of the position. For intermediate offset values, for example offset=4, a clear increase in the signal strength is observed after the object is displaced to 30% of the tank radius.

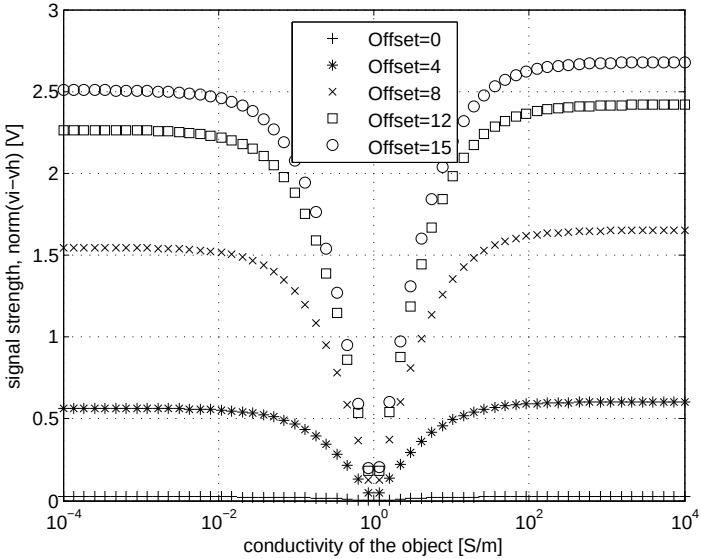

Figure 3.12: Illustration of the effect of the conductivity variation of a centered object of fixed size calculated for various types of injections and measurement offsets. The idea behind this simulation was to do a qualitative check of the analytic solution found in figure 3.8. By comparing both figures we can conclude that the analytical and FEM model produce similar curve shape.

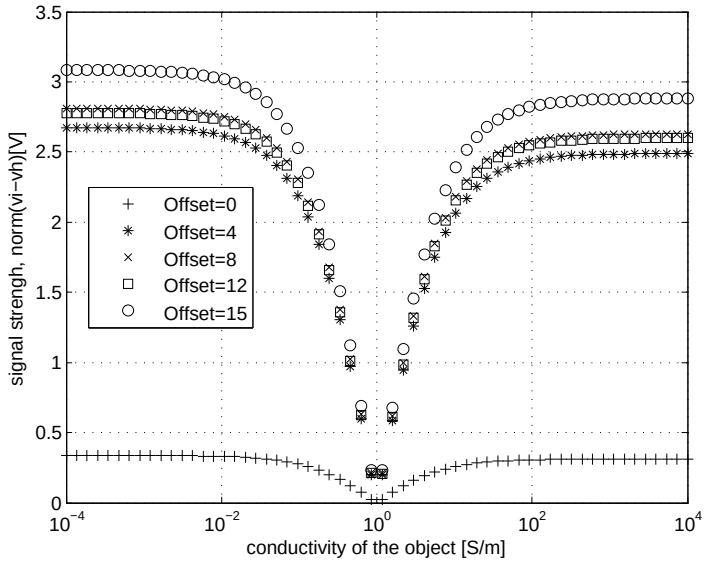

Figure 3.13: Illustration of the effect of the conductivity variation of an object of fixed size placed at 80% of the radius calculated for various types of injection and measurement offsets. One can notice an overall increase of the signal strength compared to the case where the object is placed at the center as in figure 3.12. One observes that offset 4 to 15 curves tend to become very similar for conductivity changes smaller than 1 order of magnitude. As far as the signal strength is concerned the larger the offset is the higher is the signal strength.

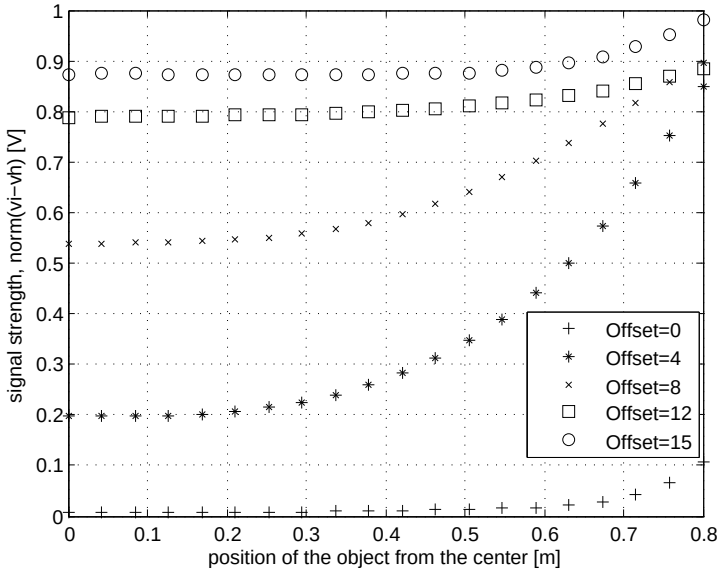

Figure 3.14: Illustration of the effect of the object position for a fixed conductivity contrast calculated for various types of injection and measurement offsets. Interestingly offset 4 is strongly influenced by the object radial position whereas offset 12 exhibits an almost flat behavior.

3.3.5.2 Three-dimensional simulations

In this section three-dimensional FEM meshes are used for the simulations. In this way the simulations are closer to the measurements done in the laboratory with real 3D objects. The idea is to use a cylindrical mesh[13] of radius R=1 and height H=2 to simulate a saline tank. The 32 electrodes are assumed to be uniformly distributed on a circle at the cylindrical tank border at height h=1. This geometry has been arbitrarily chosen to perform the simulations[14]. Using the simulations presented in this section, we can analyze the three-dimensional effects occurring in EIT, as far as the signal is concerned, and make comparisons with the two-dimensional case.

In Figure 3.12 the conductivity of an object (a=10% of R) placed at the center (0,0,0) is varied. As already observed in the 2D case an asymmetry of the signal strength result is observed. The signal strength of objects with higher conductivity than the medium is calculated to be larger than for objects of lower conductivity.

The variation of the signal strength in function of the position of an object (a=10% of R) of fixed conductivity along the $\mathbf{M}_R$ vector at constant height h=1 (in the electrode plane) is depicted in figure 3.16. The latter is the 3D counter-part of figure 3.14. Except for the adjacent measurement strategy all curves show a significant increase of the signal strength after the object has been displaced by more than 30-40% of the radius of the tank.

In a 3D medium, so-called out-of-plane objects are interesting because they may influence the measurements of in-plane objects. The simulation results presented in figure 3.17 and 3.18, depict the vertical move of the object in the direction of vector $\mathbf{M}_V$ from height 0.2 to 1.8 at r=0 and r=0.8, respectively. In case the object is close to the medium border a "sharpening" of the curves is observed compared with the centered object case, highlighting the superposition of two different effects. First, the signal strength is influenced by the position of the object in the horizontal plane and secondly by the position of the object in the vertical plane. When the object crosses the electrode plane[15] the calculated signal strength reaches a maximum.

3.3.6 Intrinsic resolution

The term intrinsic resolution is used to mean the resolution that can be obtained with the best possible algorithm. In the present work, it has to be

[13] The space is meshed using tetrahedrons.

[14] Simulations emulating the real size and geometry of the laboratory test media are done in the results section [6.4.2.1]

[15] Its geometrical center is at h=1.

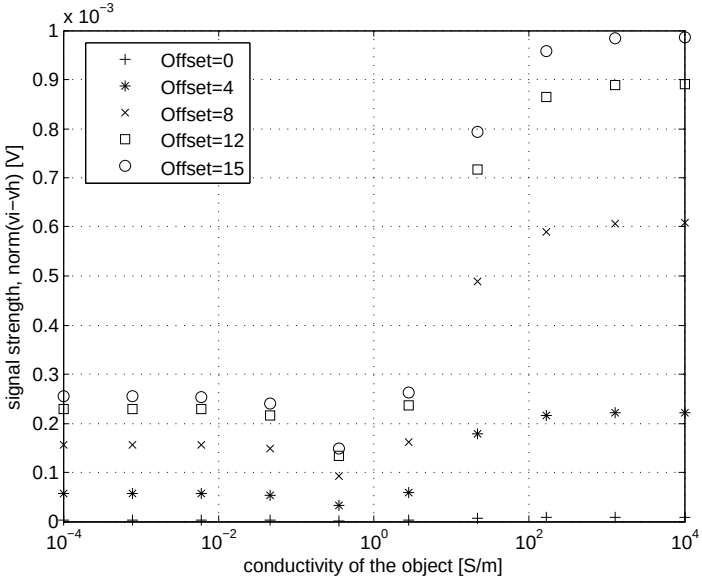

Figure 3.15: Illustration of the effect of the conductivity variation of a centered object of fixed size calculated for various type of injection and measurement offsets.

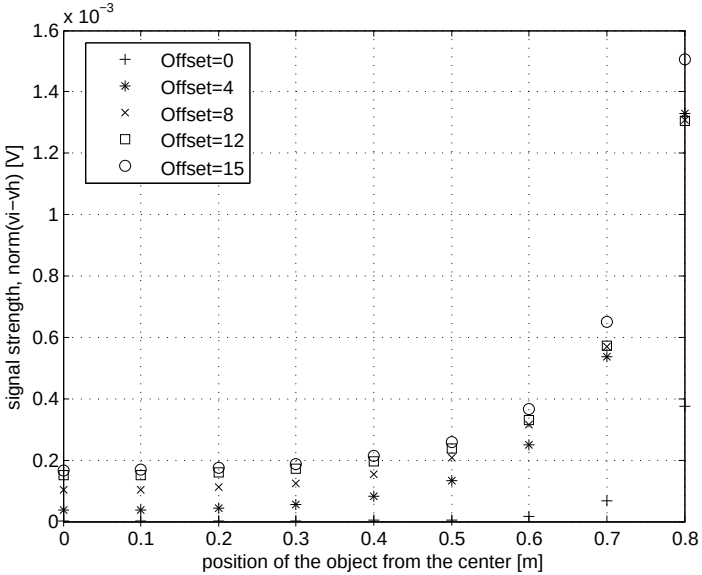

Figure 3.16: Illustration of the effect of the position of the object for a fixed conductivity contrast calculated for various types of injection and measurement offsets.

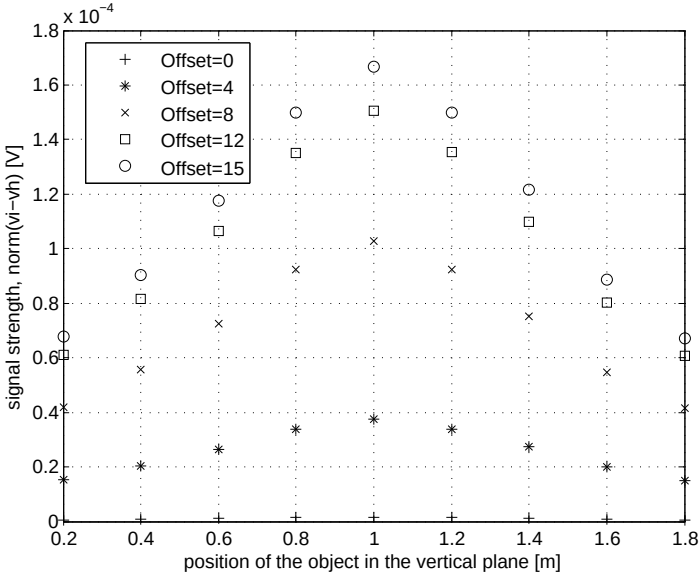

Figure 3.17: Illustration of the effect of the vertical position of the object (at the center r=0) for a fixed conductivity contrast calculated for various types of injection and measurement offsets.

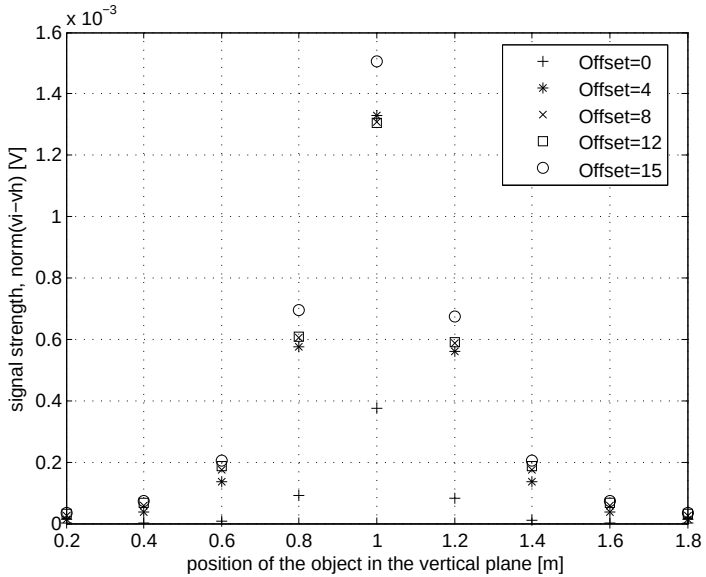

Figure 3.18: Illustration of the effect of the vertical position of the object (r=0.8) for a fixed conductivity contrast calculated for various types of injection and measurement offsets.

understood as the mathematical and geometrical aspects having an influence on the spatial resolution criterion and the distinguishability of an object. This intrinsic resolution is strongly linked with the notion of independent measurements. The ultimate distinguishability limit of an EIT system is by no means only defined by the intrinsic resolution.

The technique proposed by Adler et al [83] is able to calculate the number of independent measurements at a given noise level. The noise level plays a central role in the number of independent measurements, because it limits the statistical relevance of the smallest contributions to the EIT signal. Thus an increasing noise level leads to a decreasing number of statistically relevant independent measurements. The equation, which links conductivity changes inside a medium $\Delta\boldsymbol{\sigma}$ with the corresponding potential change $\Delta\mathbf{v}$ at its boundary, is given by:

$$\Delta\mathbf{v} = \mathbf{J}\Delta\boldsymbol{\sigma} \tag{3.58}$$

where $\mathbf{J}$ is the Jacobian of the sensitivity matrix, see equation 3.3. Equation 3.58 linearly links both conductivity changes and voltage changes. The number of statistically independent equations based on the above relation gives the number of statistically independent measurements. The number of independent measurements inside $\mathbf{J}$ is mathematically measured by calculating the Singular Value Decomposition (SVD) of $\mathbf{J}$:

$$\mathrm{SVD}(\mathbf{J}) = \mathbf{U}\mathbf{D}\mathbf{V}^* \tag{3.59}$$

where

$\mathbf{U}$	is the unitary matrix of the left-singular vector,
$\mathbf{V}$	is the unitary matrix of the right-singular vector,
$\mathbf{D}$	is a diagonal matrix which contains the singular values in descending order,
*	denotes the conjugate transpose.

The left-singular and right-singular vector can be seen as a two parameter spaces, and indeed the column vectors of $\mathbf{U}$ and $\mathbf{V}$ constitute an orthogonal basis. Therefore, one can intuitively interpret the diagonal matrix $\mathbf{D}$ as the link between these two parameter spaces, like weighting or filtering terms. In other word, the diagonal values of $\mathbf{D}$ indicate which basis vector contributes

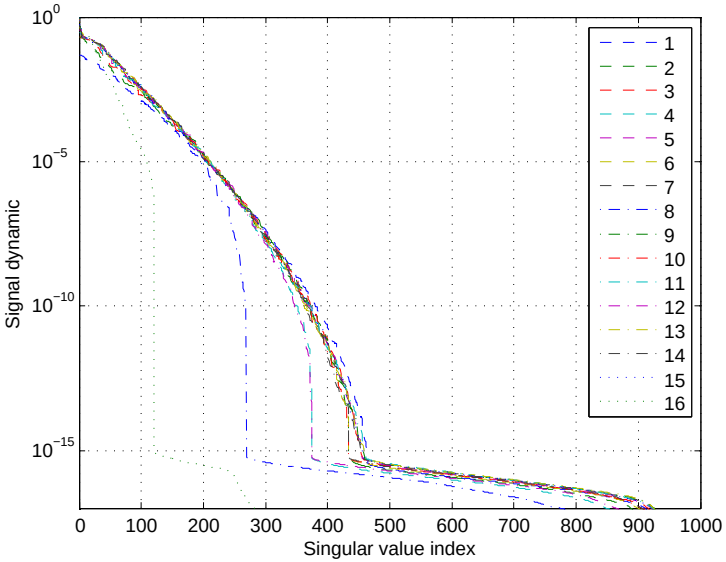

Figure 3.19: The singular values calculated using the SVD of the Jacobian of the sensitivity matrix. The various curves, corresponding to different offset values, are labeled in function of the number of spacings between the electrodes (i.e. offset=0 is labeled 1 in the legend).

most to **J**. If a contribution term is found to be lower than the noise level, one considers it as statistically irrelevant.

Using EIDORS to calculate the Jacobian of the sensitivity matrix for a given 3D geometry, one gets the result depicted in figure 3.19. The values of the diagonal matrix **D** are normalized by the largest singular value and plotted in decreasing order. The various curves correspond to the calculated offsets, labeled in function of the number of spacings between the electrodes. The number of spacings is the relevant geometrical parameter for the calculation of the independent number of measurements. Clearly, it should be avoided to use measurement strategies involving an even number of spacings and especially the ones with a strong symmetry such as (from left to right on figure 3.19: 16, 8, 4 and 12). Naturally, symmetry considerations depend on the number of electrodes of the EIT system, so a way to minimize symmetries could be to work with systems using a prime number of electrodes, for instance 31.

By choosing a certain level of noise compared with the highest singular value, one can plot “horizontal cross-sections” of figure 3.19 for various noise levels

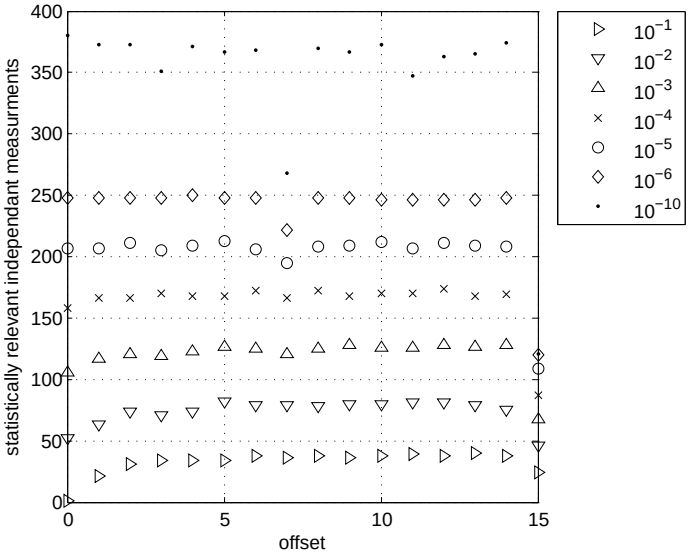

Figure 3.20: Illustration of the number of independent measurements calculated for various noise levels from 10^{-1} to 10^{-10} compared with the highest singular value.

as in figure 3.20. For large noise levels ($\geq 10^{-4}$) [16], one can observe that the optimal measurement strategy is ranging from offset 4 to 14. For small noise levels ($< 10^{-4}$) the "even" symmetries seem to be the dominant effect and their corresponding offset should be avoided. In any case opposite measurement strategies considerably reduce the system performances in terms of independent measurements.

Assuming a constant noise level of 10^{-3} which corresponds to 10 µV noise on a 10 mV signal, one can calculate the number of independent measurements in function of this noise level. As shown in figure 3.21 the number of statistically relevant independent measurements saturates and a further increase in the number of electrodes does not significantly increases the number of independent measurements. Using the same plot, one can also observe that it is particularly interesting to work with 32 electrodes instead of 16 because there are almost 3.5 times more independent measurements. Thus this relatively simple theoretical calculation supports the design decision to develop a 32-

[16] Means that the noise is considered to be 10^{-4} times smaller than the largest signal value.

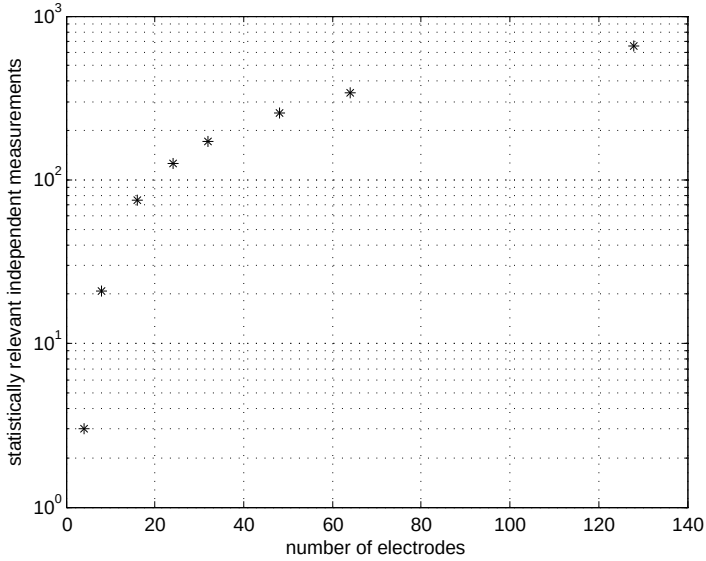

Figure 3.21: Illustration of the number of statistically relevant independent measurements in function of the number of electrodes.

electrode system instead of only 16 electrodes. Not mentioning the dramatic increase in hardware cost and system complexity, going from 32 electrodes to 64 electrode increases the number of independent measurement by 2.2 at best.

3.3.7 Correlation effects

The signal strength is not the only parameter to consider for optimizing the EIT signal, and as already stated in the previous section, symmetry effects should also be considered, as well. Since the signal strength is calculated to be maximal for offset equal to 15 (i.e. opposite measurement strategy), one could conclude that this is the best strategy to pursue. As we demonstrated in the previous section, the opposite strategy is the worst choice as far the number of independent measurements is concerned. By applying this strategy with the developed EIT system, one observes that the image of the object is mirrored in a central symmetry fashion. This means that most of the position information about the object is gone (i.e. due to the symmetry); it cannot be decided if the object is in one position or in the symmetrical counterpart

location of the same position. The element of the FEM mesh are correlated. The obvious question at this point is to calculate whether this effect is limited to offset 15 or whether it is also observed for other offset values. We saw in equation 3.4 that:

$$\Delta \mathbf{v} = \mathbf{J}\Delta\boldsymbol{\sigma} + \mathbf{n} \tag{3.60}$$

Letting the noise tend towards zero for this reasoning, leads $\Delta\mathbf{v}$ to be proportional to $\Delta\boldsymbol{\sigma}$ with the proportionality factors given by the Jacobian of the sensitivity matrix $\mathbf{J}$. Thus if 2 elements of the Jacobian are correlated with each other the solution obtained, the EIT image, will also exhibit correlated elements. Using EIDORS, the auto-correlation of the Jacobian matrix (i.e. $\mathbf{J}^{\mathrm{t}} * \mathbf{J}$) for a simple two-dimensional disk is calculated. The result depicted in figure 3.22 shows that the correlation between the highlighted elements becomes significant for offset values larger than 12.

3.3.8 Summary of the findings for the EIT signal

The factors influencing the signal strength defined as $\|\Delta\mathbf{v}\|$ are:

- the amount of current injected in the medium (increasing the current increases the signal strength),
- the conductivity contrast $|\Delta\boldsymbol{\sigma}|$ (increasing $|\Delta\boldsymbol{\sigma}|$ increases the signal strength),
- the position of the object in relation with the current injection strategy.

On one hand the amount of maximal current that can be injected into a given medium is either limited by regulatory issues or by technical limitations of the current source, or both. On the other hand, the conductivity contrast and the system geometry are given by the object to be measured and cannot be changed. Therefore the only parameter the user has really access to, is the measurement strategy. We demonstrated that due to the legal limitation to fix the sum of the absolute injected current amplitudes below 10 mA, the optimal current injection strategy was pair drive. The FEM simulation in the previous sections demonstrated that the largest signal strength is obtained using the measurement strategy corresponding to offset 15 (opposite). But we also discovered that using offsets with even symmetry or an offset larger than 12 may not be favorable. The problem was that the image becomes difficult to interpret due to correlation effects. A good compromise seems to use offset 12 with 32-electrode system, which corresponds to 11 spacings between the electrodes. In units of angle, offset 12 gives 123°.

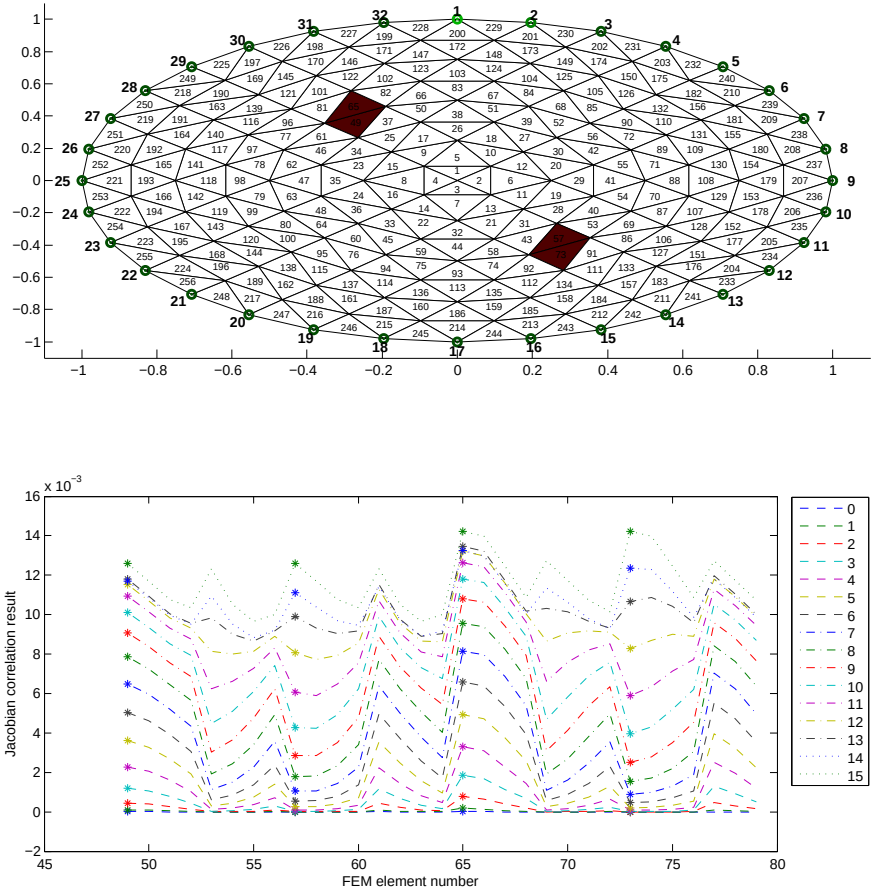

Figure 3.22: Illustration of the auto-correlation of the Jacobian of the sensitivity matrix calculated for a simple two-dimensional mesh with 32 electrodes. The offset varies between 0 (adjacent) and 15 (opposite). Considering element 65 and its symmetric (central symmetry) counterpart, element 73, one observes that both elements are correlated for offsets ranging from 15 to 12. Therefore selecting offsets of 12 or below should be safe to avoid auto-correlation issues.

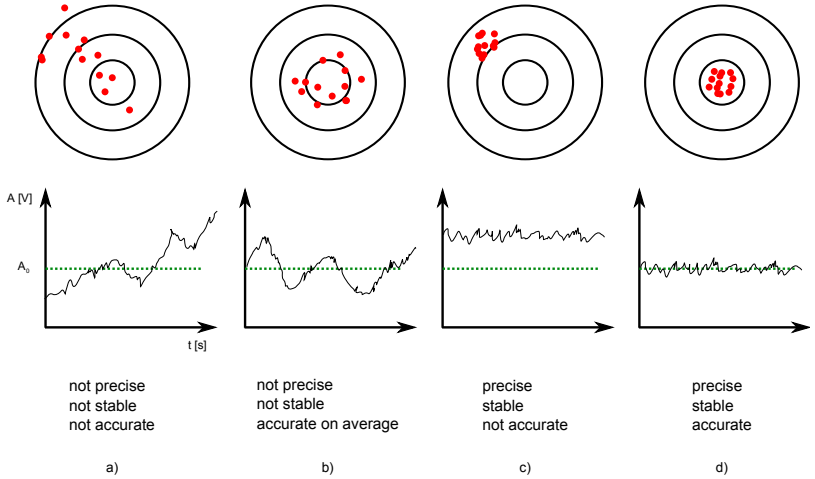

Figure 3.23: An intuitive explanation of the difference between precision, stability and accuracy, modified from [31, 98].

3.4 Study of the Noise

3.4.1 Definition

In order to clarify the notions introduced below, it is necessary to introduce a clear definition of noise. People often confuse precision and accuracy, therefore to provide the reader with an intuitive explanation for the two definitions, the analogy with the shooting result on a bull's eye target is chosen, see Figure 3.23. This section deals with the noise in terms of precision. The non-random errors resulting in a lack of accuracy are discussed in section 3.5.

3.4.2 Variance and Standard deviation

The simplest and probably most popular way to characterize the noise of a signal X is the variance:

$$\mathrm{var}[X] = (\mathrm{std}\,[X])^2 = \mathrm{E}\left[(X - \mathrm{E}\,[X])^2\right] = \mathrm{E}\left[X^2\right] - \mathrm{E}^2\,[X] \tag{3.61}$$

where

$\mathrm{E}\,[\cdot]$ is the expectation operator (i.e. the mean),

X is the random variable describing the statistical process.

In order to estimate the variance of a sampled signal the following estimator can be used:

$$\text{var}\,[X] = \sigma_x^2 = \frac{1}{N}\sum_{i=1}^{N}(x_i - \bar{x})^2 \tag{3.62}$$

where

σ_x^2 is the estimated variance

N is the number of samples

x_i denotes a sample i of the random variable X

$\bar{x}$ is the estimated mean of X

The difficulty here is to get the "true" value of E$[X]$ estimated using the so-called sampled mean $\bar{x} = \frac{1}{N}\sum_{i=1}^{N} x_i$. Therefore one can apply the Bessel corrections in order to compensate for the error introduced by the use of the sampled mean estimator instead of the "true" E$[x]$:

$$\sigma_x^2 = \frac{1}{N-1}\sum_{i=1}^{N}(x_i - \bar{x})^2 \tag{3.63}$$

The difference between equation 3.62 and 3.63 becomes small if the number of sample N is large enough. If the signal has a trend like in figure 3.23 the estimated variance may be completely wrong due to drift in the system. To overcome this difficulty, it may be necessary to detrend the sampled signal before the calculation of the variance[17]. Nevertheless, this method only works if the drift is linear. Thus in the next section the Allan variance is presented. The latter provides statistical insights about the signal variance and the influence of the drift.

[17] Matlab: detrend(X), this command removes a linear trend from the data.

3.4.3 Allan variance

The variance is often use to characterize a signal; nevertheless it does not take into account the time component associated with the observation of the statistical process. In reality, it is impossible to get samples from a given signal with infinitely small acquisition time. The measured samples are always integrated (averaged) over a given integration time. Intuitively, one understands that varying the integration time of the measurement set-up varies the result of the calculated variance. Moreover as already emphasized in section 3.4.2 when the signal exhibits some trend or drift, it becomes difficult to get a good estimate of the variance; therefore a new mathematical tool is needed. The Allan variance, also known as the two-samples variance (see figure 3.24), was originally proposed by David W. Allan [8] to characterize the frequency stability of clocks. One can adapt the original formulation for our situation:

$$\mathrm{Avar}_\tau[X] = \frac{1}{2}\mathrm{E}\left[(\overline{y_{k+1}} - \overline{y_k})^2\right] \tag{3.64}$$

Where $\overline{y}$ is the normalized fractional signal:

$$\overline{y} = \frac{\mathrm{E}[X_\tau] - \mathrm{E}[X]}{\mathrm{E}[x]} \tag{3.65}$$

The estimator for the Allan variance is:

$$\sigma^2_{x,\tau} = \frac{1}{2(K-1)} \sum_{i=1}^{K-1} (\overline{y_{k+1}} - \overline{y_k})^2 \tag{3.66}$$

where $\overline{y_k}$ becomes:

$$\overline{y_k} = \frac{\frac{1}{K_\tau}\sum_{k_\tau=1}^{K_\tau} x_{k_\tau} - \frac{1}{N}\sum_{n=1}^{N} x_n}{\frac{1}{N}\sum_{n=1}^{N} x_n} \tag{3.67}$$

where

τ	is the sampling integration time,
K_τ	is the number of samples of X during the integration time τ,
K	is the number of samples of X,
k	is the index of the averaged random variable calculated using equation 3.67 (the averaging time is τ).

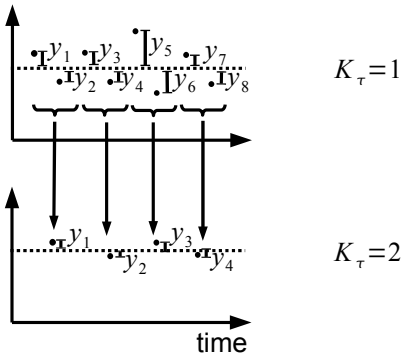

Figure 3.24: Illustration of the calculation of the Allan variance is for $K_\tau = 1$ and $K_\tau = 2$.

Usually it is interesting to calculate the Allan variance in function of various values of τ and plot the results in a graph (see figure 3.27).

3.4.4 Sources of noise

3.4.4.1 Thermal noise

Thermal noise also called Johnson–Nyquist noise, is generated by the thermal agitation of the discrete charge carriers. Johnson noise represents the smallest noise level achievable with a physical system. Its spectral density is given by:

$$S_{th} = \sqrt{4k_B T} \tag{3.68}$$

S_{th} is a current density per $\sqrt{\text{Hz}}$ and is only measured as a potential if the noise current drops over a given impedance:

$$\sigma_{th} = \sqrt{4k_B T R(f)} \tag{3.69}$$

where

σ_{th} is the thermal noise spectral density $[\text{V}/\sqrt{\text{Hz}}]$,

k_B is the Boltzmann constant $= 1.38 \cdot 10^{-23}\text{JK}^{-1}$,

T is the temperature [K],

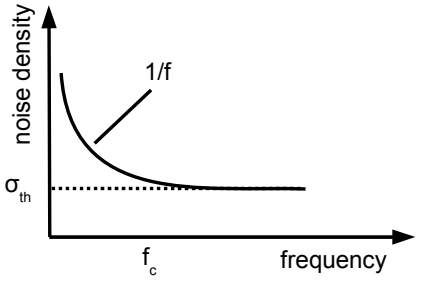

Figure 3.25: Illustration of the typical noise density observed in operational amplifiers. f_c is the corner frequency above which Johnson noise becomes the main noise source.

$R(f)$ is the impedance (i.e. the equivalent resistance at frequency f) [Ω].

3.4.4.2 Electronic noise

The electronic noise is generated by the thermal agitation of the charge carriers (Johnson noise) and by the crystal defects of the semi-conductor (flicker noise). The flicker noise is also called 1/f noise and is observed only at relatively low frequencies. As its name indicates, its density decays according to $1/f^a$ with a larger than 0. Typically, the flicker noise decays until it reaches the level of the Johnson noise; this point is called the corner frequency f_c (see figure 3.25). Past the corner frequency the dominant source of noise of the system is the Johnson noise. Typical operational amplifiers have corner frequencies between 1 and 10 kHz. But especially high-speed circuit using short transistor channel lengths could also exhibit flicker noise up to the MHz range [46].

3.4.4.3 Shot noise

Shot noise seeks it origin in the discrete nature of the charge carriers that gives rise to statistical fluctuation of the observed current. One intuitively understands that a certain amount of shot noise will be observed by the electrodes due to the presence of ions (i.e. discrete charge carriers) in the saline solution. Calculating the exact value of shot noise in this situation is very difficult. Therefore, we propose to estimate the latter by using a simplified model assuming that the applied current is 1 $\mathrm{mA_{rms}}$ at the injecting electrode

pair. The current density between the measurement electrodes will be the key factor for the observed shot noise value. Using EIDORS one calculates the current density reduction factor between the injecting and the measuring pair of electrode, see figure 3.26.

Shot noise is well described in the literature for semi-conductor and resistors and is assumed to be generated by discrete charge carriers (i.e. electrons and holes) flowing through a potential barrier at a random flow rate which creates short term variations of the current density (noise). It is also claimed that this phenomenon only occurs with a DC current and that the shot noise in the case of an AC current would be negligible compared to the thermal noise[18] . This theory is only applicable to electrons in semi-conductors, and can only be partially applied to the EIT case because of the different mass and transport proprieties of the ions compared to the electrons. Yet, it was not possible to find in the literature any reference concerning shot noise in ionic solutions nor AC shot noise. Intuitively shot noise in ionic solution should also exist due to the corpuscular nature of the ions and the independent nature of their motion through matter. Even under AC excitation current charge carriers seen by the measuring electrodes fluctuate in and out of the observation zone of the measuring electrode pair. Even in the absence of thermal energy the ions would be scattered by the surrounding water molecules and their positions would become unpredictable, which will create shot noise. Therefore, the shot noise will probably depend on the ionic concentration, the ionic radius, the mass of the ion, the electrical charge of the ion and the frequency of the injected current. According to [80] shot noise eventually vanished in the absence of an electric field, and only thermal noise is observed. This means that in the AC current case, one has an intermediate case between a DC electric field and no electric field.

As an initial starting point for a model, we assume that shot noise in EIT follows the same rules as electrons in semi-conductors, which represents the worst case scenario. According to the findings of numerical simulations (see figure 3.26 b)) the current density between the injection electrodes is 1000 times larger than the current density between the measurement electrodes, far away from the injection site. Then one can calculate the number of charge carriers involved in this process:

$$N_q = \frac{I}{c_I} \cdot N_{e^-} \cdot \tau_m = \frac{10^{-3}\mathrm{A_{rms}}}{1000} \cdot 6.24 \cdot 10^{18} \frac{\mathrm{e^-}}{\mathrm{C}} \cdot 100 \cdot 10^{-6}\mathrm{s} = 6.24 \cdot 10^{8}\mathrm{e^-} \quad (3.70)$$

where

[18] http://www.phy.duke.edu/∼hx3/physics/ShotNoise.pdf

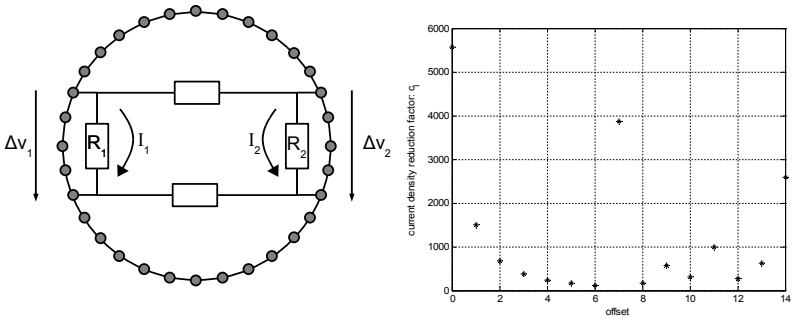

Figure 3.26: Schematic representation of the current density distribution inside the electrode well. a) Depicts the model used to calculate the current density reduction factor. b) depicts the result obtained for the calculation of the current density reduction factor c_I as function of the offset.

I	is the average current injected into the system,
c_I	is the current density reduction factor,
N_{e^-}	is the number of electrons (or charge carriers) per Coulomb ,
N_q	is the number of charge carriers playing a role in the shot noise,
τ_m	is the measurement time.

According to the usual interpretation of shot noise, the SNR is given by:

$$\mathrm{SNR}_q = \frac{N_q}{\sqrt{N_q}} = 2.5 \cdot 10^4 \equiv 88\,\mathrm{dB} \tag{3.71}$$

Assuming that the classical interpretation of shot noise is valid, one can calculate the shot noise spectral density:

$$\sigma_s = \sqrt{2q\frac{I}{c_I}} = \sqrt{2 \cdot 1.6 \cdot 10^{-19}\mathrm{C} \cdot \frac{10^{-3}\mathrm{A_{rms}}}{1000}} = 0.56\frac{\mathrm{pA}}{\sqrt{\mathrm{Hz}}} \tag{3.72}$$

This value is smaller than the noise measured at the output of the current source divided by the reduction factor c_i:

$$2.65\frac{\text{nA}}{\sqrt{\text{Hz}}}/c_i = 2.65\frac{\text{pA}}{\sqrt{\text{Hz}}} \tag{3.73}$$

For the limit of miniaturization calculated in section 3.9.6, we decided to neglect the effect of the shot noise because it only contributes to a small degree to the current source noise. It probably also represents the lower noise limit of the injected current. In other words the shot noise adds to the type of noise which scales inversely proportional to the scaling factor s, see section 3.9.

3.4.4.4 Quantization noise

The quantization noise is the noise generated by the quantization process due to the analog to digital converter. The noise spectral density is given by Kester [51]:

$$\sigma_q = \frac{2V_{\text{ref}}}{2^{N_{\text{bit}}} \cdot \sqrt{12}} \tag{3.74}$$

where

σ_q	is the noise spectral density for the quantization noise $[\text{V}/\sqrt{\text{Hz}}]$,
$2V_{\text{ref}}$	is the voltage swing of the ADC input [V],
N_{bit}	is the resolution of the ADC in bit.

The quantization noise is a white noise over the whole Nyquist frequency range. In other words the noise spectral density is uniformly distributed from DC to half of the sampling frequency. Consequentially, this implies that by selecting only a limited portion of the BW around the signal of interest one decreases significantly the contribution of quantization noise to the measured value. An interesting application of this effect is the use of oversampling strategies to increase the system process gain [50].

3.5 Non-random errors

Non-random (or systematic) errors degrade the system precision but not the system accuracy. They can also often be compensated using various strategies such as:

- differential imaging,
- channel per channel calibration for gain and CMRR [63],
- data modeling.

The term data modeling suggests for example that by measuring external parameters such as the temperature(s) or the instantaneous current produced by the current source one should be able to predict the changes in the observed signal. Clearly non-random errors have an effect on the EIT signal and not on the noise component of the raw signal.

3.5.1 Drift

Drift phenomena cause signals that are not stable around a given value as is the case for pure random noise. Drift is often caused by effects whose sources are of no particular interest for the experiment. For example temperature has an influence on the measurements in a non-random fashion (i.e. it contributes to the EIT signal) but in most cases the user is not interested in measuring this phenomenon on the EIT signal. Ideally, one would only measure the signal generated by the phenomenon of interest. The drift is often linked to environmental factor such as the temperature, chemical reactions, the humidity and the geometry. In EIT drift can also be generated by contact impedance changes that directly influence the current delivered by the current source and the common mode of the measurements. Moreover micro-EIT measurements in a saline tank or in a micro-well also exhibit drift due to changes in the ionic concentration induced by the liquid evaporation or the sample handling. When working with small (milliliter) fluidic well the insertion of the sample could induce a significant liquid level increase inside the well, which has a direct influence on the measured EIT signal. The direct consequence of drift in a signal is to limit the coherent integration time of the signal. In figure 3.27 (lower plot right) the added linear drift limits the integration time to 15 samples (i.e. up to the point where the Allan deviation curve increases again).

3.5.2 Aging

Aging is a kind of drift related to the deterioration over time of some parts of a given system. Although there is no strong evidence that this long term ($\tau \simeq$ days) effect is detrimental for EIT systems, it is valuable to mention it. The mechanical part, the electronics and the time references are often subject to this kind of issue. The mechanical parts of the system such as the contacts,

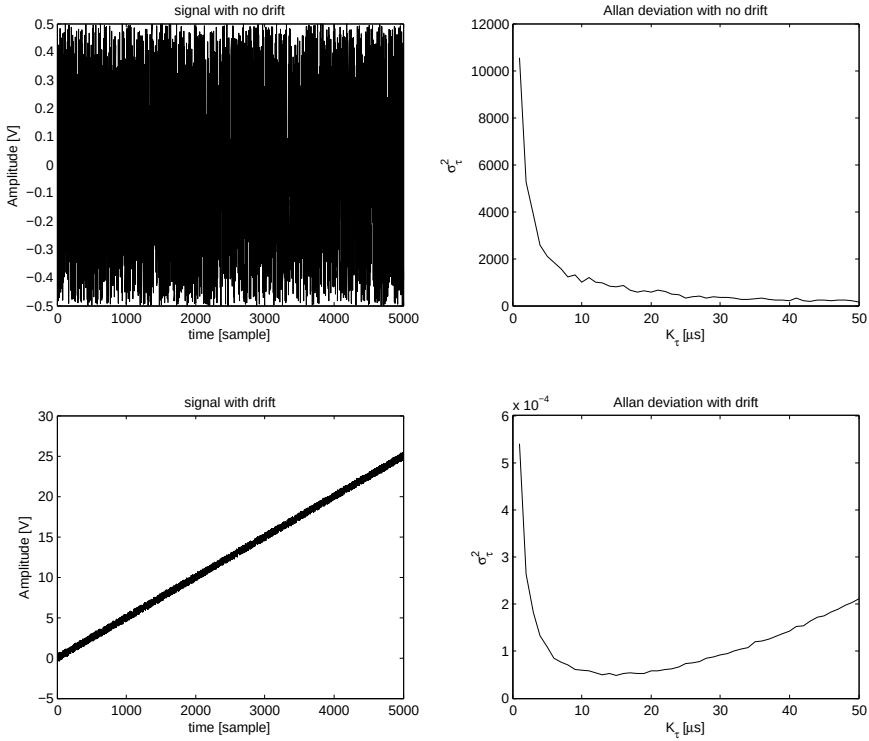

Figure 3.27: Illustration of the Allan deviation versus the integration time τ plotted assuming a purely random and drift-free signal (upper plots). In the other case, a linear drift term with time is added to the signal (lower plots).

the electrodes and many others, change their chemical and geometrical characteristics over time, for example by becoming oxidized or mechanically deformed. The electronics and the time references undergo aging due to atomic migration, water infiltration and mechanical deformation.

3.5.3 Common Mode

The common mode error is essentially generated at the instrumentation amplifier stage. An ideal instrumentation amplifier only amplifies the difference signal, but real instrumentation amplifiers also amplify voltage values common to both inputs as follows:

$$V_{\text{out}} = (V_1 - V_2)G_{\text{diff}} + \left(\frac{V_1 + V_2}{2}\right) G_{\text{cm}} \tag{3.75}$$

where

$V_{1,2}$ are the voltages at the instrumentation amplifier inputs,

G_{diff} is the differential gain,

G_{cm} is the common mode gain.

The performance of instrumentation amplifiers regarding the ability to reject the common mode is assessed with the Common Mode Rejection Ratio (CMRR). The CMRR is calculated as the ratio of the differential gain divided by the common mode gain:

$$\text{CMRR} = 10 \cdot \log \left(\frac{G_{\text{diff}}}{G_{\text{cm}}}\right)^2 \tag{3.76}$$

The CMRR value decreases with increasing frequency [62]. This effect originates from the stray capacitance of the integrated circuit and from the connection traces. Therefore, cautious PCB layout is needed to minimize CMRR degradation.

3.6 Miscellaneous sources of errors

3.6.1 Crosstalk

Crosstalk is difficult to be experimentally measured and theoretically calculated. Crosstalk can generate both noise and non-random errors. The

crosstalk between bus lines can be minimized by placing low impedance lines between the signal lines. This strategy is adopted in this thesis for the developed EIT system. For this task, ground lines or the DC power supply lines are appropriate.

3.6.2 Electromagnetic Field (EMF)

EMF induced signals on the transmission line, on the electronics or even on the measured medium can affect the measurements. Often such parasitic signals are generated by nearby RF transceivers or by the electronics of the EIT system itself. For instance rapid digital signals (such as the FPGA clock) can easily cause interferences within the frequency band of the acquisition chain of the EIT system. Proper system shielding does usually minimize the EMF issues. The system should also emit only a restricted amount of EMF radiation, the maximal allowed values are regulated by law depending of the usage of the device. One can also imagine an EIT system scanning the frequency range of interest to find an operational frequency where the EMF interferences are the lowest and thus minimize their influence on the measured signal.

The use of low impedance analog measurement lines on the electrode belt bus also minimizes EMF coupling in the EIT measurements. Careful electrode cable shielding is required if no active electrodes are used.

3.7 Noise propagation

This section treats the subject of noise variance propagation through the acquisition chain. The text is based on the architecture of the developed EIT system to illustrate the theory. Nevertheless the same theoretical principles apply to other possible architectures or systems. The acquisition chain is composed of two parts, the analog front end depicted in figure 3.28 and the digital demodulator depicted in figure 3.29.

The noise appearing at both electrodes is assumed to be uncorrelated. Therefore one can apply the sum of the noise power rule for the acquisition chain (i.e. summing of the variance). For instance the noise just before the single ended to differential stage in figure 3.28 is given by:

$$\sqrt{\left(\sqrt{\left(\sqrt{\sigma_0^2+\sigma_0^2}\right)^2+\sigma_1^2}\;G_1\right)^2+\sigma_2^2}\;G_2 \tag{3.77}$$

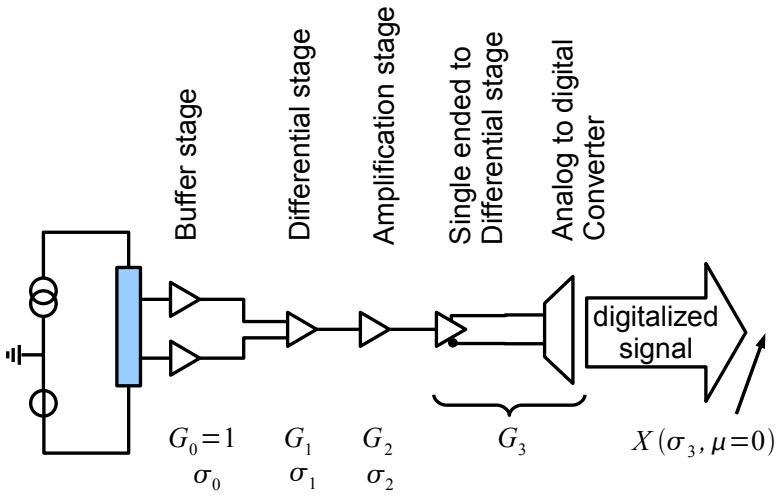

Figure 3.28: The analog front end is used to calculate the analog difference between the two analog input signals A1 and A2, and it processes the differential signal to obtain digital data.

where

σ_0	is the noise spectral density after the buffer,
σ_1	is the noise spectral density of the instrumentation amplifier,
σ_2	is the noise spectral density of the amplification stage,
$G_0 = 1$	is the unity gain of the buffers,
G_1	is the gain of the instrumentation amplifier,
G_2	is the gain of the amplification stage.

As expected, the largest contributors to the noise are the noise sources located before the first amplifier stage, in this case the instrumentation amplifier. The electronic noise of the subsequent amplifier or signal processing stage do often not contribute significantly to the noise.

Based on the demodulation scheme depicted in figure 3.29, one can calculate the variance propagation through the digital processing chain. The digitized signal X is assumed to be Gaussian with the variance σ_3^2 and the mean μ=0. This last assumption is not really necessary but it simplifies the calculation

without loss of generality. The first operation implying a variance change is the multiplication of the noise by the two orthogonal sinusoidal signals at the demodulation frequency. Using the definition of the variance, one can write:

$$\begin{aligned} \mathrm{Var}\left[X_I[n]\right] &= \mathrm{Var}\left[X\cos\left(2\pi Fn\right)\right] && (3.78)\\ &= \mathrm{E}\left[X^2\cos^2\left(2\pi Fn\right)\right] + \mathrm{E}^2\left[X\cos\left(2\pi Fn\right)\right] && (3.79)\end{aligned}$$

The random variable X and the reference signal $\cos\left(2\pi Fn\right)$ are composed of independent random variables. Thus one can use the well known expectation formula[19] and the fact that the mean of the reference signal is equal to zero:

$$\mathrm{Var}\left[X_I[n]\right] = \mathrm{E}\left[X^2\cos^2\left(2\pi Fn\right)\right] + \underbrace{\mathrm{E}^2\left[X\right]\mathrm{E}^2\left[\cos\left(2\pi Fn\right)\right]}_{=0} \qquad (3.80)$$

Then using the trigonometric identity for the power reduction of the cosine and the formula $\mathrm{Var}[X] = \mathrm{E}\left[X^2\right] + \mathrm{E}^2\left[X\right] = \mathrm{E}\left[X^2\right] = \sigma_3^2$ with $\mathrm{E}\left[X\right] = 0$, we obtain:

$$\begin{aligned} \mathrm{Var}\left[X_I[n]\right] &= \mathrm{E}\left[X^2\cos^2\left(2\pi Fn\right)\right] && (3.81)\\ &= \mathrm{E}\left[X^2\right]\mathrm{E}\left[\frac{1}{2} + \frac{1}{2}\cos(4\pi Fn)\right] = \frac{1}{2}\sigma_3^2 && (3.82)\end{aligned}$$

At this point, one needs to consider the effect of the coherent integration stage on the variance. Using the independence property of the X_I samples and the result found with equation 3.82, one gets:

$$\begin{aligned} \mathrm{Var}\left[\frac{1}{N}\sum_{n=1}^{N}\left(X_I[n]\right)\right] &= \frac{1}{N^2}\sum_{n=1}^{N}\mathrm{Var}\left[X_I[n]\right] && (3.83)\\ &= \frac{1}{N^2}N\mathrm{Var}[X_I[n]] && (3.84)\\ &= \frac{\sigma_3^2}{2N} \overset{def}{=} \mathrm{Var}[I[n]] = \sigma_5^2 && (3.85)\end{aligned}$$

A similar derivation can be done for the Q branch. In summary, the noise standard deviation at the output of the demodulator integration stage is reduced by a factor inversely proportional to the square-root of the number of averaged samples.

[19] $\mathrm{E}\left[AB\right] = \mathrm{E}\left[A\right]\mathrm{E}\left[B\right]$, with A and B being two independent random variables

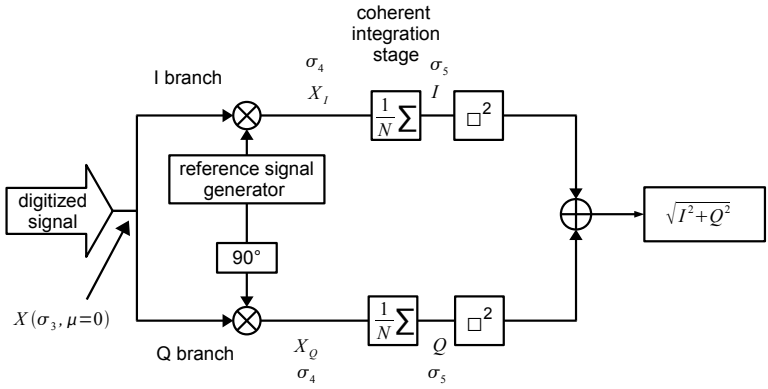

Figure 3.29: The IQ demodulator wherein the input signal is multiplied by two orthogonal sinusoids and coherently integrated.

3.8 Miscellaneous optimizations

3.8.1 Spectral purity of the signal

In order to maximize the signal strength, it is necessary to inject the right amount of current necessary to image the medium of interest. However, arbitrarily high currents are not allowed by the physical, technical and regulatory issues, see section 3.3.2. Therefore, it is important to ensure the spectral purity of the signal used. In this way one maximizes the part of the injected signal that will be demodulated at the reference frequency. In spectroscopic applications [75], it could be desirable to construct a signal that gathers many frequencies and then demodulates each one separately to recover spectroscopic information. Since the total amount of current is limited, doing so decreases the signal strength for each of the particular frequencies.

3.8.2 ADC design

From equation 3.85 one can deduce that the higher the number of samples the smaller the noise on I will be. This is especially true for the quantization noise of a given ADC with resolution N_{bit} and acquisition frequency F_s. For a given acquisition time T_s this gives N_{F_s} samples. Keeping T_s constant and varying F_s by a factor k_s changes N_{F_s} also by a factor k_s. One can also add or subtract a certain amount of bits ΔN_{bit} to the ADC resolution N_{bit}. Taking these parameters into account, the quantization noise is given by:

$$\sigma_{q\Delta} = \frac{2V_{\text{ref}}}{\sqrt{12}} \cdot \frac{1}{2^{(N_{\text{bit}}+\Delta N_{\text{bit}})}\sqrt{k_s N_{Fs}}} = \sigma_q \frac{1}{2^{\Delta N_{\text{bit}}}\sqrt{k_s}} \tag{3.86}$$

As an example, let's assume that the original design was using a $N_{\text{bit}} = 12$ and $F_s = 100\,\text{MHz}$ high end ADC, and that during a redesign phase the engineering team decides to buy a much cheaper ADC with 14 bits resolution and a sampling frequency of 4 MHz (i.e. $\Delta N_{\text{bit}} = 2$ and $k_s = \frac{1}{25}$). This gives a $\frac{\sqrt{25}}{2^2} = 1.25$ increase in the quantization noise on I and Q (i.e. 25% more quantization noise).

3.9 Effect of geometrical scaling

3.9.1 Scaling of the quasi-static potential

The effect of scaling have be studied by Griffiths et al. [35]. The following development is partially adapted from the previously cited sources.

Starting with the same assumptions already used in section 2.4, one can use the quasi-static approximation for the potential given in equation 2.26. For a given path S, it therefore follows:

$$\overrightarrow{E} = -\nabla V = -\frac{dV}{ds} \tag{3.87}$$

where

$\overrightarrow{E}$ is the electrical field,

V is the quasi-static potential.

The previous expression can be integrated over an arbitrary path[20] S on both sides of the equation. One gets an expression for the potential difference between two points S1 and S2:

$$\int_{S1}^{S2} \overrightarrow{E} ds = -\int_{S1}^{S2} \frac{dV}{ds} ds = -\int_{S1}^{S2} dV = \Delta V \tag{3.88}$$

From Ohm's law, equation 2.16, it follows that $\frac{\overrightarrow{J_c}}{\sigma} = \overrightarrow{E}$. Then one can combine this result with equation 3.88:

[20] the quasi-static potential is a conservative field

$$\int_{S1}^{S2} \frac{\overrightarrow{J}_c}{\sigma} ds = \int_{S1}^{S2} \frac{1}{\sigma} \overrightarrow{J}_c ds = \int_{S1}^{S2} \rho \overrightarrow{J}_c ds = \Delta V \tag{3.89}$$

where

σ is the conductivity [S/m],

ρ is the resistivity [$\Omega \cdot$ m].

The idea is to find the expression for $\Delta V^{'}$(the quasi-static potential) when all dimensions are multiplied by a scaling factor s. The conduction current density is defined as:

$$\overrightarrow{J}_c = qn\overrightarrow{V}_d \tag{3.90}$$

where

q is the total charge in Coulomb [C] of the charge carriers,

n the density of charge carriers [1/m^3],

$\overrightarrow{V}_d$ the drift velocity [m/s], respectively.

The drift velocity is defined as:

$$\overrightarrow{V}_d = \frac{I}{nqA} \tag{3.91}$$

where

I is the current in [C/s],

n is the charge carrier density [1/m^3],

A is the cross-section of the considered conductor [m^2].

By combining equations 3.90 and 3.91, we obtain:

$$\overrightarrow{J}_c = qn\frac{I}{nqA} = \frac{I}{A} \tag{3.92}$$

Then $\overrightarrow{J}'_c$ being the new current density after scaling the medium by a geometric factor s is given by:

$$\overrightarrow{J}'_c = \frac{I}{As^2} = \frac{\overrightarrow{J}_c}{s^2} \tag{3.93}$$

Apart from the necessity that the dimension of the path S must also be correctly scaled, by performing a variable change, $sf = s'$, and by using equation 3.93 we find:

$$\Delta V' = \int_{S1'}^{S2'} \rho \frac{\overrightarrow{J}_c}{s^2} ds' = \int_{S1f}^{S2f} \rho \frac{\overrightarrow{J}_c}{s^2} f ds = \frac{1}{s} \int_{S1}^{S2} \rho \overrightarrow{J}_c ds = \frac{1}{s} \Delta V \tag{3.94}$$

Thus the potential ΔV scales inversely proportional with s. This reveals that scaling the dimension by a factor $s < 1$ (reduction) leads to larger potentials. Inversely, increasing the dimension by a factor $s > 1$ results in a smaller potential difference. Clearly the signal strength also follows the $\frac{1}{s}$ scaling rule.

3.9.2 Scaling of the resistance

This section presents a reasoning based on a simplified geometry, the rectangular parallelepiped. Nevertheless one intuitively understands that more complex shapes (such as cylinder, "wires",...) will behave in the same way, it is just more involved to calculate the exact scaling law for the corresponding resistance. The electric resistance of a rectangular parallelepiped is given by:

$$R = \rho \frac{l}{A} \tag{3.95}$$

where

ρ	is the characteristic resistance or resistivity [Ω·m],
l	is the height of the parallelepiped [m],
A	is the surface of parallelepiped's base (i.e. the cross section of the conductor) [m^2].

One calculates the new resistance R' after scaling all dimensions by a factor s:

$$R' = \rho \frac{ls}{As^2} = \frac{R}{s} \tag{3.96}$$

3.9.3 Scaling of the capacitance

This section presents a reasoning inspired by the parallel plate capacitor case. Clearly the real world case is much more complex, but this simplification is still a good and intuitive approximation. The capacitance of a parallel plate capacitor is given by:

$$C = \epsilon_r \epsilon_0 \frac{A}{d} \tag{3.97}$$

where

ϵ_o is the vacuum permittivity [$= 8.85 \cdot 10^{-12} \frac{\mathrm{H}}{\mathrm{m}}$],

ϵ_r is the relative permittivity of the medium [-],

d is the distance between the two plates [m],

A is the surface of a capacitor plate [m^2].

One calculate the new capacitance C' after scaling the surface by a factor s:

$$C' = \epsilon_r \epsilon_0 \frac{As^2}{d} = Cs^2 \tag{3.98}$$

In this calculation, we make the assumption that the distance d stays effectively constant and is not scaled with the surface capacitor plate, which corresponds in the EIT case to the electrode surface. The distance d in the case of EIT measurements can be identified as the amount of non-conductive material between the electrode and the body, for example dead skin cells.

3.9.4 Scaling of the electrode contact impedance

Using the simple model for the electrode contact impedance of a capacitance in parallel with a resistor, one can calculate the resulting impedance:

$$Z = \frac{R}{1 + i\omega C} \tag{3.99}$$

Resulting in a modulus and phase:

$$\|Z\| = \sqrt{\frac{R^2}{1 + \omega^2 R^2 C^2}} \tag{3.100}$$

$$\text{phase}(Z) = -\arctan\left(\frac{1}{\omega RC}\right) \tag{3.101}$$

Applying the formulas of scaling for resistor 3.96 and capacitance 3.98, new $\|Z\|$ and phase(Z) values are calculated:

$$\|Z'\| = \sqrt{\frac{\frac{R^2}{s^2}}{1+\omega^2 R^2 C^2 s^2}} \tag{3.102}$$

$$\text{phase}(Z') = -\arctan\left(\frac{1}{\omega RCs}\right) \tag{3.103}$$

3.9.5 Scaling of the Joule Heating effect

The difference in heat energy for a mass of material in thermal equilibrium at two temperature (no heat loss, no changes in entropy, no work done) is given by:

$$\Delta Q = mc\Delta T \tag{3.104}$$

where

ΔQ is the difference in heat energy [J],

m is the mass of the considered material [kg],

c is the specific heat constant of the material $\left[\frac{\text{J}}{\text{kg}\cdot\text{K}}\right]$,

ΔT is the temperature difference [K].

The mean power necessary to heat the material is given by $\frac{\Delta Q}{\Delta t} = P$. The mass of the material can be deduced from the volume and material density, $m = \rho_m v$. Introducing these formulas in equation 3.104, one gets:

$$P \cdot \Delta t = \rho_m v c \Delta T \tag{3.105}$$

and since the electrical power is given by $P = I^2 R$, one obtains:

$$\frac{\Delta T}{\Delta t} = \frac{I^2 R}{\rho_m v c} \tag{3.106}$$

We found that R scales with $\frac{1}{s}$, the volume clearly scales with s^3, therefore $\frac{\Delta T}{\Delta t}$ scales with $\frac{1}{s^4}$ if the current is kept constant. As expected, for a smaller medium the temperature increases much faster if the probing current I is not varied.

3.9.6 Scaling of the z-score and miniaturization limit

The z-score, given in equation 3.33, can be used as a benchmark for the distinguishability of objects given the signal strength and the noise. One can assume that the noise observed at the demodulator output is only due to Johnson noise and electronic noise. Moreover it is also assumed that the noise is the same for each channel. If the noise sources are uncorrelated, one can use the sum of variance rule:

$$\sigma_n = \sqrt{\sigma_e^2 + 4k_B T R} \tag{3.107}$$

Additionally, the noise generated by the current source should be considered. This noise, denoted σ_{ICS}, is a current noise given by the performance of the current source and the DAC. One can assume that this current noise behaves like the injected current. Thus the resulting voltage noise standard deviation at the electrode, denoted σ_{cs}, scales with $\frac{1}{s}$. Thus the overall expression for the system noise becomes:

$$\sigma_n = \sqrt{\sigma_e^2 + 4k_B T R + \sigma_{cs}^2} \leq \sigma_e + \sqrt{4k_B T R} + \sigma_{cs} \tag{3.108}$$

The last inequality is based on the triangular inequality theorem. Then by using the scaling rules found in equations 3.94 and 3.96, the expression for the system z-score calculated in equation 3.33 combined with the expression for the calculated noise in equation 3.108, we find:

$$\begin{aligned} z(s) &= \frac{\left\| \frac{1}{s} \Delta \mathbf{v}_{\mathrm{ROI}} \right\|}{\sqrt{\sigma_e^2 + 4k_B T \frac{R}{s} + \left(\frac{1}{s}\sigma_{cs}\right)^2}} && (3.109) \\ &= \frac{\frac{1}{s} \left\| \Delta \mathbf{v}_{\mathrm{ROI}} \right\|}{\sqrt{\sigma_e^2 + 4k_B T \frac{R}{s} + \left(\frac{1}{s}\sigma_{cs}\right)^2}} && (3.110) \\ &\geq \frac{\frac{1}{s} \left\| \Delta \mathbf{v}_{\mathrm{ROI}} \right\|}{\sigma_n + \sqrt{4k_B T \frac{1}{s} R} + \frac{\sigma_{cs}}{s}} && (3.111) \\ &= \frac{\frac{1}{\sqrt{s}} \left\| \Delta \mathbf{v}_{\mathrm{ROI}} \right\|}{\sqrt{s}\sigma_n + \sqrt{4k_B T R} + \frac{\sigma_{cs}}{\sqrt{s}}} && (3.112) \end{aligned}$$

The previous result assumes that the current injected into the system I_{cs} is kept constant during the scaling process. The problem with this approximation is that Joule heating of the sample by the current I_{cs} is not taken into account. Clearly, it is desirable to keep the sample temperature at a constant level to avoid temperature drift or sample damage. Therefore, one should not produce more heat than one is able to cool. The heat loss, ϕ_{cool} , of a system is proportional to its external surface so it scales with s^2. On the other hand, Joule heating scales with $\frac{1}{s}$. Therefore, to balance the term on both sides of the equation, the current I_{cs} should scale with $s^{\frac{3}{2}}$.

$$\underbrace{\left(\left(s^{\frac{3}{2}}I\right)^2 \frac{R}{s}\right)}_{\text{Joule heating}} = s^2\Phi_{\text{cool}} \tag{3.113}$$

Figure 3.30 graphically summarizes the findings of this section by calculating an example. The idea is to start with a z-score of 200 obtained during the measurements with the large tank (about 15 cm radius and 30 cm height) with a 2.5 cm spherical non-conductive object. Then one applies the z-score scaling rule for the four following cases:

1. the noise of the system is only Johnson noise,
2. the noise of the system is Johnson noise and the electronic noise,
3. the noise of the system is Johnson noise, electronic noise and current source noise[21],
4. the noise sources are the same as in the previous case but the current, respectively, the signal strength is scaled to avoid sample heating.

Experimentally, it has been observed that a z-score of 10 is necessary in order to distinguish a single object clearly. In figure 3.30 this z-score threshold is represented by the bold horizontal line. Then the crossing points of the z-score curves with this threshold give the miniaturization limit of the system. A shortcoming of this extrapolation method is that the system geometry is assumed to be kept identical, which may not be the case while miniaturizing a real EIT system.

The main limiting factors for the miniaturization are the noise of the current source and Joule heating. Concerning Joule heating the way it is calculated in figure 3.30, it is assumed that the system is continuously running and that

[21] for the calculation we assume it equal to $8\,\text{nV}/\sqrt{\text{Hz}}$ which corresponds to the noise generated by the op-amp of the current-source

no temperature difference is allowed between the liquid in the well and the environment. Thus one can imagine a system that measures with a duty cycle, D_{cycle}, of 50% (for example measuring during one second and then pausing for one second), this would allow to increase the current by a factor of $D_{\text{cycle}}^{-\frac{1}{2}}$. Similarly any improvement, k_Φ, on the cooling rate of the system also allows to increase the current by a factor of $\sqrt{k_\Phi}$. The cooling rate of the electrode well can be improved by:

- adding an active cooling element, such as a Peltier element, a fan, a water cooling system (potentially with micro channels),...
- allowing a temperature difference between the well medium and the external world[22].

Another limiting factor is the restricted supply voltage. Even if a large amount of voltage was available, if the electrical field increase above 1 kV per mm in air, there will be creation of discharge flashes (i.e. the air is no more isolating). Assuming an impedance of 100 Ohm and a current of 1 mA, the breakdown voltage is reached with a scaling factor of s=0.001.

Based on the findings of this section, one can draw general four rules for the miniaturization limit of EIT systems:

- If Johnson electronic noise are the main contributors to an EIT system's input noise sources, the z-score increases with the reduction of the micro-EIT well size (z-score scales with $1/\sqrt{s}$),
- If the injected current also contains noise, the z-score increases with decreasing well size up to a given saturation level.
- In contrast, with increasing well size, the electronic noise becomes the dominant noise in the system and it finally limits the distinguishability (z-score scales with s),
- In the decreasing well size case, the distinguishability in only limited by the ability of the system to cool itself down (z-score scales with s^2).

3.10 Summary of the theoretical findings

As already stated in the introduction of this chapter, there is no simple answer to the question of resolution limit of an EIT system. The reason is that the

[22] the cooling rate is proportional to the temperature difference $\Phi_{\text{cool}} \sim (T_{\text{well}} - T_{\text{ext}})$

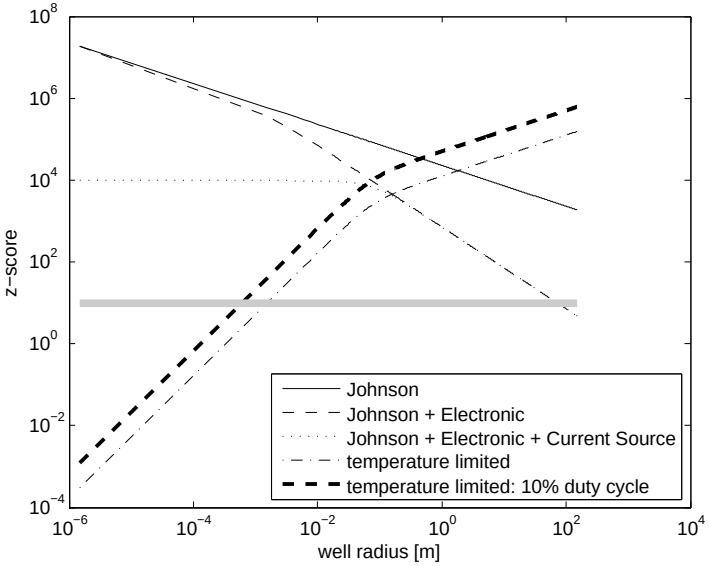

Figure 3.30: Scaling of the z-score with the size reduction of the electrode well, where each curve corresponds to a particular noise condition.

question is not precise enough for seeking a specific answer. A frame needs to be set to refine the question. The criteria and parameters needed to set this frame include the following:

1. a definition of the resolution criterion,
   (a) parameters to extract from the data (i.e. position, shape, presence),
   (b) methodology of calculation (i.e. the link between the data and the distinguishability benchmark),
2. the geometry of the test system,
   (a) size and shape of the test system,
   (b) conductivity of the medium,
   (c) number and position of the electrodes,
3. the type of observed object,
   (a) size and shape,
   (b) conductivity,
   (c) position with respect to the electrodes,
4. the noise level in the measurement,
   (a) acquisition speed,
   (b) environmental conditions (for example temperature).

Depending of the resolution criterion, some of the above listed parameters can conveniently be summarized in a few parameters. Typically, given the resolution criterion of distinguishability defined in section 3.2, all the effects linked to points 2 and 3 are combined in an unique value called signal strength. The distinguishability using the proposed statistical approach can be formulated as follow:

$$z = \frac{\|\Delta \mathbf{v}_{\mathrm{EIT}}\|}{\sqrt{\sigma_e^2 + 4k_B T R + (\sigma_{cs})^2}} \tag{3.114}$$

In this formula only the three most relevant noise sources are considered, namely Johnson noise on the measured object, the electronic noise σ_e and the current source noise σ_{cs}. The EIT signal $\Delta \mathbf{v}_{\mathrm{EIT}}$ is the relevant signal used

as input for the image reconstruction algorithm. The delta sign Δ expresses the fact that the signal is primarily a differential signal between two states, which produces differential images.

Apart from the technical discussion, it should not be forgotten that the information delivered by an EIT system are ultimately presented to human eyes, and are (miss)interpreted by the observer's brain in an interesting manner, see Smith [87]. Clearly this topic is beyond the scope of the present work and will not be further discussed.

Chapter 4

Hardware Design

The present chapter explains the final hardware design. At first constraints and guidelines are emphasized and their influences on the system architecture design are explained. Then the final design decisions are explained in detail and enhancement and alternative design ideas are described.

4.1 Introduction

The present engineering work was confined by several technical, practical and economical constraints, which lead us to issue design guidelines for the system architecture. The goal of the EIT system designed during the present thesis is twofold: first it will serve as a demonstrator and prototype system for the startup company Swisstom AG[1] and second it will be used to support the research work of this thesis. The role of the guidelines is to give a frame to the engineering work and indicate the direction to pursue. Then, the fundamental design choices taking into account these guidelines and the lessons we learn during the implementation process are presented in section 4.1.1. It is clear to the author that several other implementations and architectures for an EIT system are possible, and some of them may also deliver better performance, nevertheless the present work intends to deliver the best solution according to the design guidelines and not according to what is the very best technical solution.

The guidelines are the result of the brainstorming work of the whole design team taking into account all the technological, regulatory and economical

[1] www.swisstom.com

aspects of the problem statement. The main goal was to produce an EIT system demonstrator for medical chest imaging (ventilation imaging). The main focus was to produce a demonstrator using a realistic technical solution that can be developed into the end solution of Swisstom's product. For this matter, we direct our reflection towards the available technology (also for future mass production), the target performances of the device, the target price of the end solution, security issues and regulations. The following is a list of the guidelines taken into account to layout out the overall system architecture.

1. The same acquisition electronic circuits should be used in both medical-EIT application (for Swisstom) and in micro-EIT application (for this thesis). Both set-ups should only differentiate themselves by the interface to the medium of interest[2], by the software settings and the analog gain settings of the amplifiers in the acquisition chain.

2. In order to comply with guideline 1, both medical-EIT and micro-EIT devices are restrained to work within the same frequency and image frame rate range, which is defined as 50 kHz to 500 kHz and 3 images/s to 40 images/s, respectively.

3. For the medical-EIT application the electrode set should form a wearable belt-like structure.

4. The belt-like structure should be designed to facilitate its future use on real patients. Unlike volunteers, real patients may be severely injured or sick. This could have strong influences on the contact impedance of the electrodes with the skin, for example due to skin dryness or, on the contrary, over-wet skin. Real patient could also sweat, bleed, and/or vomit on the belt.

5. The connection between the belt-like structure and the rest of the apparatus should be as easy to handle as possible, meaning that it is desirable to minimize the number of bus lines. The goal is to avoid a cumbersome cable connection solution.

6. The patient being in a severe physical condition also has consequences on the way the belt-like structure is going to be placed around the patients. The design of the belt should take into account the procedure that will be required to place it around a lying, possibly unconscious, patient by a trained nurse.

[2]The interface to the medium is the generic name for the electrode belt structure for the medical-EIT (The medium is the patient.) or the electrode well for the micro-EIT (The medium is the content of the well.).

7. The belt-like structure should minimize the skin and body injuries caused by the wearing of the belt or by lying several hours on it.

8. The patient and user electrical safety are important issues, and need to be addressed according to regulations in force.

9. Since constraint 1 should be respected, there must be a way to connect the electrodes around the micro-EIT well.

10. The amplitude of the current and the acquisition gain should be adaptable with minor hardware changes for medical and micro-EIT application.

11. The system architecture and each individual element of it, should represent a technically realistic solution for the end design.

12. Every single part of the design should be mass producible at a reasonable cost for the final circuit solution.

4.1.1 Fundamental choices in architecture design

Since the acquisition electronics has to accommodate constraints linked to two different usages (medical-EIT and micro-EIT), the design choices are influenced by both, and some trade-offs have been made. This section intends to explain the original design idea concerning the architecture principles based on the guidelines presented in the previous section. The intent is also to show the path from the original design idea to the final implemented solution explained in detailed in section 4.1.3. In this way the lessons learned during the engineering process are recorded and openly shared with the research community.

At the beginning of the project the idea was to put the electronics as close as possible to the medium of interest to minimize problems related to the analog transmission of signal on high impedance lines. The obvious way to do that is of course to place an Analog to Digital Converter (ADC) on each node and communicate in a digital manner with the rest of the system. Identically for the signal generation the idea was to generate the analog signal locally on each electrode. Unfortunately having local ADC and Digital to Analog Converter (DAC) with sufficient precision and bandwidth, meeting the price and size requirement for each active electrode was not possible. Therefore we decided to move all the costly and bulky pieces of hardware to a central location; we called it the Sensor Belt Connector (SBC). Since the analog signal should still not be transmitted from the electrode to the SBC on high impedance lines

using simple wires. The solution was to implement a voltage buffer as closely as possible to the electrode.

When the electrode belt is used on real patients, there are good chances that it gets soiled. For example sweat or blood could enter in contact with the belt structure or the electronic and induce damages, which will prevent the system from properly functioning. This is why, even at an early stage in the project, we began considering this issue as a very relevant factor for the design. It is also a hygiene requirement for the belt to be carefully cleaned between patients. It should even be sterilized, if there is any chance for the same belt to get in touch with open wounds or mucous membranes. Since washable/sterilizable electronics are still experimental and their reliability not yet demonstrated, we decided to adopt a one-time use belt strategy. Yet another reason for this choices is the fact that even if washable electronics would exist, it would be necessary after each wash cycle to run tests to ensure the hardware was not damaged and is ready to be used reliably on the next patient. These tests are very time and money consuming, and medical care professionals are often already on tight schedule and do not have spare time for additional work.

Adopting a one-time use belt strategy has direct consequences on the architecture design. Since the goal of the present technology demonstrator was also to be as close as possible to the end product, it was important to meet realistic end-price and end-technology solutions. For example, implementing the ADC and the DAC at a central location was a decision made in this direction. This is also well supported by the fact that each individual active electrode in the end-solution should be implemented in a dedicated ASIC, which cannot cost more than 1 Swiss franc to mass produce[3].

The location of the current source in the system architecture is also not obvious . At the end the decision was made to work with a unique current source placed at a central location on the SBC. A detailed description of the current source design is to be found in the section 4.2.1.1. In summary, a centrally located current source versus many distributed current sources offers several advantages in the technical as well as in the financial domain such as for example saving silicon die surface in the final ASIC.

4.1.2 Safety measures

There is an inherent danger with injecting current into a living organism. Therefore, the amount of current injected into a patient is limited by law, see section 3.3.2. The main issues are:

[3] 1 million unit per year

1. to expose living tissues to large (more than 10 µA [1]) Direct Current (DC),
2. to expose living tissues to excessive AC current (see section 3.3.2),
3. to accidentally get the main power supply connected to the experimenter or the person wearing the belt in the case of system malfunction.

Point 1 is solved in practice by decoupling the current source with large capacitor in series, which are almost transparent for 100 kHz AC but blocking for DC. Point 2 is hardcoded into the circuitry by the choice of resistor R_3 in figure 4.3 and by the voltage limitation of the command signal of the current source. Point 3 is addressed according to the recommendation of [1] by decoupling the instrument from the main grid potential using an isolation transformer.

During the test it has also been observed that small electrical discharges can be experienced by the user, if the EIT instrument was powered with +- 15 V. This was produced by the saturation of the instrumentation amplifiers during the transition state of the multiplexing process. Therefore, to avoid unpleasant electrical shock experienced by the user while using the system, we decided to limit the power supply swing to 10 V (i.e. +- 5 V).

4.1.3 Final system architecture and nomenclature

This section presents a summary of the system architecture and defines names for the different parts of the system, see figure 4.1. The decision was made to split the system into three physically separate subsystems:

- the belt containing the active electrodes,
- the Sensor Belt Connector (SBC) containing the analog front end, the ADC, the DAC, and the control electronic implemented in a Field-Programmable Gate Array (FPGA),
- the display and user control unit implemented in a PC program.

It is also useful to give names to the different part of the EIT signal, see figure 4.2:

- the skip window contains the part of the signal that is discarded,
- the demodulation window contains the part of the signal that is demodulated and used by the EIT system,

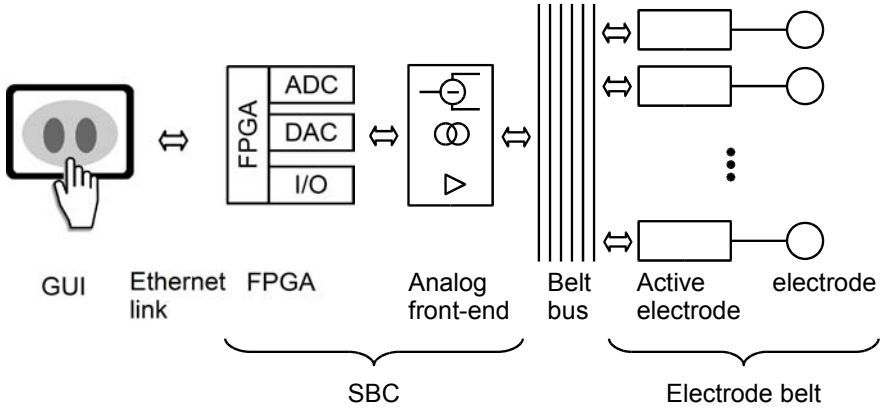

Figure 4.1: Illustration of the system architecture adopted in the developed prototype.

- together the skip window and the demodulation window form the measurement window, which is the time slot available for each measurement on each electrode pairs,
- a measurement frame contains is n measurement windows length, where n is the number of measurement taken for each image,
- a sequence of the same measurement (i.e. taken on the same electrode pair) is called a channel,
- a sequential set of measurement frame constitute a measurement sequence.

In the everyday use the "measurement frame" is also sometimes simply called "frame".

The text also follows this organization for the presentation of the design of the various system parts starting with active electrode design presented in section 4.2. The SBC is presented in section 4.3. The PC program is described in section 5.4.

4.2 Active electrode design

This section presents and justifies the design choices made for the active electrodes. The text is subdivided between the analog design and the digital

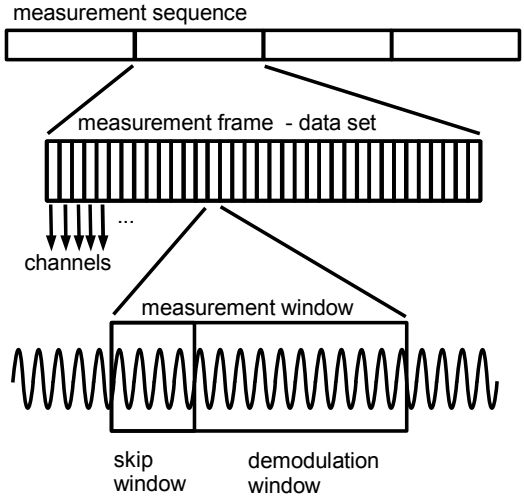

Figure 4.2: Illustration of the EIT signal nomenclature.

design in section 4.2.1 and in section 4.2.2, respectively. This division corresponds to the functions of the node and the way to control them. The state of the hardware at the time of writing (version 2.6B_2, December 2010) is also presented together with alternative design including advantages and disadvantages for each solution.

In the text the term node is sometime used instead of active electrode. The reader should note that "node" refers to the logic entity and that the term "active electrode" refers to one of the functions of the node. It is also possible to have a node with multiple active electrodes, which is not the case in this work.

4.2.1 Analog part

The basic tasks of a node in the present EIT system are:

- injecting a current (in figure 4.3 switch SW_2 is in close position),
- sinking a current (switch SW_3 is in close position),
- buffering a voltage and write it on one of the two analog lines of the bus (switches SW_4 or SW_5 are in close position),

- do nothing (switches SW_2, SW_3,$SW_4$and SW_5 are in open position).

The switching between the four basic functions is implemented with analog switches like the Maxim DG412F. These switches do not have to be considered as relay or real mechanical switches. They are in fact composed of Field-Effect transistors (FET), and therefore exhibit particular characteristics that need to be carefully considered. Figure 4.3 depicts the designed architecture necessary to realize these four tasks.

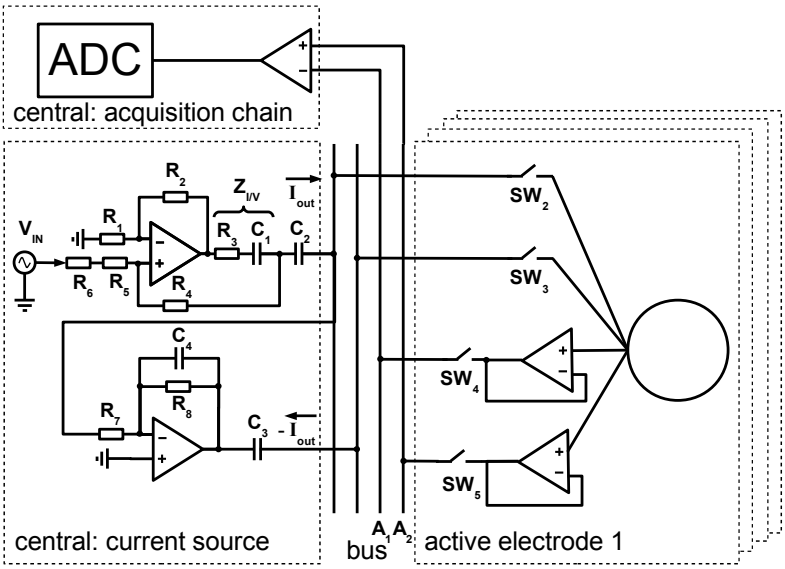

Figure 4.3: The central current source with the feedback circuit (on the left side of the bus) and the basic elements of an active electrode (on the right side of the bus) are depicted. Capacitors $C_{1-3} = 220$ nF are the DC blocking filters. Resistors $R_{3,6} = 390\ \Omega$ determine the conversion factor between voltage and current. Resistors R = 10 kΩ. Resistors $R_{7,8} = 5.6$ kΩ are made equal to get a unity gain inverter. Capacitors $C_4 = 15$ pF avoid oscillations of the circuit at high frequency.

The ratio ($R_{en} = \frac{\#electrodes}{\#nodes}$) number of electrodes versus number of nodes is assumed to be equal to 1 in this thesis. In other words one node is used only by one single active electrode. Of course by adding multiplexing capabilities to the node, it is relatively straightforward to envisage nodes sharing multiple active electrodes. For the final implementation in the ASIC this topic should be discussed in detail, and the trade-off between hardware, signal integrity

and ASIC complexity should be examined in detail. Moreover increasing R_{en} decreases automatically the number of ASICs used per belt and therefore the number of ASICs produced per year decreases. This yields an automatic increase in the average unit price of individual ASICs. Nevertheless, the price for an ASIC is essentially given by the silicon die surface used and its packaging. If one desires to implement a node with $R_{en} > 1$ without compromising on the system flexibility, it is essential to double all the costly elements (in term of silicon surface) such as the op-amp buffer and the analog switches. So it has to be examined in detail, if the saving realized with the shared circuits and the common ASIC pads compensate the increase in complexity of each node. On the other hand, it is also possible to imagine giving up some of the multiplexing and flexibility to save on silicon surface. For example, if the node can only write on one single analog line instead of having the choice between 2 lines one saves on 1 op-amp and 1 switch on each node.

4.2.1.1 Current injection

This section presents the design of the current injection circuit. Since the final implementation uses a central current source the reader could be surprised to find this section in the active electrode section. This is done on purpose to highlight the importance of current source in the active electrode design process.

Essentially two ways for injecting the current using an active node exists. The first one is to have a remote current source at a central location and one switch on the node to contact the current carrying bus line with the electrode. The second possibility is to implement a so-called on-board current source on each node. Each on-board current source takes its voltage control signal from the belt bus. In this case, switches are used to connect the on-board current source with the electrode. The hardware version 2.6B implements both possibilities on the node.

In both cases, an EIT current source can be decomposed into 3 subsystems:

- a voltage signal acting as the current source control signal,
- a current source,
- a current sinking element.

At first, we thought it could be a good idea to integrate the current source in the active electrode itself. In this way the current losses due to the bus and

switches stray capacitance would be minimized. But adopting this architecture with the feedback circuit and the decoupling capacitors of the current source, would have led us to an unrealistic prototype from a practical and cost-effective point of view[4].

The voltage signal reference is generated using a DAC and is subsequently buffered to be supplied to a transimpedance circuit, the current source itself. The current source translates an input voltage value into a current at the circuit output. After flowing through the medium the current needs to be sinked. The first approach consists of simply sinking the current towards ground potential. Unfortunately, the test showed that this approach gave high common mode voltage errors, so a third circuit, a commanded voltage source, is used to "actively" sink the current. This balances the injection voltage and significantly reduces the common mode voltage. This unique combination of a current source with a voltage source has the advantage to be simple and not to require any fine tuning nor calibration. The result is a precise feedback controlled symmetric current source which lowers the measured common potential on the medium. The current sinking circuit is called the "feedback circuit". The basic idea is to measure the voltage at the output of the current source and invert it using a simple inverting amplifier. Then this new signal is applied on the current sinking electrode. In this way the couple current source and voltage source act as a kind of symmetric current source. From a measurement point of view this circuit enables the load of the current source to float around the ground potential and therefore drastically reduces the measured common mode. An alternative solution for symmetrical current sources found in the EIT literature Holder [43] uses two different current sources injecting current with 180° phase difference. The challenge faced by this architecture is to inject and sink the same amount of current. Since this is not trivial an external electrode, called the common mode electrode, is needed to absorb the excess current and to avoid charging the medium. Our architecture does not need this external extra electrode.

Additionally 3 decoupling capacitors are placed in the current source circuit to avoid the undesired injection of DC into the medium. This is desirable since DC is very damaging for living tissues. Moreover when injecting DC into a medium using metallic electrodes, the latter undergo undesired redox chemical reactions which ultimately create a drift in the signal.

The main drawback of this architecture is that one is forced to use a central current source, since implementing this idea with embedded current sources on each node would considerably increases the complexity of the bus structure. It would at least take one additional bus line to sense the current source output, and 2 switches and 1 op-amp more per node. Additionally the three

[4]Especially for the Swisstom ASIC based design.

necessary DC-blocking capacitors of 220 nF each cannot be embedded easily in an ASIC design; it would require to be mounted as external components. For all these reasons, we decided to implement the current source at a unique central location (hardware revision 2.6B_2). In this way, it becomes possible to pool the entire current source components and to leave the active electrodes with only 2 analog switches, one to inject the current by connecting the electrode to the current line on the bus and another one to connect the current sink line with the electrode.

Considering medical-EIT applications the electrical patient safety is important. Regulation requires the sum of current amplitudes to be under a given threshold therefore having embedded current sources on each node could lead to a potential safety issue. This could be the case, if the system enters in an undesired state where several current sources are injecting current at the same time. The control system has to make sure this situation never occurs. As a possible security mechanism the system can implement a so-called safe line (see section 4.2.1.4). Clearly this kind of problem does not arise when using a system with a single central current source. A central current source also facilitates the implementation of a current source monitoring mechanism, for example using a small resistor in series with the current source output and measuring the voltage drop over it. This measurement can be used for two purposes: 1) monitoring the injected current from a safety point of view and 2) active compensation of the current source variations in the data sent to the reconstruction algorithm.

4.2.1.2 Current source circuit

The current source circuit used in this thesis has been proposed by Tietze and Schenk [96]. This circuit (see figure 4.3) acts as a grounded commanded current source using only one operational amplifier and 6 resistors for the implementation. It converts a voltage U_1 into a current I_{out} according to the relation:

$$I_{\text{out}} = \frac{U_1}{R_m} \tag{4.1}$$

Where

I_{out} is the current injected in the medium, here modeled by the load Z_{load},

U_1 is the voltage control signal,

R_m is the resistor setting the current output for a given value of U_1 ($R_m = R_3 = R_6$).

Tietze and Schenk [96] derived an expression for the internal resistance of this kind of current sources:

$$R_{\text{int}} = \frac{R_A R_B (R_A + R_B)}{R_A^2 - R_B^2} \tag{4.2}$$

Where $R_A = R_2 = R_5$ and $R_B = R_4 = R_1$. It automatically follows that if $R_1 = R_2 = R_4 = R_5$, R_{int} can be made arbitrarily large. Of course, an obvious limitation appears when taking into account parasitic impedance and the tolerance of individual chip resistors[5]. The use of negative impedance converter to further compensate for these effects has been reported in the literature, see for example Holder [43]. The disadvantage, according to these authors, of negative impedance converter appears to be the complexity of the circuit, the individual calibration for each circuit and the long-term stability.

4.2.1.3 Current source non-ideal behavior

An ideal current source has an internal impedance $Z_{cs} = +\infty$ (see figure 4.4) but in the real world stray capacitances and resistor network mismatch lead to non-ideal current source behavior. Ideally, a perfect current source exhibits a flat current versus voltage characteristic; meaning that the value of the output current is not a function of the potential at the current source output (i.e. a function of the load). Typically, current sources tends to exhibit stronger non-ideal behavior with increasing operation frequency. This effect is mainly due to the increasing stray capacitance influence on the circuit characteristics. Current-source non-ideal behaviors are not only generated by their own non-idealities, but also generated by the stray capacitance of the bus line (about 100 pF[6]) and the one of the switches (about 15 pF in off state[7]). The main contributors for stray capacitances being the switches, it is worth considering switches with smaller "off capacitance". The capacitance of the FET based analog switches is essentially determined by the silicon surface used to build the source-drain channel. Large silicon surfaces lead to low resistance for the current going through the channel in on state (on resistance R_{on}) but to large stray capacitance in off state. Thus choosing lower off capacitance analog switches automatically means adopting higher R_{on} values.

[5] expensive 0.02% precision resistors can be used
[6] measured value on a 1m long ribbon cable
[7] according to the DG412F data sheet

The choice of the adequate analog switch is closely related with the second main limitation of current source being the limited power supply voltage[8]. With increasing load impedance, the necessary potential drop across it also increases and needs to be supplied by the circuit. This only works until the voltage drop reaches the upper or lower power supply rail voltage of the op-amp[9]. A qualitative estimate can be done considering the following values:

- $R_{on} = 80\,\Omega$ (large stray capacitance about 15 pF and +- 5 V dual power supply),
- $Z_{ci} = Z_m = 100\,\Omega$ @ 100 kHz,
- $I = 10\,\text{mA}$.

This gives a voltage drop of $U = 0.01\,\text{A} \cdot (80\,\Omega + 100\,\Omega + 100\,\Omega + 100\,\Omega + 80\,\Omega) = 4.6\,\text{V}$, which is already a half of the available power supply swing considering +− 5 V. The use of low stray capacitance switches increases the voltage drop to 5 V (i.e $R_{on} = 100\,\Omega$ for stray capacitance of 4 pF (based the DG445 data sheet)). The R_{on} value can be decreased by increasing the dual power supply voltage, for instance using +- 15 V gives $R_{on} = 30\,\Omega$.

The contact impedance (Z_{ci}) is also an important factor to manage, in order to ensure proper current source operation. Favorable contact impedance can be reached by using large electrodes, contact liquids between the electrode and the skin or higher frequency of the current source.

4.2.1.4 Safe line

This section explains the role and the idea behind using a safe line. The use of a so-called safe line is only required when each node is individually able of injecting current using its own embedded current source. In order to comply with the patient electrical safety rules, it is important to know the intensity of the current injected into the body. Therefore, an additional line could be added to the system. This line is connected with a constant current source that delivers for example 10 mA (see 4.5). Then when one node enters the injection mode, it connects a resistor of for example 100 Ω to ground with the safe line. This results in a voltage drop over the resistor of 1 V. This voltage value is continually monitored at a central location. If the voltage drops to 0.5 V, this means that a second node entered the injecting mode. It

[8] Clearly analog switches can also only work up to their rail voltages.

[9] If the op-amp used is not of the type rail-to-rail the available voltage swing is further reduced by 1 or 2 V.

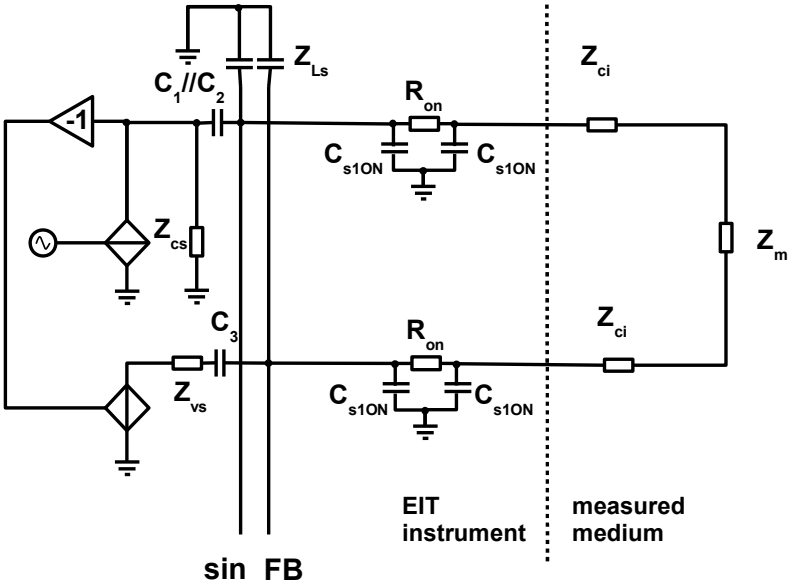

Figure 4.4: Equivalent circuit of the symmetric central current source based on the combination of a commanded current source with a commanded voltage source. On the right hand side of the figure a simple electrical model of the measured medium is depicted, where z_{ci} and z_m are the contact impedance and the bulk impedance, respectively. On the left hand side a block diagram of the symmetrical current source is depicted. The "sin" line denotes the signal generated by the FPGA to drive the current source. The "FB", feedback line carries the voltage potential used to sink the current from the measured medium.

may then be necessary to stop the system to avoid electrical current induced tissue damage.

The same idea of the safe line could be used with the potential monitoring not on a central location but on each node. In such a set-up, each node measures the potential on the line and cannot enter injection mode unless no other node is in injecting mode.

4.2.1.5 Voltage reading

This section explains how the voltage-reading task is realized on the active electrodes. Since the differential amplifier is not located on the node but

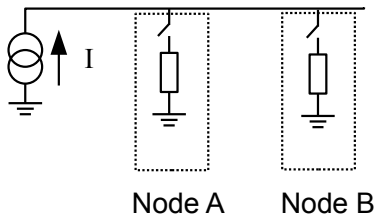

Figure 4.5: Illustration of the safe line principle of work. When node A closes the switch, meaning it enters injection mode, a potential U is established on the line. If another node B also enters injection mode at the same time and closes the switch the potential drops to $\frac{U}{2}$. This drop triggers an emergency stop mechanism to stop current injection into the body and prevent tissue damage.

at a central location, on the SBC, the only remaining task for the node is to buffer the voltage and transmit it using one of the two analog bus lines. Additionally the node also needs to implement multiplexing capabilities to serialize the voltage reading process (time multiplexing). The voltage buffer is realized in a very straightforward fashion with a simple op-amp used in non-inverting voltage follower configuration. In this way the input impedance of the active electrode is maximized; op-amp data sheets gives 500 GΩ in parallel with 2 pF (i.e. 2 pF @ 100 kHz is 796 kΩ). The use of a buffer close to the electrode allows the system to transmit the analog signals on low impedance lines, which limits the undesirable in-coupling of external signals.

The analog lines multiplexing is realized using two switches placed after the buffer. One of the potential problems of this kind of configuration is the RC filter resulting of the combination of the on-resistance of the analog switch and the parasitic capacitance of the bus line as depicted in figure 4.8. Therefore one of the ideas to overcome this problem was to connect the feedback loop of the voltage follower after the switch (see figure 4.9) in this way the resistive effect of the switch is mitigated by a factor equal to the open-loop gain of the op-amp. This configuration suffers from severe drawbacks in terms of timing issues during the multiplexing process. This is because when the node is not connected to any analog lines the buffer output saturates towards one of the power supply rail. Then as soon as the analog switch connects the output of the buffer with the line, the rail voltage appears on the analog bus line and produces a voltage spike. Then it takes about 10 µs for the op-amp to stabilize the signal. A further drawback of these voltage spikes is that they saturate the very sensitive differential instrument amplifier internal circuit,

which leads to longer stabilization delay of the output of the latter. A further disadvantage of this kind of configuration is the use of one buffer per analog switch and per analog line. In comparison the other configuration without the special feedback loop only uses one single buffer and n analog switches for n analog lines. Given all these arguments the last hardware revision (2.6b_2) does not implement the idea presented in figure 4.9 anymore. A reduction of stray capacitance could be realized by selecting higher R_{on} switch but low stray capacitance[10]. In this case the use of high R_{on} switches is not a problem because no current flows through the switches.

The signal acquisition chain, implemented in the hardware revision (2.6b_2), is represented in figure 4.6. The bus is composed of only two analog lines thus only 2 of the L [11] active electrodes can work at the same time in measurement mode. Each of the working electrodes copies the signal read at the electrode on the bus using a voltage buffer. Then an instrumentation amplifier calculates the analog difference between line A1 and A2 and multiplies the result by a gain G_d. After the instrumentation amplifier and high-pass filter it is necessary to avoid the propagation of the DC level that could saturate the acquisition chain. Then the signal is amplified one more time to be scaled to best fit the ADC input scale. Eventually, an anti-aliasing filter is implemented before the signal is differentially transmitted to the ADC.

4.2.2 Digital part design

The previous section describes how the features of the node are implemented, whereas this section presents how these features are controlled and how many nodes can communicate with each other and share the common communication bus. The text is based on the current implementation (version 2.6B), which is micro-processor based. Originally, the plan was to have programmable micro-processors in the final ASICs, but it turns out that this solution would have been by far too expensive to manufacture. This is why we needed to reconsider the digital architecture of the electrode belt. An alternative daisy chain based implementation is therefore presented in section 4.2.2.2.

The node state switching is the main task of the digital electronic integrated in each on-board of each node. Essentially each node has four switches to control, two for injecting and sinking the current and two for the measurement multiplexing between analog lines A1 and A2. Each node needs to switch as synchronously as possible with the other nodes in order to smooth out the

[10] Analog switches have the property of having lower R_{on} resistance at the cost of higher stray capacitance caused by increasing the silicon die surface needed to achieve low R_{on}.

[11] L is the total number of active electrodes of the EIT instrument

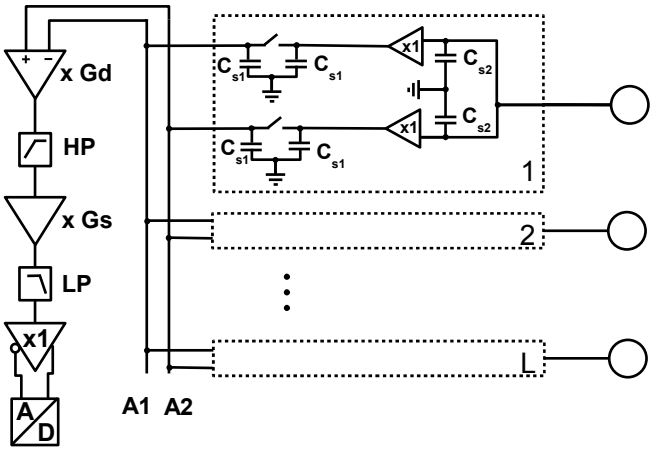

Figure 4.6: The acquisition chain from the electrode to the differential instrument amplifier and the ADC. The stray capacitance of the switches (C_{s1}) and of the op-amp (C_{s2}) are also represented.

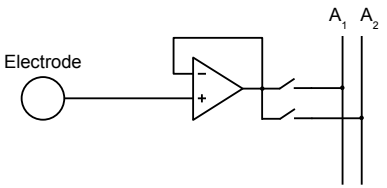

Figure 4.7: Illustration of the buffering scheme using a single op-amp used as an non-inverting voltage follower.

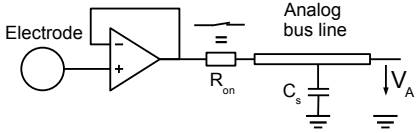

Figure 4.8: Illustration of the RC filter resulting from the combined effects of the on-resistance of the analog switch and the analog bus line stray capacitance.

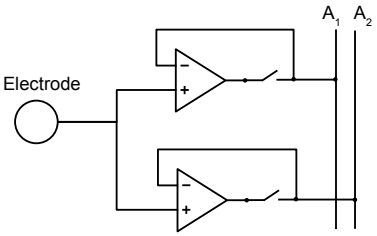

Figure 4.9: Illustration of the voltage buffer feedback loop connected after the analog switch to reduce the filtering effect shown in figure 4.8.

transitions. In summary, the digital electronics should fulfill the following requirements:

- it needs to be flexible enough to allow various measurement strategies to be easily programmed,
- the transition time between the node states needs to be quick compared with the measurement window,
- once running the nodes, the complete network needs to stay synchronized,
- it needs to be implementable at reasonable cost in a custom ASIC design (for the end product),
- it needs to minimize operations[12] at the assembly stage of the active electrode (for the end product).

4.2.2.1 Distributed table based system

This section presents the design of the digital control system implemented in the hardware revision 2.6 for the EIT instrument demonstrator. In this implementation, the on-board digital electronic is an Atmel ATmega328p microprocessor. The advantage of this approach is to enable quick implementation of new measurement strategy idea without undergoing time-consuming hardware changes. It is clearly understood that alternative implementations are also possible; for example using dedicated digital electronics and ROM[13] memory. In fact this could be a perfectly viable alternative to the daisy chain solution presented in section 4.2.2.2.

[12] such as chip individual programing and node populating
[13] Read-Only Memory

In a distributed table architecture (see figure 4.10) each node implements a memory with all the states of the node stored in a table. Additionally an associated table pointer points at the current state. The node state is incremented (i.e. the pointer value is incremented) each time the node sees a synchronization signal broadcasted by the node network master to the whole system. The synchronization signal is generated by the FPGA on the SBC.

The main challenge faced with this architecture is to assign unique identification numbers to each individual node. A first solution could be to hardcode the node ID with pull-up resistors on each node. This would require an individual custom mounting of each node with the appropriate coding. Alternatively, one can imagine a coding pattern on the bus itself which could easily be done, if the bus is implemented in a flexprint. A second solution is to program a given node identification number (ID) in each node, which may require individual programming of each node once mounted on the belt.

Since the demonstrator implementation was done using a microprocessor, we chose the second solution. Each node has exactly the same state table programmed in it, but the state pointer starts at a different location given the programmed node ID and the knowledge of the number of nodes. Then each time the node receives a pulse on the synchronization line, it increments its state pointer. When the state pointer reaches the end of the table, it loops back to the begin of the table (see section 5.2 and figure 5.3 for more details).

The node software revision 4.1 also offers the possibility to select a particular table between several pre-stored tables in each micro-processor. This selection process is done without the need for the system operator to reprogram each node individually. The central control unit implemented in the FPGA simply sends a set of commands to the node and the latter switches to the chosen table. Clearly, this idea could be implemented in the final product using simple logic and ROM memory on the ASICs. This could be an effective and simple way to have programmable active electrodes.

The 4.1 revision of the node firmware is shipped with a complete 32-node table library from offset 0 (adjacent) to 15 (opposite).

4.2.2.2 Daisy chain

As we saw in the previous section, the distributed table solution suffers from the drawback of having to assign unique node ID to each of the nodes. Additionally the programming of the individual nodes with the table increases the costs and the manufacturing complexity of the ASIC based end-product. Fortunately, there is an alternative implementation possible. Active electrode nodes can be implemented in a daisy chain fashion. In this way there is no

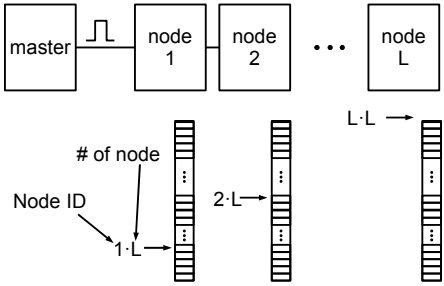

Figure 4.10: Schematic representation of the distributed table based system for the developed EIT instrument. The network master sends a pulse each time the belt needs to increment its states. The horizontal arrows represent the nodes individual pointers being incremented. The positions of the pointers given in the picture are the "reset" or "start" positions, which is where the node begins to read the table (i.e. tables are the same in each node). Additionally an identification number (ID) is also assigned to each node.

more need for node ID nor for individual programming. The node network is entirely managed by the network master.

This architecture (see figure 4.11) is composed of 2 individual daisy chains, one for the measurement commands and one for the current injection commands. Each chain has its own clock line (clockI and clockM). The nodes are connected to these clock lines in a parallel fashion, as opposed to the data lines that require a serial connection between the nodes. [14]The digital commands are shifted into the daisy-chain by the network master, which controls chain entry states and both clock lines. Locally each node has a register to store the commands and set the switches. Then each time the registers receives a clock pulse they store their new digital state.

The daisy chain architecture takes advantage of very regular injection and measurement patterns. Often, it is only necessary to shift the current node state to the next node. At first the network master needs to fill the daisy chain with the starting states. Then, depending on the measurement strategy the network master needs to move the command around the belt. For example,

[14]Clearly, there are various implementations possible of the same idea. For example transmitting the data serially using one unique data line for each daisy chain reduces the number of necessary digital bus lines, but also increases the required register and logic hardware.

for a 32-node system using an adjacent measurement strategy minimizing the current source transition time the sequence looks as follow:

- all node are reset (i.e. no operation state),
- node 1 and 2 are filled with inject and sink command respectively; measure on A1 and measure on A2, respectively,
- then the measurement command is moved from node 1 and 2 to 2 and 3 by broadcasting a pulse on the clockM line,
- then the measurement command is moved from node 2 and 3 to 3 and 4 by broadcasting a pulse on the clockM line,
- then the measurement command is shifted to the next pair of electrodes until all possible pairs are measured once,
- then the measurement command is moved from node 31 and 32 to 32 and 1 by broadcasting a pulse on the clockM line,
- then the injection command needs to be shifted from node 1 and 2 to 2 and 3 by broadcasting a pulse on the clockI line,
- then the measurement and injection command are shifted inside the daisy chain until all combinations of injecting and measurement electrode pairs are processed

For this particular pattern, the adjacent strategy, the clockM pulse frequency is L (number of electrodes) times quicker than the signal on the clockI line.

The main advantages of the daisy chain solution is that it does not require software nor hardware node identification. Moreover the digital electronics embedded in each node is very sparse, which reduces the power consumption and the costs.

4.3 Sensor Belt Connector

4.3.1 Analog front end

The analog front end on the SBC is the interface between the FPGA and the electrode belt. The role of the analog front end is to process outgoing and ingoing signal for the digital electronics to be used. It is composed of four main circuits:

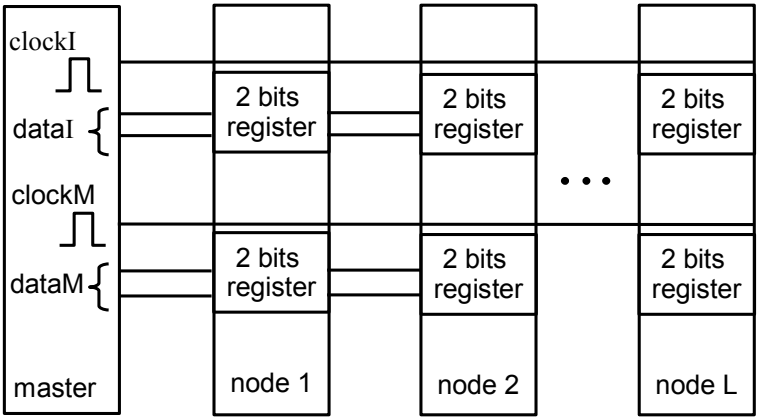

Figure 4.11: Illustration of the daisy chain solution to operate nodes switches. In fact two daisy chains are implemented, one for the measurement commands and one for the injection commands, each having its own clock line. This architecture enables the two chains to move the commands at different pace. Locally the commands are stored in simple register.

- the signal generator,
- the central current source,
- the analog difference amplifier and acquisition chain,
- the digital section controlling the synchronization signal and the auxiliary digital signals.

The digital signal synthesizer is implemented in the FPGA using the Altera IP core design, which enables the creation of any signal shape necessary. After leaving the FPGA the digital data flow is transformed into an analog signal using a Digital to Analog Converter (DAC) from Burr Brown/ TI (DAC904). The analog signal generation is done with a precision of 14 bits at 100 MS/s. Then a simple analog band pass filter (12 kHz to 2.4 MHz) is implemented to prevent the undesired propagation of DC and to cut-off the high frequency component of the signal. The processed analog signal is then scaled to be transmitted to the current source circuit discussed in section 4.2.1.1.

The acquisition chain is composed of a differential instrument amplifier manufactured by Analog Devices (AD8221) determining the analog difference between both analog bus lines A1 and A2. The AC-coupling (the high pass

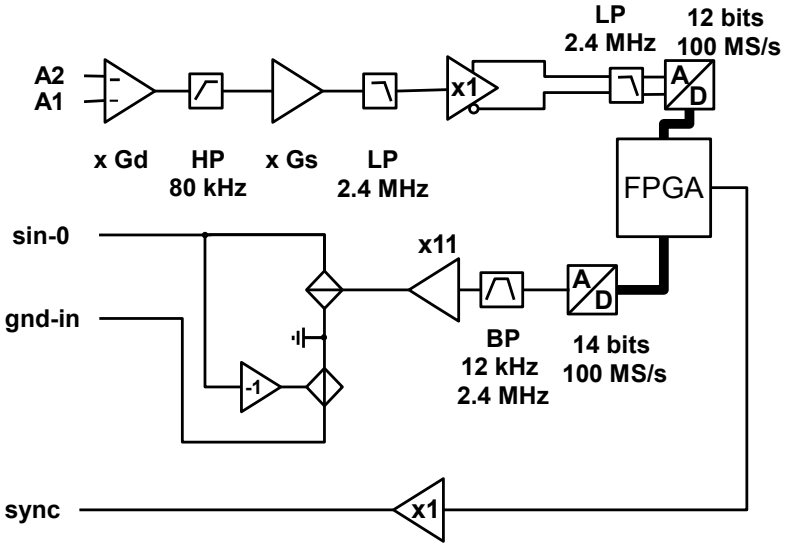

Figure 4.12: Implementation of the acquisition chain and signal generator. The gain of the instrumentation amplifier, G_d, is set in combination with the gain, G_s, of the second amplifier stage to best fit the voltage input range of the ADC.

filter) is implemented as suggested in the AD8221 data sheet using a feedback circuit AnalogDevices [10]. Then a second amplification stage is inserted to adjust the signal range to fit the entire input voltage swing of the ADC. This stage is implemented with a Burr-Brown operational amplifier (OPA134, TexasInstruments [93]) configured as a non-inverting amplifier. Then the signal needs to be converted from single-ended to differential to meet the ADC input requirement. This is realized using a fully differential amplifier from Texas Instruments (THS4502). As suggested in the data sheet TexasInstruments [95] the anti-aliasing filter is directly integrated in the feedback paths. Since this last stage and the ADC are on separate board an additional RC low pass filter is implemented in close vicinity to the ADC to avoid high frequency parasitic voltage glitches.

The differential instrument amplifier is one of the key components of the analog measurement chain. Therefore, the choice of the differential instrument amplifier is critical to meet the required signal quality. Key features are good CMRR, bandwidth and high slew rate (rapid settling time). Table 4.1 provides a non-exhaustive comparison of instrument amplifiers.

The use of digital gain setting based instrumentation amplifiers was long ignored during the design and testing phase. Initially, one was using a capacitance in the analog gain setting loop to implement the AC-coupling of the differential instrument amplifier. The digitally controlled amplifier often exhibits better performance in terms of CMRR than its resistor gain setting based counterpart. The CMRR performance of the latter are degraded by the stray capacitance of the IC pins and of the PCB traces at the gain resistor connections on the instrumentation amplifier. Clearly the AD8253 appears to be the best choice for the next generation prototype with enhanced CMRR, bandwidth and slew rate compared to the AD8221.

4.3.2 FPGA board

This section presents an overview of the functionality and architecture of the FPGA. The implementation and design work has been realized in collaboration with Scuola Universitaria Professionale della Svizzera Italiana (SUPSI) and a detailed documentation can be found in the SBC-FPGA manualRogantini [76][15]. Thus the goal of this section is not to present in detail how it works, but to give a brief overview.

The tasks taken over by the FPGA are the following:

- digital signal generation,

[15]This document is not public, an interested reader is invited to ask the author for a copy.

Table 4.1: Comparison of differential instrument amplifiers.

name	manufacturer	CMRR [dB] @ 100 kHz, gain=10	bandwidth [kHz], gain=10	slew rate [$V\,\mu s^{-1}$]	gain setting
AD8221	Analog Devices	80	400	2	analog
INA111	Texas Instruments	55	1000	17	analog
INA128	Texas Instruments	50	500	4	analog
AD8253	Analog Devices	85	1000	20	digital

- digital signal demodulation,
- synchronization signal generation,
- communication with the computer over the Ethernet port.

The FPGA board is based on commercial off-the-shelf Altera development kit (Stratix II EP2S180 DSP Development Board) with integrated ADC, DAC and Ethernet interface. The Altera board (see figure 4.13) communicates with the electrode belt through a custom developed analog front end, see section 4.3.1.

4.3.3 IQ demodulator

The IQ demodulator (see figure 4.14) is one of the key components of the FPGA design. It enables the demodulation of the incoming signal using a local copy of the signal generator output. The desired values at the demodulator output are the amplitude of the incoming signal and the phase between the incoming signal and the reference signal. The basic idea is to multiply the incoming sinusoidal signal, with a reference sinusoidal signal (sine) on one branch (I: in-phase) and with a 90 degree shifted reference (cosine) on the other branch (Q: quadrature). The obtained samples are then accumulated at the integration stage. At the end of the measurement window, the values of the accumulation registers are read and their respective values stored. The FPGA does not evaluate the incoming signal any further but for theoretical completeness and text coherency, the mathematical development leading to

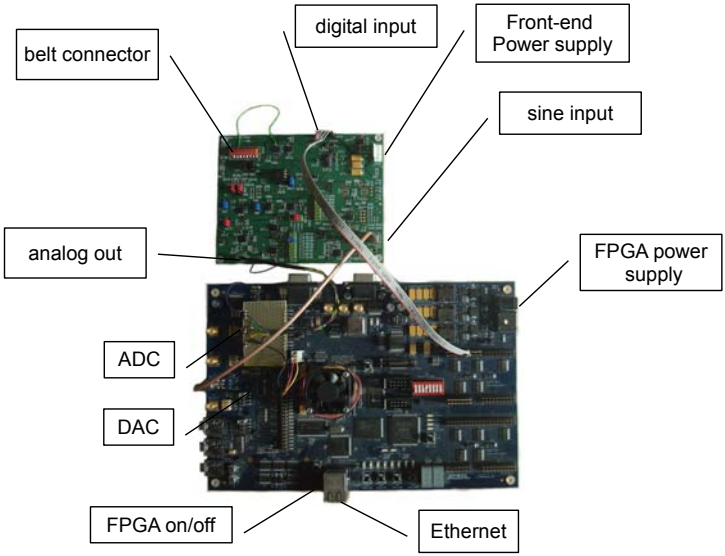

Figure 4.13: Altera Evaluation board and analog front end.

the calculation of the incoming signal amplitude and phase delay is presented as well:

$$X_I = \underbrace{A_1 \sin(\omega_1 n t_s + \phi_1)}_{\text{incoming signal}} \quad \underbrace{A_2 \sin(\omega_2 n t_s + \phi_2)}_{\text{reference signal}} \tag{4.3}$$

$$X_Q = \underbrace{A_1 \sin(\omega_1 n t_s + \phi_1)}_{\text{incoming signal}} \quad \underbrace{A_2 \cos(\omega_2 n t_s + \phi_2)}_{\text{reference signal}} \tag{4.4}$$

where

A_1 is the amplitude of the incoming signal (i.e the value of interest),

A_2 is the amplitude of the reference signal,

ω_1, ω_2 is the angular frequency of the incoming signal and the reference signal respectively,

ϕ_1, ϕ_2 is the phase of the incoming signal and the reference signal respectively,

t_s is the sampling period,

n is the sample index number.

Since the mathematical treatment for the two branches is similar, the following development only presents the I branch case. By using a trigonometric identity and equation 4.3 one gets:

$$X_I = A_1 A_2 \cdot \frac{\cos\left(\omega_1 n t_s + \phi_1 - \omega_2 n t_s - \phi_2\right)}{2} \tag{4.5}$$

$$+ \frac{\cos\left(\omega_1 n t_s + \phi_1 + \omega_2 n t_s + \phi_2\right)}{2} \tag{4.6}$$

At this point one needs to make the assumption $\omega_1 = \omega_2 = \omega$, meaning that the local reference signal exactly matches the frequency of the incoming signal. Since both signals share the same digital source this should be a safe assumption to make. The demodulation process acts as a bandpass filter placed around ω_2.

$$X_I = A_1 A_2 \cdot \frac{\cos\left(\left(\omega_1 - \omega_2\right) n t_s + \left(\phi_1 - \phi_2\right)\right)}{2} \tag{4.7}$$

$$+ \frac{\cos\left(\left(\omega_1 + \omega_2\right) n t_s + \left(\phi_1 + \phi_2\right)\right)}{2} \tag{4.8}$$

$$= A_1 A_2 \cdot \frac{\cos\left(\phi_1 - \phi_2\right) + \cos\left(2\omega n t_s + \left(\phi_1 + \phi_2\right)\right)}{2} \tag{4.9}$$

The coherent integration stage removes the high frequency component of the X_I signal[16], and we obtain:

$$I = A_1 A_2 \cdot \frac{\cos\left(\phi_1 - \phi_2\right)}{2} \tag{4.10}$$

and similarly for the Q-branch we obtain:

$$Q = A_1 A_2 \cdot \frac{\sin\left(\phi_1 - \phi_2\right)}{2} \tag{4.11}$$

Then, to calculate the amplitude value of the incoming signal, one needs to square I and Q, add them together and finally take the square root:

$$Z_A = \sqrt{I^2 + Q^2} \tag{4.12}$$

$$= \frac{A_1 A_2}{2} \cdot \underbrace{\sqrt{\cos^2\left(\phi_1 - \phi_2\right) + \sin^2\left(\phi_1 - \phi_2\right)}}_{=1} = \frac{A_1 A_2}{2} \tag{4.13}$$

[16] This stage can be seen as a low pass filter (averaging)

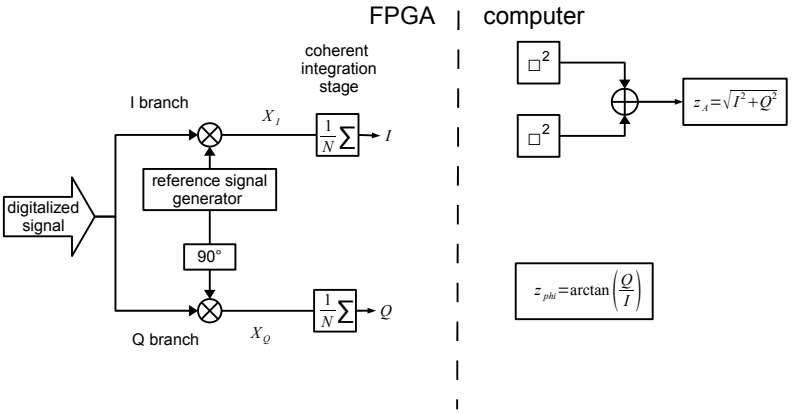

Figure 4.14: Illustration of the IQ demodulator module on the FPGA side and the use of the I and Q values on the computer side.

Thus the desired incoming amplitude (A_1) is:

$$A_1 = \frac{2Z_A}{A_2} \tag{4.14}$$

The phase delay ($\Delta\phi$) between the incoming signal and the reference signal can be retrieved by taking the arc tangent of I over Q:

$$\begin{aligned} Z_\phi &= \arctan\left(\frac{Q}{I}\right) = \arctan\left(\frac{\sin(\phi_1-\phi_2)}{\cos(\phi_1-\phi_2)}\right) && (4.15)\\ &= \arctan(\tan(\phi_1-\phi_2)) = \Delta\phi && (4.16)\end{aligned}$$

The bandpass characteristics of the IQ demodulator are essentially given by the integration time (t_i), which defines a rectangular measurement window in the time domain. This leads to a squared sinc shaped frequency response as depicted in figure 4.15. The first zeros of the filter in the frequency domain are given by $\frac{1}{t_i}$, then a bandwidth estimation of the IQ demodulator is derived to by $BW_{IQ} = \frac{2}{t_i}$. The half-width maximum can be estimated by taking $\frac{1}{3}$ of BW_{IQ}. In other words, longer integration time gives narrower filter around the demodulation frequency, which lead to less noise on the final amplitude result by filtering out larger portions of the background noise.

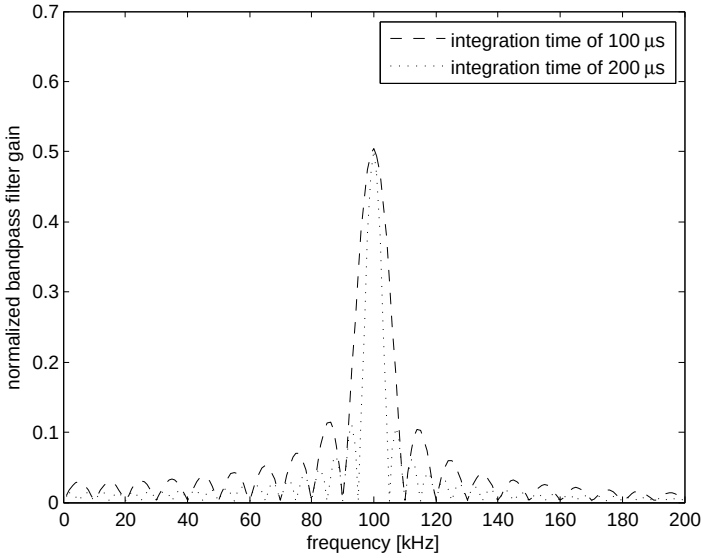

Figure 4.15: Illustration of the band pass characteristic of the IQ demodulator for two particular measurements windows 100 µs and 200 µs.

4.4 Thoracic-EIT: belt

This section describes how the nodes are assembled to realize the belt used in thoracic-EIT application. The nodes (hardware revision 2.6) can be connected to each other using two 16 pins Flat Flexible Cable (FFC) connectors to form a belt-like structure, see figure 4.16. Because FFC cables are not available in lengths longer than 10 cm, it was necessary to build an interface PCB between the FFC and ribbon cable to connect the SBC. The same interface board also includes power Light Emitting Diodes (LED) that enable a quick and convenient control of the power line voltage. Ribbon cables have also the advantage to be cheap and easily customizable in their length.

The electrode-patient contact is realized using gold-plated copper blades directly soldered on the active electrode PCB. In this way the path between the electrode and the voltage buffer is minimized. The electronics is then placed into a fabric, which gives additional mechanical stability to the belt and protects the electronic from water projection. The fabric based belt also allows easy handling for the experimentation on volunteers. It is even possible for the volunteer to don the belt alone, without the help of an external person.

4.5 Micro-EIT: well

This section describes how the node can be assembled to build the micro-EIT instrument. The motivation for developing the micro-EIT device was to be able to make EIT measurements on a smaller medium than the human thorax. Target media are ranging from 50 to 9 mm in diameter depending of the configuration of the instrument. The upper limit is fixed by the size of the hole in the baseboard and the lower limit is set by the PCB fabrication technology used to manufacture the well.

The nodes (hardware revision 2.6) can be connected to each other using two 16-pin FFC connectors to realize the thoracic-EIT belt. Alternatively one of the two FFC connectors can be unsoldered, which offers the possibility to connect the node on the side of the PCB using a standard 1.27 mm pitch 2-row header connector. This option allows building a compact system on a single baseboard which gather all the nodes PCBs. The baseboard acts also as a system bus to connect all the nodes. The baseboard itself is very simple and is composed of the following elements:

- the bus line (PCB traces) linking electrically all the nodes together,
- the 16-pin micromatch connector to make the connection to the front end using standard ribbon cable (2.54 mm pitch),

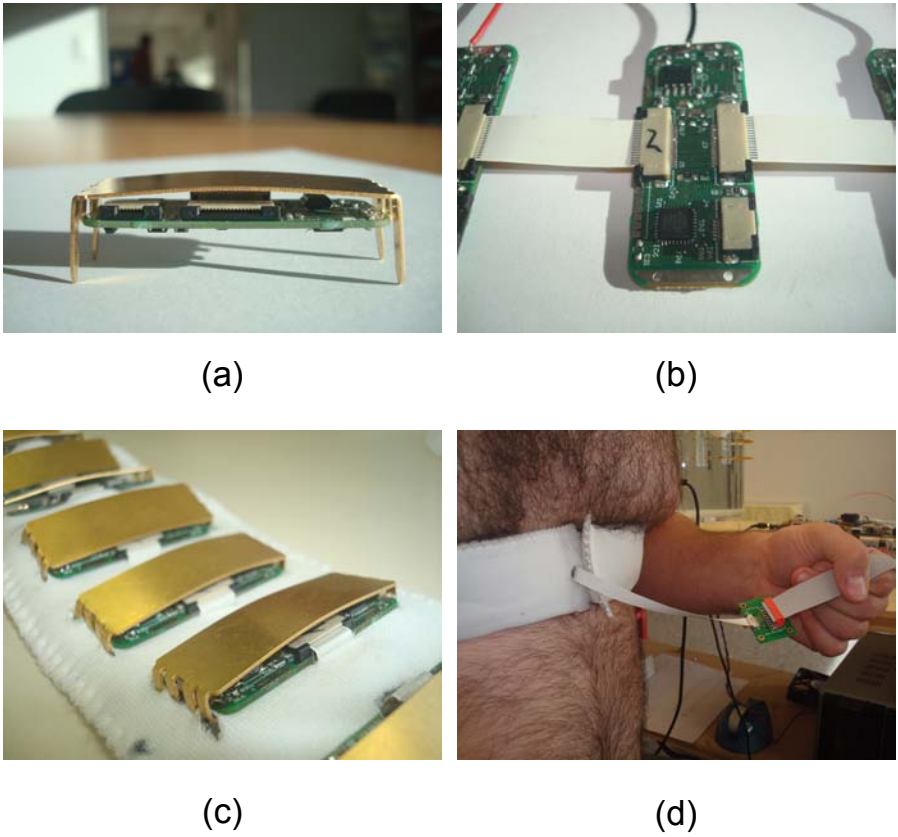

Figure 4.16: Illustration of the developed thoracic-EIT system. a) the active electrode PCB with the gold-platted copper electrode, b) the active electrodes are connected in a belt-like structure using FFC cables, c) the belt-like structure can be incorporated within a bio-compatible fabric and d) the active electrode belt worn by a male volunteer.

- power line blue LEDs for each line (+5 V, -5 V and +5 V (digital)),
- the 32 active electrodes PCB,
- the central connection to the micro-EIT well using an interface PCB.

The central connector with its 5.5 cm hole in the middle (see figure 4.17) was designed to allow the user to assemble the device in two different configurations.

In the first configuration, the user is interested to measure objects with a size ranging from 5 to 1 cm in diameter. For this purpose, the baseboard can even be placed vertically and the object under study can be placed through the hole, as in a CT-scanner. This configuration enables the electrode cable to be made as short as possible.

In the second configuration, an additional adapter (see figure 4.18) is placed to cover the hole. This adapter is equipped with a ZIF connector, which is used as a zero-force connector to plug in the micro-EIT well chip (see figure 4.19).

The micro-EIT well chip has been manufactured for this project using standard PCB technology. The basic idea was to place vias in a circular fashion and then drill a hole to take out half of each of the vias. This operation creates an electrode ring. In this case, the well is 9 mm in diameter and the electrodes are 1.65 mm in height and 0.65 mm in diameter. The electrodes are gold coated during the PCB fabrication process, which stabilizes the electro-chemical interface between the medium and the electrode. Then by assembling a bottom and a cylindrical piece on the other side one obtains a well that can be filled, for example, with a saline solution.

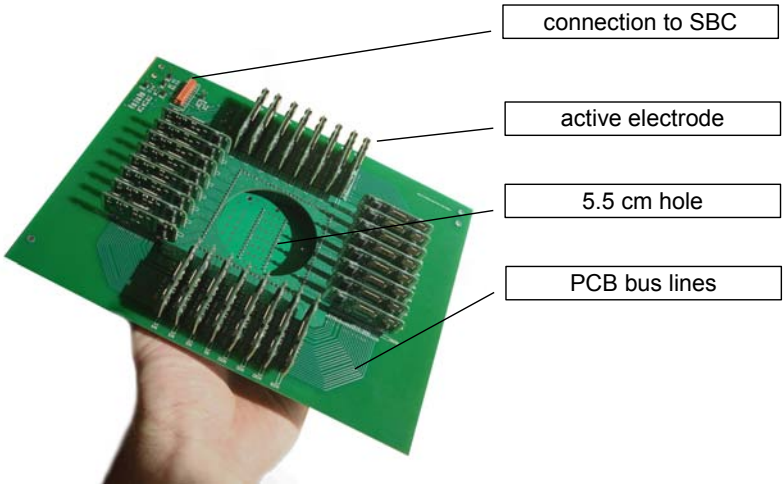

Figure 4.17: The baseboard bottom side with 32 active electrodes PCB and the central hole.

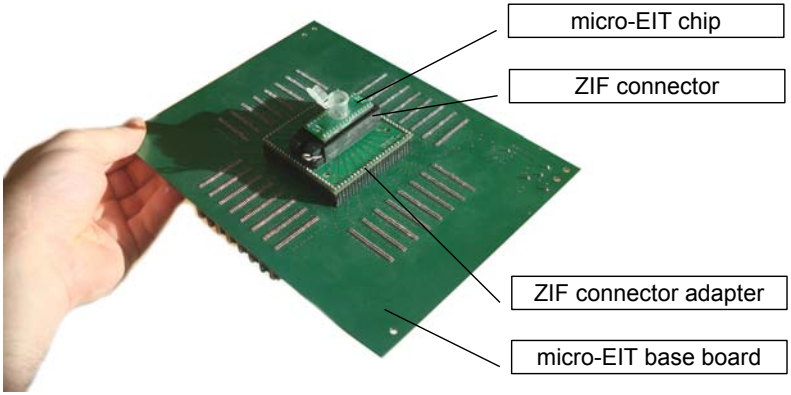

Figure 4.18: The baseboard assembled in the micro-EIT configuration with the ZIF adapter and a micro-EIT chip plugged in.

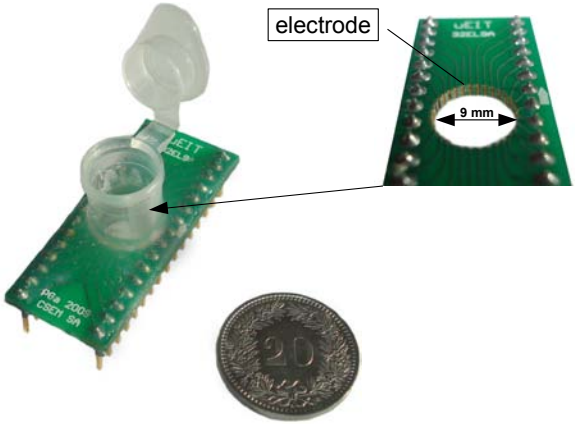

Figure 4.19: Details of a micro-EIT chip with 32 electrodes manufactured using standard PCB technology. The diameter of the well is 9 mm and the electrodes are 1.65 mm in height and 0.6 mm in width. On the right hand side the electrode well is displayed before the fluidic tank is assembled.

Chapter 5

Software Design and Architecture

The main purpose of this chapter is to explain how the software and hardware are interacting together to make the system work properly. Not every code line in each of the programs of the system will be explained, but rather an overview of their working principles is given and their interactions with each other are explained.

There are essentially three different pieces of software implemented in the three main hardware components (active electrode node, SBC and PC) of the EIT instrument. The hardware and software version described in this chapter are given in table 5.1.

5.1 Interfaces and protocol

A PC program called EITSurfer has been developed to act as the system master. Its role is to play the intermediary between the user and the EIT device. This kind of interface is also commonly called Graphical User Interface (GUI).

Table 5.1: Hardware and software version described in this chapter.

Name	Hardware	Software
GUI	Computer PC, win32, vista	EITSurfer 1.8.5
SBC	front end: 2.1, FPGA: 0.6	0.6
Node	2.6B_2	4.1

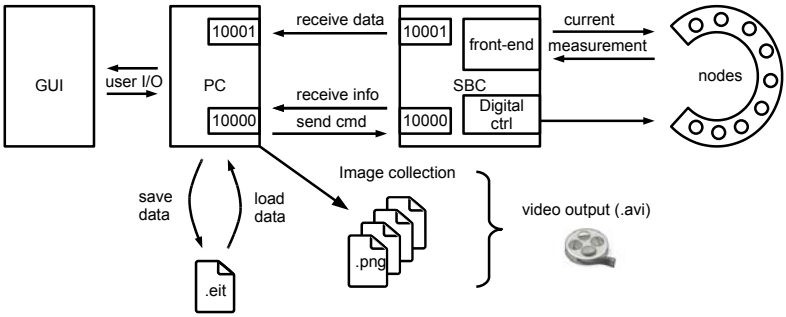

Figure 5.1: The EIT system interfaces and communication protocols.

The primary task of EITSurfer is to communicate with the SBC over an Ethernet connection (see figure 5.1) using the standard TCP/IP protocol. The port 10000 is used to send and receive ASCII coded commands and information. An exhaustive list of commands can be found in table 5.2. The port 10001 is used to receive the digital measurement data from the SBC (see section 5.3 for protocol details).

The EITSurfer program can also save the acquired data in a custom binary format with the ".eit" extension (see figure 5.1). It can also reload the saved data file and play them back. Moreover, since only the raw data are saved, it enables the user to select new reconstruction methods and fully analyze the data inside the same software. Additionally EITSurfer can export the data into an image format and build a video out of a collection of images.

The SBC itself needs to communicate with the node network. Therefore it can send and receive analog signals using its analog front end described in section 4.3.1. Digital signal clock signals are used to broadcast simple commands to all nodes, such as "go to next state" or to select a measurement strategy table.

5.2 Node state diagram

The goal of this section is to explain how the node software works and how it receives commands from the SBC. Each microprocessor on the nodes is programmed with exactly the same software except for their respective IDentification number (ID), thus node 1 gets ID=1, node 2 gets ID=2 ... Since we chose to work according to the principle of the distributed tables described in section 4.2.2.1, the microprocessor flash memory is programmed with a set of tables. Version 4.1 implements 16 tables for a 32-electrode system. Each

table represents a particular measurement strategy. In this case, all offsets ranging from 0 (adjacent) to 15 (opposite) are programmed.

When the nodes are turned on, they enter in the "Wait for commands" mode (see figure 5.3 for the node state diagram), meaning that the microprocessor closes switches sw7 and sw8 and opens switches sw4 and sw5 (see figure 5.2). In this way it can listen to commands broadcasted on the analog lines. Pull-up resistors are connected to the microprocessor pins to avoid floating potentials in the case the analog lines are not actively driven. The FPGA is able to write digital commands on the analog lines using a general input-output register. In order to write something on the analog lines switches swA and swB have to be closed. In the case line A1 (portC:5 on the microprocessor) drops to logic zero, the nodes enter the "programming mode". In this state the nodes trigger on the rising edge of line A2 (portC:4), and each time an event occurs a counter gets incremented. If A1 rises to logic one again, the node enters the "link table" mode. In the "link table" mode the node links the selected state table based on the number of pulses received during the programming mode. Thus if 1 pulse have been received the table corresponding to measurement strategy offset 0 will be linked, for 2 pulses table for offset 1,... up to 16 pulses for offset 15. Once the table is linked the node automatically returns to the "wait for commands" mode. The link (memory pointer) to the chosen state table is stored in the EEPROM memory of the microprocessor, meaning that at the next power up, it can reload the stored setup and one does not need to reprogram the nodes. If at any moment the clock signal (sync line) rises, the node fetches immediately the entry point to the linked table and opens sw8 and sw7. If a clock signal has been generated, it means that swA and swB have also been disconnected.

The table entry point is calculated based on the node ID and the number of table states[1]. For example node 1, with ID=1, will enter the table at state $(1024 - \mathrm{ID} \cdot 32) = 992$ (i.e. the table state pointer is set to 992). Then for each subsequent clock pulse, the table state pointer is incremented by one state. At the end of the table, it cycles back to the first state of the table. If no clock signal is measured by the microprocessor within 1.5 ms after the last received pulse, the node goes back in the "wait for commands" mode. This timeout value can be customized for the user needs. Larger values enable the system to use slower image acquisition rates, but also increase the time necessary for the system to enter the "wait for commands" mode (i.e. to reset).

[1] 1024 in this case

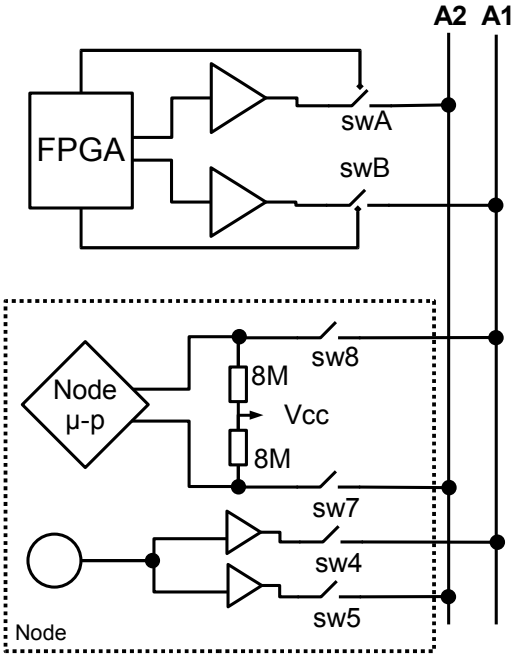

Figure 5.2: The hardware architecture used to broadcast measurement strategy selection commands to all nodes of the network.

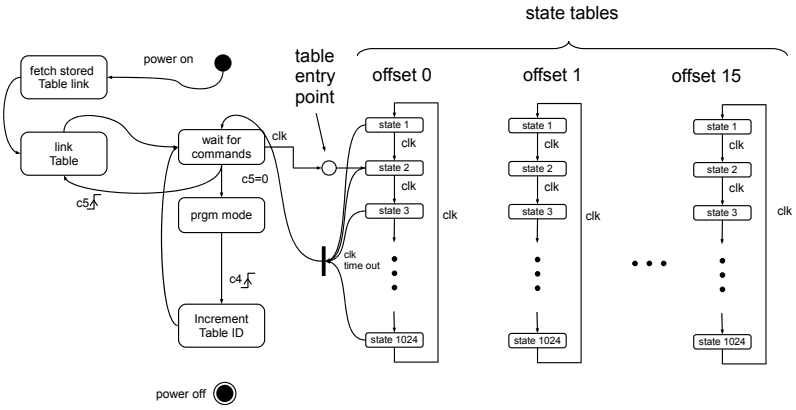

Figure 5.3: The node state diagram from the power on state to the power off state using Unified Language Modeling (UML) state diagrams.

5.3 SBC

The software developed[2] for the embedded NIOS core of the FPGA runs under a real-time operating system. Its task is to manage the FPGA hardware and to communicate with the user client software (in this case EITSurfer) over the Ethernet ports. Since SBC to node communication protocols have already been addressed in section 5.2, this section focus on the communication protocol with EITSurfer over the Ethernet connection.

There are two ways of connecting the SBC. First, if the board is plugged into a network environment, it will ask the DHCP server for an IP address. The second way is to connect the computer with the SBC board directly; in this case the board takes the default IP address. Once the connection is established two ports are opened over the 10000 and the 10001.

The port 10000 is reserved for sending and receiving commands. Commands are coded in ASCII code and separated with the new line char ("\n" or ASCII 0x0A). The main commands to be sent are the commands used to set the acquisition mode. The important fact to remember is that the SBC is designed as a synchronous machine, the synchronization signal being the digital sine values generated by the Numerically-Controlled Oscillator (NCO). Thus the actions of the hardware are synchronized with the sine signal crossing the zero line (zero-crossing detector). The direct consequence is that not all combinations of acquisition parameters are valid. EITSurfer verifies the validity of the parameter set before sending it to the SBC (see section 5.3.1 for detail).

The port 10001 is reserved for the SBC to send data to EITSurfer. Data are sent in a binary format, each value is a 32-bit integer with no separation signs. For example, a measurement strategy, demanding $32 \cdot 32 = 1024$ measurements per image (per data frame), will send at first the demodulated I (I1) value corresponding to the first measurement and then the Q (Q1) value of the first measurement, then I2, Q2, I3,...I1024 and Q1024 are sent. After sending the first data frame, it continues with sending the first data of the second image: I1, Q1..., Q1024 without sending any "end-of-frame" sign. The apparent lack of protocol is compensated by the use of the well-known and robust TCP/IP protocol, which makes sure that the data flow is not corrupted. In this way the data flow receiver only needs to count the number of data received to know to which frame each data belongs.

[2]The software has been developed in collaboration with the Scuola Universitaria Professionale della Svizzera Italiana (SUPSI)

Table 5.2: The most important SBC parameters and their commands.

name	syntax	range	comments
nco_frq	set frq	[0, $2^{32} - 1$]	
nco_gain	set gain	[0, 255]	0 means 100%, otherwise nco_gain/256 in percent
measurement frame per image	set fpi	[0, 1023]	0 =1024
sine period per measurement frame	set ppf	[0, 1023]	0 =1024
clock per sample, acq_cps	set cps	[0, 255]	0 means 100MS/s, 1 means 50MS/s,2 means 33 MS/s,..., 100 means 1MS/s,...
periods to ignore at frame begin, acq_pign	set pign	[0, 1023]	
periods to consider for measurement	set psmpl	[0, 1023]	
start	start [nb of frame]		
stop	stop		
syn_tboim	set tboim	[0, 1023]	synchronization pulse duration between 2 images, step of 10 ns
syn_tbofr	set tboif	[0, 1023]	synchronization pulse duration between 2 frames, step of 10 ns
binary data format, acq_fmt.macX	set mac0	[0, 7]	see section 5.3.3
binary data format, acq_fmt.bigend	set endian	0, 1	0=little-endian, 1=big-endian
acq_rawfrn	set rawfrn	[0, 1023]	set the first recorded frame in raw
raw mode	set rawmode	0, 1	0 = raw + nco wave form, 1 = raw only
raw	raw [nb of times]		start raw acquisition [nb of time to repeat the measurement]

5.3.1 Setting the data acquisition parameters

The parameter set (see table 5.2) needs to be calculated to match the constraint of having an integer number of sine periods inside a single measurement time frame. Since the SBC hardware is a synchronous machine (sine zero-crossing), this is necessary to ensure proper internal system operation. Consequently, not every parameter combination is possible. Typically, the user can decide about the frequency to use and the acquisition speed (images per second) which automatically sets all other parameters. For instance the user decides to work with a sine at frequency f=100 kHz and 10 images per second. At first, the correct "frq" parameter is calculated using:

$$\text{frq} = \text{round}\left(\frac{f}{100 \cdot 10^6} \cdot 2^{32}\right) = 4294967 \tag{5.1}$$

Under the assumption of using fpi=1024 measurement frames per image (i.e. with 32 electrodes) and I_{rate} =10 images per second the "ppf" parameter is deduced:

$$\text{ppf} = \frac{1}{\text{fpi}\, I_{\text{rate}}} \cdot \frac{1}{\text{frq}} = 10 \tag{5.2}$$

This means that each measurement frame contains 10 sine periods. The user can also choose to skip data after and before each measurement frame, see figure4.2 for the nomenclature. This has been implemented to give the system time to settle the signal before beginning the demodulation. It is especially useful to skip the first t_{skip} microseconds after a transition, it improves the demodulated signal stability. Since the number of sine periods within one measurement frame must remain integer, it is required to remove integer numbers of periods only. In the above example in order to skip 20 µs at the beginning and 10 µs at the end of the measurement frame the parameter needs to be set as follow: pign=2 and psmpl=7.

The nco gain parameter defines the amplitude of the generated waveform. The user chooses the value in percent of nominal (gp), with the convention of nco_gain=0 meaning 100% of nominal. Then for the other value, the parameter is calculated as follow:

$$\text{nco\_gain} = \frac{\text{gp}}{100} 255 \tag{5.3}$$

The last parameter to be defined is the clock per sample, cps. This parameter controls the number of samples to take into account for the demodulation.

The ADC produces 100 MS/s, which cannot be changed, but the samples entering the demodulator could be decimated[3]. By convention cps=0 means that every single sample is used in the demodulator. Then cps=1 means that 1 sample of 2 is sent to the demodulator, cps = 2 send 1 sample of 3 to the demodulator, and so forth. To obtain optimal noise performance the user should consider using cps=0. Using other values for the cps parameter allows the user to simulate the acquisition of data using a slower ADC. This feature has been implemented to enable the simulation of the performances of lower end ADCs.

5.3.2 Setting the raw data acquisition parameter

Besides the normal acquisition mode, the SBC has also the possibility to record and send the values coming directly out of the ADC (i.e. undemodulated). Since there is only 16 Kbytes memory available on the SBC, only short acquisition times are possible. The acquisition time can be controlled with the cps parameter. For example by setting cps=1 (skipping 1 of 2 samples) this allows doubling the measurement time period by omitting half of the samples (i.e. using half of the nominal sampling rate). The rawfrm parameter sets at which measurement frame the raw data acquisition begins. Therefore by setting rawfrm=0, it begins at the first measurement frame after acquisition started.

By setting the parameter rawmode to 0, it is also possible to acquire the NCO output. However, since both data sources are sharing the same memory, this feature decreases by 2 the acquisition time of the raw data.

5.3.3 Setting the advance SBC acquisition parameter

The user can also choose the clock pulse duration (synchronization signal). Since the node software needs a minimum pulse length of 6 µs , it is recommended to use pulses of 10 µs (tboim=tboif=1000). The 6 µs limit is given by the average time the node firmware needs to execute the interrupt routine triggered by the pulse (clock signal) rising edge. The user can also choose to send a pulse with a different length every (ppf*fpi) periods (i.e. at the beginning of a new image), but this feature is not used by the node firmware at the moment.

The demodulation[4] is implemented using a Multiply and ACcumulation unit (MAC), see figure 5.4. As input the MAC takes the signal coming from the

[3] In signal processing this is also called undersampling.
[4] see section 4.3.3for the mathematical details

Table 5.3: Values of the mac0 parameter, controlling the truncation block of the MAC unit.

mac0	fix-point format
0	sQ15.17
1	sQ14.18
2	sQ13.19
3	sQ12.20
4	sQ11.21
5	sQ10.22
6	sQ9.23
7	sQ8.24

NCO (14 bits, sQ1.13[5]) and the ADC (12 bits, sQ1.11). Each sample x of both signals should be interpreted as a fixed point number: $-1 \leq x < 1$, in this way after the multiplication stage the result becomes a sQ2.24 number[6]. Then each number coming out of the multiplier is added to the value stored in the accumulator and the result is stored into the accumulator (39-bit register). Since the numbers sent to the user by the Ethernet connection are 32-bit integers, a truncation block needs to select 32 bits from the 39 bits of the accumulation register. This selection is determined by the user by setting the mac0 parameter according to table 5.3.

Each binary number can also be represented in the big or little-endian number notation, EITSurfer assumes little-endian numbers (parameter: endian=0).

5.4 GUI

The Graphical User Interface (GUI) has been developed in the C# programming language. This language is strongly object oriented and well integrated into Windows systems. The basic principle of work is almost the same as the Java programming language, which uses a virtual machine (JVM) and a just-in-time compiler. In the case of C#, which is part of the .NET language family, the "virtual machine" is called CLR (Common Language Runtime).

[5] see section B.1.4 for more explanations about the fixed-point notation

[6] The corner case $(-1) \cdot (-1)$ should be considered. Therefore one cannot use sQ1.24 numbers

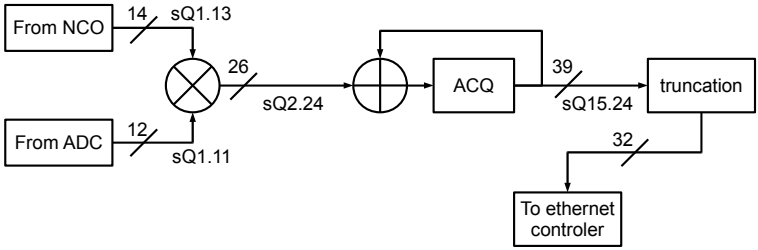

Figure 5.4: Detailed implementation of the demodulator inside the FPGA.

This means that once the source code is "compiled" there is no binary executable created. The source code is translated into a language common to all the .NET programming language, called the Common Intermediate Language (CIL). The CIL code, sometimes also called the byte code, is a platform and architecture independent code. Then at the time of the execution the just-in-time compiler transforms the CIL code into native code to be executed on the processor. The Common Language Infrastructure including the CIL and the CLR has been standardized by the European Computer Manufacturer Association [28]. The code being executed inside the CLI is called "managed code".

The use of managed code offers lots of advantages for example in the memory management[7]. The debugging is also facilitated by the CLR, which has a better knowledge where the program stops. In general, program crashes are also prevented by the CLR. The main advantage of using C# and .NET in comparison with Java for example is that C# offers the possibility to execute so called "unsafe code"[8] inside managed code. This means that the programmer can deliberately choose to work with pointers to speed up the execution of critical parts of the code. Doing so the program could also write everywhere in the computer RAM memory, which can cause the computer to crash. This feature was important to implement quick matrix multiplication in EITSurfer.

The GUI name is EITSurfer. In the background, it uses a library called EITSurf (see figure 5.5) which implements all the core functions. The idea here was to decouple the GUI implementation from the core functions necessary to

[7]garbage collector: http://msdn.microsoft.com/en-us/library/ee787088.aspx, accessed on the 10.01.2010

[8]Security and Programming (C# and Visual Basic) and Unsafe Code and Pointers (C# Programming Guide), accessed on the 10.01.2010

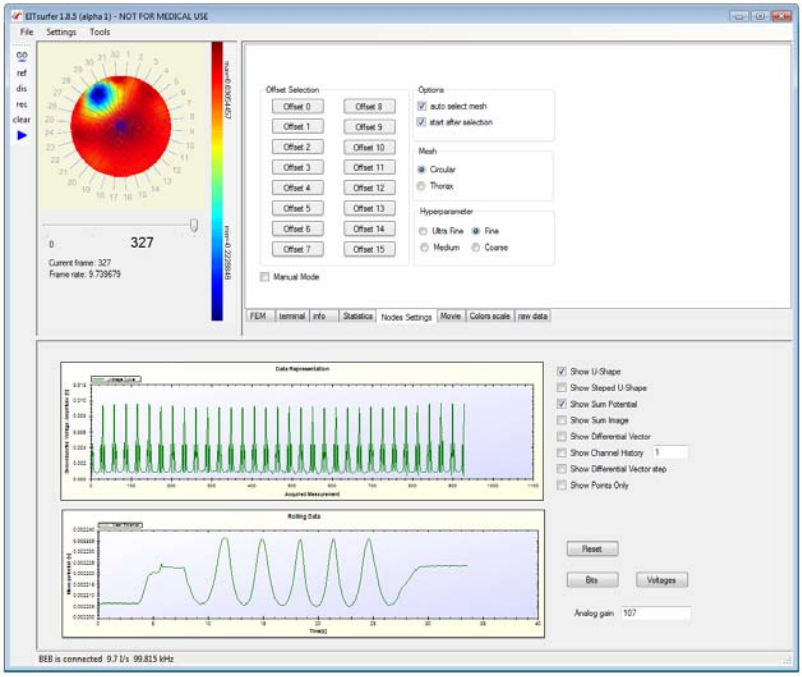

Figure 5.5: Screen shot of the EITSurfer program.

run an EIT system. EITSurfer 1.8.5 version is based on the WinForms[9] and XNA[10] libraries for the Windows and 3D display, respectively. This choice is independent of the core library (EITSurf) implementation.

In a future development, one could still use the EITSurf library, while implementing a new GUI based for instance on the new graphic framework WPF[11]. This future development may be necessary because the XNA library is limited to 32-bit Windows system. Microsoft has not yet ported XNA to 64-bit Windows platform.

5.4.1 Data flow

The data are acquired in an asynchronous manner over an Ethernet socket linked to the port 10001 (see figure 5.6). The term asynchronous means that the software only executes the received data function when there are data

[9] The WinForms API is a part of .NET
[10] http://create.msdn.com
[11] Windows Presentation Foundation: http://windowsclient.net/

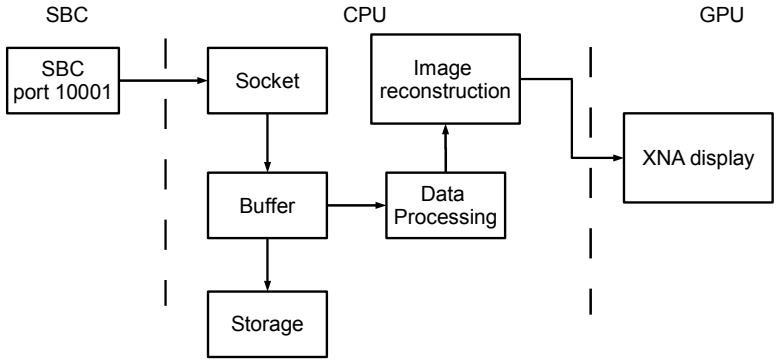

Figure 5.6: Illustration of the data flowing from the SBC to the GPU.

coming, and is not waiting for data. Continuously waiting for data would completely freeze the GUI. In other words, a separate program thread is opened to handle the communication socket. Incoming data are then provisionally stored into a first buffer containing a list of individual bytes. This buffer is then read in such manner that the individual bytes can be assembled to form 32-bit integers. The 32-bit integers themselves are then further assembled to form a complete data set (an image). This data set is then stored in the memory for further use. At the same time, a copy of the last complete incoming data set is sent to the data processing unit which shapes the data set to send it to the image reconstruction unit. The image reconstruction unit multiplies the data set with the reconstruction matrix to produce the image values to be transmitted to the graphic card.

5.4.2 Image reconstruction

The image reconstruction[12] is the process of creating an image based on the acquired data. This section presents in detail how the data are processed after leaving the buffer in figure 5.6. The c data vector is not usable as is; it needs to be shaped. The shaping step removes the undesired measurements from the data frame. Undesired measurements are measurements taken with electrodes that do not make contact correctly or measurements done using one or both injecting electrodes. In the last case, these measurements are discarded because they do not respect the four-point measurement scheme.

[12] One may argue that this is in fact a construction and not a reconstruction, but the term reconstruction seems to be much more intuitive.

This prevents the introduction of undesired artifacts in the image. [13]Moreover the present hardware version of the analog front end does not allows dynamic gain adjustment. This implies that measurements taken with the injecting pair are often saturated after the amplification stages and therefore unusable.

After the shaping step, it is necessary to calculate the demodulated amplitude of each measurement by calculating $\sqrt{I^2 + Q^2}$. At this stage normalization is also possible (for example to obtain Volts). Preferably, these two operations are done in the same program loop (iterating over the number of data) to speedup the execution (i.e. complexity of n instead of 2n). Alternatively the phase of the measured signal with the local reference can be calculated (see section 4.3.3).

The next step consists in calculating the differential vector by taking the difference between the incoming data vector (c*) and the stored reference data vector (r). There are many ways for creating a reference data set, in EITSurfer only the most trivial one is implemented: the r vector is a stored copy of a c* vector taken at a given time. The user indicates to the program when to take the reference (i.e click on the "ref" button of the toolbar or press ctrl+r).

Calculating the difference between the incoming vector c* and the reference vector can also be done in two ways: 1) simply subtracting one with the other ($c^*[i] - r[i]$ for all i) or 2) subtracting one with the other and normalizing with the average ($(c^*[i] - r[i]) / \frac{c^*[i]+r[i]}{2}$ for all i). The last case is the data processing option by default in EITSurfer. The reconstruction matrix library have also been generated for this case. To deactivate the difference normalization go to: tab "FEM" -> unchecked "normalize difference".

After this operation, the differential vector d is multiplied with the user selected reconstruction matrix. The resulting vector contains the values to apply at each node of the FEM model. This multiplication is implemented using C# "unsafe" environment, which enables the use of pointers within a managed code. Additionally the new parallel.for[14] command is also used to speed-up the execution by taking advantage of all CPU-cores available on the computer. At this point, it is necessary to map the calculated value on a certain color map. In EITSurfer, there are several color maps to choose, the default value corresponds to the Matlab Jet color map. Then each calculated

[13]In case the 4-points measurement scheme is not respected, the measurements taken on the injecting electrodes will strongly depend of contact impedance. This is the current that flows through the contact impedance that creates unpredictable measurement and eventually artifacts.

[14]This instruction (since .net4.0 or the system.threading.dll technical preview of June 2008) is the same as the usual for loop but the iterations are executed simultaneously on all CPU-core.

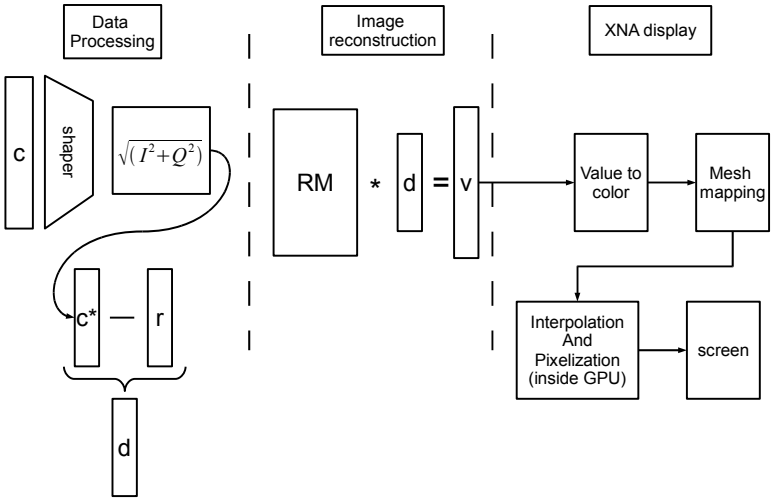

Figure 5.7: Detailed data processing inside EITSurfer.

color can be attributed to the corresponding vertices on the XNA 3D mesh. At this stage the mesh is processed by the graphic card to interpolate the colors between the vertices. This is a very computationally intensive operation but a graphic card's specialized hardware circuits enable rapid parallel computation of the image. At the end of this process chain the graphic card delivers a pixel based image onto the screen, this is what the user looks at. This architecture enables one to distribute the computing charge between the CPU and the GPU.

If the computer hardware is at times not powerful enough to display all the images (sufficiently fast refresh of the screen), the image sequence may appear "jerky". In fact, the program has been instructed to favor the storage of the incoming data into the memory, meaning that the real-time screen update has a lower priority. In this way high frame rate data flow can be properly recorded without the need to display every single image, which may lead the program to crash due to lack of resources. To save resources the other graphical elements of the EITSurfer window are also only refreshed once the program enters idle mode (i.e. when there are no other operations to execute).

5.4.3 Display of the EIT image

The display of the FEM mesh is one of the key components of the GUI. The basic idea is to use to our advantage the mesh coding convention of the 3D graphic card, which is similar to the mesh used for FEM models. In this way it is relatively straightforward to map the 2D FEM mesh used by the EIT reconstruction software (in this case EIDORS) into the graphic card. This integration is done by using a Microsoft technology called XNA[15], which is a managed framework for directX that can be implemented into the WinForms framework[16]. The main benefit of this architecture is to share the computational load between the CPU and the GPU. In this way the GPU takes care of the interpolation and pixelization of the image, which are very computation intensive and resource demanding operations.

5.4.4 Data visualization

This section presents a brief overview of the data analysis and data display strategy used by EITSurfer. The obvious way to analyze EIT data is to calculate an image as explained in section 5.4.2. Yet other alternative ways to analyze EIT data graphically are possible. The four analysis tools implemented in EITSurfer are:

- the u-shape graph,
- the step u-shape graph,
- the composite EIT signal,
- the differential signal.

The u-shape graph is the most classical way to represent data coming out of an EIT system. It simply consists of plotting the current data vector without the discarded measurements (c* in figure 5.7). Of course the obtained result entirely depends of the measurement strategy. A way to get measurement strategy independent graph is to reorganize the data to map a defined measurement strategy. An interesting way to reorganize the data consists in gathering the measurements having the same relative position with respect to the current injecting pair of electrodes. For example, supposing an adjacent

[15] a good tutorial on XNA mesh can be found in http://www.riemers.net, accessed on the 10.01.2011

[16] Microsoft instructions for doing so can be found in: http://create.msdn.com/en-US/education/catalog/sample/winforms_series_1, accessed on the 10.01.2011

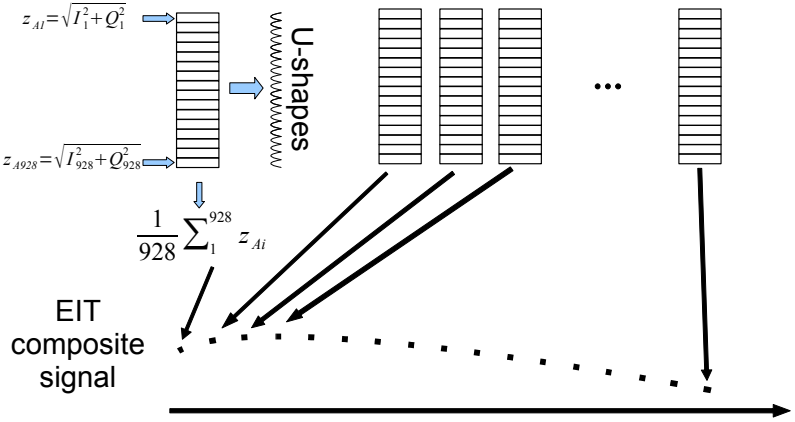

Figure 5.8: Calculation of the EIT composite signal.

measurement strategy, the measurement [1-2, 3-4] (see section B.1.5 for notation) will be associated with [2-3 , 4-5], [3-4 , 5-6], ... This newly formed set of measurements gathers all measurements taken just after the injecting pair. Then the measurements taken after the measuring pair plus one are gathered (i.e {[1-2, 4-5], [2-3, 5-6],...,[31-32, 2-3]}). By iterating this procedure for all measurements, one gets a u-shape with 32 steps of 32 data points each. Theoretically, a perfectly symmetric medium, such as a cylindrical tank, would give perfectly flat steps.

The EIT composite signal is a way to look at the temporal variation of the EIT signal. For each data set c* each individual measurement is summed together (see figure 5.8). The resulting value constitutes one point of the EIT composite signal. The next point is obtained by summing all the data of the next acquired measurement data set c*. If such a point is calculated and displayed each time a new measurement vector c* is available, one obtains a graph representing the average variation of the voltage measurements around the medium of interest. Optionally a normalization factor can be applied to the result of the sum, for example normalizing with the number of samples and/or scaling the value to real potential given in Volts.

The differential signal (d in figure 5.7) is the signal multiplied with the reconstruction matrix to calculate the image. Clearly, it is interesting to monitor what happens to the data just before the reconstruction. Again there are two ways of plotting the data: 1) one can simply plot the vector d as is or 2) reorganize the data in the same manner as for the step u-shape.

Chapter 6

Practical Tests and Experimental Results

6.1 Introduction

This chapter describes the testing of the developed EIT system. In section 6.3, basic tests are carried out on the electronic circuits only. Then in section 6.4, resistor and saline phantoms are used to assess the performance of the electronics when measuring well defined objects. The overall goal of these tests is to assess and verify the correct functioning of the electronics and to measure the limitations of the current set-up. By means of jumper connectors, the developed analog front end allows to connect several test circuits directly on the PCB. Thus the test set-ups used in this chapter are already implemented on the front end PCB and do not require external circuits. The basic tests are organized as follow:

- section 6.3.1: measures the gain characteristic of the acquisition chain,
- section 6.3.2: measures the noise performances of the acquisition chain,
- section 6.3.3: measures the behavior of the DAC,
- section 6.3.4: measures the voltage to current characteristic and the internal impedance of the current source,
- section 6.3.5: measures the noise generated by the current source.

In section 6.4, saline phantoms are used to test the EIT system. Saline phantoms are de facto the standard means to test EIT systems. These tests are organized as follow:

- section 6.4.1: measures the noise component of the EIT signal,
- section 6.4.2 : measures the z-score obtained with the macro-EIT system and compares the results obtained with the theoretical calculation of section 3.3.5.2,
- section 6.4.3: measures in a qualitative manner the correlation effect theoretically calculated in section 3.3.7.

Qualitative tests and proof of concept measurements are described in the next chapter. Thus readers who are not familiar with EIT may want to read chapter 7 first to get a more intuitive insight into the system performances.

6.2 Test tools

This section lists the tools and instruments used for the tests presented in this chapter:

- oscilloscope: LeCroy, WaveRunner 204MXi (LCRY0611M17051),
- 100 MHz differential probe: TESTEC, TT-SI 9101,
- resistor decade box: Lutron, RBOX-408,
- circular resistor phantom: CSEM, circular resistor phantom 1,
- saline tank: CSEM, 3DEITPh000001.

The version of the tested circuits and programs are:

- front end: 2.1,
- FPGA: 0.6,
- active electrodes: 2.6B_2,
- active electrode firmware: 4.1.

6.3 Basic tests

6.3.1 Normalization and gain factors

The tests presented in this section are designed to calibrate the system analog and digital gains in order to be able to display the measured potentials in Volts. The first step of the calibration process is to measure the behavior of the voltage generator as a function of the frequency and amplitude settings.

The set-up used for the measurement is depicted in figure 6.1. The idea was to work only with the signal generator (i.e. DAC and Amplifier) directly looped back into the acquisition chain. In order to avoid saturation of the signal in the acquisition chain, the input signal is attenuated using a resistor bridge. The measurements are recorded at two points:

1. directly at the output of the generator after the amplifier ($\times 11$), labeled TP1 on figure 6.1 using an oscilloscope,
2. the demodulated amplitude values coming out of the demodulator are recorded as well.

The oscilloscope is able to directly process the incoming signal, average it, and calculate the peak-peak amplitude. The results of the measurements are depicted in figure 6.2 for various amplitude and frequency settings. Then knowing the attenuation factor of the resistive bridge (11 in this case), it is possible to calculate the amplitude of the signal at the acquisition chain input A1. The known input values are then used together with the measured demodulated amplitude value to calculate the gain frequency characteristic of the system.

In order to successfully convert the demodulated amplitude values in Volts, one needs to calculate the mathematical relationship between the I and Q value and the ADC values. Fortunately, the FPGA does some of the converting work for us. The digital process chain assumes that the incoming digital data flow from the ADC ranges from +1 V to -1 V with a 12-bit precision. The latter is internally represented as a number between -1 and +1. Additionally one knows that the output values of the demodulator (I and Q) are stored in a fixed-point format defined by the user (see section 5.3.3). Thus the only conversion required is to calculate the defined fixed-point format from the raw 32-bit I and Q values. For this operation the received 32-bit integer (I or Q) is divided by the decimal part of the fixed-point format. For example, if the format is sQ15.17, one divides by 2^{17}. In this way the 32-bit integer is cast into a floating-point variable (double):

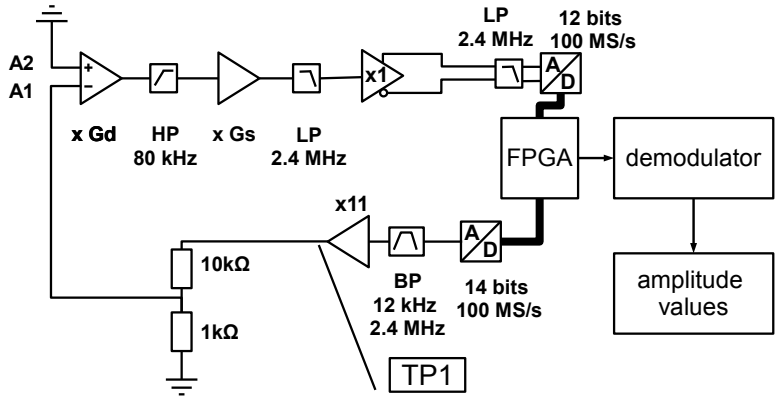

Figure 6.1: The measurement set-up used to characterize the analog and digital gain of the electrode circuit.

$$\begin{aligned} I &= (\text{double})\ \frac{I^{\#}}{2^{F_{\text{pos}}}} \\ Q &= (\text{double})\ \frac{Q^{\#}}{2^{F_{\text{pos}}}} \end{aligned} \tag{6.1}$$

where

F_{pos} is the number of fixed bits representing the floating part (see section 5.3.3),

$\#$ denotes the raw 32-bit integer transmitted by the FPGA.

Then one can calculate the voltage read by the ADC V_{ADC} (in amplitude) using the equations 6.1 and 4.14:

$$V_{\text{ADC}} = \frac{2\sqrt{I^2 + Q^2}}{N_{\text{ADC}} A_{\text{ref}}} \tag{6.2}$$

where

N_{ADC} is the number of ADC samples accumulated in a single I or Q,

A_{ref} is the amplitude of the signal used to demodulate the incoming signal, in this case $A_{\text{ref}} = 1$.

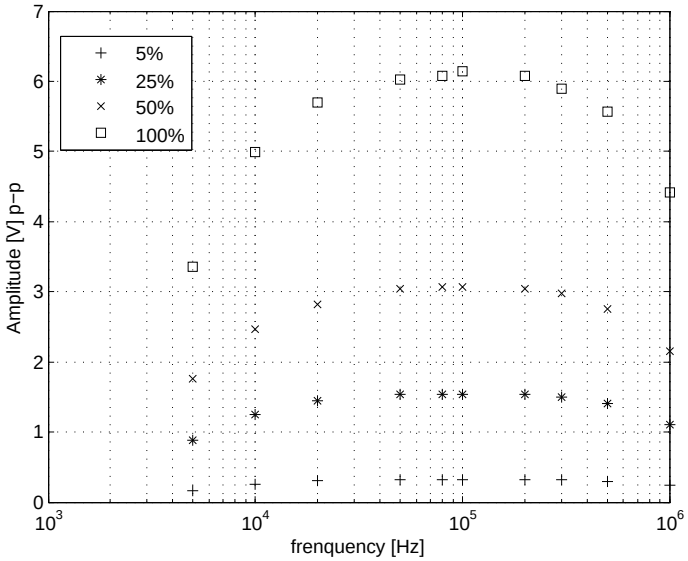

Figure 6.2: The output of the signal generator in function of the frequency and amplitude settings. The amplitude settings are given in percent of the maximum of the DAC output. It corresponds to the parameters the user needs to set in EITSurfer. The data of the plots have been measured at test point TP1 depicted in figure 6.1.

Subsequently, V_{ADC} can be multiplied by a factor 2 to get a peak-to-peak value. At this point, we are able to calculate the gain of the system by comparing the data shown in figure 6.2 with the demodulated amplitude value recorded at the same time, which gives the calibration curve depicted in figure 6.3. Normalized gain is to be understood as gain per unit of set analog gain. The set analog gain is the gain set by the SMD resistor on the front end PCB. For example, if the analog gain is set to 100 the overall process gain at 200 kHz is $0.55 \cdot 100 = 55$. So the approach is to calculate a calibration curve, which gives a correction factor between the set analog gain and the true system gain. . The EITSurfer program uses a linearly interpolated model of the calibration curve (continuous black line on figure 6.3), thus knowing the frequency and the set analog gain, the program can calculate the voltage amplitude in Volt at the input of the acquisition chain on A1.

The mismatch between the presumed gain and the true gain depends of many factors:

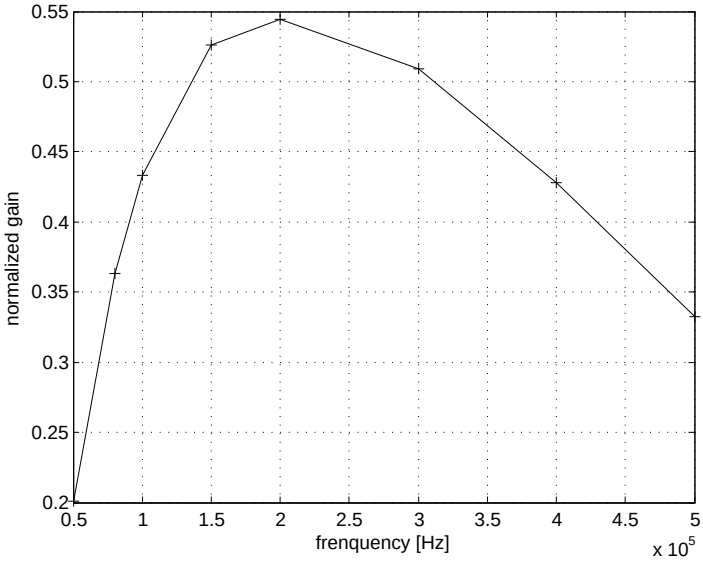

Figure 6.3: The normalized gain of the acquisition chain in function of the frequency. The continuous line represents the linear interpolated model used to calculate the analog gain of the acquisition chain in EITSurfer and in the Matlab toolbox ReadEIT (function EIT2volt).

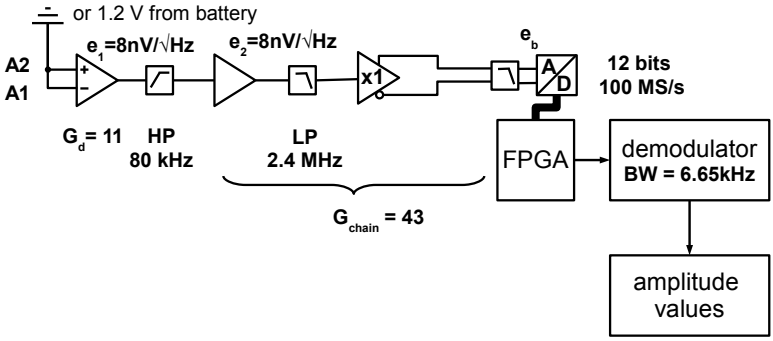

Figure 6.4: The set-up used for the measurement of the noise and the drift of the acquisition chain. The analog lines A1 and A2 are short-circuited and set to a stable voltage source such as the ground or a simple battery.

- the precision of the gain resistors,
- the temperature dependency of the gain,
- the stray capacitances,
- the demodulation process.

Therefore, an automatic calibration procedure should be implemented in future versions of the front end. In this way, the system could regularly check its calibration values against a stable reference.

6.3.2 Acquisition chain noise and drift

The aim of this section is to measure the noise and the drift baseline of the acquisition chain. The set-up used for this test is described in figure 6.4. In order to exclude all external influences, both analog lines A1 and A2 are short-circuited at the input of the differential instrument amplifier and set to a stable voltage, for example GND (0 V) or a battery (1.2 V). Then the analog gain is made high (473 in this case). In this way, the noise is also amplified by the same factor and it becomes possible to accurately measure it.

As already seen in section 4.3.3, the bandwidth of the whole acquisition chain is defined by the integration time (i.e. the length of the measurement window). In this case, we choose to measure 1024 points at 10 images/s, which gives a integration time of $t_i = 1/10/1024 = 100\,\mu s$. Using the half-width maximum

bandpass definition for the IQ demodulator, the bandwidth is given by:

$$BW_{IQ} = \frac{2}{3}\frac{1}{t_i} = 6.65\,\text{kHz} \tag{6.3}$$

The instrumentation amplifier manufactured by Analog Devices, AD8221, uses a noise model based on an input voltage noise spectral density of $8\,\text{nV}/\sqrt{\text{Hz}}$ and an output voltage noise spectral density of $75\,\text{nV}/\sqrt{\text{Hz}}$ [10]. Since in our case the source impedance is very small, it possible to neglect the input noise current contribution and directly use the formulas given in [2] for calculating the input voltage referred noise:

$$e_{\text{rti}} = \sqrt{e_{\text{ni}}^2 + \left(\frac{e_{\text{no}}}{G}\right)^2} \tag{6.4}$$

where

e_{ni} is the input voltage noise density $8\,\text{nV}/\sqrt{\text{Hz}}$,

e_{no} is the output voltage noise density $75\,\text{nV}/\sqrt{\text{Hz}}$,

e_{rti} is the input referred noise density,

G is the differential instrument amplifier gain set by the SMD resistor.

For example the input referred noise for an analog gain of 1 is $75\,\text{nV}/\sqrt{\text{Hz}}$ and falls to $11\,\text{nV}/\sqrt{\text{Hz}}$ for an analog gain of 10. The measurements are done using the set-up presented in figure 6.4. The noise density is calculated based on the standard deviation of the demodulated values, divided by the analog gain and the square root of the bandwidth:

$$e_{\text{rti}} = \frac{\sigma_{IQ}}{\sqrt{BW_{IQ}}}\frac{1}{G} \tag{6.5}$$

The values measured for the input referred noise density are $77\,\text{nV}/\sqrt{\text{Hz}}$ and $13\,\text{nV}/\sqrt{\text{Hz}}$ for gain 1 and 10, respectively. These results match well with the theoretical expectations. The consequence for the system designer is that the gain of the instrumentation amplifier should at least be 10 in order to avoid excessive noise at the output. Clearly, having a much greater gain factor does not significantly decrease the noise, which is limited by the input voltage noise source.

6.3.3 DAC behavior

6.3.3.1 DAC temperature drift

The Digital to Analog Converter (DAC) is the component that converts the digital sine signal into its analog counterpart. In other words, it generates the analog signal used to drive the current source, which itself is based on a voltage to current converter. Therefore an important parameter of the DAC, is its "gain drift", which, as one might expect, indicates the changes of the internal gain of the DAC due to variations in temperature. According to the DAC data sheet (DAC904 from Burr-Brown/TI [94]) the gain drift is 120 ppmFSR $°C^{-1}$ (in this case Full Scale Range (FSR) is 0.5 V). This means that the full-scale drift is about $60\,\mu V\,°C^{-1}$. In order to have an idea of the variations in temperature to expect, a Negative Temperature Coefficient (NTC) resistor (Epcos B57540G1103F005) has been used to sense the temperature directly on the DAC casing. The set-up is depicted in figure 6.5. This particular NTC resistor has a very small thermal mass that enables it to measure small and rapid variations in temperature. The temperature sensor is coupled to the DAC casing using a Heat Transfer Compound paste (Electrolube EHTCP20S). The experimental set-up makes use of the acquisition chain, characterized in the previous sections, to record the voltages coming out of the DAC.

In order to get rid of any parasitic gain factor and to be able to measure the voltage produced by the DAC, a gain calibration procedure is followed prior to beginning the measurements. An oscilloscope probe is attached to the DAC output (at TP1 on figure 6.5) and the demodulated amplitude gain is adjusted to match the probe values. In this way the processing gain of the acquisition chain is completely compensated.

In the first test situation, the set-up has been up and running continuously for at least 10 minutes prior any measurement. The measured signals were the temperature and the demodulated voltage amplitude. In this configuration peak-to-peak variations of 30 µV (see figure 6.6) are observed. For comparison purposes the peak-to-peak variations measured with short-circuited input was also measured. It was found to be only a few hundred nano volt (200 nV). Therefore the increase of the noise amplitude can only be attributed to the DAC.

During this experiment temperature variations of 0.5 °C are measured on the DAC casing, which corresponds to "gain drift" induced variations of $0.5\,°C \cdot 60\,\mu V\,°C^{-1} = 30\,\mu V$. Figure 6.6 shows that the experimental results confirm the previously established theoretical prediction about the noise. In this case, both curves shapes are not exactly matched, which is probably due

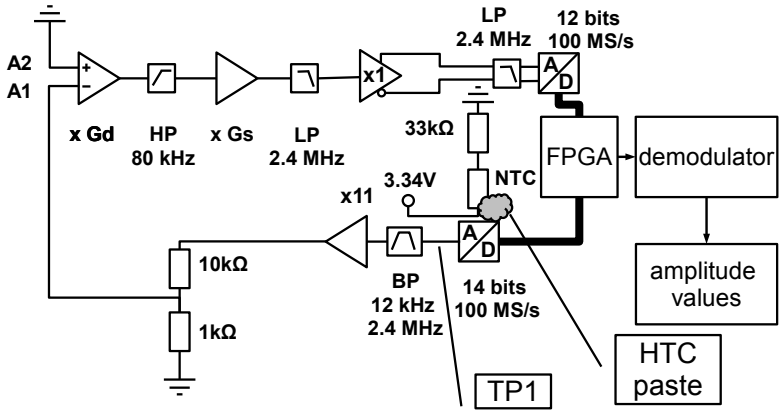

Figure 6.5: The set-up used to measure the temperature influences on the DAC gain.

to the thermal coupling mismatch between the real electronic temperature and the casing temperature. This is why we compare the size of the variations and not their shape. If one compares the drift or noise generated by the DAC (30 µV) and the noise generated by the acquisition chain, one observes that the latter is almost 10 times smaller. Therefore, the DAC appears to be one of the main contributor to the noise or drift of the current source.

In the second test situation, the signal generator was turned on and off [1]. The first observation is that when the DAC is turned on (EITSurfer "start" command sent) the temperature on the DAC casing increases by 2 °C within 10 seconds , which translates into 150 µV variation on the demodulated values, see figure 6.7. The temperature and the demodulated amplitude signal curve also exhibit similar characteristic shapes. This is the experimental evidence that the temperature of the DAC electronics strongly influences the measured output value.

6.3.3.2 DAC noise

Clearly, the noise produced by the DAC has an impact on the measurement carried out with the acquisition chain. This is why it is important to measure and understand its origin. Since the output of the DAC is essentially composed

[1] Not in the power up/down sense. For example turned on means the start working command was sent to the DAC.

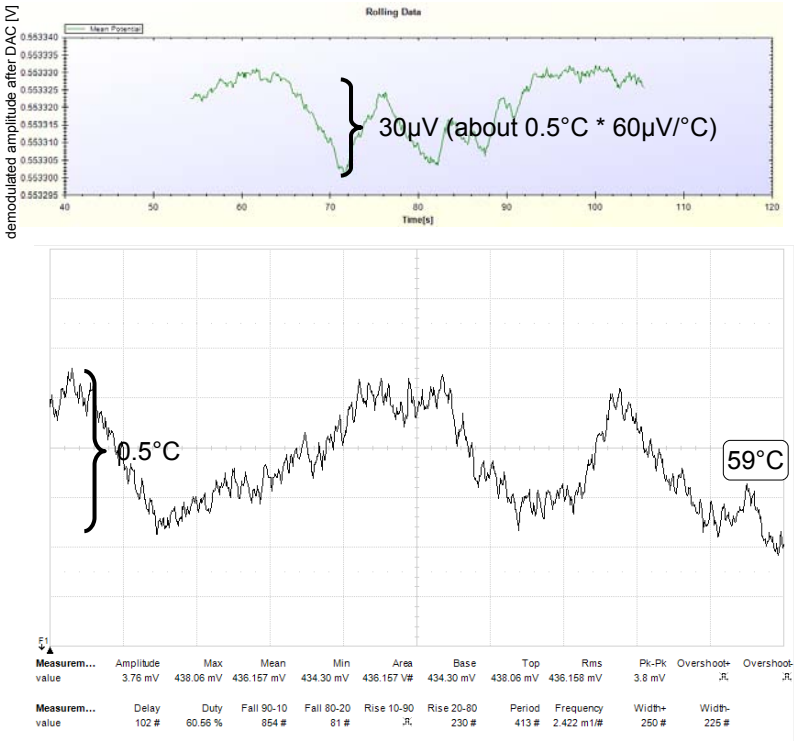

Figure 6.6: The variations in temperature and the demodulated DAC amplitude variation, in the situation when the system is running continuously. The upper figure is a screenshot taken from EITSurfer that plots the demodulated amplitude output directly after the DAC. The lower figure is a screenshot from the LeCroy Oscilloscope which recorded the temperature changes on the DAC casing. Thus the x-axis is the time scale with 5 seconds per division. Please note that both time scales do not exactly match.

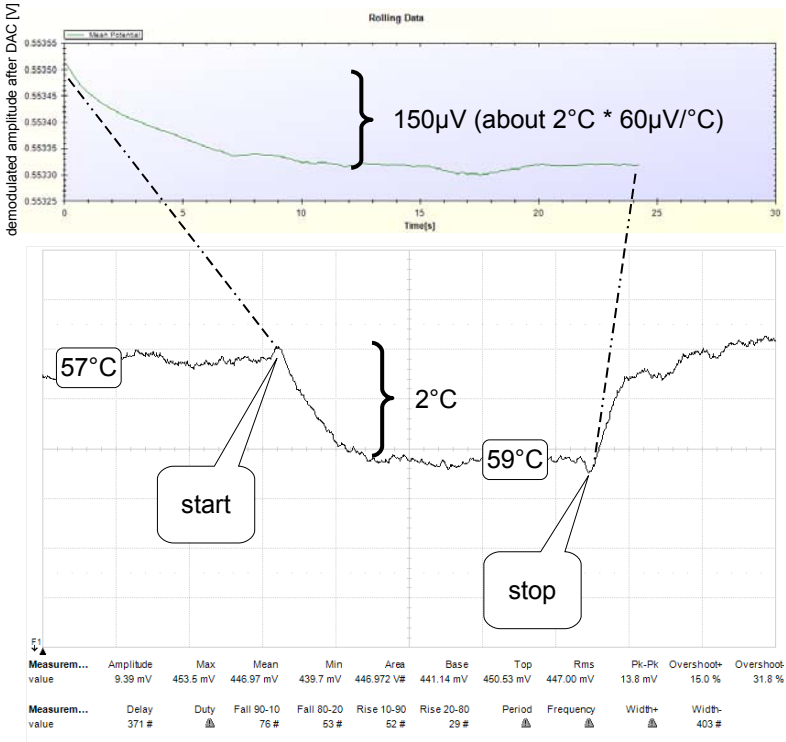

Figure 6.7: The variations in temperature and demodulated DAC amplitude variation, in the situation when the system is turned on / off (i.e. start /stop commands are sent from EITSurfer). The upper figure is a screenshot taken from EITSurfer that plots the demodulated amplitude output directly after the DAC. The lower figure is a screenshot from the LeCroy Oscilloscope which recorded the temperature changes on the DAC casing. Please note that both time scales do not match.

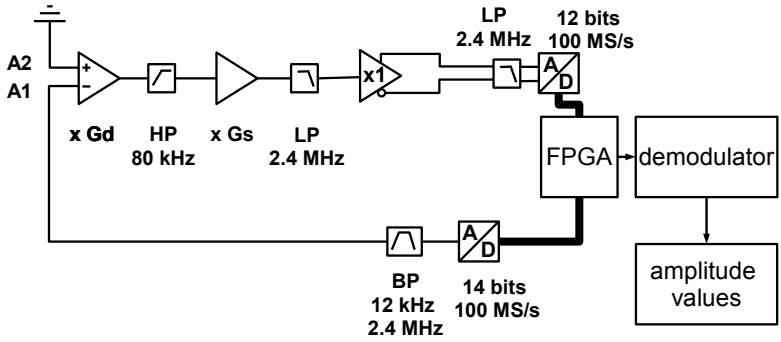

Figure 6.8: The set-up used to measure the DAC noise.

of MOS transistors, possible noise sources are the thermal noise and the flicker noise produced in the channel of the output transistor. Additionally, noise can be added by timing errors due to the reference clock and PLL[2] jitter [52]. The thermal noise is given in the data sheet of the DAC and is equal to $50\,\mathrm{pA}/\sqrt{\mathrm{Hz}}$, which corresponds to $1.25\,\mathrm{nV}/\sqrt{\mathrm{Hz}}$ voltage drop over a $25\,\Omega$ resistor.

The acquisition chain is directly used to measure the DAC output as shown in figure 6.8. For comparison purposes an acquisition chain noise baseline has also been measured with both input lines A1 and A2 short-circuited as shown in figure 6.4.

The data presented in figure 6.9 show a decrease of the noise density in function of the frequency. This behavior suggests that the noise produced at low frequency (<2 MHz) follows a $1/f^a$ noise rule. This conclusion is supported by the experimental evidence found in literature that the flicker noise is large for small transistors (i.e. high-speed transistors) [46]. Since the measured voltage noise density at 100 kHz is about $100\,\mathrm{nV}/\sqrt{\mathrm{Hz}}$ and the expected thermal noise density is $1.25\,\mathrm{nV}/\sqrt{\mathrm{Hz}}$, the main noise source is clearly not the thermal noise.

6.3.4 Current source characterization

In this section three different tests are carried out on the current source:

1. The current versus frequency in function of the amplitude of the command signal is measured (figure 6.11),

[2]Phase-Locked Loop

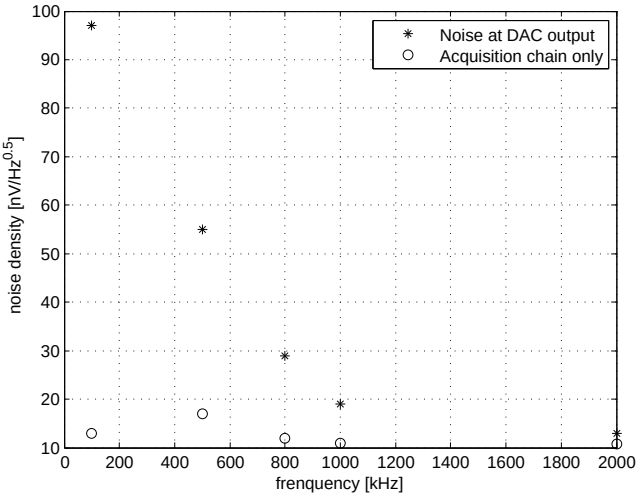

Figure 6.9: The noise measured at the DAC output, it also depicts for comparison purpose the acquisition chain noise floor.

2. The current versus output voltage in function of the frequency is measured (figure 6.12),

3. The current versus output voltage in function of the stray capacitance and the current source configuration in measured (figure 6.13).

For all measurements the same principle is used, one measures the current flowing through the load resistance; the voltage drop over a known and fixed resistor $R_M = 150\,\Omega$ is measured using a differential probe and an oscilloscope. It is important to measure the voltage drop over a fixed resistor to avoid accuracy issues linked to resistor properties, oscilloscope gain and differential probe tolerances.

The first test is to measure the frequency response of the current source in function of the amplitude of the command signal. The amplitude is given in percent of the maximally available command signal amplitude. As depicted in figure 6.11 the amplitude response is almost flat in the frequency range of interest (i.e. 100 to 300 kHz), which is desired.

The aim of the second test is to determine the internal impedance of the current source. The basic measurement principle is the same as in the first test but instead of using the symmetrical current source one uses the current source in grounded mode. In this way, one is able to characterize the current

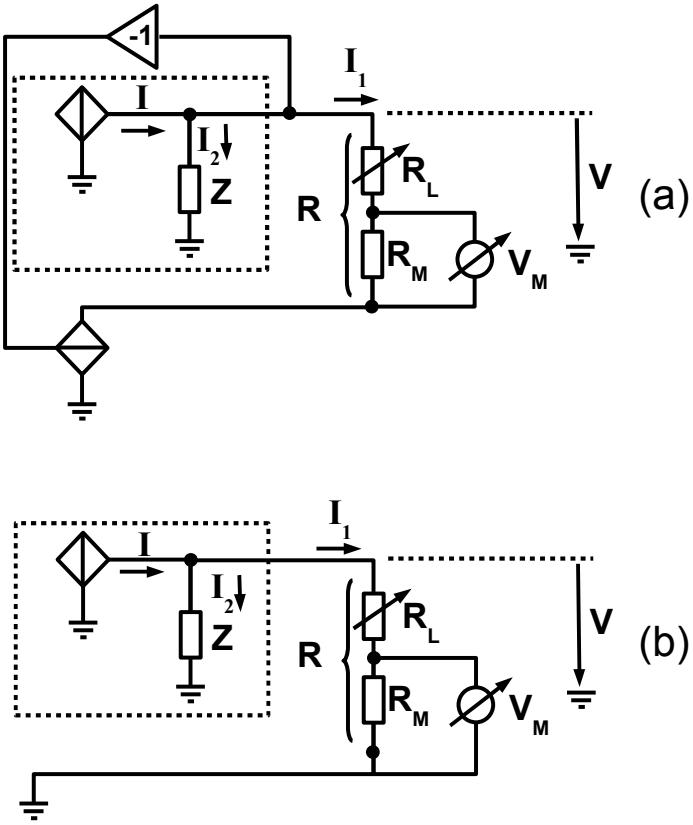

Figure 6.10: Experimental set-ups used to characterize the current source: in a) the symmetrical current source is composed of a real current source (inside the dotted square) and a commanded voltage source, in b) the grounded current source configuration is depicted.

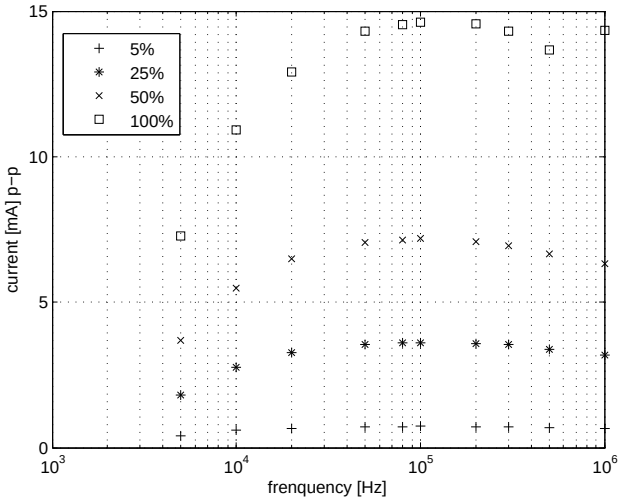

Figure 6.11: The amplitude response of the current source in function of the command signal frequency and amplitude (in percent of nominal = 5.7 V @ 100 kHz).

source alone. The load resistor R_L is varied from $0\,\Omega$ to $1150\,\Omega$ and the current I_1 and the voltage V are measured. Applying basic circuit theory to the circuit figure 6.10 b), one can calculate an expression for the internal impedance:

$$V = I_2 Z \tag{6.6}$$

Where $I_2 = I - I_1$; thus one can write:

$$V = (I + I_1)Z \tag{6.7}$$

which after algebraic manipulation becomes:

$$-\frac{V}{Z} + I = I_1 \tag{6.8}$$

where

V is the voltage drop as indicated in figure 6.10 [V],

R_M	is the fixed measurement resistor of 150 Ω,
R_L	is the variable load resistor [Ω],
I	is the current produced by the ideal current source [A],
I_1	is the current flowing trough the resistor R [A],
I_2	is the current flowing trough the internal impedance Z [A],
Z	is the internal impedance of the current source [Ω].

Equation 6.8 can be identified as a straight line equation of the type $ax+b=y$ where the slope is given by $a=-\frac{1}{Z}$. Therefore, using the experimental result presented in figure 6.12, it is possible to calculate the current source's internal impedance. The effect appears not to be linear, thus the idea is to fit the data with two straight lines, one for load resistances under 550 Ω (first 3 data points) and one for load resistances above 550 Ω. Then from these line equations one gets the slope value that corresponds to the internal impedance of the source. Table 6.1 presents the estimated value of the internal impedance from the data displayed in figure 6.12. From these internal impedance data, one can conclude that as far as the internal impedance of the current source is concerned the most favorable working frequency in this case is 50 kHz. As expected the lower the frequency the smaller is the effect of the stray capacitance. But even if on one side lower excitation frequency shows beneficial effects on the internal impedance performance, one should keep in mind that on the other side increasing the current frequency allows injecting more current into the body (i.e. up to 10 mA), and that it is also easier for the current to flow through the body and the electrode-body contact impedance. Moreover working with low excitation frequency also restrains the achievable frame rate, because at least one complete sine period is needed to correctly demodulate the signal amplitude. For example, working at 10 kHz means that the maximal frame rate would be 10 images per second[3], which is already fairly slow. Thus a tradeoff between the above mentioned parameters should be found; qualitatively and according to figure 6.12 an appropriate frequency range is certainly between 50 and 200 kHz. At this point, it is appropriate to mention that the Dräger Medical AG Pulmovista 500 EIT system current excitation frequency range according to the published data sheet [27], is extending from 80 to 130 kHz, which is probably not a coincidence.

In a third experiment one compares the differences between the symmetrical and the grounded current source in term of internal impedance as measured above. The measurements are done using both circuits depicted in figure 6.10.

[3]For a 32-electrode serial EIT system.

Table 6.1: The internal impedance measurement corresponding to the data depicted in figure 6.12. The data corresponding to the 50 kHz measurement are approximately aligned on an horizontal line whose slope is near zero, thus the numerical results are sensitive to measurement error. This is why the numerical values are given in parentheses. The negative internal impedance for the 100 kHz measurement is not a mistake and it can be consistently reproduced.

frequency [kHz]	internal impedance for $R \leq 550\ \Omega$ [kΩ]	internal impedance for $R > 550\ \Omega$ [kΩ]
50	(-1058)	(-2000)
100	-116	9
200	44	4
300	17	3
400	10	2

Two cases are considered: 1) the internal impedance, Z, equals the internal impedance of the current source and 2) Z equals 1 nF. In other words, in the second case a 1 nF capacitor is added in parallel to the current source to emulate the stray capacitance in the case the node belt is connected. As depicted in figure 6.13, one can observe that the internal impedance of the source is degraded for the symmetrical current source compared with the grounded current source. But if the stray capacitance of the current source is degraded by the transmission line and the switches, as it is the case once the electrode belt is connected and simulated here with a 1 nF capacitor in parallel with the current source, the symmetrical current source is able to deliver a much more stable current for an equivalent load resistor. This can be explained using the simplified stray capacitance model presented in figure 6.14. It can be seen that the voltage against ground potential, $V_{1,2}$, is divided by 2 in the symmetrical current source compared with the grounded current source; therefore the leakage current, $I_{11,12}$, is also reduced. In other words the developed symmetrical current source maximizes the current which flows through the load resistance.

Using the model of both the grounded current source (figure 6.14 (a)) and symmetrical current source (figure 6.14 (b)), one can calculate the current flowing trough the stray impedance Z_s for each case. The stray current for the grounded current source is:

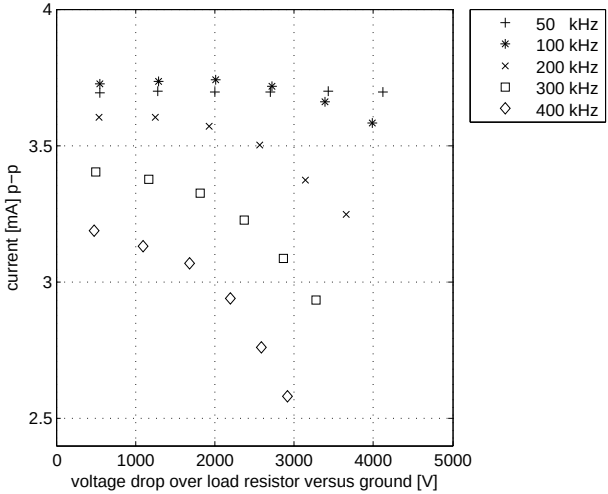

Figure 6.12: The output current versus output voltage diagram of the current source for various frequencies and load with a fixed current setting.

$$\frac{R}{Z_s + R} I = I_{11} \tag{6.9}$$

The stray current for the symmetrical current source is:

$$\frac{R}{2Z_S + R} I = I_{12} \tag{6.10}$$

Obviously I_{12} is smaller than I_{11}; thus the symmetrical current source behaves closer to an ideal current source.

6.3.5 Noise of the current source

As consequence of the findings of section 6.3.3.2 the noise generated by the DAC is also transferred to the current source itself. Therefore, it is possible to calculate the theoretical noise value at the current source output based on equation 4.1 with $\mathrm{R}_m = 390\,\Omega$:

$$97\,\mathrm{nV}/\sqrt{\mathrm{Hz}} \cdot \frac{11}{390\,\Omega} = 2.7\,\mathrm{nA}/\sqrt{\mathrm{Hz}} \tag{6.11}$$

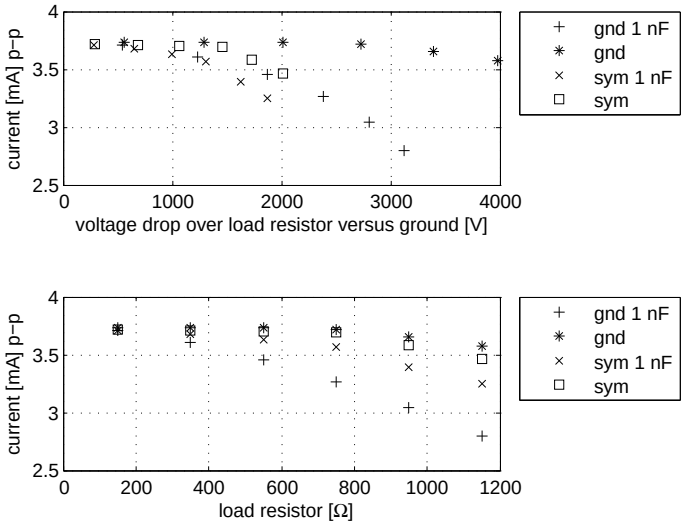

Figure 6.13: Comparison between symmetrical current source (sym) and grounded (gnd) current source for AC current at 100 kHz. In one case, denoted (1 nF), the stray capacitance of the current source is artificially increase to 1 nF by placing a 1 nF capacitor in parallel with the current source.

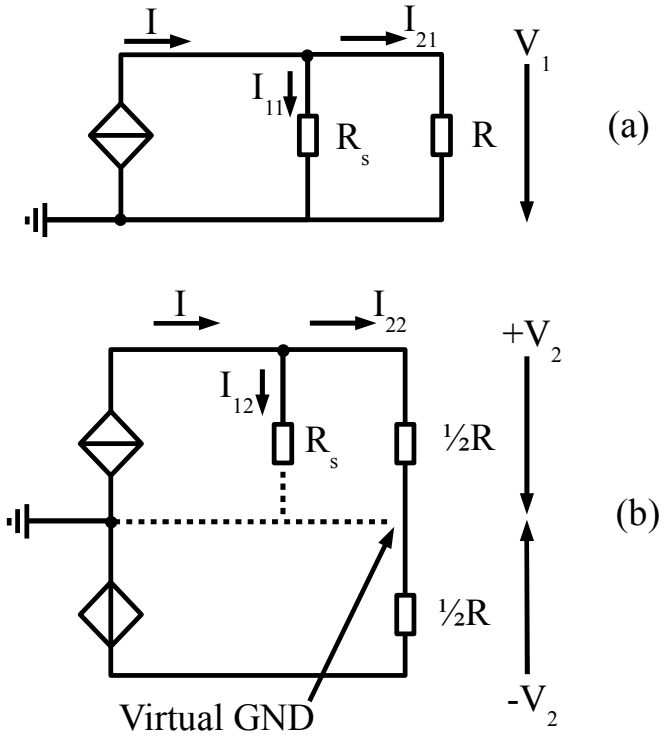

Figure 6.14: Stray capacitance model for a) the grounded current source and b) the symmetrical current source.

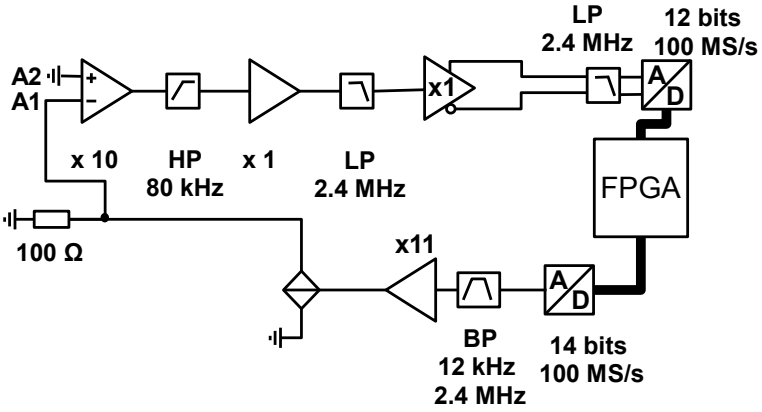

Figure 6.15: The experimental set-up used to characterize the noise of the current source.

Table 6.2: The noise results of the current source for the frequency range of interest.

frequency [kHz]	noise density [nA/$\sqrt{\text{Hz}}$]
100	2.65
200	2.05
300	1.7

Clearly the gain of the amplifier after the DAC also amplifies the current source noise, therefore a trade-off between the current amplitude to be injected and the acceptable noise level needs to be defined. The measurements are done using the set-up depicted in figure 6.15. The current source is used in grounded mode (i.e. without the symmetrical voltage source). The voltage drops over a fix 100 Ω resistor is acquired using the acquisition chain of the front end.

The measured values are presented in table 6.2. In the frequency range of interest, from 100 kHz to 300 kHz the measured noise values correlate well with the DAC voltage noise values depicted in figure 6.9. Thus it shows that the noise of the current source has its origin in the noise of the DAC. The current source circuit itself does not contribute much to the noise.

An obvious consequence of the experimental fact that the noise of the current

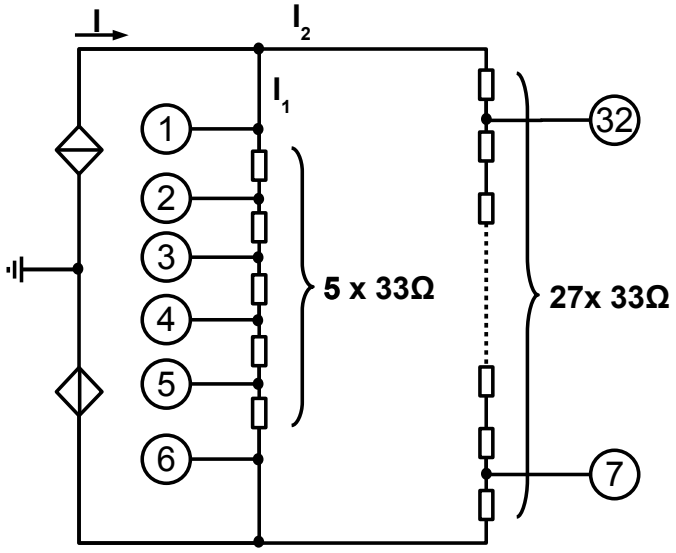

Figure 6.16: The circular resistive phantom used for assessing the noise distribution theory. The configuration of the current source depicts an offset 4 measurement strategy.

injected into the medium of interest is relatively large compared with the thermal noise of the medium, is that the current noise is one of the main source of noise of the EIT system. Thus the current source noise will impact the measurement quality. The measurement with the largest noise values will be the one close to the injection electrodes, where the current density is highest. This effect can be illustrated with a simple resistor network phantom (see figure 6.16). This phantom consists of a circular array of resistors (33 Ω) where an electrode is connected between all consecutive resistors. This set-up provides a simple and effective way to check the EIT system and to measure basic parameters, such as the noise in this case.

As predicted, figure 6.17 clearly shows that the noise values are separated according to the injection and the measurement pattern. In this case an offset 4 strategy has been used; therefore the voltage drop can take 6 different values. The highest peak corresponds to the measurements done with the electrode that sinks the current I_2 in figure 6.16. Whereas the rightmost peak corresponds to the voltage drop over the injecting electrodes (current I_1). The other four peaks correspond to intermediate measurements mixing the two

current flows I_1 and I_2, which are directly linked to the measurement strategy (i.e. an adjacent measurement strategy would only exhibit two peaks).

The width of the peaks corresponds to the noise, to current loss due to the stray capacitance of the system and to the CMRR of the differential amplifier. In order to highlight this phenomenon, the same measurements have been repeated with a grounded current source (i.e. the current is sunk by the system ground potential). In this configuration, one expects broader peaks, which is confirmed in figure 6.17. This can be explained by the fact that using a symmetrical current source mitigates the effect of the stray capacitance of the current source[4] and the effect of the CMRR.

With this simple experiment, two important lessons are learned:

1. The noise produced by the current source is distributed according to the current density distribution into the medium. Under particular conditions, such as in micro-EIT, where the current density is high, the noise amplitude per channel will exhibit the familiar U-shape.
2. The proposed symmetrical current source and inverting voltage source combination (i.e. symmetric current source) developed during the present thesis, allows more precise measurement by mitigating the effect of the current source stray capacitance (i.e. system precision) and the CMRR, but has almost no influence on the system accuracy (i.e. the noise).

6.4 Saline tank experiments

Saline tank experiments represent the classical way described in EIT literature to perform tests on EIT systems [5, 65]. For this thesis, we developed our own saline phantom made of a transparent acrylic cylinder of 900 mm in perimeter and 380 mm in height. The mechanical drawing[5] in figure 6.18 shows four planes of electrodes which are connectible on the user side with standard 4 mm laboratory "banana" connectors. On the electrode side, the threaded part of the connector is directly used as the electrode. The metal itself is coated with a gold layer to ensure optimal chemical stability in the aggressive saline medium.

On top of the tank, a rotation table can be placed. It is used to precisely position objects of known conductivity, size and shape inside the tank. Alternatively a Lego[6] based robot developed at CSEM can also be positioned on

[4] including also the bus lines
[5] The mechanical drawing and construction have been realized by Fuchs Engineering AG
[6] http://mindstorms.lego.com, 10.12.2010

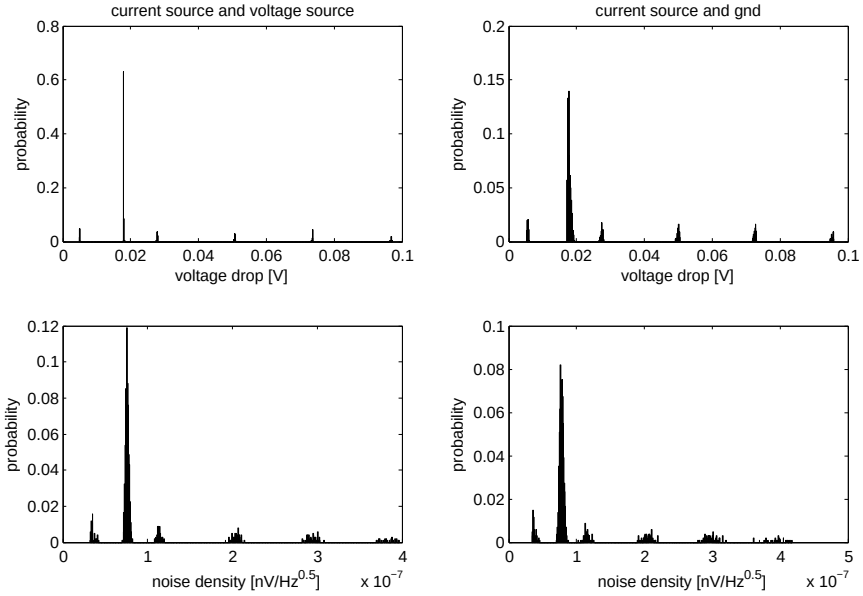

Figure 6.17: The histogram of the measurements done with the circular resistive phantom with an offset of 4. The upper figures plot the histogram of the signal, whereas the lower figures plot the histogram of the noise density. The data in the figures to the left have been recorded using the symmetrical current source, whereas the data to the right were recorded with a grounded current source.

top of the tank to control the position of two separate and movable objects. A first use of this robot for the performance assessment of EIT system has been reported in [61, 7]. In this work, the use of the robot is not necessary and all the experiments are done using the rotation table.

6.4.1 Signal stability and noise

The signal instabilities can be categorized in two categories: the slow (larger than seconds) variations and the short (shorter than seconds) term noise contributions. For the first category, it has already been shown in section 6.3.3.1 that the temperature plays an important role at the signal generation stage. For example, it is required to let the system warmup for at least 10 minutes in a temperature stable environment before it is used. This kind of instability needs to be addressed as drift and not as random noise. For instance, in a future system a compensation mechanism based on the continuous monitoring of the current source can be implemented; it could directly measure the current source output and apply adjustements to the reconstruction algorithm to correct the image accordingly.

Since long term system drift could only be addressed using a new hardware, in the remainder of this section the aim is to explore the experimental aspect of the short (< 1 s) term variations of the signal. In the first part of this chapter, we found experimental evidence that the noise of the developed EIT system is caused by the electronic noise of the acquisition chain, the thermal noise of the medium and only a fraction of the noise is generated by the current source.

Besides that, additional noise can be generated due to the EIT system architecture and the active electrode multiplexing mechanism. As a first step, this type of phenomenon will be studied, in order to minimize their contributions to the other tests.

6.4.1.1 Multiplexing noise

The developed EIT system is completely serial, in other words, only one single measurement using a pair of active electrodes is performed at the same time. The instrumentation amplifier, which determines the analog difference between both analog lines, needs a certain time before the signal at its output meets the stability requirements and is ready for use . According to the data sheet [10] a 10 V step is stabilized after 13 µs within 0.001% of precision. Since during the transition states between two measurements the output of the AD8221 can reach its power supply rails (± 5 V), it is judicious to demand that

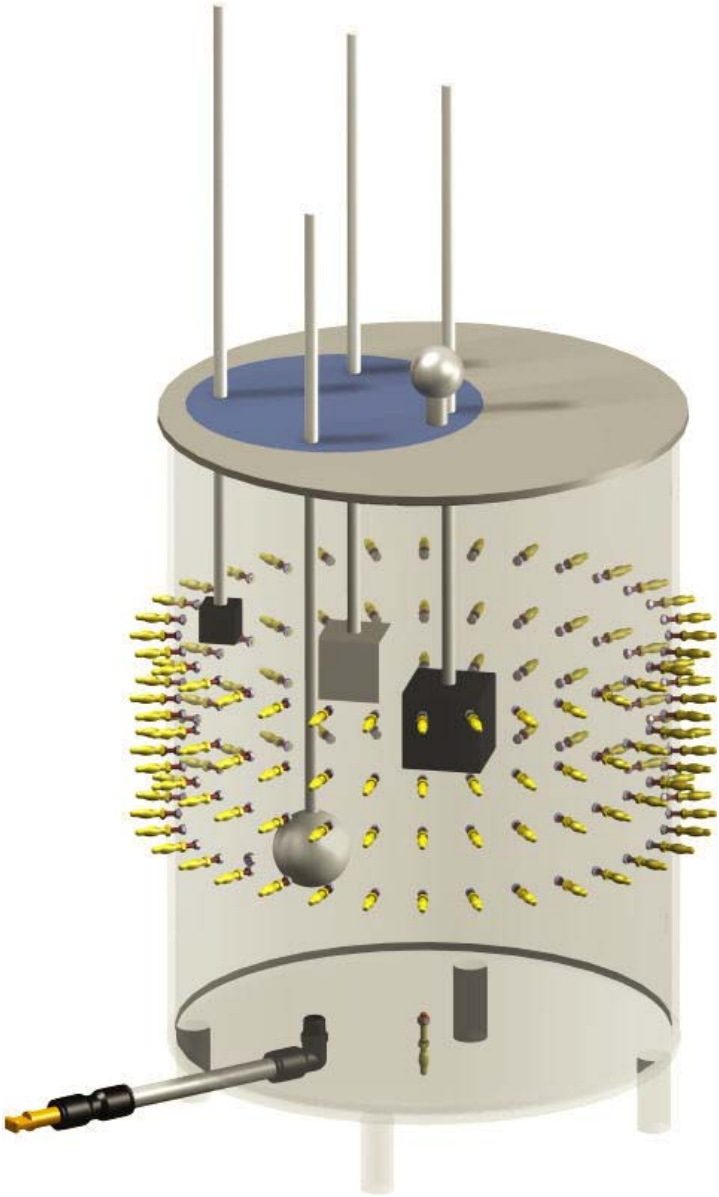

Figure 6.18: The technical drawing of the acrylic tank with the rotation table used as object holder. (courtesy: Fuchs Engineering AG)

the system should wait for about 15 to 20 µs before demodulating the signal. The exact value and state of the input and output of the instrumentation amplifier during the transition phase is not controlled; this is why the settling time varies so much from one measurement to another.

Clearly, there are some techniques that can be used in future systems to ensure cleaner transitions. For instance, both analog lines could be short-circuited during transitions; it should provide the system with a much more stable settling time. Indeed for differential imaging, it is only important to stabilize the transition time to get a better system accuracy.

The strategy used in the developed prototype to mitigate the transition time dependencies of the measurements is to wait for a constant amount of time at the beginning of each measurement window. This waiting time allows the signal to stabilize. The digital IQ-demodulator can skip integer numbers of signal periods before starting to demodulate the incoming signal. The idea of this approach is to measure the best trade-off between the skip time and the measurement time. The measurement window length is given by the number of measurements per frame (image) and the image rate. From signal processing theory, it is known that one should maximize the integration time of the signal in the demodulator to reach the best signal to noise ratio. But one also knows that if one does not wait until the signal is stabilized before demodulation begins, one will introduce a large amount of multiplexing noise into the demodulated values. In order to measure the best trade-off between skip window length and demodulation window length for the developed EIT system, one can design a simple experimental set-up composed of the 32 active electrodes system placed around the saline phantom without any object inside. The data are recorded for various image rates and skip times, then for each parameters combination, the noise content is assessed and reported on a graph. Since each channel has potentially its own noise value, a way to assess the noise of one data frame is to sum the power of the noise and normalize[7] by the number of measurements (i.e. number of channels):

$$\sqrt{\frac{1}{N_{\text{ch}}}\sum_{i=1}^{N_{\text{ch}}}\sigma_i^2} = \sigma_{\text{frame}} \tag{6.12}$$

where

N_{ch} is the number of channels,

σ_i is the noise of the i-th channel,

[7] One is looking for a single value representing the noise content of every channel.

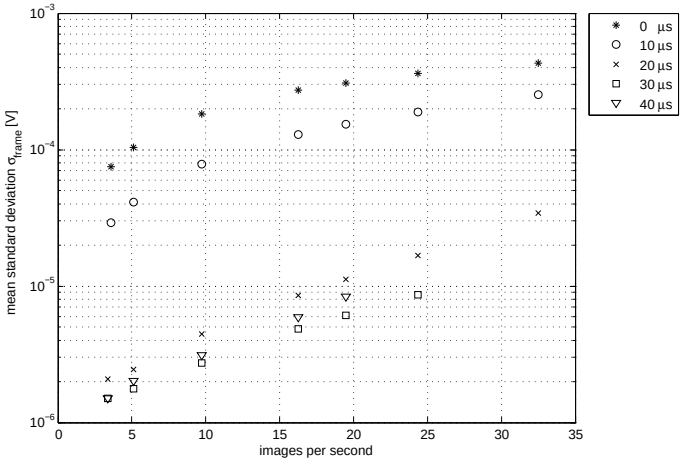

Figure 6.19: The effect of the skipped time (in µs) on the frame noise has been studied in function of the frame rate. The working frequency for these measurements was 100 kHz.

σ_{frame} is the mean noise for the whole measurement frame (frame noise).

In figure 6.19, one can observe that for a skip time of 30 µs the frame noise is minimal among all tested frame rate. Clearly, this value is a compromise between the integration time (demodulation window) and the available measurement window length. In this particular case waiting 40 µs before demodulating the signal exhibits worse noise performance than the "skip 30 µs" strategy. Waiting only 20 µs is suboptimal in terms of noise performance, but enables to reach much higher frame rates (i.e. at least one complete sine period is necessary to demodulate the signal correctly).

6.4.1.2 Current source generated noise

As already observed in section 6.3.5 the current source contributes to the noise observed in the medium; this effect can be highlighted my measuring the frame noise (see equation 6.12) in function of the distance between the injecting electrodes (i.e. by varying the offset). Since a larger offset means a larger impedance between the two injecting electrodes the influence of the noise generated by the current source on the measuring electrode pair is potentially larger. Figure 6.20 depicts the experimental result obtained at 100 kHz and

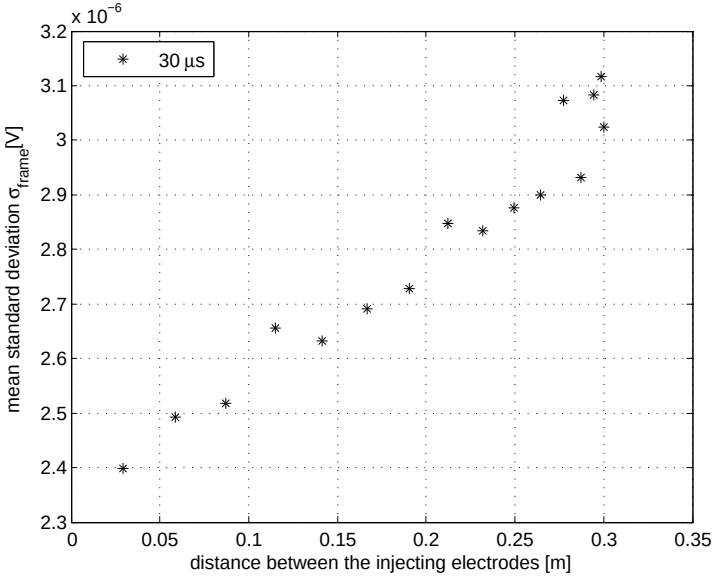

Figure 6.20: The frame noise in function of the offset (here converted in distance between the injecting pair). These measurements have been recorded with a skip time of 30 µs.

using a skip time of 30 µs. An almost linear increase in the frame noise amplitude is observed in function of the distance between the injecting electrodes. Interestingly, slightly larger noise values appear for offsets corresponding to electrode spacings 2, 4, 8, 12, 14 and 15[8].

6.4.2 Signal strength and z-score

The aim of this section is to measure the signal strength as calculated in section 3.3.5.2 using the real acrylic phantom. The test objects are positioned inside the tank using the rotation table depicted in figure 6.18. For every tests the same data acquisition protocol has been followed:

- Before starting the measurement series the saline tank has been thoroughly cleaned using commercially available cleaning agent containing

[8]This could be an effect related to the symmetry of the system but, it has not been further investigated.

sulfamic acid[9]. This product cleans the electrode surface and removes the calcareous deposit.

- The tank is carefully rinsed to eliminated all the cleaning agent residue.
- The tank is filled with a saline solution with an ionic concentration of 9 g per liter, which corresponds to the 0.9 %[10] physiological solution.
- Before starting the experiments one waits at least 12 hours for the water to reach room temperature and for the salt to diffuse uniformly.
- If the EIT system is startedup (cool start-up), a warm-up time of 10 minutes is necessary to ensure proper signal stability (temperature drift). In this way, the electronics has time to reach its working temperature.
- Each measurement sequence follows the same experimental protocol:
  - F frames: transition (discarded in the measurement evaluation),
  - F frames: first measurement (with object),
  - F frames: transition (discarded),
  - ...continues according to the same pattern until the last measurement,
  - F frame: last measurement,
  - F frame: transition (discarded),
  - F frame: homogenous tank (without object).

For the measurements in this section F=100, thus it possible to average the results over 100 measurements, which mitigates the short term variations of the signal. The following situations have been measured on the real tank and compared with the EIDORS simulation result:

- signal strength in function of the object position and offset,
- signal strength in function of the object conductivity and position,
- signal strength in function of the object size.

Since the tank geometry is symmetrical in the horizontal plane, it is possible to use the rotation table to place objects at various distances from the tank center. By recording the angle set on the rotation table, simple geometrical calculation gives the distance between the object geometrical center and the tank center.

[9] Cillit Bang Grime & Lime, bare code: 4002448017684
[10] volume / mass ratio

6.4.2.1 Signal strength and offset

The signal strength in function of the measurement strategy and object position is studied. The object was a non-conductive[11] sphere of radius 2.25 cm. The object is placed at different positions from the center of the tank to near the border by rotating the object holder. The object is placed in the same plane as the electrodes. The obtained measurements are also compared with the EIDORS simulation results in figure 6.21. The simulation and measurements are in good agreement for an object near the center. On the other hand, when the object is closer to the border the simulated signal strength appears weaker than in the measurements; this could be caused by numerical artifacts or non-linear effects not taken into account in the simulations.

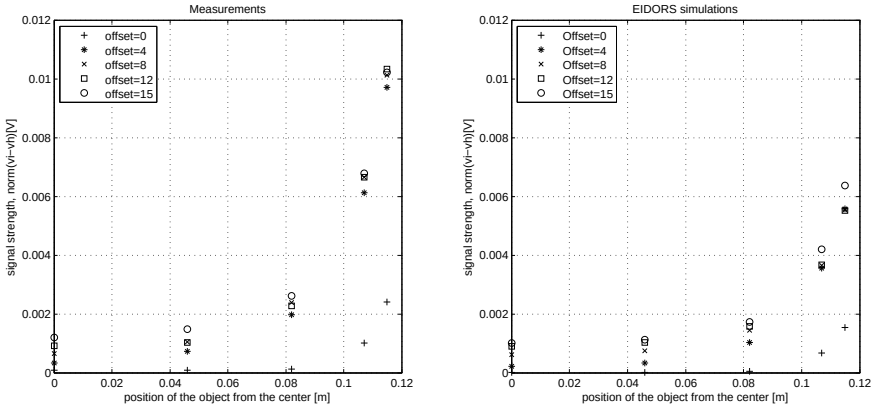

Figure 6.21: The signal strength measured (on the left hand-side) and the same situation simulated in EIDORS (on the right hand-side).

6.4.2.2 Signal strength and conductivity

The goal of this test was to experimentally support the finding of section 3.3.5.2, which was that the signal strength is not the same for conductive and non-conductive objects of the same geometrical shape and placed at the same positions. A similar experiment as described in section 6.4.2.1 is done, once with a non-conductive object and then with a conductive object. The figure 6.22 confirms the theoretical result of the existence of such a difference. Conductive objects produce about 2 to 3 times more signal than their non-conductive counter-parts sharing the same geometrical size.

[11] made of Polyoxymethylene (POM)

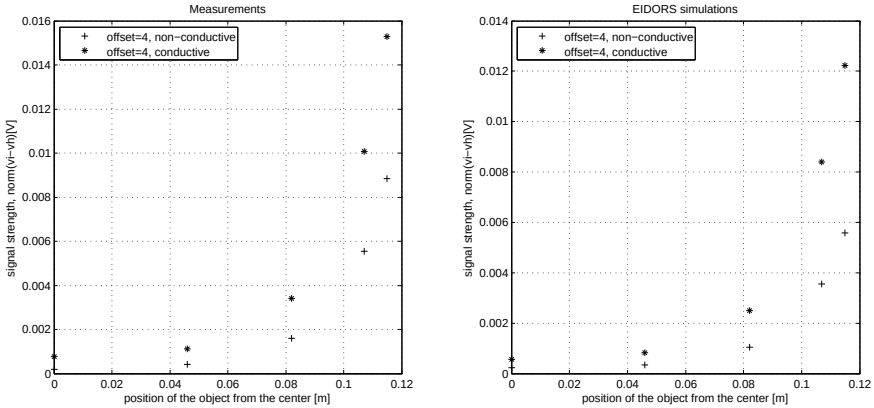

Figure 6.22: The signal strength in function of the position for an offset 4 measurement strategy using in one case a conductive sphere (Aluminum) and in the other case a non-conductive sphere. The measurement are compared with the EIDORS simulation results on the right hand-side.

6.4.2.3 Z-score and image

The goal of this section is to determine experimentally the minimum value of the z-score required to spot the object in a sequence of images (movie). Similar experiments as in sections 6.4.2.1 and 6.4.2.2 are conducted. We recorded the data for three different situations:

1. The object is a large (radius=2.25 cm) non-conductive sphere, at 10 images per second, with offset=0 measurement strategy, and the current injected is 0.6 mA,
2. The object is a large (radius=2.25 cm) non-conductive sphere, at 10 images per second, with offset=4 measurement strategy, and the current injected is 0.3 mA,
3. The object is a small (radius=1.13 cm) non-conductive sphere, at 5 images per second, with offset=4 measurement strategy, and the current injected is 0.3 mA.

Then three movies, each for one of the three situations, were displayed to volunteers who had to say when they think they began to spot something on the image (lower threshold, z-score=6) and when they were absolutely sure of their observation (upper threshold, z-score=15). The movie was played starting with no object in the tank, followed with the object in the center

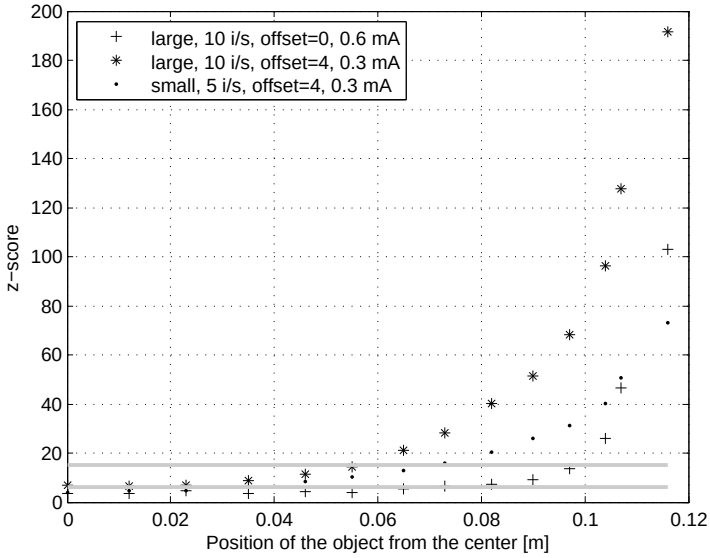

Figure 6.23: The distinguishability threshold. The horizontal lines show the detection threshold region. It has been empirically discovered that the object is spotted on the EIT image with high certainty once the z-score value reaches 15 (upper horizontal threshold line).

of the tank. Then the object is slowly moved towards the edge of the tank. The result of this qualitative test is reported in figure 6.23, where the two horizontal lines represent the two above mentioned threshold. The object began to be spotted as soon as the z-score value reached 6 and it appears clearly to the observer after the z-score reaches 15.

6.4.3 Symmetry issues

This section illustrates with an example the theoretical finding of section 3.3.6 and 3.3.7. In this experiment, a conductive sphere of radius 2.25 cm was placed 8 cm from the saline tank center. Then using the reconstruction algorithm corresponding to the offset measurement strategy, one calculates the images. The figure 6.24 shows that the same situation can produce very different outputs.

Qualitatively, one can observe that the images taken with offset strategies between offset 0 and offset 3 exhibit a deformation of the shape of the object.

Offset strategies between 5 and 12 exhibit a strong ringing effect together with a blurring effect. Then from offset 13 to 15 the correlation effect began to appear on the image. Therefore, in this case offset 4 seems to produce the visually most reliable to interpret images.

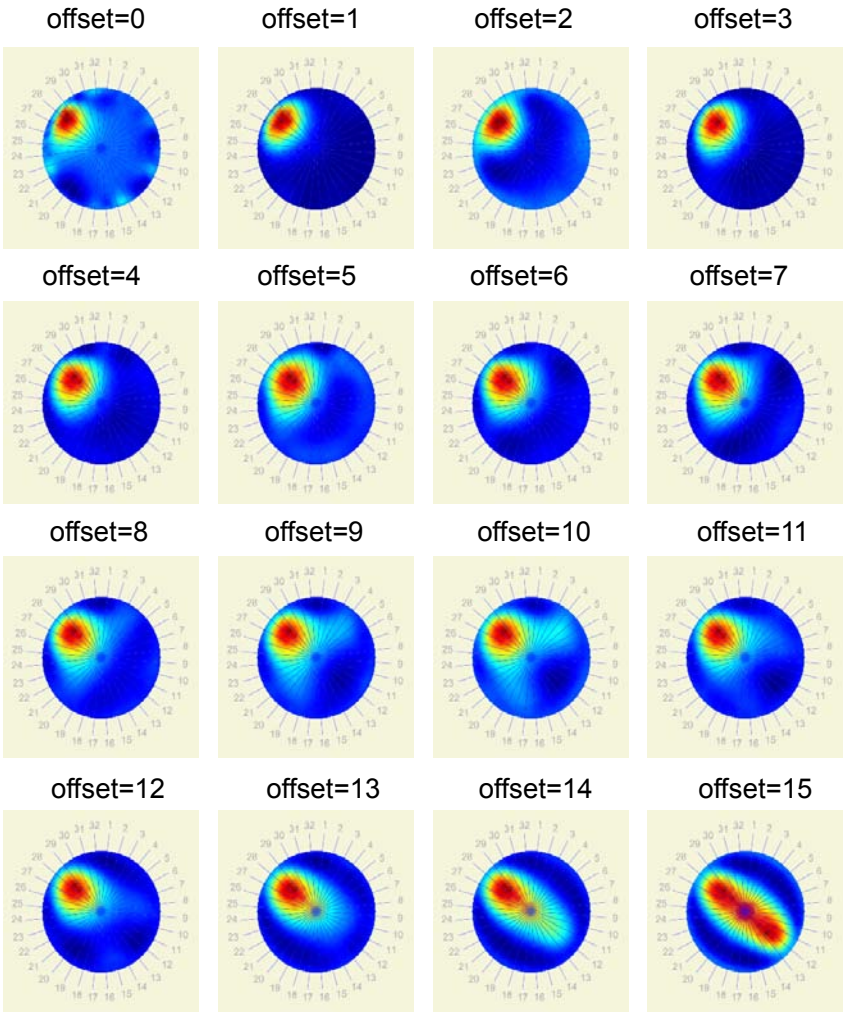

Figure 6.24: EIT reconstructed images of the same situation measured with various offsets.

Chapter 7

Applications

7.1 Introduction

In this chapter, practicality of two highly promising applications of EIT are investigated, micro-EIT and thoracic-EIT, making use of the theoretical and experimental tools developed as part of this thesis. In each case two or more practical application examples are described together with the obtained measurements results. One of our goal is also to give an intuitive insight about the performance of EIT under various conditions. The measurements presented in both sections 7.2 and 7.3 are differential, which means that the images are subtracted from a baseline, called "reference image". Thus the spatial impedance depicted in the reconstruction images are changes relative to the reference measurement (or image).

Section 7.2 focuses on micro-EIT applications and demonstrates the use of the developed micro-EIT electrode well, see figure 4.19. The images are acquired using a homogeneous medium as reference, see figure 3.1. Thus it allows the system to produce "almost absolute" images.

Section 7.3 focuses on medical-EIT applications and more specifically on thoracic applications. Ventilation and cardiac induced impedance changes are demonstrated. The EIT time difference imaging strategy adopted in this section allows the user to image the functional activity of the human body based on spatial impedance changes. As opposed to other medical imaging techniques such as X-ray CT scanners that produce anatomically accurate images, EIT delivers real-time functional images.

7.2 Micro-EIT

This section shows applications and practical usage examples of the micro-EIT hardware[1]. Possible usages of this technology arise in the industrial and life science domain. The developed system can make images of small objects such as human hair and biological important effects such as ionic flows. In comparison with an optical technique, EIT exhibits several advantages:

- It produces functional[2] images based on the conductivity without having recourse to special molecular labels,
- It can measures samples in the absence of light,
- It can image the inside of an optically opaque but electrically conductive medium.

However, EIT compared with optical techniques lacks of high spatial resolution. As a consequence EIT is for the time being not a competitive technology for optical microscopy, it is rather a complementary analysis tool. Micro-EIT could also be considered as the evolution of the classical two or four points impedance measurement, with the additional capability to measure the spatial distribution of the electrical conductivity. It is even possible to retrieve spatial spectroscopic information by performing multi-frequency measurements.

For the tests presented in this section, one of the challenges was to find test objects that were small enough and that would allow reproducible results. Therefore in section 7.2.2, we introduce the idea of using chip resistors and capacitors as test objects. In order to image ionic flow, we propose to observe the dissolution of a salt grain (NaCl) inside a saline solution. Based on these experiments, we learned a few important lessons for future micro-EIT system developments:

- the temperature drift of the sample is very important and needs to be stabilized before any measurement can be performed,
- the variation of the liquid level by evaporation or tilt plays a role in the measured EIT signal,
- the sample handling can introduce variations of the liquid level and therefore measured effective resistance value by adding or removing small quantities of liquid,

[1] See section 4.5 for details about the hardware.
[2] The spatial distribution of the electrical conductivity.

- the sample itself could also introduce liquid level variations because of the volume of water displaced by its own volume,
- the electrode surface is very sensitive and should not be touched during the measurement process, otherwise the reference will be invalidated,
- the surface tension of the saline solution needs to be reduced by using a non-ionic surfactant like tween 80 (Polyoxyethylene (20) sorbitan monooleate[3]). The reduction of the surface tension is necessary to ensure proper electrode-liquid contact, otherwise the liquid tends to wet completely the electrode's surface only incompletely.

7.2.1 Methodology

This section gives the experimental protocol followed for the experiments presented hereafter. It also describes the saline solution used to fill the micro-EIT well.

Since the micro-EIT well is not clean enough after fabrication, the following washing steps are necessary when a pristine micro-EIT chip is used or each time the user needs throrough cleaning of the well.

1. 10 minutes in the ultrasonic cleaner at 30 °C in pure isopropanol, which dissolves the soldering residue,
2. 10 minutes with the well filled with a solution of KCl (0.1 molar), which chemically cleans the electrode's surface,
3. rinse the well with pure water,
4. rinse the well with ethanol[4].

Between experiments, a reduced cleaning protocol consisting of step 3 and 4 is usually enough to guaranty proper function.

After step 4 is completed, the micro-EIT electrode well is ready to start the experiments. The well is filled with a water based saline solution (9 g/l NaCl). In addition to the water, it is necessary to add a chemical to lower the surface tension otherwise the electrodes do not get wet. For this purpose, we developed a special saline solution containing a non-ionic surfactant called tween 80. For the experiments presented hereafter the concentration of tween 80 was 0.5 % of volume (5 ml/l). About 0.6 ml of solution is necessary to

[3] This chemical is approved for food use up to 0.5% of water volume [3]
[4] 96% alcohol: Sigma/Aldrich 02583, denatured with 4.8% isopropanol

fill the well up to the maximal filling mark placed 1 cm above the well floor. After the solution is injected inside the well, it is required to wait up to 20 minutes for the temperature of the liquid to stabilize and to be able to start with the experiment.

When using the micro-EIT setup the gain of the acquisition chain often needs to be reduced in comparison with the thoracic-EIT settings. In these experiments, one uses a gain of 5 whereas the gain for thoracic-EIT was 50. The current injection was also reduced to 10 % of nominal (0.75 mA amplitude) to avoid excessive Joule heating. The reference was acquired just before the beginning of each experiment with no object in the well (i.e. homogeneous medium), see figure 3.1 b).

7.2.2 Chip resistors and capacitors as test objects

The basic idea of this section was to test the micro-EIT system with standard objects of known conductivity. At first the micro-EIT electrodes well was prepared as described in section 7.2.1. For each test a tank filled with a saline solution with no objects inside is taken as reference. Then the chip resistor respectively capacitor is placed inside the well between electrode number 17 and 22 and in the middle between the well center and the well wall. The chip components used were of the form factor 0603 [5] and were placed flat on the micro-EIT well floor with one conductive pad towards the edge and the other one towards the well center.

All measurements were made at 100 kHz with skip time of 30 µs. The chip capacitor's theoretical impedance values at 100 kHz are 1.59 MΩ and 1.59 Ω for the 1 pF and 100 nF capacitor, respectively. The result presented in figure 7.1 shows that the system was able to measure the conductivity changes in the right direction for the purely resistive case and for the capacitive case.

[5] length 1.8 mm, width 0.8 mm, height 0.5 mm

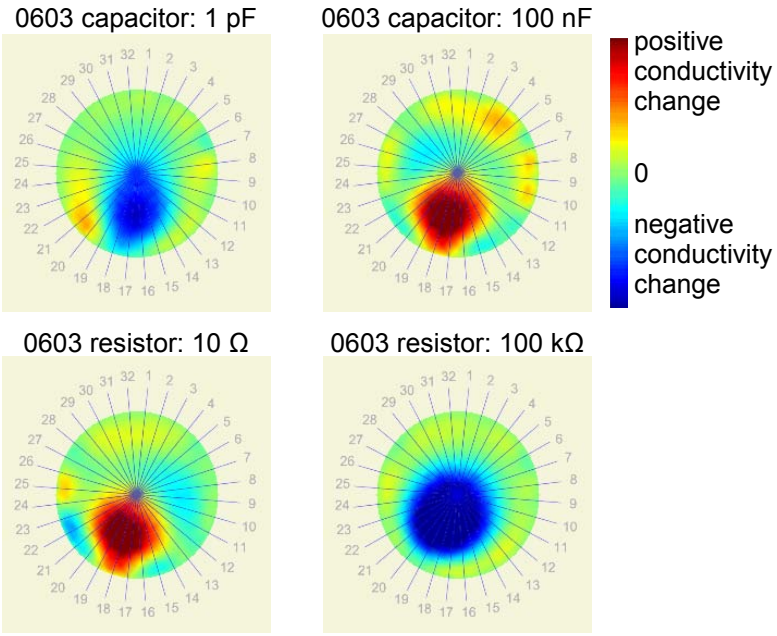

Figure 7.1: Chip resistors and capacitors 0603 placed inside the micro-EIT well. The color coding represents the conductivity changes compared with the homogeneous reference. Red corresponds to positive conductivity change (i.e. the object is more conductive than the reference), whereas blue corresponds to negative conductivity change (i.e. the object is less conductive than the reference).

7.2.3 Miscellaneous objects

The aim of this section is to present the imaging capabilities of the developed micro-EIT on various objects:

- a human hair with a cross-section diameter of 60 µm,
- a quartz stone of size 1000 × 1300 × 760 µm,
- 1 and 2 alginate beads of diameter of 1000 µm each.

The first important result presented in figure 7.2 is that it is possible to image a human hair with its bulb, which represents an object with a diameter 150 times smaller than the well itself. In this case, the hair was placed vertically

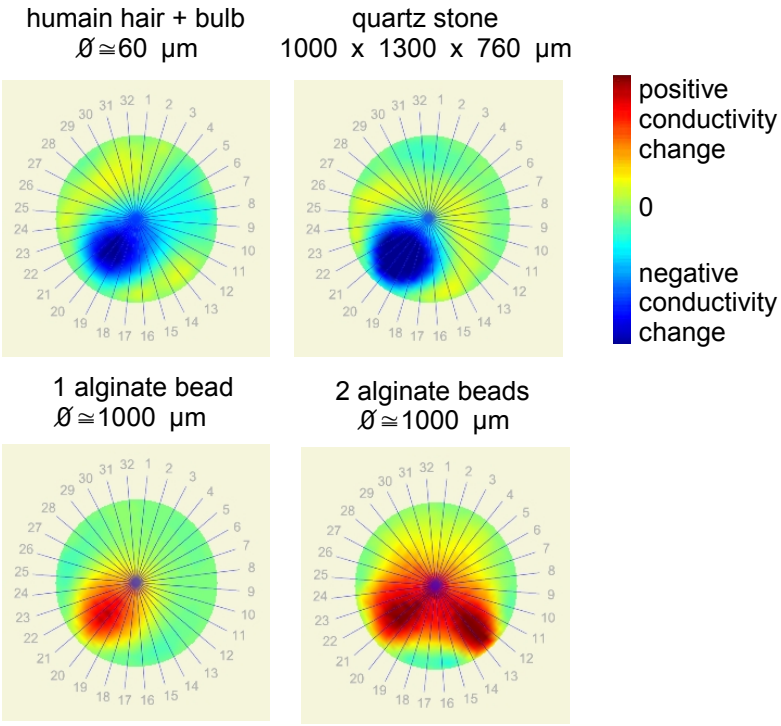

Figure 7.2: The micro-EIT image of four different objects.

in the well and properly held in place with a support. The hair appears as less conductive than the saline solution, which is expected. A quartz stone[6] was also measured and appears as less conductive than the reference.

The alginate beads are used as support for 3D cell cultures and therefore are of great interest in life science applications. Alginate beads were manufactured by dropping a sodium alginate solution inside a calcium chloride bath. The sizes of the beads are controlled by the size of the drops. The alginate beads appeared as more conductive than the reference because they contain ions, which dissolve into the saline solution. With the two alginate beads experiment the problem of imaging two objects is tackled. This image is included here for illustration purposes only; proper analysis of the distinguishability of two objects should be studied in future work.

[6]sand from the river Rhine

7.2.4 Salt grain experiment

This section presents a way to test the ionic flow imaging capabilities. The basic idea is to drop one salt (NaCl) grain inside the saline solution and observe the diffusion of ions. Before the experiment, the well was prepared as explained in section 7.2.1. After the saline solution reaches its thermal stability point, a salt grain of about 0.5 mm in diameter (NaCl) is dropped into the well center without touching the saline solution with the tweezers. Figure 7.3 presents the obtained results. In order to evaluate the results, the temporal evolution of a single pixel is reported in the middle plot. This pixel is chosen to be at the geometrical center of the location of the salt grain. One can observe that shortly after the grain enters the water, it appears as non-conductive (i.e. less conductive than the saline conductivity) object. Indeed solid salt is an isolating material. Then after 200 µs, it already appears on the image as conductive object because the salt started to dissolve itself into the saline solution. Then after 200 s the dissolution of the salt grain practically complete (i.e. the salt grain was no more visible). The problem is that after the 200 s mark, the EIT image began to suffer of severe reconstruction artifacts due to the large and homogeneous conductivity changes. Reconstruction methods, such as MAP[7], which linearize the inverse problem, can only correctly work if the impedance changes remain within reasonable bounds around the reference. This kind of large conductivity changes would rather require iterative reconstruction algorithms which do not depends on the linearization of the problem.

7.3 Thoracic-EIT

This section presents application examples of the thoracic-EIT device built for the startup company Swisstom AG within this thesis. The primary motivation behind EIT thoracic imaging is the continuous monitoring of the respiratory and cardiovascular system of ventilated patients. The first category of patients, which could benefit from EIT, are Intensive Care Unit (ICU) patients for whom the ventilation therapy needs precise and continuous monitoring to improve outcome. Unfortunately, without convenient real time monitoring of the patient's lungs it is challenging for the medical doctor to quickly evaluate the situation and take appropriate actions. Especially the regional monitoring capabilities of EIT facilitate the implementation of lung protective ventilation strategies. Moreover, when the ventilator is removed (extubation) and the patient is breathing spontaneously again, there are even

[7] see appendix A.1

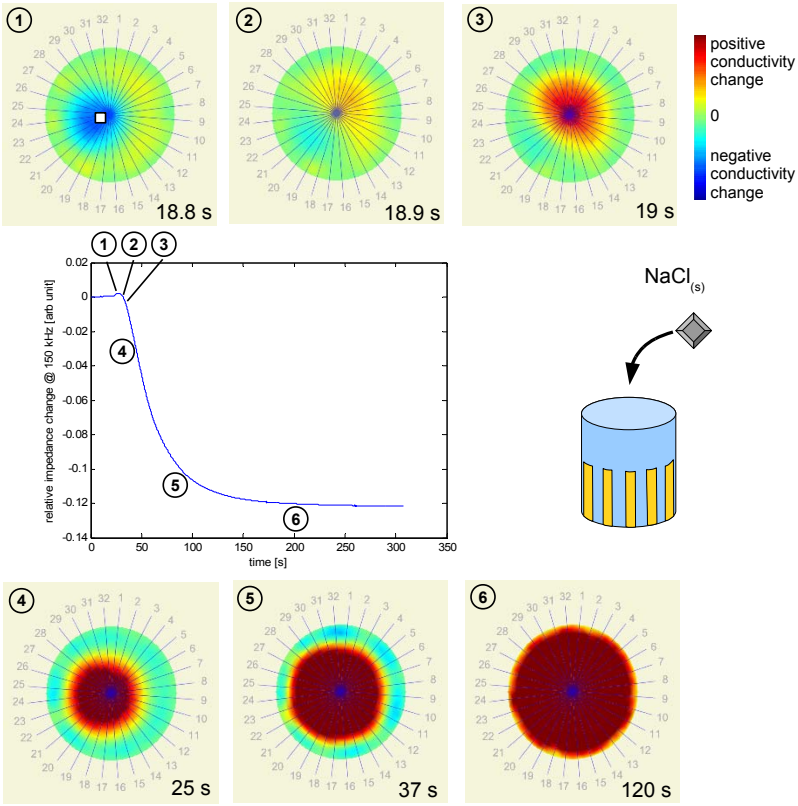

Figure 7.3: Imaging of ionic flow using the micro-EIT setup. At point ① a salt (NaCl) grain is dropped inside the well and appears as non-conductive. Then, after a transition state ②, the ions began their diffusion, and the salt grain appears as conductive ③. Then after 120 s ⑥, the dissolution is almost finished and the salt grain is no more visible to the unaided eye.

fewer monitoring capabilities as the pneumatic interface with the patients becomes ill-defined when masks or nasal cannulas are used or is lacking entirely. The second category of patients, who also would benefit from EIT, is patients in the operating theater, who need continuous monitoring not only of their lungs but also their heart and cardio-vascular system. According to several authors [54, 72, 24] EIT has the potential of becoming a useful bedside monitoring tool which is likely to increase situation awareness of medical personnel and to enable improved therapies. The main lung related problems that can be diagnosed and monitored with EIT are:

- lungs collapse [66, 21]: Lungs tends to collapse under their own weight. This can happen, for example, when people stay in the same posture for extended periods of time. Other reasons for lungs collapse are muscle relaxation, obesity, pneumonia, lung injuries and oedema. Lung collapse also happens in healthy people, for instance during sleep. But the non-ailing body is able to resolve this issue simple by taking a deep breath or changing the body posture. This solution can be emulated for example by turning the patient on the side or by increasing the ventilator pressure to open the lungs. Increasing the pressure of the ventilator above baseline pressure support levels, although having scientifically proven benefits[9], has evident risks and is thus not widely adopted in the ICUs due to the lack of adequate monitoring. EIT could provide such monitoring.
- lungs perfusion [30, 57]: The proper matching between ventilation (air) and perfusion (blood) within the lungs is a prerequisite for adequate gas exchange and is thus one of the most important pieces of information one would need to assessment a patient's lung status. Based on such information appropriate therapeutic measures can be taken.
- blood pressure: First experimental evidence suggests that continuous non-invasive measurement of the central blood pressure using EIT has become feasible [88]. This novel approach could eliminate the need for intermittently inflating classical blood pressure cuffs. Furthermore, if calibrated appropriately this approach could provide direct measures of wall stiffness of central arteries such as the aorta. EIT would eliminate the need for invasive catheters to determine these outcome-related crucial information about the mechanical properties (e.g. distensibility) of cardio-vascular system.

Besides the therapeutic benefit of EIT, which could saves lives, there are also economical benefits. Since better therapy leads to fewer medical complications and quicker patient recovery, money can be saved [8].

[8] see Swisstom AG: Business Plan, http://www.swisstom.com

Thoracic-EIT imaging is also of interest in sports applications, and could be used for real-time cardiovascular real-time performance assessment and guidance of sports training regimes.

7.3.1 Methodology

This section describes the methodology used to record the measurements presented hereafter. All the data were taken on a healthy male sitting volunteer with the electrode belt (see section 4.4) placed around the thorax in a transverse plane crossing the 5^{th} ribs and the sternum. The EIT system itself was prepared in the following way:

- the system was warmed up during 10 minutes before utilization,
- the setting was 1 mA (amplitude), 150 kHz, offset 4 and 30 µs skip time,
- the metallic, gold plated electrodes were coated using a proprietary (Swisstom AG) liquid chemical compound to ensure proper mechanical coupling on the skin and optimal electrical contact.

The system used to acquire the experimental data of this section was not the same as for the other experiments presented in this thesis. The difference is that this system, dedicated to volunteer experiments, had only a buffer after the DAC and not a factor-11 non-inverting amplifier, see figure 4.12. This prevents the system from injecting more than 1 mA into the body, ensuring patient and user electrical safety.

7.3.2 Size of the EIT signal

This section presents an example of the signal measured during volunteer experiments. The aim is to give an intuitive insight about the order of magnitude of ventilation and perfusion EIT signals. This information can be used for future system design and in specification document. The EIT amplitude signal in figure 7.4, which corresponds to the output of the differential instrument amplifier with unity gain, is in the mV range. The dynamic range of the signal given by the ratio between the largest and lowest value of the EIT amplitude signal was found to be about 50. This means that if the acquisition chain gain was designed for the largest value to accommodate the full ADC input range, the lower value only covers a 1/50 of the latter. This situation reduces the measurement precision for the lowest values. An appropriate adaptive gain strategy can solve this issue by adapting the gain value to each signal.

It can be observed on figure 7.4 that the shape of the envelope exhibited by the EIT amplitude signal is characteristic of the shape of the medium (i.e. the thorax in this case). This information could be used to retrieve useful geometrical information about the thorax, which can contribute to enhance the reconstruction algorithm performance.

The EIT time differential signal is the result of the subtraction of two EIT amplitude signals taken at two different times. In figure 7.5 a), the time difference between the beginning and the end of a respiratory (ventilation) respectively cardiac (perfusion) induced impedance change events is calculated. It was found that the ventilation signal, see figure 7.5 b), produces peak-to-peak variations less than 1 mV during one respiratory cycle. These variations are even an order of magnitude smaller for the cardiac related impedance change (i.e. 0.1 mV).

7.3.3 Ventilation monitoring

This section presents an example of ventilation monitoring performed on a sitting volunteer who was asked to slowly take a deep breath. At the beginning ① (on figure 7.6) of the respiratory cycle the diaphragm is in a relaxed state. For the air inhalation to be initiated, the diaphragm contracts which reduces the pressure inside the lungs. This creates a pressure gradient that causes air to flow ② in the lungs by the trachea. This process continues until the volunteer stops taking air in ④ and begins exhaling the air out of his lungs ⑥. This inhalation and exhalation cycle can conveniently be visualized on the EIT composite signal (see figure 5.8).

7.3.4 Cardiovascular function monitoring

This section presents an example of the cardiac and respiratory induced impedance changes. The exact same data as in the previous section are used, but instead of using only a small part of them, the whole data set is analysed. For this analysis, we stored the produced images using EIDORS. Each pixel value of one image corresponds to the conductivity changes at its position. Therefore, it is easy to select a pixel in the heart region and one in the right lung region and plot their respective value over time, see figure 7.7. The “lung pixel” shows a decrease in the conductivity with the inhalation, whereas the “heart pixel” shows an increase in the conductivity. The behavior of the “heart pixel” is explained by the fact that each time a person spontaneously breathes, the pressure decreases inside the chest which is partially compensated by the extension of the heart, which creates an increase in the net blood intake. It

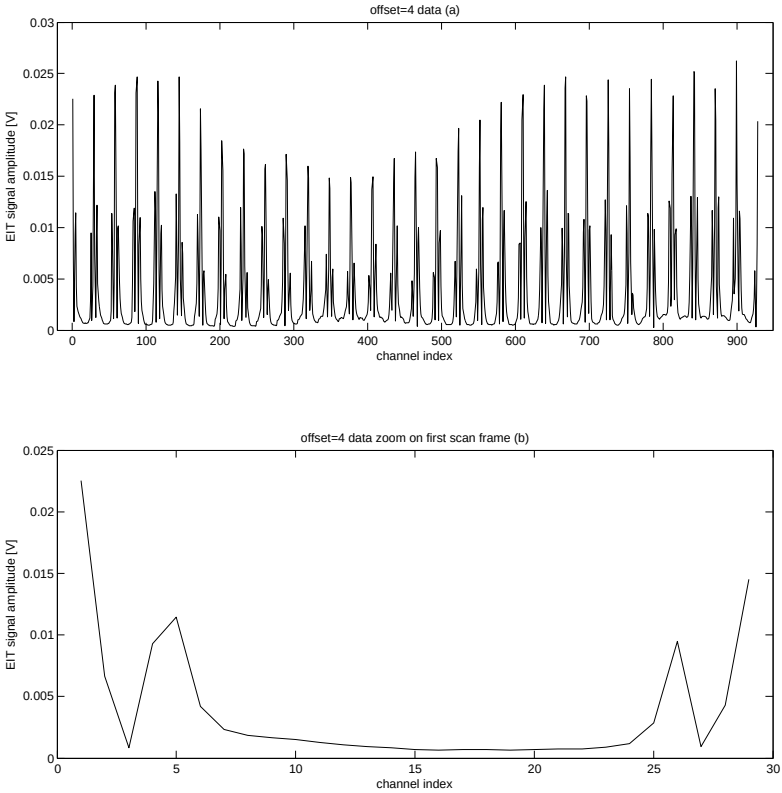

Figure 7.4: Example of the EIT amplitude signal recorded during thoracic imaging on an healthy volunteer. a) depicts the signal after the differential instrument amplifier (normalized to unity gain). b) is a zoomed view on the first "U" of the a) plot .

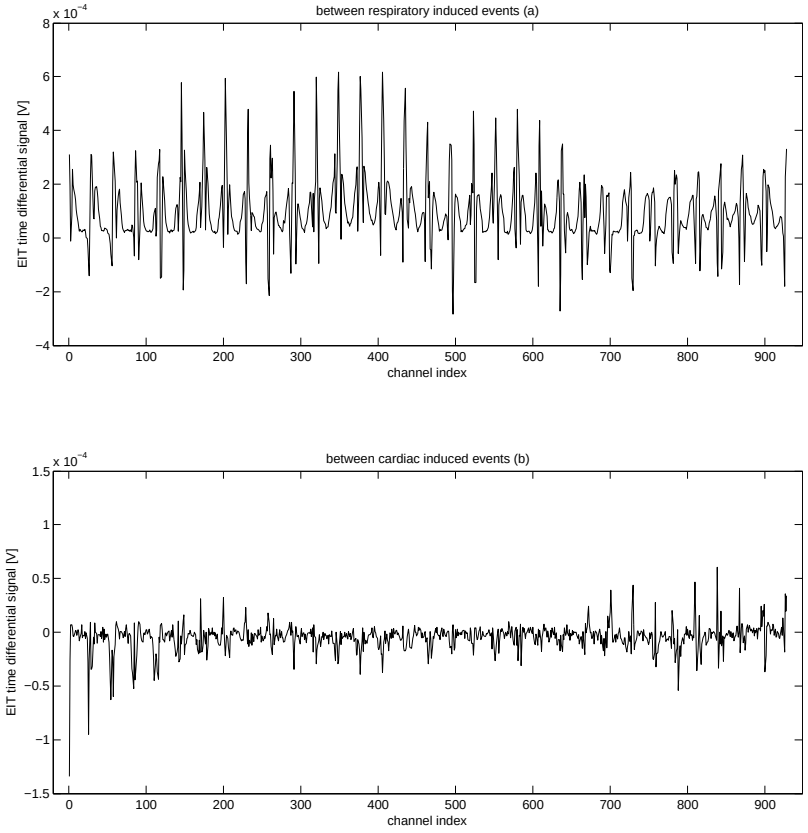

Figure 7.5: Example of the EIT differential signal recorded during thoracic imaging on a healthy volunteer. In both the a) and b) case, one measurement frame of the time differential EIT signal entering the image reconstruction algorithm is shown, see figure 5.7 signal d. In a) the reference image was taken at the beginning of the inhalation and the image at the end of the inhalation. In b) the volunteer was holding his breath during the measurement, in this way only cardiac event related impedance change could be observed. The reference image was taken when the EIT composite signal reached its lowest point and the signal image when the EIT composite signal reached its maximum.

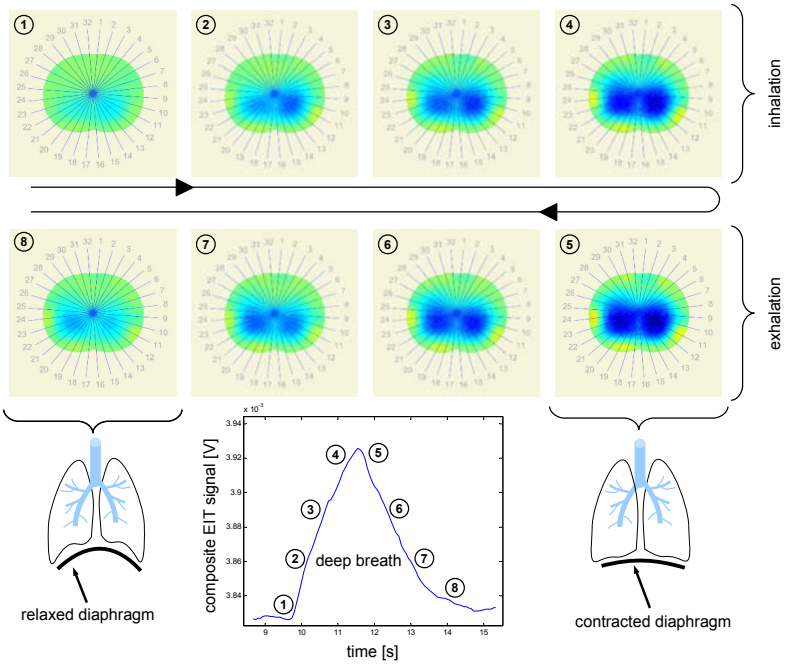

Figure 7.6: EIT tomographic images of the thorax region during one inhalation-exhalation cycle. The plot depicts the composite EIT signal of a volunteer taking a deep breath.

is also known that the heart moves inside the thorax during the respiratory cycle, which may also have an effect on the EIT images. In contrast, a mechanically ventilated patient would exhibit a "heart pixel" with similar shape as the "lung pixel", because the pressure increase created by the ventilator compresses the heart which results in a decrease of the net blood intake. In order words, for mechanically ventilated patients the air is pushed into the lungs where as for spontaneously breathing patients the air is aspirated into the lungs.

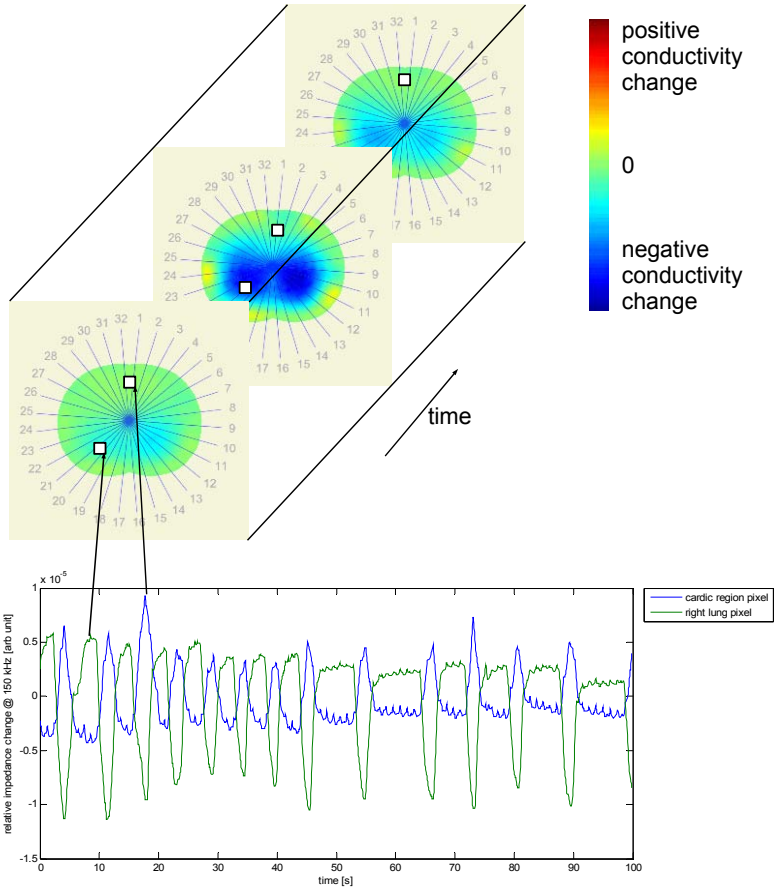

Figure 7.7: Temporal evolution of the EIT reconstructed impedance changes for two pixels, one in the heart (blue) and one in the right lung (green) region.

Chapter 8

Discussion

8.1 Conclusion

In this thesis, we pursued two main research paths: 1) we proposed a probabilistic definition for the distinguishability and 2) we successfully developed a complete active electrode based Electrical Impedance Tomography (EIT) system.

The distinguishability criterion is derived from the Maximum A posteriori Probability (MAP) approach without using a particular regularization. This is a probabilistic criterion, which corresponds to the rejection of the null-hypothesis (i.e. no impedance changes inside the Region Of Interest (ROI)); it can also be interpreted as a Signal to Noise Ratio (SNR) $z = \frac{1}{\sigma_n} \|\Delta \mathbf{v}_{\mathrm{ROI}}\|_2$, where $\Delta \mathbf{v}_{\mathrm{ROI}}$ is the differential EIT signal generated by impedance change inside the ROI and σ_n is the noise standard deviation, which is assumed to be the same for each channel.

Using the Finite Element Modeling (FEM) capabilities of the program EIDORS, we were able to calculate the forward EIT problem for two-dimensional and three-dimensional cases. Thus, we investigated the variation of the EIT differential signal, $\|\Delta \mathbf{v}_{\mathrm{ROI}}\|_2$, in function of the measurement strategy, and the test object position, size and conductivity. In all cases the EIT differential signal was maximized for the opposite measurement strategy (i.e. offset=15). Unfortunately, the offset=15 measurement strategy leads to severe reconstruction artifacts generated by the symmetry of the measurement set-up. The best images from a qualitative point of view were obtained using measurement strategies between offset 4 and offset 12, which corresponds to a current injection angle between 60 and 150 degree, respectively.

The main noise sources in the developed EIT system were found to be the current generator and the acquisition electronic noise. Strong temperature drift of the electronics was observed, which currently constitutes one of the main limiting factors of the system precision.

The variation of the distinguishability criterion in function of the geometrical size of the EIT data acquisition system (i.e. the electrode arrangement) was also studied. We found that the main limiting factor for the miniaturization of EIT system using electrode wells is the Joule heating effect that increases the temperature of the solution. Heating the solution generates three problems: 1) if the solution's temperature rises above a given threshold the possibly sensitive biological sample could be damaged, 2) the liquid evaporation is accelerated which creates drift and 3) the solution's conductivity is a function of the temperature, thus any change of temperature translates in a drift of the EIT differential signal. In the up-scaling case the distinguishability is limited by the electronic noise of the data acquisition chain.

The developed data acquisition system was designed to be used in both micro-EIT and thoracic-EIT systems. The micro-EIT specific hardware consists of a 32-electrode well fabricated using Printed Circuit Board (PCB) technology. The thoracic-EIT system makes use of a belt-like arrangement of the electrodes. The 90 cm length thoracic belt is designed to facilitate the use of EIT, for example it is even possible for a single person to operate the instrument while measuring his own lungs. In order to maximize the electrode input impedance and minimize the signal high impedance path, an active electrode architecture was implemented. In this way, a voltage buffer could be implemented as closely as possible to the electrode, which eliminates the need for shielded cables. The current source, which is one of the EIT system's key element, makes use of a novel circuit design. It is combining a current source with a voltage source. It was found that this approach minimizes the effect of the stray capacitance and the Common Mode Rejection Ratio (CMRR). The major advantage of this new design compared with other symmetrical current sources is that it does neither need calibration nor extra electrodes. The current source internal impedance was found to be above 1 MΩ at 50 kHz. Each active electrode is also equipped with a micro-processor whose task is to manage the node functions following a common synchronization signal. An alternative design for the active electrode node management is also proposed; it makes use of a daisy chain arrangement of the nodes, thus the state commands are shifted from one node to the next one using two daisy chains, one for the current injection and one for the measurement.

The tests carried out on the micro-EIT hardware demonstrated promising ionic flux detection capabilities. We were able to observe the dissolution of a grain of salt and the resulting diffusive transport of the ions inside the

solution. The developed micro-EIT also demonstrated the detection of objects of biological nature such a human hair that represents an object of 150 µm in diameter in a 9 mm in diameter well.

The thoracic-EIT system demonstrated the measurement of real-time ventilation and cardiac related impedance change on healthy volunteers. For this application the EIT hardware needs to be further miniaturized, to better fit the thoracic belt and thus increase both the patient comfort and the device ease of use.

The EIT medical market is, at the time of writing, almost unaddressed by commercial products, and EIT technology still needs to be validated by the medical community on a large scale. Several authors in the literature and many research groups all around the world already demonstrated the tremendous potential of EIT not only in the medical domain but also in many other fields such as industrial processes, geophysics, agriculture, and life sciences. The EIT technology needs now to be brought to an advanced maturity stage and gain in reliability.

8.2 Future work

The goal of this section is to give an outlook on possible future work and research paths, which can be pursued based on the findings of the present thesis. The future works are listed in three different categories: EIT hardware, micro-EIT and theory.

The EIT hardware concerns all the hardware commonly shared by both micro and macro EIT. This comprises the active nodes, the analog front end and the FPGA. Hardware enhancement suggestions are listed hereafter:

- Active node: The register based daisy-chain principle should be implemented to control the nodes (in progress),
- Active node: The size of the active nodes needs to be further reduced (in progress),
- Active node: Other operational amplifiers for the node buffer should be evaluated (less power consuming, less expensive),
- Active node: Other analog switches for the node multiplexing should be evaluated (smaller C_{off} capacitance, and minimal R_{on} resistance)
- Analog front end: For optimal performance, it is necessary to merge the front end and the FPGA on a custom common PCB (in progress),

- Analog front end: A current measurement circuit, which gives the amplitude of the applied current should be implemented. It could be used to compensate for the current source drift and to ensure electrical patient safety,
- Analog front end: An adaptive gain mechanism for the acquisition chain should be tested (in progress),
- Analog front end: A less noisy DAC should be evaluated (in progress),
- Analog front end: Automatic signal generation and acquisition chain gain measurement.

The micro-EIT, which shows very promising results, should be further investigated:

- Micro-EIT well: The electrode well needs to be further miniaturized using silicon-based micro fabrication technology. In this way even smaller objects could be imaged,
- High resolution: One could combine a high resolution Multi Electrode Array (MEA), such as described by Imfeld et al [44], with the developed micro-EIT well. The latter would be used to inject the current and the former to read the voltage at high resolution on the bottom of the chip. This unique combination could provide micro-EIT images of very high resolution.
- 3D: The PCB technology allows the fabrication of multilayer PCBs with blind and buried vias[1]. Therefore, one can imagine a micro electrode well integrating two or more rings of electrodes one on top of the other. This could be used to produce 3D EIT images of the well content.
- Pipes application: In the thesis one side of the micro-EIT well is close to form a well. However, one could also imagine a set-up where both sides are connected to a pipe which would enable EIT analysis of the flow inside the pipe.
- Drift issue: The measurements and tests undertaken show that the control of the temperature of the micro-EIT well was of prime importance to ensure minimal drift. Therefore a Peltier element could be used to stabilize the temperature,

[1] Blind vias are only visible on one side of the PCB; Buried vias are not visible from the PCB surface

- Living cell: Subordinated to the above listed enhancement micro-EIT picture of living cell cultures should be investigated with the aim of counting individual cells and possibly observe changes in the ionic content of individual cells,
- Saline: The composition of the micro-EIT saline solution should be investigated to allow proper cells culture growth.

The theoretical research undertaken during the present thesis answers several important questions but also raises others, which could be addressed in the future:

- Quasi-static approximation: As pointed out, the quasi-static approximation may be used at its limit of validity. The impact of the quasi-static approximation on the image reconstruction should be further investigated,
- EIT fundamentals: Study the number of independent measurements for non-constant noise level and different measurement strategies,
- Distinguishability: Study the distinguishability of two objects,
- Shot noise: An in-depth investigation should be conducted to fully understood the contribution of shot noise in EIT,
- Miniaturization limit: The preliminary research work presented in this thesis should be pursued and a new miniaturization model including the shot noise should be proposed.

In my view, the work presented in this thesis describe the development and optimization of the first complete and practically useful active electrode based EIT system; this has led to the creation of a first Swiss startup company which might have the chance to become one of the world leaders in the envisaged huge field of EIT imaging applications in medicine, in the life sciences and in industry.

Appendix

Appendix A

Image Reconstruction

A.1 Maximum A Posteriori Probability

This section gives the derivation of the Maximum A posteriori Probability (MAP) approach for the image reconstruction.

Let $\mathbf{m}$ be the model of the data and $\mathbf{d}$ be the associated data. With these two variables, the problem to solve is to calculate which choice of the model parameter $\mathbf{m}$ gives the highest likelihood knowing a given data set $\mathbf{d}$. In the EIT problem $\mathbf{m}$ can be identified to the conductivity $\boldsymbol{\sigma}$ of the medium and the data $\mathbf{d}$ to the time differential EIT amplitude signal (i.e. the voltage difference between the current measurement and a given reference). Using Bayesian mathematics, it can be formulated as follow:

$$\mathbf{m}_{\mathrm{MAP}} = \underset{\mathbf{m}}{\operatorname{argmax}} \left(\mathrm{P}(\mathbf{m} \mid \mathbf{d}) \right) \tag{A.1}$$

where

$\underset{\mathbf{m}}{\operatorname{argmax}}$ is a function maximizing the probability $\mathrm{P}(\mathbf{m} \mid \mathbf{d})$ by doing a good choice of $\mathbf{m}$ (see section B.3),

$\mathbf{m}_{\mathrm{MAP}}$ is parameter set that maximizes the probability $\mathrm{P}(\mathbf{m} \mid \mathbf{d})$.

Then by using Bayes theorem given in equation B.13 the probability becomes:

$$\mathrm{P}\left(\mathbf{m} \mid \mathbf{d}\right) = \frac{\mathrm{P}\left(\mathbf{d} \mid \mathbf{m}\right) \mathrm{P}(\mathbf{m})}{\mathrm{P}(\mathbf{d})} \tag{A.2}$$

the combining equations A.1 and A.2 gives:

$$\mathbf{m}_{\mathrm{MAP}} = \underset{\mathbf{m}}{\operatorname{argmax}} \left(\frac{\mathrm{P}\left(\mathbf{d} \mid \mathbf{m}\right) \mathrm{P}(\mathbf{m})}{\mathrm{P}(\mathbf{d})} \right) \tag{A.3}$$

Since we are only interested in terms containing $\mathbf{m}$, it is possible to consider the others one as proportionality constant, which do not affect the result of the argmax function:

$$\mathbf{m}_{\mathrm{MAP}} = \underset{\mathbf{m}}{\operatorname{argmax}} \left(\mathrm{P}\left(\mathbf{d} \mid \mathbf{m}\right) \mathrm{P}(\mathbf{m}) \right) \tag{A.4}$$

Assuming that the noise statistics is Gaussian, one can write the probability of the data knowing the model using the probability density function (pdf) for a multivariate Gaussian noise distribution:

$$\mathrm{P}\left(\mathbf{d} \mid \mathbf{m}\right) = \frac{1}{(2\pi)^{\frac{\mathrm{rank}(\mathbf{d})}{2}}\sqrt{\det(\mathbf{d})}} e^{-\frac{1}{2}(\mathbf{d}-\boldsymbol{\mu})^t \boldsymbol{\Sigma}^{-1}(\mathbf{d}-\boldsymbol{\mu})} \tag{A.5}$$

$$= \frac{1}{\sqrt{\det(2\pi\mathbf{d})}} e^{-\frac{1}{2}(\mathbf{d}-\boldsymbol{\mu})^t \boldsymbol{\Sigma}^{-1}(\mathbf{d}-\boldsymbol{\mu})} \tag{A.6}$$

where

$\boldsymbol{\mu}$ is the expected value of the vector $\mathbf{d}$; in the EIT case, one can estimate its values by using the linearization proposed in equation 3.4 $\boldsymbol{\mu} = \mathbf{J}\mathbf{m}$

$\boldsymbol{\Sigma}$ is the covariance matrix of the noise.

The expression for $\mathrm{P}(\mathbf{m})$ is a little more difficult to determine. Indeed it is very difficult to know what is the probability of an object for which, one do not have any information about. That being said, in most case it is possible to assume that the object[1] as some particular proprieties, for instance being spatially "smooth" or homogenous. For the moment, it is not necessary to define what $\mathrm{P}(\mathbf{m})$ exactly is, we will only assume, it has the following form:

$$\mathrm{P}(\mathbf{m}) = \mathrm{e}^{-\frac{1}{2}\mathrm{A}_P(\mathbf{m})} \tag{A.7}$$

where

$\mathrm{A}_p(\mathbf{m})$ is the a priori operator which contains alleged information about the object, the return value of this operator is a scalar.

At this point, one can put together equation A.5, A.7 and A.4. Since the terms that do not contain $\mathbf{m}$ or that are not linked to $\mathbf{m}$ do not influence the result of the argmax function, they can be discarded:

$$\mathbf{m}_{\mathrm{MAP}} = \underset{\mathbf{m}}{\mathrm{argmax}} \left(\mathrm{e}^{-\frac{1}{2}(\mathbf{d}-\boldsymbol{\mu})^{\mathrm{t}} \boldsymbol{\Sigma}^{-1}(\mathbf{d}-\boldsymbol{\mu})} \mathrm{e}^{-\frac{1}{2}\mathrm{A}_P(\mathbf{m})} \right) \tag{A.8}$$

$$= \underset{\mathbf{m}}{\mathrm{argmax}} \left(\mathrm{e}^{-\frac{1}{2}\left((\mathbf{d}-\boldsymbol{\mu})^{\mathrm{t}} \boldsymbol{\Sigma}^{-1}(\mathbf{d}-\boldsymbol{\mu}) + \mathrm{A}_p(\mathbf{m})\right)} \right) \tag{A.9}$$

The function e^{-x} is maximal when x is minimal therefore:

[1] The object is modeled by the parameters contained in the $\mathbf{m}$ vector.

$$\mathbf{m}_{\mathrm{MAP}} = \underset{\mathbf{m}}{\operatorname{argmin}} \left((\mathbf{d} - \boldsymbol{\mu})^{\mathrm{t}} \boldsymbol{\Sigma}^{-1} (\mathbf{d} - \boldsymbol{\mu}) + \mathrm{A}_p(\mathbf{m}) \right) \tag{A.10}$$

Using the relation $\boldsymbol{\mu} = \mathbf{J}\mathbf{m}$, one gets:

$$\mathbf{m}_{\mathrm{MAP}} = \underset{\mathbf{m}}{\operatorname{argmin}} \left((\mathbf{d} - \mathbf{J}\mathbf{m})^{\mathrm{t}} \boldsymbol{\Sigma}^{-1} (\mathbf{d} - \mathbf{J}\mathbf{m}) + \mathrm{A}_{\mathrm{p}}(\mathbf{m}) \right) \tag{A.11}$$

Where $\mathbf{J}\mathbf{m}$ is the expected forward problem outcome given in equation 3.4. Using the matrix form of the weighted norm defined in equation B.1, one gets:

$$\mathbf{m}_{\mathrm{MAP}} = \underset{\mathbf{m}}{\operatorname{argmin}} \left(\|\mathbf{d} - \mathbf{J}\mathbf{m}\|_{\Sigma}^2 + \mathrm{A}_{\mathrm{p}}(\mathbf{m}) \right) \tag{A.12}$$

At this point, it is necessary to find $\mathbf{m}$ that minimizes $\left(\|\mathbf{d} - \mathbf{J}\mathbf{m}\|_{\Sigma}^2 + \mathrm{A}_{\mathrm{p}}(\mathbf{m}) \right)$ and per extension maximizes $\mathrm{P}(\mathbf{m} \mid \mathbf{d})$. For this purpose, a minima-maxima search is undertaken by taking the derivative of $\left(\|\mathbf{d} - \mathbf{J}\mathbf{m}\|_{\Sigma}^2 + \mathrm{A}_{\mathrm{p}}(\mathbf{m}) \right)$ relative to $\mathbf{m}$ and identify the result to zero. The notation of the derivative hereafter assumes a component per component derivation. Thus the "0" zero is in fact a vector with all component identified to zero.

$$\frac{\partial}{\partial \mathbf{m}} \left(\|\mathbf{d} - \mathbf{J}\mathbf{m}\|_{\Sigma}^2 + \mathrm{A}_p(\mathbf{m}) \right) = 0 \tag{A.13}$$

$$\frac{\partial}{\partial \mathbf{m}} \left((\mathbf{d} - \mathbf{J}\mathbf{m})^{\mathrm{t}} \boldsymbol{\Sigma}^{-1} (\mathbf{d} - \mathbf{J}\mathbf{m}) + \mathrm{A}_p(\mathbf{m}) \right) = 0 \tag{A.14}$$

$$\frac{\partial}{\partial \mathbf{m}} \left(\mathbf{d}^{\mathrm{t}} \boldsymbol{\Sigma}^{-1} \mathbf{d} - \mathbf{m}^{\mathrm{t}} \mathbf{J}^{\mathrm{t}} \boldsymbol{\Sigma}^{-1} \mathbf{d} - \mathbf{d}^{\mathrm{t}} \boldsymbol{\Sigma}^{-1} \mathbf{J}\mathbf{m} + \mathbf{m}^{\mathrm{t}} \mathbf{J}^{\mathrm{t}} \boldsymbol{\Sigma}^{-1} \mathbf{J}\mathbf{m} + \mathrm{A}_p(\mathbf{m}) \right) = 0 \tag{A.15}$$

We will take the derivative of equation A.15 in 3 separate steps before gathering all the sub-results in equation A.27. The first step consists in noticing that the result of the norm operator $\left(\|\mathbf{d} - \mathbf{J}\mathbf{m}\|_{\Sigma}^2 \right)$ is a scalar, therefore the sum of terms $\mathbf{d}^t \boldsymbol{\Sigma}^{-1} \mathbf{d} - \mathbf{m}^{\mathrm{t}} \mathbf{J}^{\mathrm{t}} \boldsymbol{\Sigma}^{-1} \mathbf{d} - \mathbf{d}^{\mathrm{t}} \boldsymbol{\Sigma}^{-1} \mathbf{J}\mathbf{m} + \mathbf{m}^{\mathrm{t}} \mathbf{J}^{\mathrm{t}} \boldsymbol{\Sigma}^{-1} \mathbf{J}\mathbf{m}$ is a scalar too. Ultimately each term of the sum is also a scalar. The covariance matrix $\boldsymbol{\Sigma}$ is per definition symmetric (i.e. $\boldsymbol{\Sigma} = \boldsymbol{\Sigma}^{\mathrm{t}}$). Therefore using the distribution of the transpose B.10, one obtains that the second term of the sum is equal to $\mathbf{m}^{\mathrm{t}} \mathbf{J}^{\mathrm{t}} \boldsymbol{\Sigma}^{-1} \mathbf{d} = \left(\mathbf{d}^{\mathrm{t}} \boldsymbol{\Sigma}^{-1} \mathbf{J}\mathbf{m} \right)^{\mathrm{t}}$. In other words, the second term of the sum is the transpose of the third one. Since each term of the sum was identified to a scalar and that the transpose of a scalar is itself, one can write:

$$-\mathbf{m}^{\mathrm{t}}\mathbf{J}^{\mathrm{t}}\boldsymbol{\Sigma}^{-1}\mathbf{d} - \mathbf{d}^{\mathrm{t}}\boldsymbol{\Sigma}^{-1}\mathbf{J}\mathbf{m} = -2\mathbf{d}^{\mathrm{t}}\boldsymbol{\Sigma}^{-1}\mathbf{J}\mathbf{m} \tag{A.16}$$

or equally

$$-\mathbf{m}^{\mathrm{t}}\mathbf{J}^{\mathrm{t}}\boldsymbol{\Sigma}^{-1}\mathbf{d} - \mathbf{d}^{\mathrm{t}}\boldsymbol{\Sigma}^{-1}\mathbf{J}\mathbf{m} = -2\mathbf{m}^{\mathrm{t}}\mathbf{J}^{\mathrm{t}}\boldsymbol{\Sigma}^{-1}\mathbf{d} \tag{A.17}$$

the result of the derivation of equation A.17 is:

$$\frac{\partial}{\partial \mathbf{m}}\left(-2\mathbf{m}^{\mathrm{t}}\mathbf{J}^{\mathrm{t}}\boldsymbol{\Sigma}^{-1}\mathbf{d}\right) = -2\mathbf{J}^{\mathrm{t}}\boldsymbol{\Sigma}^{-1}\mathbf{d} \tag{A.18}$$

The fourth term of the sum $\mathbf{m}^{\mathrm{t}}\mathbf{J}^{\mathrm{t}}\boldsymbol{\Sigma}^{-1}\mathbf{J}\mathbf{m}$ can be rewritten using equation B.1:

$$\mathbf{m}^{\mathrm{t}}\mathbf{J}^{\mathrm{t}}\boldsymbol{\Sigma}^{-1}\mathbf{J}\mathbf{m} = \|\mathbf{J}\mathbf{m}\|^2_{\Sigma^{-1}} \tag{A.19}$$

Then using the definition of the norm, one calculates the partial derivatives:

$$\begin{aligned}
\frac{\partial}{\partial \mathbf{m}}\left(\|\mathbf{J}\mathbf{m}\|^2_{\Sigma^{-1}}\right) &= \frac{\partial}{\partial m_i}\left(\sum_j \sum_i m_i^2 \left(J^{\mathrm{t}}\Sigma^{-1}J\right)_{i,j}\right) \;\forall\, i,j & \text{(A.20)}\\
&= 2\sum_j \sum_i m_i \left(J^{\mathrm{t}}\Sigma^{-1}J\right)_{i,j} & \text{(A.21)}\\
&= 2\mathbf{m}\left(\mathbf{J}^{\mathrm{t}}\boldsymbol{\Sigma}^{-1}\mathbf{J}\right) & \text{(A.22)}
\end{aligned}$$

The last transition between A.21 and A.22 is done by identifying the double sum with the definition of the standard matrix multiplication.

The last expression for which one needs to calculate the derivative is $\mathrm{A}_p(\mathbf{m})$. The idea is to approximate the latter with the first three terms of its Taylor series:

$$\mathrm{A}_p(\mathbf{m}) = \mathrm{A}_p(\mathbf{a}) + \frac{\mathrm{A}'_p(\mathbf{a})}{1!}(\mathbf{m}-\mathbf{a}) + (\mathbf{m}-\mathbf{a})^{\mathrm{t}}\frac{\mathrm{A}''_p(\mathbf{a})}{2!}(\mathbf{m}-\mathbf{a}) + O(\mathbf{m}^k) \tag{A.23}$$

One assumes that the Taylor series converges toward $\mathrm{A}_p(\mathbf{m})$, under the restrictive conditions given by the Landau notation $O(\mathbf{m}^k)$:

$$|\mathrm{A}_p(\mathbf{m})| \leq M \left|(\mathbf{m}-\mathbf{a})^k\right| \qquad \text{for } k > 2 \tag{A.24}$$

In other words, the absolute value of the function is bounded by $M \cdot (\mathbf{m}-\mathbf{a})^k$ with a suitable choice of $M, k \in \mathbb{R}$. Thus the derivative of $\mathrm{A}_p(\mathbf{m})$ is approximated by taking the first three terms of the Taylor expansion:

$$\frac{\partial}{\partial \mathbf{m}}\mathrm{A}_p(\mathbf{m}) = \underbrace{\frac{\partial}{\partial \mathbf{m}}\mathrm{A}_p(\mathbf{a})}_{=0} + \frac{\partial}{\partial \mathbf{m}}\frac{\mathrm{A}'_p(\mathbf{a})}{1!}(\mathbf{m}-\mathbf{a}) + (\mathbf{m}-\mathbf{a})^{\mathrm{t}}\frac{\partial}{\partial \mathbf{m}}\frac{\mathrm{A}''_p(\mathbf{a})}{2!}(\mathbf{m}-\mathbf{a}) \tag{A.25}$$

$$\frac{\partial}{\partial \mathbf{m}}\mathrm{A}_p(\mathbf{m}) = \mathrm{A}'_p(\mathbf{a}) + \frac{2\mathrm{A}''_p(\mathbf{a})(\mathbf{m}-\mathbf{a})}{2} = \mathrm{A}'_p(\mathbf{a}) + \mathrm{A}''_p(\mathbf{a})(\mathbf{m}-\mathbf{a}) \tag{A.26}$$

The vector $\mathbf{a}$, that can be interpreted as the estimate of the model $\mathbf{a} = \mathrm{E}[\mathbf{m}]$, is set to 0. In the EIT case, this is a reasonable assumption since the probability of an increase or decrease of conductivity is assumed to be the same. Then one can assemble the expressions A.26, A.22 and A.18 in A.15,

$$-2\mathbf{J}^{\mathrm{t}}\boldsymbol{\Sigma}^{-1}\mathbf{d} + 2\mathbf{m}\mathbf{J}^{\mathrm{t}}\boldsymbol{\Sigma}^{-1}\mathbf{J} + \mathrm{A}'_p(0) + \mathrm{A}''_p(0)\mathbf{m} = 0 \tag{A.27}$$

$$2\mathbf{m}\mathbf{J}^{\mathrm{t}}\boldsymbol{\Sigma}^{-1}\mathbf{J} + \mathrm{A}''_p(0)\mathbf{m} = 2\mathbf{J}^{\mathrm{t}}\boldsymbol{\Sigma}^{-1}\mathbf{d} - \mathrm{A}'_p(0) \tag{A.28}$$

$$\mathbf{m}\mathbf{J}^{\mathrm{t}}\boldsymbol{\Sigma}^{-1}\mathbf{J} + \frac{\mathrm{A}''_p(0)}{2}\mathbf{m} = \mathbf{J}^{\mathrm{t}}\boldsymbol{\Sigma}^{-1}\mathbf{d} - \frac{\mathrm{A}'_p(0)}{2} \tag{A.29}$$

$$\mathbf{m}\left(\mathbf{J}^{\mathrm{t}}\boldsymbol{\Sigma}^{-1}\mathbf{J} + \frac{\mathrm{A}''_p(0)}{2}\right) = \mathbf{J}^{\mathrm{t}}\boldsymbol{\Sigma}^{-1}\mathbf{d} - \frac{\mathrm{A}'_p(0)}{2} \tag{A.30}$$

$$\mathbf{m} = \left(\mathbf{J}^{\mathrm{t}}\boldsymbol{\Sigma}^{-1}\mathbf{J} + \frac{\mathrm{A}''_p(0)}{2}\right)^{-1}\left(\mathbf{J}^{\mathrm{t}}\boldsymbol{\Sigma}^{-1}\mathbf{d} - \frac{\mathrm{A}'_p(0)}{2}\right) \tag{A.31}$$

Assuming that an appropriate choice of A_p gives $\mathrm{A}'_p(0) = 0$, it follows:

$$\mathbf{m} = \left(\mathbf{J}^{\mathrm{t}}\boldsymbol{\Sigma}^{-1}\mathbf{J} + \frac{\mathrm{A}''_p(0)}{2}\right)^{-1}\mathbf{J}^{\mathrm{t}}\boldsymbol{\Sigma}^{-1}\mathbf{d} \tag{A.32}$$

Using the notation $\frac{A_p''(0)}{2} \equiv \mathbf{A}_{\text{prio}}$, one gets:

$$\mathbf{m} = \underbrace{\left(\mathbf{J}^{\text{t}}\boldsymbol{\Sigma}^{-1}\mathbf{J} + \mathbf{A}_{\text{prio}}\right)^{-1}\mathbf{J}^{\text{t}}\boldsymbol{\Sigma}^{-1}}_{\underset{\text{def}}{=\mathbf{R}}}\mathbf{d} \tag{A.33}$$

or

$$\mathbf{m} = \mathbf{R}\mathbf{d} \tag{A.34}$$

where $\mathbf{R}$ is the MAP reconstruction matrix, which enables to find the best estimate of $\mathbf{m}$ knowing $\mathbf{d}$ with a certain noise covariance $\sum$ and a given knowledge $\mathbf{A}_{\text{prio}}$ of $\mathbf{m}$.

A.2 Regularization

This section gives a first general idea about regularization. Regularization is used to stabilize the solution of inverse problem [2] to ensure convergence. Inverse problems are very common in the nature, and arise each time one desires to fit data to a given model. In other words to fit one parameter space with an other. The scientists and engineers use regularization efficiently (possibly in conjunction with FEM) to solve various problems such as for instance:

- reconstructing the inside structure of an object knowing certain boundary condition (3D scanner, EIT and other objects from which surface measurements are made),
- image de-blurring,
- non-destructive testing.

EIT inverse problem is both ill-posed[3] and ill-conditioned[4], therefore regularization strategies are often needed in order to find a solutions[41]. The user of regularization technique should be aware that abusing of them could led to misleading solutions as extensively examined in [4]. In a medical application a misleading solution could potentially be harmful to the patient because the

[2] Textbooks about inverse problems are [92, 29]

[3] In ill-posed inverse problem small changes on the data have dramatic influences on the result.

[4] In ill-condition problem the number of unknowns is larger than independent equations.

medical care personal did not get the right information from the EIT imaging system.

Starting with equation A.12, and slightly modifying it by adding a scalar term λ in front of the operator $\widetilde{\mathrm{A}_p}$, then the MAP equation becomes:

$$\mathbf{m}_{\mathrm{MAP}} = \underset{\mathbf{m}}{\operatorname{argmin}} \left(\|\mathbf{d} - \mathbf{J}\mathbf{m}\|_{\Sigma}^2 + \lambda \widetilde{\mathrm{A}_p}(\mathbf{m}) \right) \tag{A.35}$$

where

λ is a scalar called the hyperparameter or regularization parameter,

$\widetilde{\mathrm{A}_p}(\mathbf{m})$ is equal to $\lambda \mathrm{A}_p(\mathbf{m})$.

Without doing the linearity assumption, one could consider a more general solution. This new solution is no more a one-step calculation, it is an iterative process:

$$\mathbf{m}_{\mathrm{it},k} = \underset{\mathbf{m}}{\operatorname{argmin}} \left(\|\mathbf{d} - \mathrm{F}(\mathbf{m})\|_{\Sigma}^2 + \lambda \|\mathbf{m} - \mathbf{m}_k\|_{\widetilde{\mathrm{A}_p}}^2 \right) \tag{A.36}$$

where

F is the forward model operator,

k is the iteration index starting from 0,

$\mathbf{m}_k$ if $k = 0$, $\mathbf{m}_0$ is the first guess of the solution; if $k > 0$, $\mathbf{m}_k$ is the previous solution.

By identifying F to the Jacobian operator and $\mathbf{m}_0 = 0$, one gets the one-step calculation solution obtained in equation A.35.

Regularization can be understood as finding the right balance between trusting the term $\|\mathbf{d} - \mathrm{F}(\mathbf{m})\|_{\Sigma}^2$ generated by the real data $\mathbf{d}$ and the noise Σ, and the term $\lambda \|\mathbf{m} - \mathbf{m}_k\|_{\widetilde{\mathrm{A}_p}}^2$ which contains certain knowledge about the observed medium, called prior (or a priori) information. The hyperparameter λ which multiply $\|\mathbf{m} - \mathbf{m}_k\|_{\widetilde{\mathrm{A}_p}}^2$ gives more or less weight to the latter compared to the $\|\mathbf{d} - \mathrm{F}(\mathbf{m})\|_{\Sigma}^2$ term and controls the above mentioned balance.

A.2.0.1 Tikhonov

Tikhonov proposed a simple regularization matrix which is the identity matrix. In other words, it means that one tries to fit the data but not if the model, $\mathbf{m}$, becomes to large.

$$\widetilde{\mathbf{A}_p} = \begin{bmatrix} 1 & 0 & 0 & 0 \cdots & 0 \\ 0 & 1 & 0 & \cdots & 0 \\ 0 & 0 & 1 & \cdots & 0 \\ \vdots & \vdots & \vdots & \ddots & 0 \\ 0 & 0 & \cdots & 0 & 1 \end{bmatrix} \tag{A.37}$$

A.2.0.2 Laplacian

The Laplacian regularization is a possible spacial smoothness filter, penalizing sharp transitions.

$$\widetilde{\mathbf{A}_p} = \begin{bmatrix} 1 & \frac{1}{2} & 0 & 0 \cdots & 0 \\ \frac{1}{2} & 1 & \frac{1}{2} & \cdots & 0 \\ 0 & \frac{1}{2} & 1 & \cdots & 0 \\ \vdots & \vdots & \vdots & \ddots & \frac{1}{2} \\ 0 & 0 & \cdots & \frac{1}{2} & 1 \end{bmatrix} \tag{A.38}$$

A.2.0.3 A priori spacial filter

A priori knowledge about what is inside the medium of interest can be used to construct a custom penalty operator privileging solutions matching closely the a priori information. This could be useful in medical imaging to highlight certain characteristics of a given signal. This procedure should be understood as a stronger interpretation of the data and not as an image resolution enhancement technique.

A.2.0.4 Kalman filter

Up to this point, we only take into account static information about $\mathbf{m}$ to construct the penalty term. But we could also considerate the temporal evolution of $\mathbf{m}$ and for example use temporal low pass filter. This technique is based on the well known Kalman filters. Using Kalman filters in conjunction with spacial filters would allow us to build spatio-temporal filters that filter

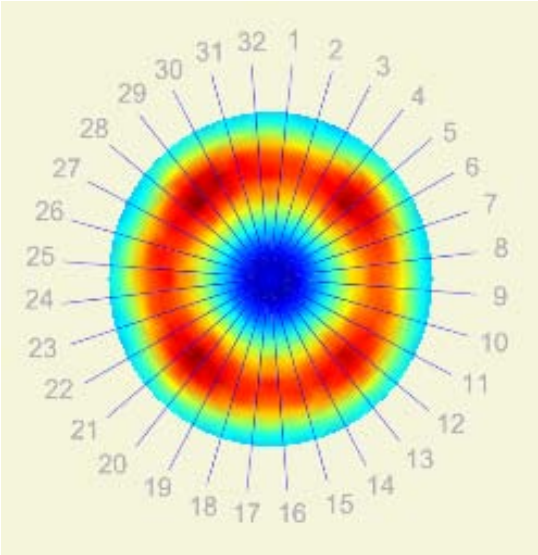

Figure A.1: EIT image obtained in the case the reference data set was not corresponding to the measurement strategy.

given frequencies in specific areas and other frequencies in other areas. For example, one could apply an high pass filter tuned for the heart signal on each pixel corresponding to the region where the heart is assumed to be. This technique could highlight the heart activity by filtering out the ventilation related impedance changes, without penalizing the solution for the lung regions.

A.3 Eigen EIT image

As already explained in section 3.3.6, the SVD can be used to decompose the sensitivity matrix $\mathbf{J}$ into its singular parameter space of voltage given by the $\mathbf{V}$ matrix of the SVD calculation. Now using the columns of $\mathbf{V}$ as inputs for the reconstruction algorithm, one can image the eigen EIT images, see figure A.2. Interestingly, some of the eigenimages obtained in figure A.2 are similar to the image obtained with the reconstruction algorithm when the reference data set was not corresponding to the correct measurement strategy. For example, if the reference corresponds to a measurement strategy with offset equal to 4 and the data are acquired with offset 7 this gives an EIT image with concentric circles (i.e. like the eigenimage last line, third column in figure A.2):

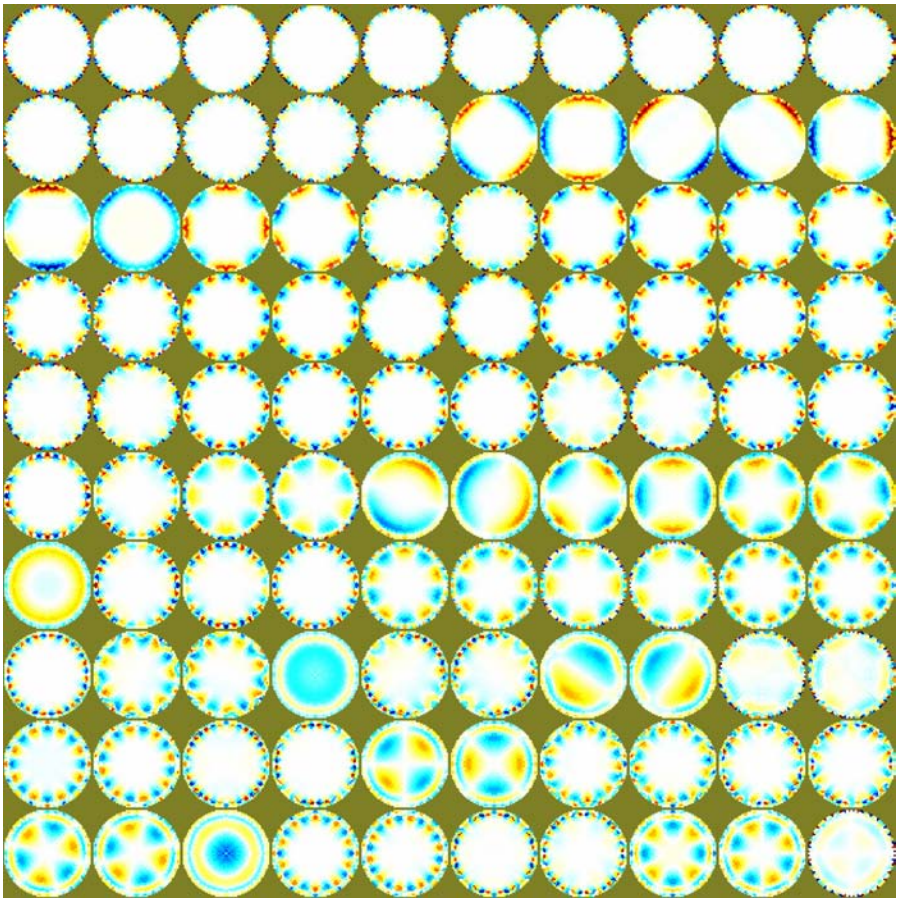

Figure A.2: The 100 first eigen EIT images produced by the 100 first singular vectors.

Appendix B

Mathematical Formulas

B.1 Notation

The mathematical expression in this thesis use the following notation convention:

- $\mathbf{A}$, $\mathbf{a}$: bold straight represents a matrix or a vector,
- A, a: normal italic represents a scalar (constant or variable),
- A, a: normal straight represents a function.

B.1.1 Linear Algebra

Name	Notation
Transpose	$\mathbf{A}^{\mathrm{t}}$
Inverse	$\mathbf{A}^{-1}$
Determinant	$\det(\mathbf{A})$
Trace	$\mathrm{trace}(\mathbf{A})$

B.1.2 Norm

Name	Notation	Formula
L_1norm	$\lvert\cdot\rvert$	$\sum_{i=1}^{N} \lvert x_i \rvert$
L_2 norm	$\lVert\cdot\rVert$	$\sqrt{\sum_{i=1}^{N} x_i^2}$
L_2 weighted norm	$\lVert\cdot\rVert_{\mathbf{D}}$	$\sqrt{\sum_{i=1}^{N} x_i^2 d_{ii}}$

where

$\mathbf{D}$ is square matrix $N \times N$

In the matrix form the L_2 weighted norm becomes for an arbitrary matrix $\mathbf{A}$:

$$\lVert \mathbf{A} \rVert_{\mathbf{D}} = \left(\mathbf{A}^{\mathbf{t}} \mathbf{D}^{-1} \mathbf{A} \right)^{\frac{1}{2}} \tag{B.1}$$

B.1.3 Vector Calculus

Name	Notation	Formula in Cartesian coordinate
Gradient	∇	$\nabla \mathbf{a} = \frac{\partial \mathbf{a}}{\partial x}\hat{\mathbf{x}} + \frac{\partial \mathbf{a}}{\partial y}\hat{\mathbf{y}} + \frac{\partial \mathbf{a}}{\partial z}\hat{\mathbf{z}}$
Divergence	$\nabla \cdot \mathbf{A}$	$\nabla \cdot \mathbf{A} = \frac{\partial \mathbf{A}_x}{\partial x} + \frac{\partial \mathbf{A}_y}{\partial y} + \frac{\partial \mathbf{A}_z}{\partial z}$
Curl	$\nabla \times$	$\nabla \times \mathbf{A} = \left(\frac{\partial \mathbf{A}_z}{\partial y} - \frac{\partial \mathbf{A}_y}{\partial z}\right)\hat{\mathbf{x}} + \left(\frac{\partial \mathbf{A}_x}{\partial z} - \frac{\partial \mathbf{A}_z}{\partial x}\right)\hat{\mathbf{y}} + \left(\frac{\partial \mathbf{A}_y}{\partial x} - \frac{\partial \mathbf{A}_x}{\partial y}\right)\hat{\mathbf{z}}$
Laplacian	$\triangle = \nabla^2$	$\nabla^2 = \nabla \cdot \nabla \mathbf{a} = \frac{\partial^2 \mathbf{a}_x}{\partial x^2} + \frac{\partial^2 \mathbf{a}_y}{\partial y^2} + \frac{\partial^2 \mathbf{a}_z}{\partial z^2}$

Where

$\mathbf{a}$ is a vector,

$\mathbf{A}$ is a vector field $\mathbf{A} = \begin{pmatrix} \mathbf{A}_x \\ \mathbf{A}_y \\ \mathbf{A}_z \end{pmatrix}$

B.1.4 Fixed-point number

The fixed-point number notation convention is the following: sQx.y. Where s stand for signed, x is the number of bits dedicated for the representation of the integer part of the number, and y is the number of bits dedicated for the representation of the decimal part of the number.

For example, a number R defined between $-1 \leq R < 1$ is represented with sQ1.y fixed-point number, then by setting y to 11 one gets a 11 bits precision of the decimal part (0.0005).

B.1.5 Measurement strategy notation convention

In this thesis, one proposes a notation to facilitate the description of measurement strategies. A single measurement is noted as follow [i-j, k-l], which

means that the current injecting pair was electrode i-j and that the differential voltage was measured between electrode k and l. A set of measurement is noted by gathering single measurement between braces as follow: {[i-j, k-l],[i-j, (k+1)-(l+1)],...}

B.2 Fourier transform of rect(at)

The rectangular function is given by:

$$\mathrm{rect}(a \cdot t) \quad = \quad \begin{cases} 0 & \text{if } |at| > \frac{1}{2} \\ \frac{1}{2} & \text{if } |at| = \frac{1}{2} \\ 1 & \text{if } |at| < \frac{1}{2} \end{cases} \equiv \begin{cases} 0 & \text{if } |t| > \frac{1}{2a} \\ \frac{1}{2} & \text{if } |t| = \frac{1}{2a} \\ 1 & \text{if } |t| < \frac{1}{2a} \end{cases} \tag{B.2}$$

it follows that the width Δt of $\mathrm{rect}(a \cdot t)$ is:

$$t = \frac{1}{2a} \tag{B.3}$$

using the Fourier transform ($\mathcal{F}$) of B.2 and B.3, on gets:

$$\mathcal{F}(\mathrm{rect}(a \cdot t)) = \frac{1}{|a|}\mathrm{sinc}(\frac{f}{a}) = \frac{1}{|a|}\frac{\sin(\frac{\pi f}{a})}{\frac{\pi f}{a}} = |2t|\,\frac{\sin(2\pi f t)}{2\pi f t} \tag{B.4}$$

A conservative approach to calculate the bandwidth of the sinc function is to search for its first zero. Thus for $\sin(\pi f \Delta t)$ to be 0, f should be:

$$|\Delta t|\,\frac{\sin(\pi f \Delta t)}{\pi f \Delta t} = 0 \qquad \text{if } f = \frac{1}{\Delta t} \tag{B.5}$$

Of course many other definition of the bandwidth could be used, such half-width maximum:

$$\mathrm{BW}_{\mathrm{hm}} = \frac{2}{3}\frac{1}{\Delta t} \tag{B.6}$$

B.3 argmax and argmin functions

Those special functions are noted as follow:

$$x_{\max} = \underset{x}{\operatorname{argmax}}(\mathrm{f}(x)) \tag{B.7}$$

$$x_{\min} = \underset{x}{\operatorname{argmin}}(\mathrm{f}(x)) \tag{B.8}$$

They maximize, or respectively minimize the function $\mathrm{f}(x)$ for a good choice of x.

B.4 Linear Algebra

B.4.1 Propriety of the transpose

$$(a\mathbf{A})^{\mathrm{t}} = a\mathbf{A}^{\mathrm{t}} \tag{B.9}$$

$$(\mathbf{AB})^{\mathrm{t}} = \mathbf{B}^{\mathrm{t}}\mathbf{A}^{\mathrm{t}} \tag{B.10}$$

$$\left(\mathbf{A}^{-1}\right)^{\mathrm{t}} = \left(\mathbf{A}^{\mathrm{t}}\right)^{-1} \tag{B.11}$$

B.5 Statistics and Probability

B.5.1 Bayes formulas

Let A and B be two statistical events, the Bayes theorem gives:

$$\mathrm{P}(A \cap B) = \mathrm{P}\left(A \mid B\right) P(B) = \mathrm{P}\left(B \mid A\right) \mathrm{P}(A) \tag{B.12}$$

after rearranging the terms this gives to Bayes theorem:

$$\mathrm{P}\left(A \mid B\right) = \frac{\mathrm{P}\left(B \mid A\right) \mathrm{P}(A)}{\mathrm{P}(B)} \tag{B.13}$$

B.5.2 Z-score

The z-score or standard score is a dimensionless quantity measuring the distance between the raw score and the mean, μ_x , in units of standard deviation of a given random variable, x.

$$z = \frac{x - \mu_x}{\mathrm{std}[x]} \tag{B.14}$$

Example of use: Let H_0 be a random variable with $\mu_{H_0} = 0$ and $\mathrm{std}[H_0] = \sigma$ and H_1 be a second random variable with $\mu_{H_1} \neq 0$ and $\mathrm{std}[H_0] = \mathrm{std}[H_1] = \sigma$. Then by measuring the random variable H_0 or H_1, one estimates the standard deviation σ. Both random variables having the same standard deviation, it is possible to measure the distance between μ_{H_0} and μ_{H_1} in unit of standard deviation:

$$z = \frac{\mu_{H_1} - \mu_{H_0}}{\sigma} = \frac{\mu_{H_1}}{\sigma} \tag{B.15}$$

For instance the result of $z = 3$ means that the chance that the measured value x is linked to an event H_0 is smaller than 0.13%, a contrario the probability that x is linked with the event H_1 is equal to 99.87%.

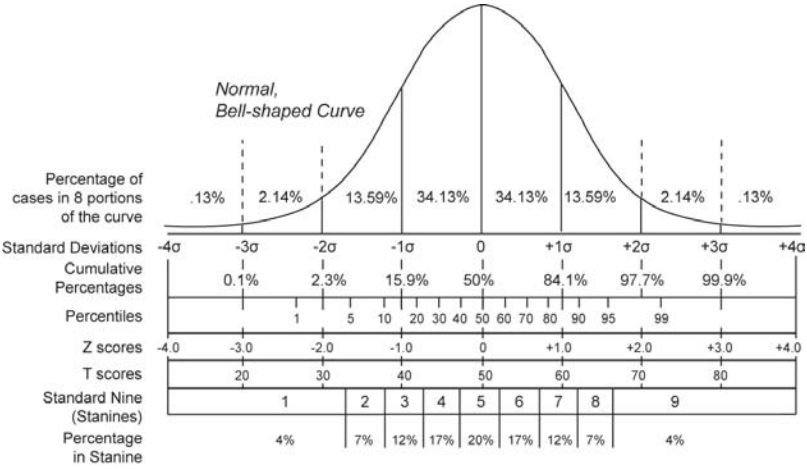

Figure B.1: The z-score and different other type of statistical tools are depicted on a normal bell-shaped curve. [source: http://en.wikipedia.org/wiki/File:Normal_distribution_and_scales.gif]

Appendix C

Physical and Chemical Formulas

C.1 Electrical conductivity for dissolved electrolyte

The electrical conductivity of a solution can be calculated using the value reported in table C.1. For example to calculate the conductivity of the physiological saline solution of 9 g/l of NaCl, one first has to calculate the weight of each of the salt component for a given quantity of salt, here 9 g. Thus the weight ratio relative to the salt (NaCl) is determined using the atomic weight of each of the salt component, which gives 39.6 % and 60.4 % for the Natrium (Na) and the Chlorine (Cl), respectively. Based on this information, the conductivity of the solution can be calculated:

$$5400\,\mathrm{mg/l} \cdot 2.14 \frac{\mu\mathrm{S/cm}}{\mathrm{mg/l}} + 3600\,\mathrm{mg/l} \cdot 2.13 \frac{\mu\mathrm{S/cm}}{\mathrm{mg/l}} = 1.9 \frac{\mathrm{S}}{\mathrm{m}} \tag{C.1}$$

The value reported in table C.1 have been measured at 298 K. A linear correction factor of $1.91 \cdot 10^{-7}\ \frac{\mathrm{S}}{\mathrm{m \cdot K}}$ can be introduced for temperature variation around 298 K.

Table C.1: Conductivity factor per ion type at 298 K., from [71]

Ion	conductivity Factor [μS/cm per mg/l]
cations	
Ca^{2+}	2.6
Mg^{2+}	3.82
K^{+}	1.84
Na^{+}	2.13
anions	
HCO_3^{-}	0.715
Cl^{-}	2.14
SO_4^{2-}	1.54
NO_3^{-}	1.15

C.2 Speed of Ion in water

The speed of ions in water $\overrightarrow{v_{\text{ion}}}$ resulting of the application of an external electrical field $\overrightarrow{E}$ can be calculated as follow [1]:

$$\overrightarrow{v_{\text{ion}}} = \frac{zq_0}{6\pi\eta R_{eh}}\overrightarrow{E}$$

where

z	is the number of charges,
q_0	is the elementary charge,
η	is the viscosity of the medium (about 1 mPa $\cdot$ s),
R_{eh}	is the effective hydrodynamic radius (about 100 pm).

Let the electrical field be 1 V/cm, a rough estimate of the ionic speed gives:

$$\overrightarrow{v_{\text{ion}}} = \frac{zq_0}{6\pi\eta R_{eh}}\overrightarrow{E} = \frac{1 \cdot 1.69 \cdot 10^{-19}\text{C}}{6 \cdot \pi \cdot 10^{-3}\text{Pa} \cdot \text{s} \cdot 100 \cdot 10^{-12}\text{m}} 100\frac{\text{V}}{\text{m}} = 8.97 \cdot 10^{-6}\frac{\text{m}}{\text{s}} \tag{C.2}$$

C.2.1 Physical Units

Table C.2: The basic physical units.

Name	Notation
meter	[m]
second	[s]
mass	[kg]
Coulomb	[C]

[1] BioMEMS Lecture 4. Electrophoresis and PCR on chip, Prof. Olivier Guenat

Table C.3: The derivated physical units.

Name	Notation	In basic physical units
Ampere	[A]	$[\mathrm{A}] = \left[\frac{\mathrm{C}}{\mathrm{s}}\right]$
Newton	[N]	$[\mathrm{N}] = \left[\frac{\mathrm{kg}\cdot\mathrm{m}}{\mathrm{s}^2}\right]$
Farad	[F]	$[\mathrm{F}] = \left[\frac{\mathrm{A}\cdot\mathrm{s}}{\mathrm{V}}\right] = \left[\frac{\mathrm{s}}{\Omega}\right]$
Tesla	[T]	$[\mathrm{A}] = \left[\frac{\mathrm{V}\cdot\mathrm{s}}{\mathrm{m}^2}\right]$
Ohm	[Ω]	$[\mathrm{A}] = \left[\frac{\mathrm{m}^2\cdot\mathrm{kg}}{\mathrm{s}^3\cdot\mathrm{A}^2}\right]$
Siemens	$[S]$	$[S] = \left[\frac{1}{\Omega}\right]$

Appendix D

Raw EIT Signals

D.1 Introduction

The goal of this appendix is to give the reader some insight about the raw signals generated by the developed EIT system. The signals are directly recorded using the oscilloscope (LeCroy, WaveRunner 204MXi). The three most interesting situation or measurement setups are depicted:

- Figure D.1: General view of the EIT signal over a whole measurement frame,
- Figure D.2: Transition signals during a current source switch,
- Figure D.3: Transition signals during a measurement switch.

The signal after the differential amplifier measured over a whole measurement frame exhibit the known “U-shape”. The “spikes”, see figure D.1, on the same signal are generated by the differential amplifier saturating to the rail voltage almost each time a transition occurs. A transition is characterized by the switching of the current source or the measuring pair of electrodes. During the transition process the signal values are of no use for the image reconstruction. As seen in section 6.4.1.1, the signal needs a while after the switching occurs to stabilize itself. Those transitions are observed in figure D.2 and D.3 in detail. The transitions are pretty stable overtime and exhibit similar pattern, which is very convenient for time difference imaging, because one do not need to wait for the signal to stabilize around an absolute value, but it only has to follow the same “path”.

D.2 General overview

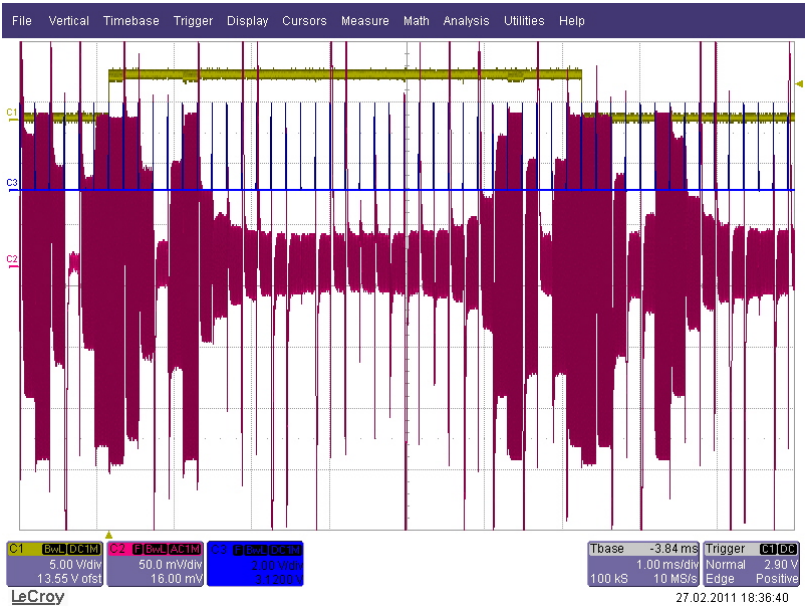

Figure D.1: Raw signal offset=4 “U-shape”. The yellow signal, used as trigger, corresponds to the injection switch digital command signal of active electrode 1. The red signal is measured directly after the differential instrument amplifier. The portion of the red signal comprised underneath the yellow signal at 5 V corresponds to a whole measurement frame period with injection between electrode 1 and 6. The blue signal is the synchronization signal, each time a pulse is generated the node fetch its next state in the scanning table. The red signal comprise between two blue signal pulse corresponds to a whole measurement windows.

D.3 Current source transition

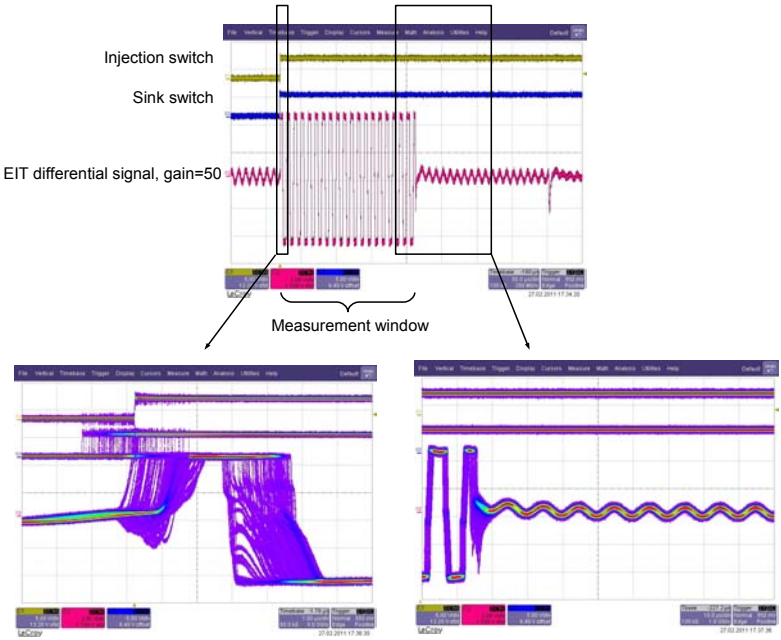

Figure D.2: Transition signals during a current source switch event. As depicted in the persistence plot (i.e. the two lower plots), the transitions of the signal often follow the same scheme. First, it goes to saturation and then the signal quickly follows a stable path, which means that it is not absolutely necessary to wait for the signal to be completely stabilized around an absolute value before using it for differential imaging.

D.4 Measurement transition

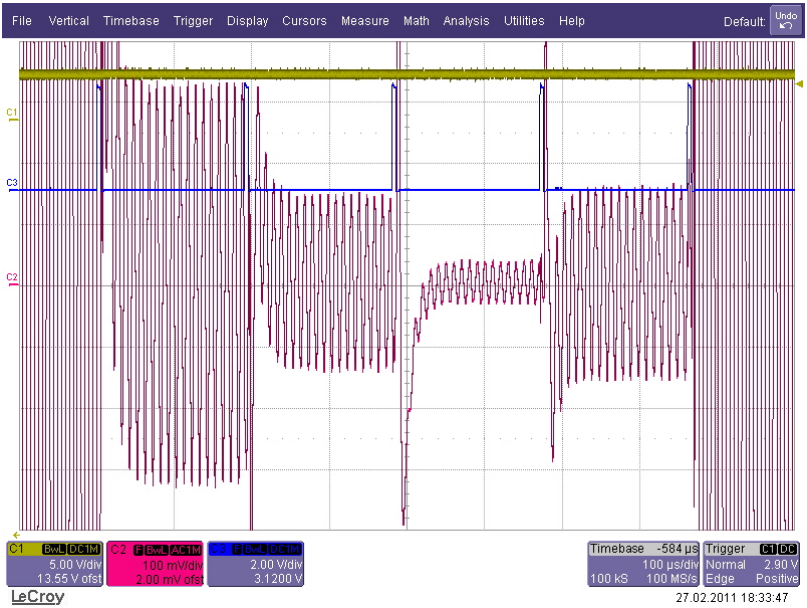

Figure D.3: Transition signals during a measurement switch event. The yellow signal correspond to the injection switch digital command signal of active electrode 1. The red signal is measured directly after the differential instrument amplifier. The blue signal is the synchronization signal. One can clearly see the output of the differential instrument amplifier saturating between two measurements. The transition signals can also be observed.

Bibliography

[1] Medical electrical equipment part 1: General requirements for basic safety and essential performance, iec 60601-1:2005, 2005.

[2] In-amp noise. 2008. URL http://www.analog.com/static/imported-files/tutorials/MT-065.pdf.

[3] Code of federal regulations: Title 21 - food and drugs, 2010. URL http://www.gpo.gov/fdsys/pkg/CFR-2010-title21-vol3/pdf/CFR-2010-title21-vol3-sec172-840.pdf.

[4] A. Adler and W. R. Lionheart. Uses and abuses of eidors: an extensible software base for eit. *Physiol Meas*, 27(5):S25–S42, 2006. doi: 10.1088/0967-3334/27/5/S03.

[5] A. Adler, R. Youmaran, and W. R. B. Lionheart. A measure of the information content of eit data. *Physiological Measurement*, 29(6):S101, 2008. URL http://stacks.iop.org/0967-3334/29/i=6/a=S09.

[6] A. Adler, P. O. Gaggero, and Y. Maimaitijiang. Distinguishability in eit using a hypothesis-testing model. *Journal of Physics: Conference Series*, 224:012056, 2010.

[7] A. Adler, Y. Maimaitjan, P. Gaggero, S. Reidt, and S. Böhm. Phantom based system to evaluate electrical impedance tomography (eit) performance. *CSEM scientific and annual report 2010*, 2010.

[8] D. W. Allan. Time and frequency (time-domain) characterization, estimation, and prediction of precision clocks and oscillators. *IEEE Transactions on Ultrasonics, Ferroelectrics and Frequency Control*, 34 (6):647–654, 1987. URL http://tf.boulder.nist.gov/general/pdf/752.pdf.

[9] M. B. Amato, C. S. Barbas, D. M. Medeiros, R. B. Magaldi, G. P. Schettino, G. Lorenzi-Filho, R. A. Kairalla, D. Deheinzelin, C. Munoz,

R. Oliveira, and et al. Effect of a protective-ventilation strategy on mortality in the acute respiratory distress syndrome. *The New England Journal of Medicine*, 338(6):347–354, 1998. URL http://www.ncbi.nlm.nih.gov/pubmed/9449727.

[10] AnalogDevices. *ad8221 datasheet*. URL http://www.analog.com/static/imported-files/data_sheets/AD8221.pdf.

[11] ARDSN. Ventilation with lower tidal volumes as compared with traditional tidal volumes for acute lung injury and the acute respiratory distress syndrome. the acute respiratory distress syndrome network. *The New England Journal of Medicine*, 342(18):1301–8, 2000. URL http://www.ncbi.nlm.nih.gov/pubmed/10793162.

[12] M. Assenheimer, O. Laver-Moskovitz, D. Malonek, D. Manor, U. Nahaliel, R. Nitzan, and A. Saad. The t-scan technology: electrical impedance as a diagnostic tool for breast cancer detection. *Physiological Measurement*, 22(1):1–8, 2001. URL http://www.ncbi.nlm.nih.gov/pubmed/11236870.

[13] D. C. Barber. A review of image reconstruction techniques for electrical impedance tomography. *Medical Physics*, 16(2):162–169, 1987. URL http://www.ncbi.nlm.nih.gov/pubmed/2654593.

[14] J. Batlle-Aguilar, S. Schneider, M. Pessel, P. Tucholka, Y. Coquet, and P. Vachier. Axisymetrical infiltration in soil imaged by non-invasive electrical resistivimetry. *Soil Science Society of the America Journal*, 73:510–520, 2009.

[15] A. Borsic, R. Halter, Y. Wan, A. Hartov, and K. D. Paulsen. Electrical impedance tomography reconstruction for three-dimensional imaging of the prostate. *Physiological Measurement*, 31(8):S1–S16, 2010. URL http://www.ncbi.nlm.nih.gov/pubmed/20647619.

[16] N. Bowler. Four-point potential drop measurements for materials characterization (topical review). *Measurement Science and Technology*, 22(1):012001 (11pp), 2011. URL http://stacks.iop.org/0957-0233/22/i=1/a=012001?key=crossref.d3e26130b2f11932ff413477955ac66d.

[17] H. T. Brash Bill. Electrical safety testing, June 2006. URL www.1ash.net/ElectricalSafety-PrintVersion1.doc.

[18] V. Cherepenin, A. Karpov, A. Korjenevsky, V. Kornienko, A. Mazaletskaya, D. Mazourov, and D. Meister. A 3d electrical impedance tomography (eit) system for breast cancer detection. *Physiological*

Measurement, 22(1):9–18, 2001. URL http://www.ncbi.nlm.nih.gov/pubmed/11236894.

[19] V. Cherepenin, A. Karpov, A. Korjenevsky, V. Kornienko, A. Mazaletskaya, D. Mazourov, and D. Meister. A 3d electrical impedance tomography (eit) system for breast cancer detection. *Physiological Measurement*, 22, 2001.

[20] E. L. V. Costa, J. B. Borges, A. Melo, F. Suarez-Sipmann, C. Toufen, S. H. Bohm, and M. B. P. Amato. Bedside estimation of recruitable alveolar collapse and hyperdistension by electrical impedance tomography. *Intensive Care Medicine*, 35(6):1132–1137, 2009. URL http://www.ncbi.nlm.nih.gov/pubmed/19255741.

[21] E. L. V. Costa, R. G. Lima, and M. B. P. Amato. Electrical impedance tomography. *Current Opinion in Critical Care*, 15(1):18–24, 2009. URL http://content.wkhealth.com/linkback/openurl?sid=WKPTLP:landingpage&an=00075198-200902000-00004.

[22] T. Dahlin and B. Zhou. A numerical comparison of 2d resistivity imaging with 10 electrode arrays. *Geophysical Prospecting*, 52(5):379–398, 2004. URL http://www.blackwell-synergy.com/links/doi/10.1111/j.1365-2478.2004.00423.x.

[23] W. Daily, A. Ramirez, A. Binley, and D. LaBrecque. Electrical resistance tomography - theory and practice. *Near Surface Geophysics. Society of Exploration Geophysicists, šTulsa*, pages 525–550, 2005.

[24] J. B. De Lema, E. Serrano, T. Feixas, N. Calaf, M. V. Camacho, P. J. Riu, and P. Casan. Assessment of differential lung function by electrical impedance tomography. *Archivos De Bronconeumologia*, 44(8):408–412, 2008.

[25] S. Dharia, H. E. Ayliffe, and R. D. Rabbitt. Single cell electric impedance topography: mapping membrane capacitance. *Lab on a Chip*, 9(23):3370–3377, 2009. URL http://www.ncbi.nlm.nih.gov/pmc/articles/PMC3004743/.

[26] F. Dickin and M. Wang. Electrical resistance tomography for process tomography. 7:247–260, 1996.

[27] *Technical data sheet: PulmoVista 500*. Dräger Medical GmbH. URL http://campaigns.draeger.com/pulmovista500/en/.

[28] ECMA. Common language infrastructure (cli) partitions i to vi, ecma-335, december 2010. URL http://www.ecma-international.org/publications/files/ECMA-ST/ECMA-335.pdf.

[29] H. W. Engl, M. Hanke, and A. Neubauer. *Regularization of Inverse Problems*. Kluwer, 1996. URL http://scholar.google.com/scholar?hl=en&btnG=Search&q=intitle:Numerical+Treatment+of+Inverse+Problems+in+Differential+and+Integral+Equations#0.

[30] A. Fagerberg, O. Stenqvist, and A. Aneman. Monitoring pulmonary perfusion by electrical impedance tomography: an evaluation in a pig model. *Acta Anaesthesiologica Scandinavica*, 53(2):152–158, 2009. URL http://blackwell-synergy.com/doi/abs/10.1111/j.1399-6576.2008.01847.x.

[31] P. O. Gaggero. Effect of oscillator instability on gnss signal integration time. Master's thesis, University of Neuchâtel, 2008. URL http://www.gaggero.ch/PublicDocuments/msc_thesis_gaggero_feb08.pdf.

[32] B. M. Graham and A. Adler. Objective selection of hyperparameter for eit. *Physiol. Meas.*, 2006.

[33] D. J. Griffiths. *Introduction to electrodynamics*. Pearson Benjamin Cumming, 1998.

[34] H. Griffiths, M. G. Tucker, J. Sage, and W. G. Herrenden-Harker. An electrical impedance tomography microscope. *Physiological Measurement*, 17 Suppl 4A(2A):A15–A24, 1996.

[35] H. Griffiths, M. G. Tucker, J. Sage, and W. G. Herrenden-Harker. An eletrical impedance tomography microscope. *Physiology Measurment*, 17:A15–A24, 1996.

[36] R. Guardo, C. Boulay, B. Provost, D. Bohsina, and S. Mallette. Microcontroller based active electrodes for impedance tomography. *Engineering in Medicine and Biology Society*, 1:545 – 546, 1994.

[37] R. Guardo, J. Jehanne-Lacasse, A. P. Moumbe, and H. Gagnon. System front-end design for concurrent acquisition of electroencephalograms and eit data. *Journal of Physics: Conference Series*, 224, 2010. doi: 10.1088/1742-6596/224/1/012012.

[38] G. Hahn, T. Dudykevych, I. Frerichs, F. Thiel, and G. Hellige. A high performance electrical impedance tomography (eit) system for clinical evaluation studies and space application. *Proc Conf 2nd European Medical and Biol Eng*, pages 110–111, 2002.

[39] G. Hahn, A. Just, T. Dudykevych, I. Frerichs, J. Hinz, M. Quintel, and G. Hellige. Imaging pathologic pulmonary air and fluid accumulation by functional and absolute eit. *Physiol. Meas.*, 2006.

[40] R. Halter, A. Hartov, and K. D. Paulsen. Design and implementation of a high frequency electrical impedance tomography system. *Physiological Measurement*, 25(1):379–390, 2004.

[41] P. C. Hansen. *Rank-Deficient and Discrete Ill-Posed Problems*. SIAM, Philadelphia, 1998. URL `http://books.google.com/books?id=3vxh3p03p6AC&printsec=frontcover`.

[42] H. A. Haus and J. R. Melcher. *Electromagnetic Fields and Energy*. Prentice-Hall, 1989. doi: 9780132490207. URL `http://ocw.mit.edu`.

[43] D. Holder. *Electrical Impedance Tomography*. Institute of Physics, Bristol, UK, 1nd, edition, 2005. ISBN 0-7503-0952-0.

[44] K. Imfeld, S. Neukom, A. Maccione, Y. Bornat, S. Martinoia, P.-A. Farine, M. Koudelka-Hep, and L. Berdondini. Large-scale, high-resolution data acquisition system for extracellular recording of electrophysiological activity. *IEEE Transactions on Biomedical Engineering*, 55(8):2064–2073, 2008. URL `http://www.ncbi.nlm.nih.gov/pubmed/18632369`.

[45] D. Isaacson. Distinguishability of conductivities by electric current computed tomography. *IEEE Trans. Med. Imaging*, Mi-5(2):91–95, 1986.

[46] H.-C. Jelena. 1/f noise characterization in cmos transistors in 0.13um technology. In *Proceedings of the 24st Norchip Conference*, 2006.

[47] J. M. Kahn, C. H. Goss, P. J. Heagerty, A. A. Kramer, C. R. OBrien, and G. D. Rubenfeld. Hospital volume and the outcomes of mechanical ventilation. *The New England Journal of Medicine*, 355(1):41–50, 2006. URL `http://www.ncbi.nlm.nih.gov/pubmed/16822995`.

[48] A. Kemna. *Tomographic Inversion of Complex Resistivity*. PhD thesis, Ruhr Universitat, 2000.

[49] A. Kemna, A. M. Binley, A. Ramirez, and W. Daily. Complex resistivity tomography for environmental applications. *Chemical Engineering Journal*, 77(1-2):11–18, 2000. URL `http://www.sciencedirect.com/science/journal/13858947`.

[50] P. B. Kenington. *RF and baseband techniques for software defined radio*. ARTECH HOUSE, 2005.

[51] W. Kester. Taking the mystery out of the infamous formula, "snr = 6.02n + 1.76db," and why you should care. *Analog device Tutorial*, Mt-001, 2008.

[52] W. Kester. Dac interface fundamentals. *Analog device Tutorial*, Mt-019, 2008.

[53] D. Y. Kim, H. Wi, P. J. Yoo, T. I. Oh, and E. J. Woo. Performance evaluation of khu mark2 parallel multi-frequency eit system. *Journal of Physics Conference Series*, 224:012013, 2010. URL `http://stacks.iop.org/1742-6596/224/i=1/a=012013?key=crossref.61cea852066f851aeeab88f247c3a662`.

[54] P. W. Kunst, G. Vazquez De Anda, S. H. Böhm, T. J. Faes, B. Lachmann, P. E. Postmus, and P. M. De Vries. Monitoring of recruitment and derecruitment by electrical impedance tomography in a model of acute lung injury. *Critical Care Medicine*, 28(12):3891–3895, 2000. URL `http://www.ncbi.nlm.nih.gov/pubmed/11153631`.

[55] J. H. Li, C. Joppek, and U. Faust. In vivo eit electrode system with 32 interlaced active electrodes. *Medical & Biological Engineering & Computing*, 34(3):253–256, 1996.

[56] J. H. Li, C. Joppek, and U. Faust. Fast eit data acquisition system with active electrodes and its application to cardiac imaging. *Physiological Measurement*, 17 Suppl 4A:A25–A32, 1996.

[57] Y. Li, E. Tesselaar, J. Örman, A. Samuelsson, M. Amato, J. B. Borges, S. Böhm, and F. Sjöberg. Hyperoxia induces dose-dependent pulmonary vasodilatation and does not change ventilation as assessed by electrical impedance tomography.

[58] O. P. LINDERHOLM. *Two-dimensional microimpedance imaging for cell culture monitoring.* PhD thesis, Ecole Polytechnique Federale de Lausanne, 2006.

[59] H. Liu. *A high-resolution microscopic electrical impedance imaging modality: scanning impedance imaging.* PhD thesis, Brigham Young University, 2007.

[60] N. Liu, G. J. Saulnier, J. C. Newell, D. Isaacson, and T.-J. Kao. *ACT4: A High-Precision, Multi-frequency Electrical Impedance Tomography.* PhD thesis.

[61] Y. Maimaitijiang, S. Böhm, O. Jaber, and A. Adler. Poster: A phantom based system to evaluate eit performance. In *Int. Conf. Electrical Bio-Impedance & Electrical Impedance Tomography Gainville*, 2010.

[62] R. Mancini. *Op Amps For Everyone.* texas instruments, 2002.

[63] H. Matthiessen, D. Weismann, J. Li, and Y. Garber. Electroimpedance tomograph with common-mode signal suppression, 2007.

[64] A. McEwan, A. Romsauerova, R. Yerworth, L. Horesh, R. Bayford, and D. Holder. Design and calibration of a compact multi-frequency eit system for acute stroke imaging. *Physiological Measurement*, 27(5):S199–210, 2006. URL `http://www.ncbi.nlm.nih.gov/entrez/query.fcgi?cmd=Retrieve&db=PubMed&dopt=Citation&list_uids=16636411`.

[65] A. L. McEwan, A. Romsauerova, L. Horesh, and D. holder. Performance improvents in a mf-eit system for acute stroke: The uck mk2.5. In *IFMBE procedings*, 2006.

[66] T. Meier, H. Luepschen, J. Karsten, T. Leibecke, M. Grossherr, H. Gehring, and S. Leonhardt. Assessment of regional lung recruitment and derecruitment during a peep trial based on electrical impedance tomography. *Intensive Care Medicine*, 34(3):543–550, 2008. URL `http://www.ncbi.nlm.nih.gov/pubmed/17653529`.

[67] J. Minner. *Die Elektroimpedanztomographie als Verfahren zur Lageevaluation des Doppellumentubus*. PhD thesis, Albert-Ludwigs-Universität Freiburg im Breisgau, 2010.

[68] M. Noel and B. Xu. Archaeological investigation by electrical resistivity tomography: a preliminary study. *Geophysical Journal International*, 107:95–102, 1991.

[69] T. I. Oh, H. Koo, K. H. Lee, S. M. Kim, J. Lee, S. W. Kim, J. K. Seo, and E. J. Woo. Validation of a multi-frequency electrical impedance tomography (mfeit) system khu mark1: impedance spectroscopy and time-difference imaging. *Physiological Measurement*, 29(3):295–307, 2008. URL `http://www.ncbi.nlm.nih.gov/pubmed/18367806`.

[70] R. A. Pease. A comprehensive study of the howland current pump. *National Semiconductor Application Note 1515*, Application Note 1515, 2008. URL `http://www.national.com/an/AN/AN-1515.pdf`.

[71] H. Project. *Understanding electrical conductivity*. World Bank & Government of The Netherlands, 1999. URL `http://www.cwc.nic.in/main/HP/download/08%20Understanding%20EC.pdf`.

[72] C. Putensen, H. Wrigge, and J. Zinserling. Electrical impedance tomography guided ventilation therapy. *Current Opinion in Critical Care*, 13(3):344–350, 2007. URL `http://www.ncbi.nlm.nih.gov/pubmed/17468569`.

[73] B. Rigaud, S. Y, C. N, and M. JP. Experimental acquisition system for impedance tomography with active electrode approach. *Medical & Biological Engineering & Computing*, 31:593–599, 1993.

[74] N. Robitaille. *Developpement d un systeme de tomographie d impedance electrique multifrequence pour la detection de l oedeme pulmonaire*. PhD thesis, Universite de Montreal, 2007.

[75] N. Robitaille, R. Guardo, I. Maurice, A. E. Hartinger, and H. Gagnon. A multi-frequency eit system design based on telecommunication signal processors. *Physiological Measurement*, 30(6):S57, 2009. doi: 10.1088/0967-3334/30/6/S04. URL `http://stacks.iop.org/0967-3334/30/i=6/a=S04`.

[76] M. Rogantini. Electrical impedance tomography, sbc, hardware manual. November 2010.

[77] J. Rosell and P. Riu. Common-mode feedback in electrical impedance tomography. *Clinical physics and physiological measurement an official journal of the Hospital Physicists Association Deutsche Gesellschaft fur Medizinische Physik and the European Federation of Organisations for Medical Physics*, 13 Suppl A(1):11–14, 1992. URL `http://www.ncbi.nlm.nih.gov/pubmed/1587082`.

[78] A. S. Ross, G. J. Saulnier, J. C. Newell, and D. Isaacson. Current source design for electrical impedance tomography. *Physiological Measurement*, 24(2):509–516, 2003. URL `http://ieeexplore.ieee.org/lpdocs/epic03/wrapper.htm?arnumber=1279429`.

[79] G. D. Rubenfeld and M. S. Herridge. Epidemiology and outcomes of acute lung injury. *Chest*, 131(2):554–562, 2007. URL `http://www.ncbi.nlm.nih.gov/pubmed/17296661`.

[80] R. Sarpeshkar, T. Delbruck, and C. A. Mead. White noise in mos transistors and resistors. *IEEE Circuits and Devices Magazine*, 9(6):23–29, 1993. URL `http://ieeexplore.ieee.org/lpdocs/epic03/wrapper.htm?arnumber=261888`.

[81] G. J. Saulnier, N. Liu, C. Tamma, H. Xia, T.-J. Kao, J. C. Newell, and D. Isaacson. An electrical impedance spectroscopy system for breast cancer detection. *Conference Proceedings of the International Conference of IEEE Engineering in Medicine and Biology Society*, 2007: 4154–4157, . URL `http://ieeexplore.ieee.org/xpls/abs_all.jsp?arnumber=4353251`.

[82] G. J. Saulnier, N. Liu, C. Tamma, H. Xia, T.-J. Kao, J. C. Newell, and D. Isaacson. An electrical impedance spectroscopy system for breast cancer detection. *Conference Proceedings of the International Conference of IEEE Engineering in Medicine and Biology Society*, 2007: 4154–4157, . URL `http://ieeexplore.ieee.org/xpls/abs_all.jsp?arnumber=4353251`.

[83] O. Scherzer, M. Fornasier, and H. Rauhut. *Handbook of Mathematical Methods in Imaging*. Springer New York, 2011. URL `http://www.springerlink.com/content/l38372776p043060/`.

[84] A. Seagar, T. Yeo, and R. Bates. Full-wave computed tomography part 2: Resolution limits. *IEEE Proceedings*, 131(8), november 1984.

[85] A. Seagar, T. Yeo, and R. Bates. Fuli-wave computed tomography part 4: Low-frequency electric current ct. *IEEE Proceedings*, 132(7), november 1985.

[86] G. R. Shaw, Y. Goussard, and R. Guardo. Linearization of the forward problem in electrical impedance tomography. *Proc. IEEE/EMBS*, pages 82–83, 1993. doi: 10.1109/IEMBS.1993.978440.

[87] S. W. Smith. *Digital Signal Processing: A Practical Guide for Engineers and Scientists*. 2002. URL `http://www.dspguide.com`.

[88] J. Sola, A. Adler, A. Santos, G. Tusman, F. S. Sipmann, and S. H. Bohm. Non-invasive monitoring of central blood pressure by electrical impedance tomography (eit): first experimental evidence. *Medical & Biological Engineering & Computing*, 2011.

[89] T. Steinmetz, S. Kurz, and M. Clemens. Domains of validity of quasistatic and quasistationary field approximations. In *International Symposium on Theoretical Electrical Engineering (ISTET)*, pages 271–275, 2009.

[90] T. Sun, S. Tsuda, K.-P. Zauner, and H. Morgan. On-chip electrical impedance tomography for imaging biological cells. *Biosensors and Bioelectronics*, 25(5):1109–1115, 2010. URL `http://eprints.ecs.soton.ac.uk/18039/`.

[91] H. S. Tapp, A. J. Peyton, E. K. Kemsley, and R. H. Wilson. Chemical engineering applications of electrical process tomography. *Sensors and Actuators B: Chemical*, 92:17–24, 2003.

[92] A. Tarantola. *Inverse Problem Theory and Methods for Model Parameter Estimation*, volume 1. SIAM, 2005. URL `http://www.ipgp.fr/~tarantola/`.

[93] TexasInstruments. *opa134*, december 1997. URL http://focus.ti.com/lit/ds/symlink/opa2134.pdf.

[94] TexasInstruments. *DAC904*, May 2002. URL http://focus.ti.com.cn/cn/lit/ds/symlink/dac904.pdf.

[95] TexasInstruments. *THS4502*, January 2004. URL http://focus.ti.com/lit/ds/symlink/ths4503.pdf.

[96] U. Tietze and C. Schenk. *Electronic Circuits*. Springer, Berlin, DE, 2nd, edition, 2008. ISBN 978-3-540-00429-5.

[97] T. Urdan. *Statistics in plain English*. Lawrence Erlbaum Associates, 2005. ISBN 9780805852417. URL http://books.google.ch/books?id=1a5Jz6oa3qoC.

[98] J. R. Vig. Quartz crystal resonators and oscillators, 2004. URL http://www.nofech.co.il/Vig-tutorial%208.5.2.0_files/frame.html.

[99] R. A. WILLIAMS, A. NISBET, F. J. DICKIN, and S. E. TAYLOR. Microelectrical tomography of flowing colloidal dispersions and dynamic interfaces. *Chemical engineering journal and the biochemical engineering journal*, 56:143–148, 1995.

[100] A. J. Wilson, P. Milnes, A. R. Waterworth, R. H. Smallwood, and B. H. Brown. Mk3.5: a modular, multi-frequency successor to the mk3a eis/eit system. *Physiological Measurement*, 22:49–54, 2001.

List of Figures

List of Tables

Nomenclature

ADC	Analog to Digital Converter
DAC	Digital to Analog Converter
DSP	Digital Signal Processing
EIT	Electrical Impedance Tomography
FFC	Flat Flexible Cable
FPGA	Field-Programmable Gate Array
FSR	Full Scale Range
GUI	Graphical User Interface
LED	Light Emitting Diode
MAP	Maximum A posteriori Probability
NCO	Numerically-Controled Oscillator
NTC	Negative Temperature Coeficient
PCB	Printed Circuit Board
SNR	Signal to Noise Ratio

Abstract
Electrical Impedance Tomography (EIT) calculates an image of the conductivity distribution within a body from electrical stimulation and measurements at the body surface. This work develops advances in signal acquisition hardware, optimization of stimulation patterns, and analysis of detection limits for EIT. The EIT data acquisition and image reconstruction process is systematically analyzed with respect to the influence of noise and other measurement deficiencies on image quality. A complete EIT system with 32 active electrodes has been developed, with which the theoretical predictions could be verified and practical applications could be studied.
The novel concept of distinguishability is developed for a theoretical analysis of EIT system performance. It measures the likelihood that the measured differential EIT signal is generated by actual impedance changes and not by random fluctuations. This distinguishability criterion can be considered as a signal-to-noise ratio, and it serves as a valuable benchmark to assess the performance of EIT systems. Using numerical simulations, we have studied the optimum signal acquisition strategy for differential EIT signals, in order to maximize image quality. The most favorable angles between injecting and sinking electrode are found in the range from 60 to 150 degrees. We have also studied, theoretically as well as experimentally, the miniaturization limits of EIT systems. It is concluded that EIT system miniaturization is essentially determined by the Joule heating effect and the cooling rate of the sample volume. When scaling EIT systems up to very large dimensions, electronic noise on the sample (current injection and voltage measurements) finally limits the distinguishability in reconstructed EIT images.
A prototype of the developed hardware architecture was realized and proof-of-concept studies were carried out using both thoracic-EIT and the micro-EIT setups. As a major application of the work carried out in this thesis, we have demonstrated the capability of the developed EIT system to serve as a cost-effective real-time monitor for the reliable monitoring of the ventilation and cardiac related impedance changes on patients. The advances presented in this work can help build the capability of EIT to monitor and optimize mechanical ventilation of patients in intensive care units, which has the potential of enabling safer, automatic ventilation strategies, possibly preventing the unnecessary death of tens of thousands of patients every year.

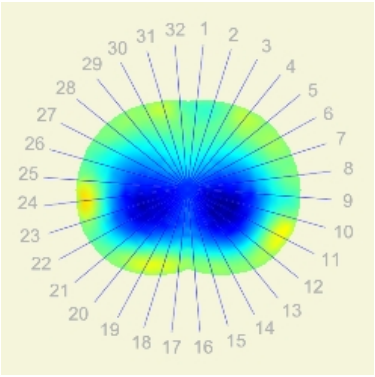

EIT tomographic images of the thorax region